TRIBOLOGY AND CONDITION MONITORING OF COMPOSITE BEARING LINERS FOR INTELLIGENT AEROSPACE BEARINGS

Konstantinos Karras

Thesis submitted in candidature for the degree of

Doctor of Philosophy at Cardiff University

Tribology Group

Cardiff School of Engineering

Cardiff University

September 2018

Declaration

DECLARATION

This work has not been submitted in substance for any other degree or award at this or any other university or place of learning, nor is being submitted concurrently in candidature for any degree or other award.

Signed ………………………………………….……(candidate) Date …………………….……………………

STATEMENT 1

This thesis is being submitted in partial fulfilment of the requirements for the degree of ………(insert MCh, MD, MPhil, PhD etc, as appropriate)

Signed ………………………………………….……(candidate) Date …………………….……………………

STATEMENT 2

This thesis is the result of my own independent work/investigation, except where otherwise stated, and the thesis has not been edited by a third party beyond what is permitted by Cardiff University's Policy on the Use of Third Party Editors by Research Degree Students. Other sources are acknowledged by explicit references. The views expressed are my own.

Signed ………………………………………….……(candidate) Date …………………….……………………

STATEMENT 3

I hereby give consent for my thesis, if accepted, to be available online in the University's Open Access repository and for inter-library loan, and for the title and summary to be made available to outside organisations.

Signed ………………………………………….……(candidate) Date …………………….……………………

STATEMENT 4: PREVIOUSLY APPROVED BAR ON ACCESS

I hereby give consent for my thesis, if accepted, to be available online in the University's Open Access repository and for inter-library loans **after expiry of a bar on access previously approved by the Academic Standards & Quality Committee.**

Signed ………………………………………….……(candidate) Date …………………….……………………

Summary

This thesis sets out to develop a condition monitoring technique for self-lubricating composite liner bearings. Self-lubricating bearings have been widely employed within the Aerospace industry since the 1950s. The focus of this thesis is primarily given towards helicopter main rotor applications, where self-lubricating bearings are located within the pitch-control link rodends. Such bearings are designed to be subjected to reciprocating motions and due to their conforming geometry they are able to handle high magnitude loads. Through the use of coupon and full-bearing test benches, an understanding of the wear characteristics of the liner composite is achieved, leading to the development of a series of condition monitoring techniques. Temperature and Acoustic Emission (AE) are chosen as the two focal points for experimental data gathering.

Within a helicopter's main rotor pitch control system, it can be assumed that all pitch-control bearings function at identical operating conditions. This assumption gave rise to a comparative condition monitoring technique being developed. Methods such as cross-sample correlation and creation of control charts are employed with successful outcomes. Acoustic Emission monitoring was successfully utilised in order to identify tribological condition changes with respect to the sliding contact surface. Such changes occur, as the liner material is consumed and in time transitions from a PTFE rich to a glass fibre rich composition. The wear depth of such transition is always constant and it's detection can therefore be employed as a condition monitoring technique.

A self-developed Acoustic Emission analysis technique was also successfully created, where the reciprocating nature of the sliding contact is exploited. Outcomes from such technique are compared with conventional methods such as RMS.

Acknowledgements

I would initially like to thank my academic supervisors, Dr Alastair Clarke, Dr Rhys Pulling and Dr Roger I. Grosvenor which have been enormously patient with my incessant questions throughout the PhD programme. Through your teachings in my undergraduate and post-graduate years at Cardiff University, you are all the reason I have become the engineer I am today. A very special gratitude goes to the EPSRC who funded this project through a joint award with SKF, which without this financial aid I would have never had the opportunity to participate in this mind expanding activity.

A huge thank you to my industrial sponsors, Mr Michael Colton and Dr Grant Dennis which have provided me with opportunities within SKF of which I could have never dreamed. You have supported me through a lot of tough times over the past four years and have become my close friends in the process, and for that I am grateful.

Many thanks to my childhood friends Matt, Jann, Lloyd, Aneesh, James which have stayed true to SEB and to my recent friends Zach, Jake, Krag, Adam, Chris and Richard which made my university years something to remember.

Finally, I am beholden to my family; My partner, Rhian Williams, which has kept me sane and ticking away throughout the process; my mother and father, Vivi and Kyriakos Karras, which made the hard decision to leave everything behind and move to Wales for the sake of their children; my sister, Andrianna Karras, which I miss a lot, that helped me grow up with a good heart and respect for others; and last, but certainly not least, my little brother by 10 years, Panagiotis Karras, which through his eyes I relive my childhood every day.

Contents

Chapter 1: Introduction

1.1 Project Background

This thesis focuses on the development of a number of condition monitoring techniques with the aim of monitoring the health state of self-lubricating plain bearings in helicopter main rotor pitch control applications. Such rotorcraft components are critical parts due to their paramount importance within the flight control system, failure of which can have catastrophic effects. A recent publication by Aerosurrance (2017) demonstrates the extent of damage that can occur if such bearings fail during flight. The report consisted of an investigation carried out into an incident on a Bell 429 tail rotor pitch change link spherical bearing failure. An image of the failure can be seen in Figure 1 –.

Figure 1 – Failed pitch control link upon the tail rotor assembly (left), Disassembled components of the tail rotor system with damaged link and bearing highlighted (right) (BOARD, 2017).

The failure was attributed to fretting, corrosion, micro pitting and wear of the bearing components. A detailed image of the failed rodend is shown in Figure 2.

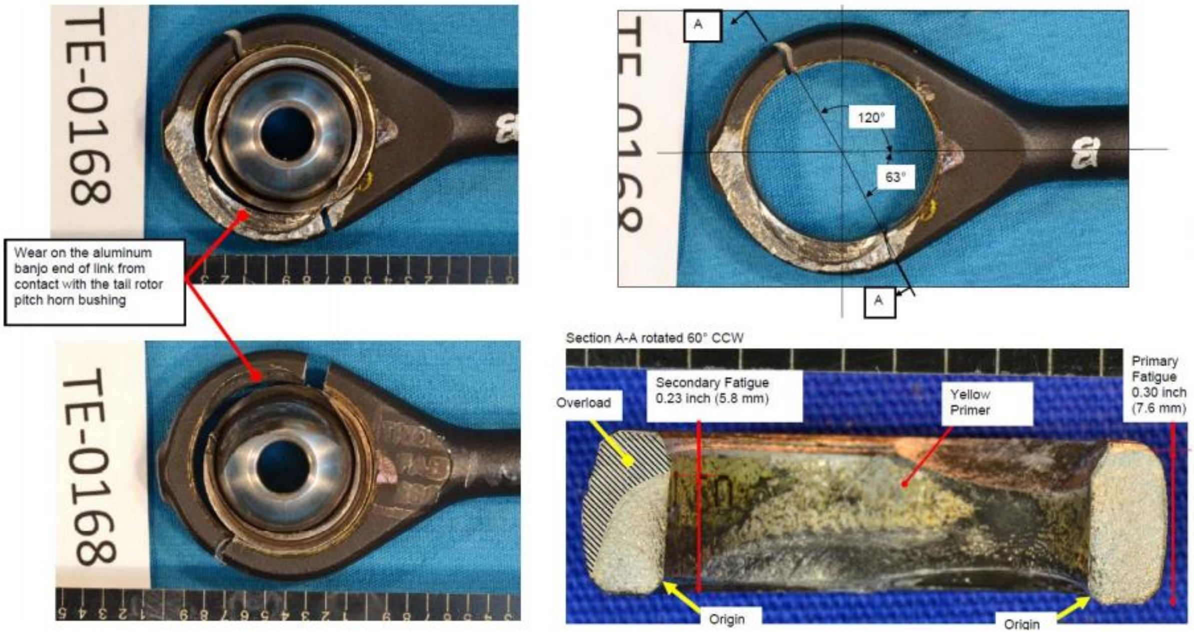

Figure 2 - Failure investigation of the pitch control link and bearing (BOARD, 2017).

This incident occurred in 2015 and the investigation was reported in 2017. Prior to this report there had been a number of similar failure reports regarding such critical components. An active damage mitigation system in the form of a condition monitoring package had therefore to be created. SKF in conjunction with Cardiff University initiated the research programme in order to develop such a system. The project scope was restricted by certain conditions which had to be met by the condition monitoring system as proposed by SKF as the industrial sponsor. These included the following:

1. The sensing instrumentation had to be of a non-intrusive nature.
2. The developed system should have the ability to be retrofitted onto existing aircraft.
3. The algorithm developed for damage detection should focus on the cross comparison of the monitored parameters of each bearing component on the main rotor. A single pitch control link, as seen in, as seen in Figure 1 (right) consists of an upper and lower

spherical bearing. A rotorcraft usually consists of 3 to 5 rotor blades, which each have their pitch controlled by a pitch link.

1.2 Uses of self-lubricating materials in industry

Self-lubricating spherical bearings are found in a wide range of applications which range from motorsport and rail to their largest field of use, the aerospace industry. Motorsport applications of such products include high load automotive suspension members and steering controls, while for rail applications such bearings are incorporated in rail bumpers, slide pads, wear plates, emergency handbrakes and bushings (Biering, 2014).

The majority of the market for self-lubricating bearings lays within the aerospace sector with a combined market share of 85%. The breakdown within this percentage includes, a 42% market share of civil rotorcraft, 18% military rotorcraft, 22% civil fixed wing aircraft and a 5% military fixed wing aircraft (SKF, Internal Sales Report, 2014).

Self-lubricating bearings are used widely within the aerospace industry where the burden of maintenance is costly in both financial and flight efficiency terms. These bearings have been branded in the past as 'maintenance free' due to their ability to operate without regular inspection or re-greasing intervals. Their ability to operate efficiently, along with their predictable failure modes, due to the consumable polymeric liner, has allowed these types of bearings to be used in many fixed and rotary-wing aircraft applications as shown within Figure 3 and

Figure 4.

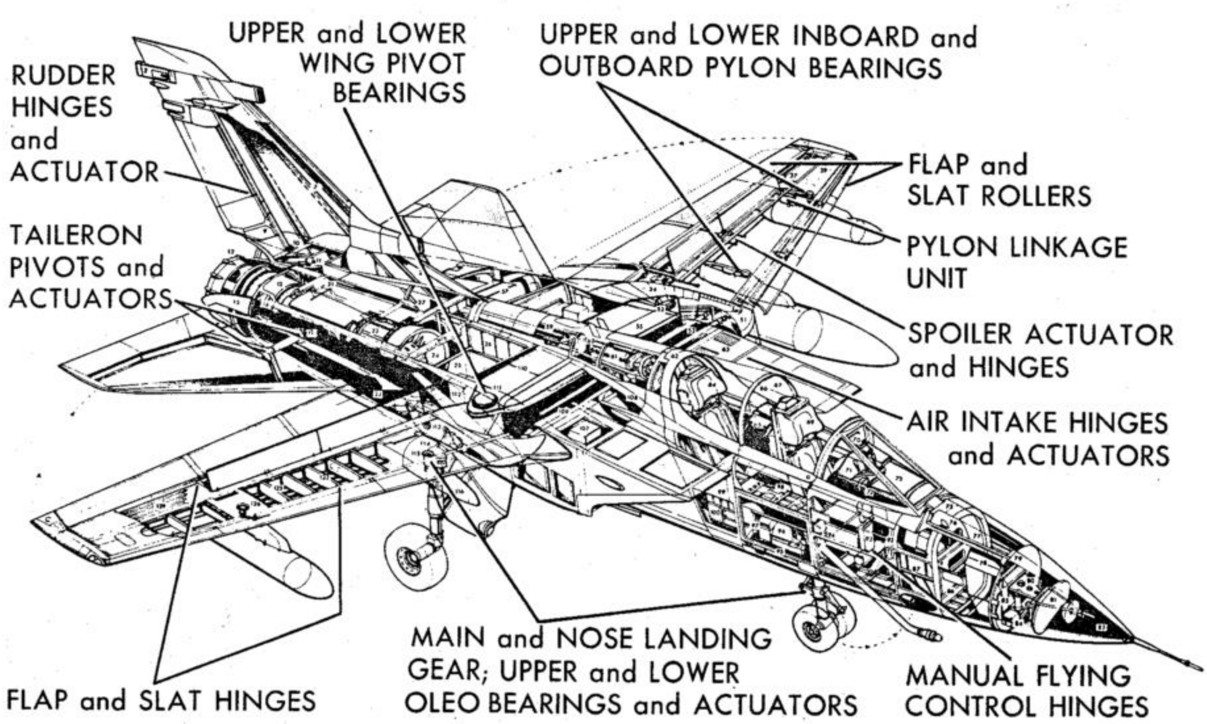

Figure 3 - Labelled fixed wing aircraft parts where self-lubricating bearings are employed. (Lancaster, 1982)

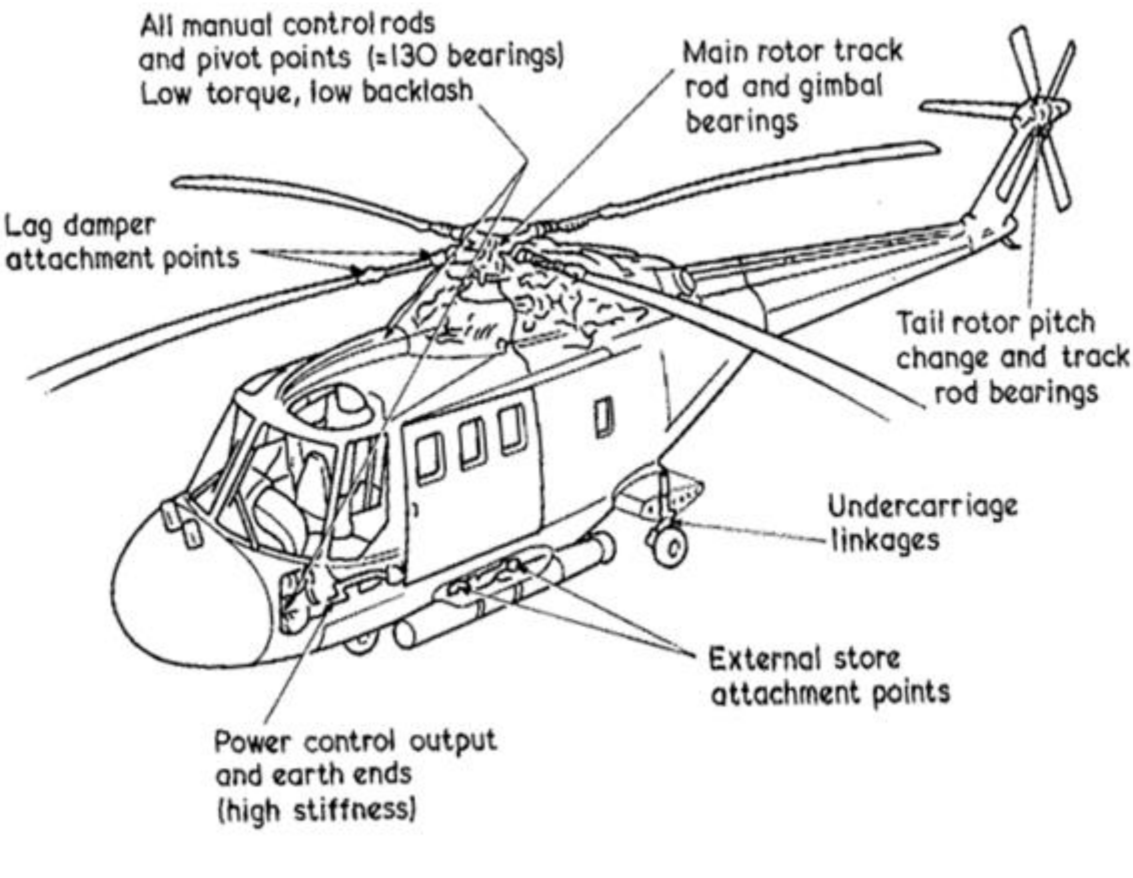

Figure 4 - Labelled rotorcraft parts where self-lubricating bearings are employed. (Lancaster, 1982)

The main focus of this thesis is on the pitch control bearings of the main rotor of a rotorcraft.

Figure 5 and Figure 6 show how these components are assembled on a main rotor.

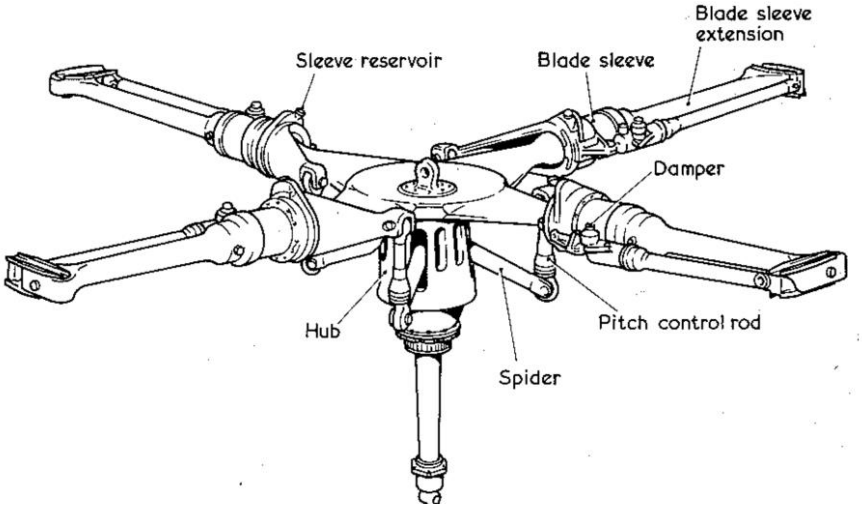

Figure 5 - Drawing representation of a main rotor of a rotorcraft, with the focused 'pitch control rod' labelled. (Lancaster, 1982)

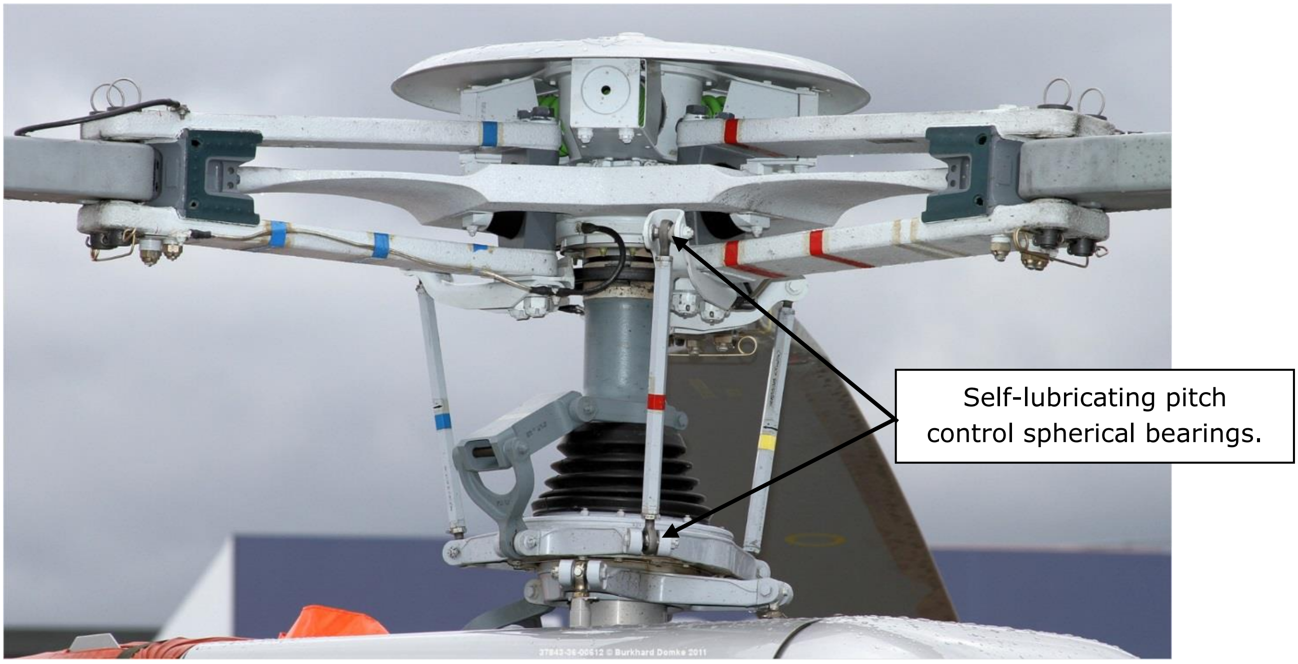

Figure 6 - Main rotor head of an Airbus Helicopters H125 rotorcraft with the its self-lubricating pitch control bearings labelled.

1.3 Current problems facing helicopter operators

The work in this thesis forms part of a wider project which, through the creation of a condition monitoring technique, aims to tackle a number of issues linked with maintenance costs for the helicopter customers. The current typical maintenance interval of pitch control bearings consists of a manual inspection, on the ground, for every 50 flight hours. A further full disassembly of the main rotor's blades and pitch links is required every 150 flight hours. Grounding the aircraft comes at a severe cost to the aircraft owner as each maintenance interval costs around £30,000 which amounts to 24% of the aircraft's annual operating costs. During the maintenance interval, if the bearings are deemed to have exceeded 0.125mm of wear, out of the possible 0.26mm total liner thickness, the pitch link is replaced as a whole with new bearings fitted in both the upper and lower sections (Bell, Private Communications., 2018).

The following section has been removed for copyright reasons and/or confidentiality reasons.

1.4 Aims and objectives

The main aims and objectives of the research project were created in order to aid the development of the condition monitoring algorithm. The contribution of each objective to the overall development of a condition monitoring capability is described below.

1.4.1 Technology for bearing monitoring

During this research programme, a test bench (Rig Q) designed and created by Cardiff University, through the support of the industrial sponsor (SKF), was to be further developed. This test bench was planned to be versatile in the parameters of which it could monitor, in order to allow for new technologies to be incorporated and evaluated if required.

Due to the length of time required for a full bearing test to be completed on bearing test rigs at the industrial sponsor (approximately one month), the test bench had to operate under accelerated conditions. Furthermore, with the focus of the condition monitoring technique being of a comparative nature, the test bench was designed with the capability of testing four coupon bearing liner samples simultaneously under the same environmental conditions.

1.4.2 Testing facilities

In parallel to the test bench development and operation, the existing test benches at SKF Clevedon were to be utilised in order to allow for the gathering of real bearing data. This would contribute to an understanding of the extrapolation of the findings made within the coupon testing to full scale bearing test results.

1.4.3 Acoustic Emission monitoring

Acoustic emission (AE) monitoring is a technique which, prior to this project, had been extensively applied to rolling element bearings and was a technique in which Cardiff University has significant expertise. Initial feasibility studies were to be conducted and, should AE be proven useful, further testing and analysis technique development was desired. Furthermore, such a technique satisfied the criteria set out by the industrial sponsor (SKF) regarding a non-intrusive monitoring method.

1.4.4 Temperature monitoring

Identified as a by-product of the frictional power dissipated during relative sliding motion, this type of monitoring technique was to be investigated. The main framework behind the project was based upon thermal monitoring. SKF possesses large temperature data sets from tests of their current products and had previously noted that during the failure stage of the bearing, a temperature increase occurs prior to failure. It was therefore envisaged to detect this temperature deviation of a defective bearing when compared to a healthy one.

1.4.5 Comparative monitoring

Regardless of the signal under consideration, an algorithm was to be created which would detect any abnormal signal deviation. This would be achieved by comparing the faulty signal with the rest of the operating bearings, which would act as the healthy references. The reason behind the creation of such a system was due to the lack of flight data available and therefore a healthy baseline signal cannot be defined. Furthermore, due to the rotorcraft's mission dependency, differences in flight environment (i.e. sand, snow *etc.*) would not allow for a perfect baseline signal signature to be determined.

1.5 Thesis outline

Chapter 2: *Review of relevant Literature:*

A review of relevant literature was conducted in order to evaluate the gaps in the current scientific knowledge. Within this study a history of tribology, along with the progression and manufacture of woven fabric bearing liners is presented to the reader. In turn, the wear mechanisms of such bearing liners are discussed, which range from the start of the bearings operation all the way to the failure region. Factors which affect bearing performance are then discussed, giving the reader a view of the limitations of the product as well as, currently available bearing monitoring techniques which include vibration monitoring, oil debris analysis, ultrasonic analysis, thermal and acoustic emission monitoring.

Chapter 3: *Overview of Experimental Test Facilities.*

An introduction to the relevant test benches utilised within the PhD programme is given, with a special focus awarded towards the Cardiff University-developed test bench; Rig Q. A detailed description of its mechanical components and instrumentation is provided, along with its operational conditions.

Chapter 4: *Rig Q – Testing results.*

The results obtained by Rig Q are presented with regards to wear and temperature. The successes and issues faced while the testing was being conducted are also discussed. Temperature and wear results are accompanied by profilometry measurements and further polymer transfer layer investigations are conducted upon the counterfaces. Finally, the outcomes of the chapter are discussed and linked to literature.

Chapter 5: *Test Bench Results – Temperature.*

The development of a comparative algorithm based on temperature monitoring is shown within this chapter. The progression of development is shown in stages and comments are made upon the accuracy and reliability of the employed techniques. Finally, a thermal study was conducted, where results from the full-bearing tests were manipulated to try and produce a useful output signal with relation to wear depth.

Chapter 6: *Test bench results – Acoustic Emission.*

The testing methodology, instrumentation and procedure of acoustic emission monitoring is described within the chapter. The results obtained from this section are compared against experimental results obtained during the research programme from full-bearing test benches. Finally the feasibility of the proposed methods is discussed with regards to power consumption and sensor integration.

Chapter 7: *Creation of a Time-Domain analysis technique for reciprocating wear conditions.*

Through the use of the gathered acoustic emission data, the author describes the development of a novel data analysis technique for acoustic emission wear monitoring, specifically designed for reciprocating conditions. The technique is based on a time domain analysis and the results are compared to the conventional analytical methods described within chapter 6.

Chapter 8: *Discussion, Conclusion and Future Work.*

A discussion of the research is conducted, where the advantages and disadvantages of each technique are presented. Furthermore, the feasibility of each of the proposed methods is evaluated with respect to the typical challenges faced when integrating new technology upon aircraft. Finally, a short description of the future steps which are in need of exploitation subsequent to this study is given.

1.6 Contribution to knowledge

Through the course of this thesis, coupon and full bearing data from tests of self-lubricating liner materials are used to develop novel analysis techniques. These techniques are created in order to monitor the wear progression of self-lubricating bearings without the need for intrusive instrumentation.

The temperature algorithm developed predominantly used knowledge from the field of econometrics and manufacturing engineering, in order to develop a system which is robust to environmental noise. Such a technique is not currently present within literature for the specific application of self-lubricating bearings.

In addition, although acoustic emission has been employed to link polymer lubricants and counterface roughness with the acoustic emission amplitude, no such work has been reported in the literature to use it as a wear monitoring technique for these materials. Finally, a novel acoustic emission time domain analysis technique was developed which can be applied to any reciprocating conditions. The developed analysis technique directly agrees with conventional techniques used within literature.

1.7 Summary of outputs

- An extensive database of temperature, wear and acoustic emission results recorded during both coupon and full bearing testing has been created.
- A Cardiff University coupon testing facility has been developed for research purposes. The test bench is capable of expanding its sensing techniques further through the use of an open LabVIEW code created by the author.
- Future expansion of the test bench with regards to the instrumentation and mechanical structure of the test bench was also provided in order to aid subsequent research projects.
- A thermal monitoring technique was developed which is capable of detecting the transition of material composition within the SKF self-lubricating bearing liners and therefore can relate these detected material changes back to a specific wear depth.
- A thermal study was conducted upon a full bearing test regarding thermal recovery. This method tries to link the time taken to reach thermal equilibrium of the bearing following a pause in operation, with the wear depth of the bearing at each bearing cooling period.
- Acoustic emission monitoring has been unutilised to detect the progression of wear and has been successful in identifying the material composition change of the bearing liners as stated above.
- A novel analysis technique has been developed using acoustic emission waveforms. This technique can be applied to any reciprocating sliding wear conditions.

Chapter 2: Review of relevant literature

2.1 History of tribology

One can picture a scene involving Neanderthal man, cast some 200,000 to 300,000 years ago where a number of key essentials for survival come to mind. Having observed the immense power of the 'mysterious' element known to us as fire, Neanderthals decided to take matters into their own hands and bypass the patient wait of natural events, such as thunderstorms. The artificial creation of fire was achieved by rubbing sticks together at high speed to generate heat, perhaps the first intelligent use of friction. Defining 'friction' was a process carried out by the Latin community roughly dating in the years of 1575 – 1585 A.D. Following this, the field of science revolving around frictional forces was established and officially named as the field of 'Tribology' in 1966 by a British mechanical engineer, Dr Peter Jost (Sutton, 2013). The word is derived from the Greek verb "τρίβω" (tribo) meaning "I rub" and the suffix "λογία" (logia) meaning "knowledge of"'. By definition, as stated in the Oxford English Dictionary, the word tribology translates to: 'The study of friction, wear, lubrication, and the design of bearings; the science of interacting surfaces in relative motion'.

Interestingly, this particular field of science can be concerned with both the desired generation of friction and the minimisation of friction. For the purpose of this thesis, the author focusses on the detection of the physical by-productions of tribological contacts, such as frictional heating and acoustic emission, during the relative sliding motion between interacting surfaces. In turn, the physical parameters recorded were related to the wear state of the sliding surfaces, in this case self-lubricating bearings. Before evaluating the recent advancements of such self-lubricating technologies, a brief historical overview of is given of the actions and discoveries which helped shape and define the fundamental laws of tribology.

Dating back to 3500 BC, the ancient civilisation of Egypt was in the process of constructing some of the most memorable burial grounds known to human history which served as a resting place for their great leaders, the Pharaohs. These buildings are now known as the Pyramids. During construction large stone carved blocks needed to be transported without causing damage to their structure. A solution was developed where large cylindrical logs smeared in olive oil were placed underneath the stones allowing them to slide smoothly to their destination. This is the first recorded form resembling a rolling bearing motion along with an initial form of lubrication (Carnes, 2005).

Leonardo da Vinci undertook the first systematic study of the effects of friction in 1498-1500. Having understood the importance of friction within mechanical machines, he composed a set of experiments which produced some of the first laws and theories of tribology. Having closely observed the behaviour of a rectangular block in relative sliding motion over a flat surface, he was able to formulate the following statements. Firstly, he speculated that 'The force of friction is directly proportional to the applied load' and secondly, that 'The force of friction is independent of the apparent area of contact' (Majumdar, 2008). Unfortunately his inventive and ground breaking work remained unpublished for a long period of time (as late as 1960), but evidence of these experiments remained within his personal journals. In a recently published paper by Pitenis & Dowson (2014), da Vinci's frictional experiments were recreated through the use of modern equipment in order to evaluate his findings. This paper combined both history, engineering and physics in order to replicate the working laboratory conditions that were expected to be present at the time of the findings roughly around the years of 1470-1500.

The three findings in question consisted of:

1) Friction is independent of aparent contact area.
2) The resistance of friction is directly proportional to applied load.
3) Friction has a constant value of μ = 0.25.

While the first two of the above findings were proven to be correct by Pitenis & Dowson's experiments, the third observation could only be achieved under certain sliding conditions. These conditions aimed to replicate the nature of the experimental procedures which were available to da Vinci at the time. These included the use of roughly cut wooden blocks which were conditioned in order to replicate repeated handling. In order to achieve this the surfaces were smeared with natural oils found in fingertips and hands, along with the application of dust as it would have been found in the surrounding air (Pitenis & Dowson, 2014).

Due to the cryptic nature of da Vinci's unrevealed discoveries, the above hypotheses were independently discovered verified by Guillaume Amontons in 1663-1705 and Charles-Augustin Coulomb in 1736-1806 respectively. This work resulted in the following three fundamental laws of friction, still applied to engineering problems to this day (Phakatkar & Ghorpade, 2009):

1. The friction force resisting the sliding at the interface is directly proportional to the normal load. (Amonton's 1st Law)
2. The friction force does not depend on the *apparent* area of contact. (Amonton's 2nd Law)
3. The friction force is independent of velocity once motion starts. (Coulomb's Law)

Alongside da Vinci's experiments, there existed pencil sketches which resembled modern bearing designs (Figure 8). Speculation of da Vinci's inspiration by scientists indicates that a lot of his ideas had been produced as a bi-product from his time spent working as a hydraulic engineer, under employment from the Duke of Milan (Bearing Specialists Association, 2014).

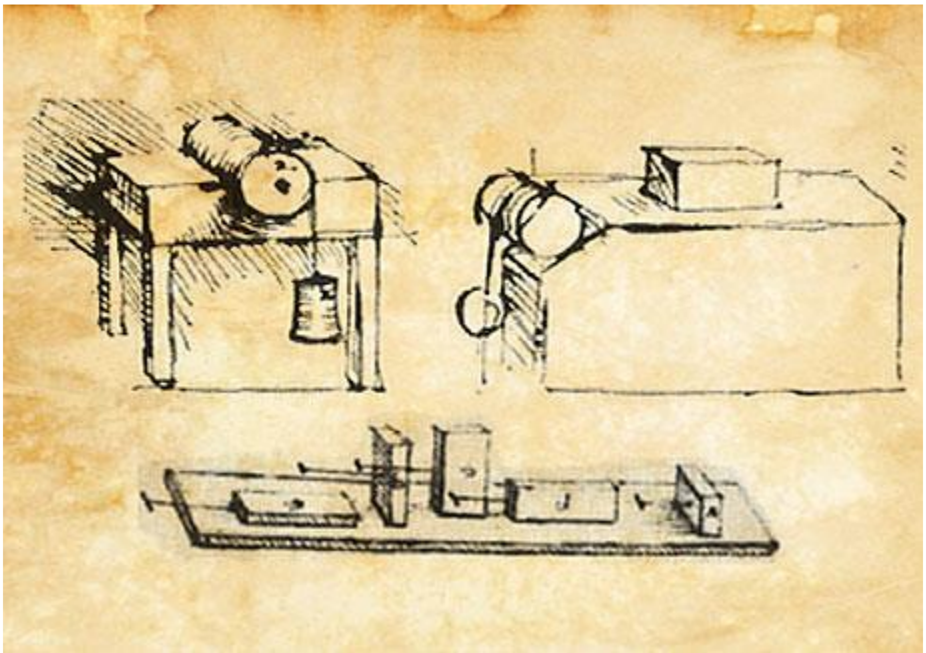

Figure 7- Sketches of Leonardo da Vinci's bearing examples. Image obtained from www.asme.org

Following these unpublished findings, a period of rapid development of industrial manufacturing processes was initiated by the increasing popularity of iron during the 1700s. Since iron started replacing wood in many industrial processes, its material properties were deemed perfect for technological progression. With the introduction of the turning lathe and the boring mill in the mid-1700s, more precise bearing designs were required to match the operational efficiency of these newly developed machine tools but unfortunately iron was not widely used as a replacement within the bearing itself and wooden bearings were still in widespread operation. Even though the first caged-roller bearing design was produced by clock maker John Harrison in the 1740's, it wasn't until 1794 that the Welsh inventor named Philip

Vaughan became the first patent holder for the well-known ball bearing mechanism (Figure 9) (Rowland, 1974).

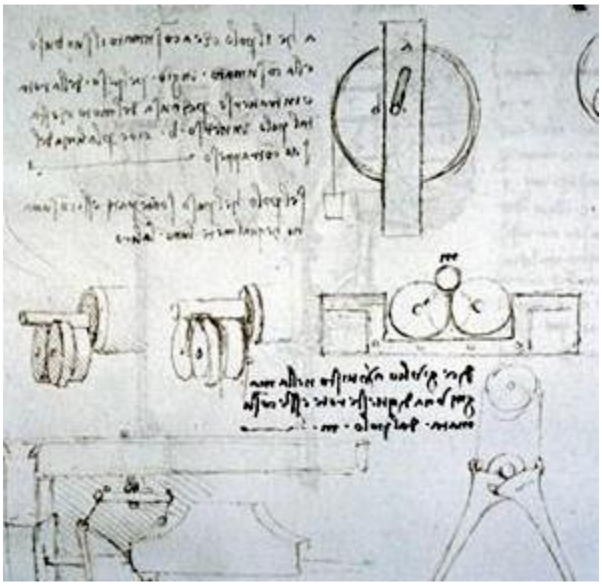

Figure 8 - Patent handed by Philip Vaughan representing the first ball bearing. Image obtained from www.patentpending.com

Whilst the concepts existed for producing such complex rolling element bearings, available metals had not advanced sufficiently to achieve critical load capabilities of such designs. In 1839 Isaac Babbit invented an antifriction alloy, used for plain bearings, with a relatively low melting temperature which allowed the first formation of ideal bearing surfaces. Complementing this 'Babbit Metal', the steel making process developed within the years of 1813-1898 leading to the gradual replacement of wooden bearings, with steel ball bearing designs becoming predominant (Bearing Specialists Association, 2014). Steel ball bearings from that point onward became widely used in the 20th century in industries such as aerospace, motorsport, and new machining processes.

This thesis focusses on aerospace bearing applications. In aerospace applications such as control mechanisms, where oscillating motions are experienced, rolling element bearings experience high maintenance costs and unpredictable or premature failure. For these applications, and many others within aircraft, plain spherical bearings are widely used, such as that shown in Figure 10. For industrial applications, such bearings are often grease lubricated, but for aerospace and other applications where minimal maintenance is required, polymeric wear liners are used, employing materials developed for optimum frictional and wear characteristics, along with load carrying capabilities which make them ideal for self-lubricating bearing designs, acting as the solid lubricant constituent within the mechanical design.

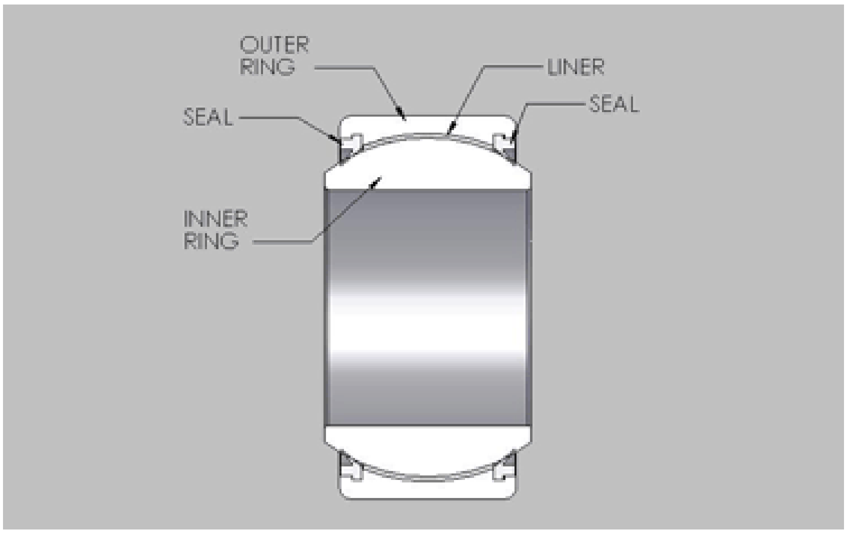

Figure 9 - Design of a self-lubricating plain bearing. The component marked as 'Liner' consists of the solid lubricant. Image obtained from www.nationalprecision.com/spherical-plain-bearings/engineering.php

To aid the understanding of such materials under operation, Figure 10 shows a self-lubricating bearing's composition with respect to its sliding surface composition.

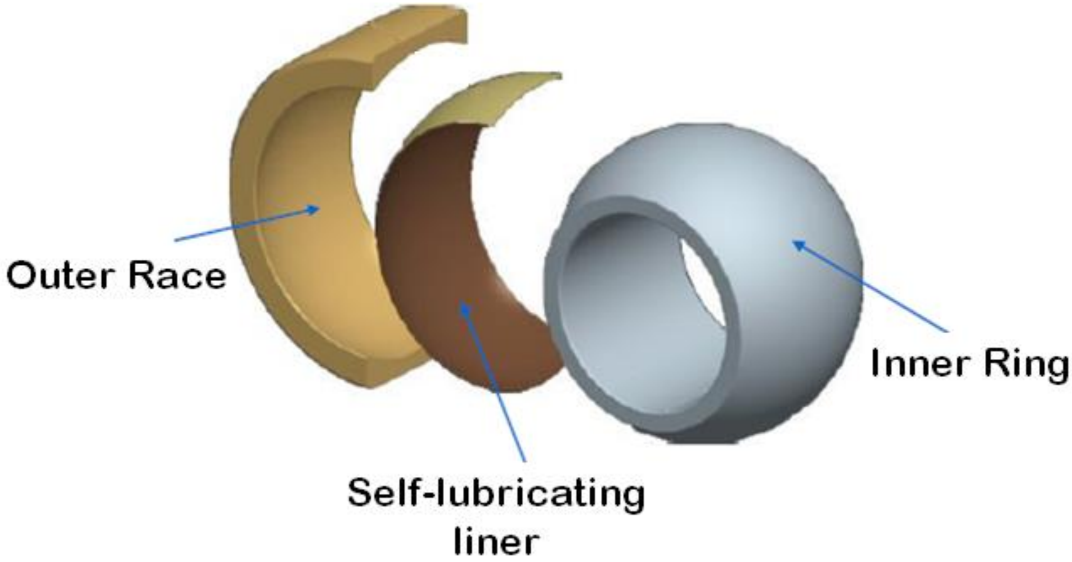

Figure 10 - Deconstructed self-lubricating bearing design showing the three fundamental components of such bearings (Bernard, 2011).

The three components labelled in Figure 11 are the outer race, the inner ring and finally the self-lubricating liner of a self-lubricating spherical bearing. The outer race component is responsible for the static load strength of the component. Its second useful feature is the provision of a concave spherical surface to which the self-lubricating liner can be bonded, located on the inside of the outer race. The self-lubricating material provides an intermediate sliding surface between the outer and inner ring. Its primary operation is to be slowly consumed throughout the bearing's operational life by adhesive or abrasive wear. While being consumed, the polymeric particles found within the liner composite, are released to the sliding environment and provide a low friction transfer layer. This layer is predominantly found upon the sliding surface of the inner ball in the form of deposited polymer particles. When such a transfer layer is achieved upon the inner ball, a steady state of wear rate is established. In order to accelerate the rate at which the transfer layer is established, the inner ball is surface treated through numerous manufacturing processes in order to achieve the desired sliding surface (Bell, Private Communication, 2017).

2.2 Self-lubricating materials

Solid lubricants have been developed over the past 70 years to replace well established liquid lubrication techniques for applications where maintenance of rotating parts is difficult to be achieved regularly due to geometric constrictions and application restrictions such as during flight. Due to their consumable nature, solid lubricants which exist within a bearing system can be described as having predictable failures, i.e. the bearing reaches the end of its life when all the solid lubricant has been converted to wear debris. This nature of operation allows the bearing system's operators to assign a number of in-application hours, during which the bearing is said to be unlikely to fail, which is highly desirable within the aerospace industry.

Furthermore, self-lubricating bearings are widely used where high sliding contact loads are present between two relative sliding components, due to their advantageous conformal geometry. As seen in Figure 10, the inner ball geometrically conforms to the outer race and during high load applications the load is allowed to dissipate over a large contact area. When compared to rolling element bearings, the same load within the application would create much higher pressures upon the outer and inner race of the bearing, due to a much smaller concentrated contact area. A disadvantage of such self-lubricating bearings exists when the type of relative sliding motion is taken into account. These types of bearings largely underperform in a rotating environment due to their inability to form a third body transfer layer upon the counterface / inner ball. This restricts their application to reciprocating conditions where the oscillatory motion favours the formation of such transfer layers. That said, these conditions are also those to which rolling-element bearings are less suited.

The following sections provide an overview of the literature which has been published regarding the optimisation of such self-lubricating plain bearings accompanied with a brief explanation of the wear mechanisms occurring during bearing operation.

2.2.1 Tribology of dry sliding

In order to understand the wear mechanisms involved during the lifetime of a self-lubricating plain bearing, the behaviour of the solid-lubricant was examined. The purpose of a solid lubricant within a bearing is to provide a low coefficient of friction throughout the bearing's lifetime without the need to be replaced or maintained, hence its widespread use within the aerospace industry. A financial study showed that throughout the lifetime of an aircraft, almost one third of the total life costs are spent on maintenance alone (Lancaster, 1982) and one can imagine the desirability of minimising this value as far as possible whilst maintaining appropriate safety margins. The way the solid lubricant is able to achieve low coefficients of friction during operation can be explained via the events which occur at a micro-scale. During relative sliding motion of two surfaces, surface roughness asperities come into contact and therefore provide resistance to the movement in the form of friction. A major factor which affects the magnitude of this frictional force is the relative surface roughness of the sliding surfaces, related to the number and shape of such asperities (Figure 12).

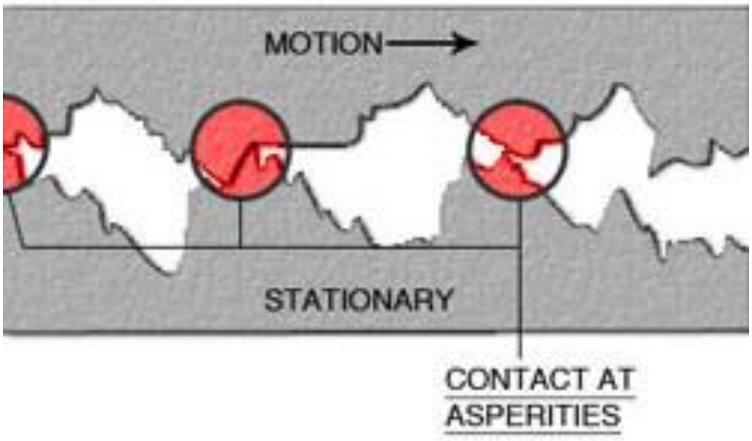

Figure 11 – Exaggerated scale representation of asperities of two sliding contact bodies. Image obtained from www.ussbearings.com/bearings_site/research_article/948/

As seen in Figure 12, during the sliding contact of these ‘peaks and valleys’, a small area of contact is present and therefore the contact pressures and temperatures (flash temperatures) which occur are of a large magnitude. A study conducted by Anderson (1982) showed that temperatures generated due to friction recorded near the bearing surface of a self-lubricating bearing are not an accurate representation of the maximum temperatures occurring during the sliding motion. This is attributed to the poor thermal conductivity of polymers which means that the flash temperatures generated at the asperities are significantly higher than the temperatures recorded at or near the bearing’s surface. Furthermore, he noted that it is extremely hard to accurately measure the exact flash temperatures produced and these can only be estimated via mathematical models which will only be as reliable as the assumptions made (Anderson, 1982). The incorporation of a solid lubricant has the primary role of ‘filling the gaps’ between asperities (Gnecco & Meyer, 2007). Achieving a larger area of contact, minimises the contact pressures present and in turn reduces the (thermal) degradation of the liner material.

2.2.2 Woven fabric bearing liners

Typical self-lubricating bearing textile liner fabrics, are formed from two major components, a self-lubricating material and a structural component. The self-lubricating material is responsible for providing a low coefficient of friction at the sliding surface of the inner and outer rings. Initially self-lubricating materials were explored in the form of polymers, with the favoured material being pure polytetrafluoroethylene (PTFE). PTFE was favoured due to its inherently low coefficient of friction, but unfortunately during low load or high speed operations, this polymer material did not perform as expected, reaching coefficients of friction of up to 0.3. Due to its poor structural composition, a reinforcing material was required in order to overcome the poor load carrying capacity of PTFE alone.

Ampep Industrial Products Ltd. (Clevedon, Somerset) was founded in 1963 and was the main supplier of self-lubricating bearings to the aerospace industry (N/A, 1970). Ampep's most popular self-lubricating material came in the form of a self-lubricating composite which was given the name "Fiberslip". Fiberslip's composition consisted of an interwoven PTFE/glass fibre composite in a phenolic resin matrix. Prior to Fibreslip's introduction, AMPEP primary product was Fiberglide which had similar material composition to the Fiberslip composite but its structural fibres were cotton rather than glass (Evans & Senior, 1982).

This Fiberslip material consisted of solid lubricant woven liner material and a structural backing. The woven liner is created through a weaving process where PTFE and glass fibre yarns were used to form a two-layer warp responsible for providing the desired lubrication and reinforcing properties. A labelled image of a textile weaving machine is shown in Figure 12 as an example of the manufacturing process.

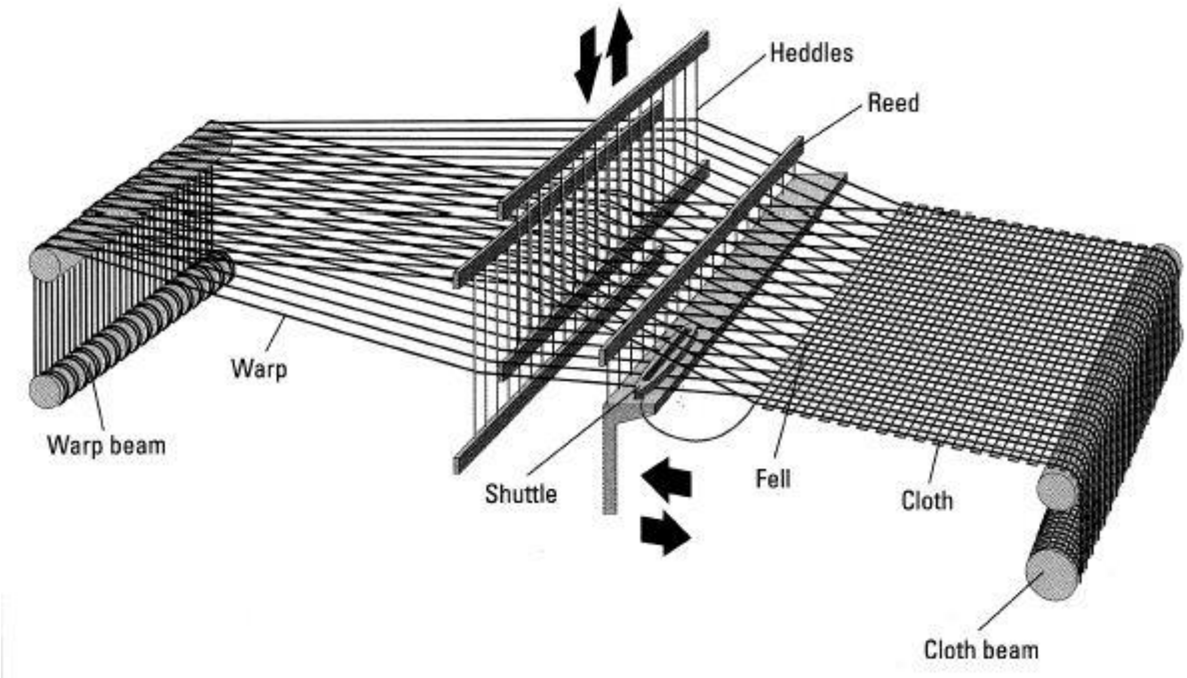

Figure 12 - Textile weaving machine with labelled components (Raaz, 2016).

This section has been removed for copyright reasons and/or confidentiality reasons.

As stated previously, a dry lubricant is responsible for providing a low coefficient of friction between sliding surfaces and a structural fibre of choice. As reported by Evans & Senior (1982), Polytetrafluoroethylene (PTFE) is widely used as a solid-lubricant due to its low friction, high load carrying capabilities and moderate freedom from stick-slip motion. Brockley, *et al.*, (1967) described the mechanism which causes a stick-slip motion as being attributed to a difference between the static and kinematic coefficients of friction during sliding.

By the addition of a structural element such as a steel backing in conjunction with PTFE, the liner is enhanced with desired characteristics such as increased load capacity and therefore reduced creep. The backing also increases the bearing's speed capability by providing a thermally conducting material, via which high temperatures within the bearing contact can be mitigated to the outside environment. This combination provides a reduced running clearance, achieved by an overall lower thermal expansion of the composite. This is backed up by Fusaro & Robert (1980), who state that a type of reinforcing component must also be used when using PTFE in dynamic applications, in order to increase the composite's thermal conductivity. PTFE, and polymers in general, are not good thermal conductors and therefore the reinforcing component plays the role of dissipating heat away from the contact region by acting as a conducting agent.

When discussing reinforcement of the liner material, Blanchet & Kennedy (1991) reported that upon the addition of a filler material to structurally enhance the PTFE component, the wear resistance can be increased by a factor of up to 1000. This was previously stated by Lancaster (1982), who confirmed that the structural component is responsible for aiding the lubricant to withstand the operational loads during its application. PTFE as a stand-alone solid lubricant tends to cold flow under load and therefore a structural reinforcement must be incorporated to increase its physical properties as a system. It had been previously concluded by Gardos (1981) that using glass fibres as a structural enhancement within the composite matrix resulted in much higher load-carrying capacity. A study by Evans (1981) reported that the load limit for dry bearings is mainly determined by the creep resistance of the composite as a whole and furthermore the allowable sliding speeds are limited by the maximum operating temperatures of the matrix.

This section has been removed for copyright reasons and/or confidentiality reasons.

Their development was reportedly accelerated by the growing aerospace industry demands for higher load carrying capability, but such composites had some disadvantages when compared to the previously used steel backing methods, including a lower thermal conductivity of the composite which prevented the heat dissipation from the contact area to the outside environment, along with a higher overall cost of construction due to more complicated manufacturing methods.

A third iteration of the material was introduced in the ‘90’s and was given the name of AMPEP XL. In this case, the self-lubricating liner composition was kept the same but the counterface material, which came into sliding contact with the self-lubricating liner, was surface treated.

The surface treatment method allowed the bearing as a system to heavily outperform the previous X1 liner, with reported performance increases of up to 350% (Harrison, 1990). These performance increases were published in the form of qualification testing results and are shown in Figure 13.

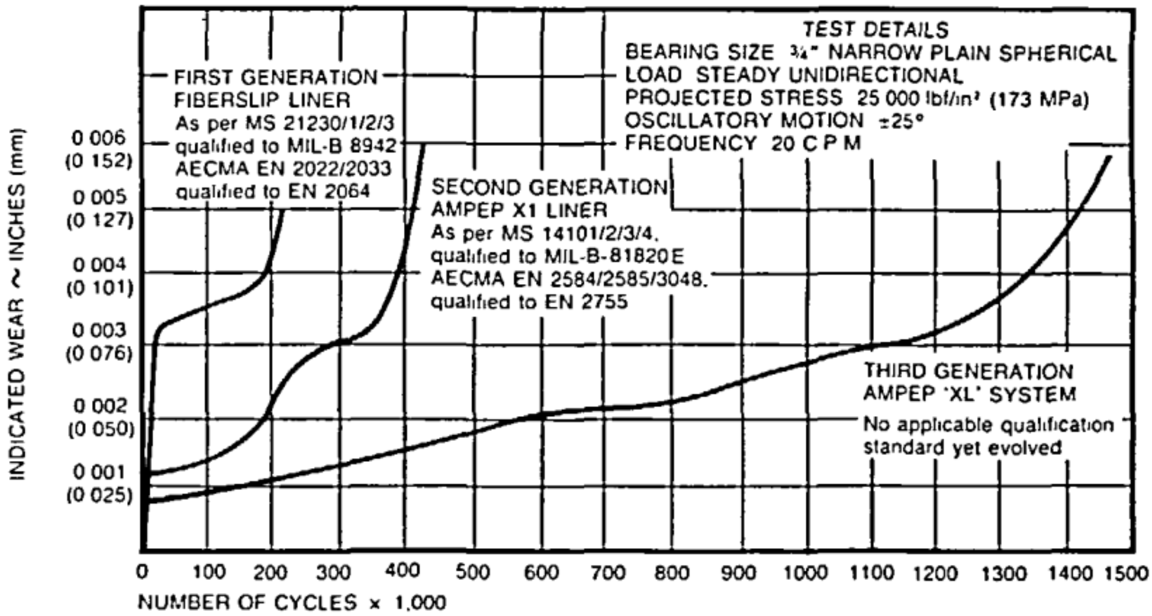

Figure 13 - Bearing performance increase of Fiberslip, X1 and XL technologies during qualification testing (Harrison, 1990).

Currently a woven structure consisting of PTFE as the dry-lubricant and glass fibre as the reinforcing material, is deemed the current market leading technology provided by SKF Aerospace. Achieving the desired mechanical characteristics for the material as a whole, was only made possible with the introduction of a phenolic resin matrix material, responsible for bonding the dry-lubricant and the structural fibres together (Figure 18).

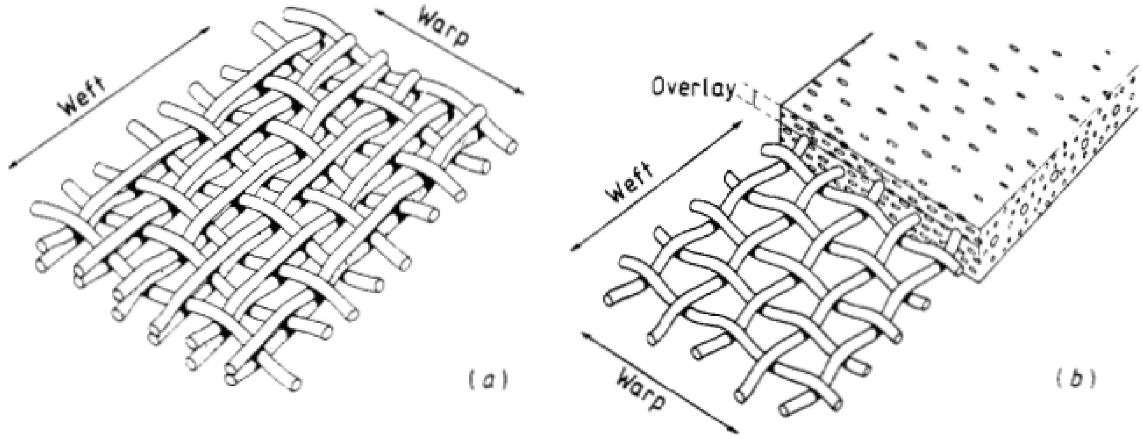

Figure 14 - Construction of typical dry-bearing liners (a) plain weave fabric + PTFE dispersed in resin and (b) PTFE fibre interwoven into fabric (Lancaster, 1982)

A study carried out by Lancaster (1981) showed the effects of altering the liner material by impregnating the matrix with different types of resins and in turn measuring the elastic modulus via ball-indentation compressions. Lancaster concluded by stating:

1) The intrinsic wear properties of the resins themselves are likely to differ.

2) The type of resin will influence the interfacial bonding between fibre and resin.

Investigations regarding the importance of the structural fibres within the matrix were also made by Giltrow & Lancaster (1967) who compared the wear rates and coefficients of friction of different polymers with and without structural fibres. As seen in Figure 15, when the polymers were reinforced by the structural fibres, both the wear rate and the coefficient of friction showed a considerable decrease which is desirable for bearing applications.

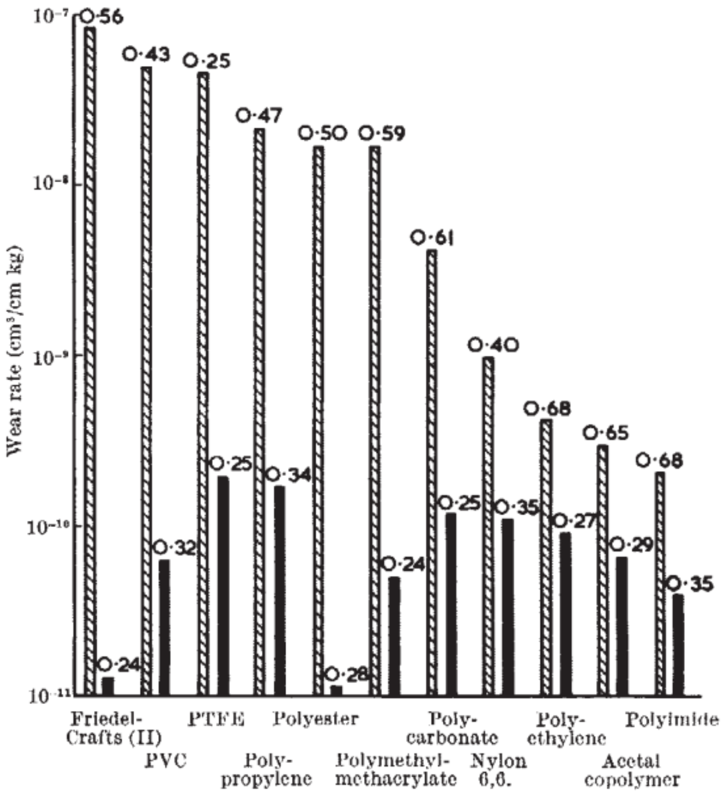

Figure 15 - Wear rates of polymers with (solid bar) and without (hatched bar) structural fibre reinforcement. The numerical value above the bars represents the coefficient of friction (Giltrow & Lancaster, 1967).

Efforts have also been made in the past towards altering the structural reinforcing fibres within the matrix, from the typical glass fibres to a more modern carbon-fibre material. Two types of carbon-fibre were used consisting of 'Type I' fibre, heat treated at 2500°C and 'Type II' fibre, heat treated at 1500°C. Both types exhibited superior composite properties when interwoven with a range of solid lubricants in comparison to their raw lubricant form and wear rates in some cases were reduced by a factor of up to 7000 (Giltrow & Lancaster, 1967). Figure 20 shows the findings of Giltrow & Lancaster (1967), with their results labelled as 'before' and 'after' carbon fibre incorporation.

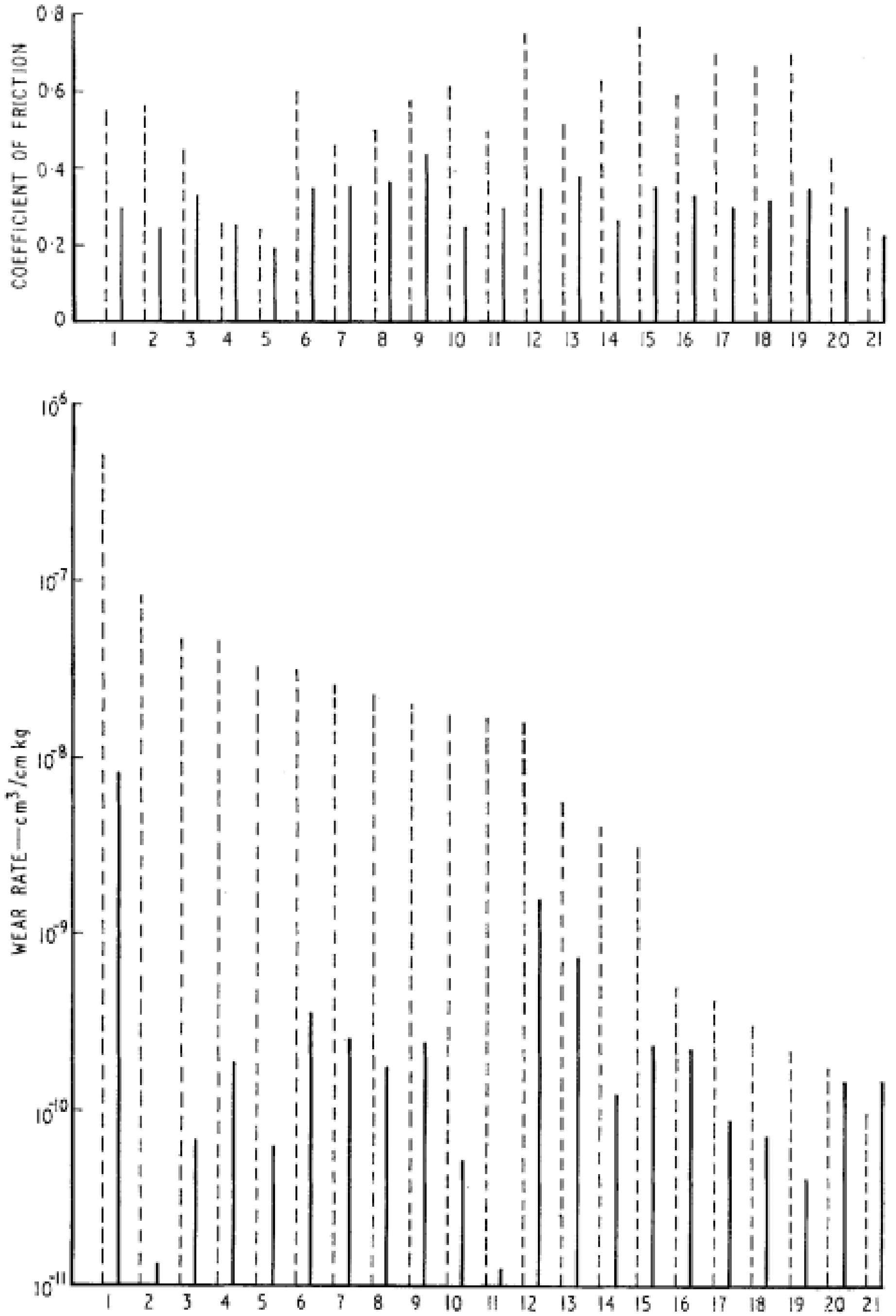

– – – Before. —— After.

1. Acrylonitrile–butadiene–styrene copolymer ('Lustran'), ABS.
2. Friedel–Crafts resin, Mk. 2.
3. Polyvinylchloride.
4. Polytetrafluorethylene ('Fluon, G.4'), p.t.f.e.
5. Polytrifluorochloroethylene ('Kel-F 81'), p.t.f.c.e.
6. Polyvinylidene chloride ('Saran').
7. Polyvinylchloride–polyvinylacetate copolymer ('Vinylite').
8. Polypropylene ('HM 20/70').
9. Epoxy resin ('815').
10. Polymethylmethacrylate ('Diakon').
11. Polyester ('SR 17449').
12. Polysulphone.
13. Polyphenylene oxide.
14. Polycarbonate ('Makrolon').
15. Phenolic resin.
16. Nylon 6:6 ('A 100').
17. Polyethylene (low density).
18. Acetal copolymer ('Kematal').
19. Polyimide.
20. Polyformaldehyde ('Delrin').
21. Polyethylene (high density) ('Rigidex').

Figure 16 – Comparison between conventional glass fibre (black bars) and carbon fibre (hatched bars) use as the structural fibre of within the self-lubricating matrix. (Giltrow & Lancaster, 1967).

Unfortunately, when compared with other types of thermosetting and thermoplastic materials reinforced by carbon fibre, it was found that no visible correlation was present and therefore it was concluded that the effect of fibre concentration with regards to the rate of wear was specific to each type of polymer. Although the results were not as positive as expected, it was concluded that the friction and wear properties of the tested composites were mainly controlled by the structural fibres rather than the solid-lubricant itself and therefore the structural fibres were responsible for supporting the majority of the applied load (Giltrow & Lancaster, 1967).

2.2.3 Wear mechanisms

Having understood the composition of the self-lubricating composite, the wear mechanism throughout the lifetime of a plain bearing could now be explained. For simplicity, the wear curve of the liner was divided into three sections (Figure 21).

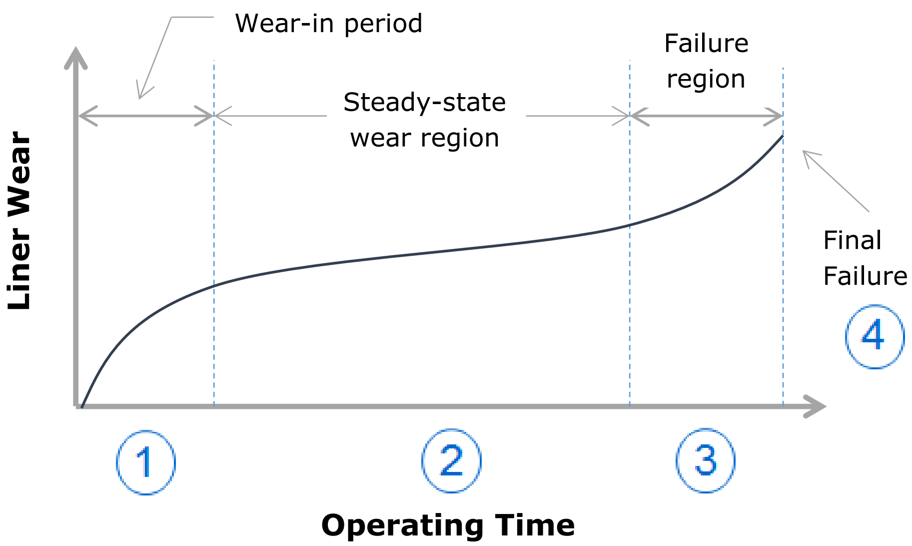

Figure 17 - Three stages of wear during the lifetime operation of a dry-lubricated plain journal bearing.

Initially the 'wear-in' period of the bearing was taken into consideration and a thorough investigation was conducted in order to quantify when this stage terminates. As seen from

Figure 21, when the liner material is initially subjected to a relative sliding motion, the rate of wear exhibited by the composite is of a high magnitude. This effect is due to the shearing and scoring of the composite during motion, caused by the asperities of the harder (usually steel) counterface. This abrasive wear mechanism, even though it may appear to be of a destructive nature, allows small particles of the PTFE solid lubricant to be detached from the liner in the form of wear debris. This debris transfers to fill the valley features on the surface roughness of the counterface material thus reducing:

1) the effective counterface roughness;
2) the localised contact stress;
3) the wear rate of the liner.

The wear debris, also known as ‘third bodies’, forms a transfer layer not only upon the counterface but these are also commonly generated on the surface of the polymer composite itself (Lancaster, 1981).

In order to investigate how the transfer layer of PTFE is formed upon the counterface, Pooley and Tabor (1972) devised an experiment where a PTFE rod with a hemispherical tip came into sliding contact with a glass substrate, at sliding velocities between 0.02 to 0.2 mm s^{-1}. The contact was loaded via a static load and the frictional force measured through deflection of a pair of leaf springs. It was reported that when third body deposition is occurring, the mechanism behind the transfer layer depends upon the PTFE chains being stretched out over the counterface, in order to form an extended chain crystal structure which has low shear properties and thus low friction. Furthermore Steijn (1968) had already reported that third body formation upon the counterface can be aided by the drawing-out of thin fibres or in-fact sheets of the PTFE polymer.

In the study, previously discussed, conducted by Lancaster (1981), it was concluded that the mechanical properties of the composite surface layer appear to influence the initial wear much more than the concentration and distribution of PTFE and it was also possible to speculate when this initial stage of wear terminates. It was stated that initial wear ceases either when the strength of the worn surface layer increases to some critical value or when the transfer layer composition reaches some optimum value to establish and maintain uniform, third-body films on the composite liner, its counterface, or both (Lancaster, 1981). Although specific values of such critical parameters were not investigated further, a 'rule of thumb' was created stating that the wear rate of a bearing in operation is roughly proportional to the counterface roughness and new studies have been initiated towards quantifying the adhesive bonding strengths of solid lubricants upon its counterpart metal substrates.

These types of studies regarding adhesive bonding strengths of solid lubricants are structured around chemical bonding forces between lubricant and metal substrates and take into consideration the micro structure and geometry of both constituents required for the formation of a third body transfer layer. To confirm the hypothesised transfer film mechanism, an investigation was carried out into the tribological properties of polyamide-bonded graphite fluoride films. In this study optical micrographs of wear tracks showed the presence of solid lubricant transfer films which were smooth and continuous (Fusaro & Robert, 1980). In turn this confirmed the speculations behind dry lubricant wear particles occupying the valley features between asperities of the counterface materials in order to provide lower contact stresses, lower flash temperatures, and lower coefficient of friction which combined allowed for optimum operating conditions.

Lancaster *et al.* (1980) carried out an investigation regarding the formation of a third body layer upon the counterface and the liner matrix itself. Counterfaces of different roughness were used in order to create a correlation between third body formation and surface roughness. It was initially found via optical examination, that transfer films increased in uniformity with both load and roughness but under further SEM investigation, it was found that the rougher counterfaces' asperities were only partially filled, whilst the smoother counterfaces appeared to have their depressions more fully filled. This absence of solid lubricant in the rougher counterfaces can contribute to further abrasive wear of the liner material when in sliding motion and therefore increase the wear rate.

In a study regarding the nature of the sliding motion, Lancaster *et al.* (1982) and Abarou *et al.* (1987) reported that wear rates in motions such as oscillation tend to have lower rates than those found in unidirectional sliding by a factor of up to 5, but this is heavily dependent upon the amplitude of the oscillatory movement. Previously, in an attempt to link the effect of the oscillatory amplitude with the wear of dry-bearing composites, Lancaster *et al.* (1982) concluded that a third body transfer layer is formed with greater ease in oscillatory conditions rather than under unidirectional motion. This in turn causes the coefficients of friction of dry-composites to be appreciably lower in oscillatory motion. To further investigate the effect of reciprocating motion amplitude upon the wear of materials such as self-lubricating composites, Abarou & Play (1986) focused on the mutual overlap coefficient (MOC) during the oscillatory motion. This was done using a pin-on-disk wear testing machine, where the self-lubricating material formed the pin and the counterface materials were manufactured in the shape of flat steel disks. The MOC is described as the area of contact on the counterface which is always in contact with the oscillating pin during reciprocation. A series of tests with different materials, of which one was PTFE with reinforcing glass fibres in a polyamide PA66 resin, were carried out and it was concluded that for small MOCs, i.e. MOC < 0.5, i.e. low levels of mutual overlap during reciprocation, the wear rate seemed to decrease in all the tested materials. It was concluded that this decrease in wear rate was credited to the contact length which allowed for smaller wear upon the polymer pin. Although counterintuitive, the findings are explained by Abarou *et al.* (1987). For a MOC < 0.5, by allowing the pin to sweep a large section of the contact area, the third body polymer layer is established throughout the sliding contact zone as opposed to the large MOC values (MOC > 0.5) where the third body layer is predominantly deposited in the central zone of constant contact. This can be seen within the optical photomicrographs recorded in Figure 18 where the third body transfer films of an Ultra-high-molecular-weight polyethylene (UHMWPE) material, were examined for different values of MOC.

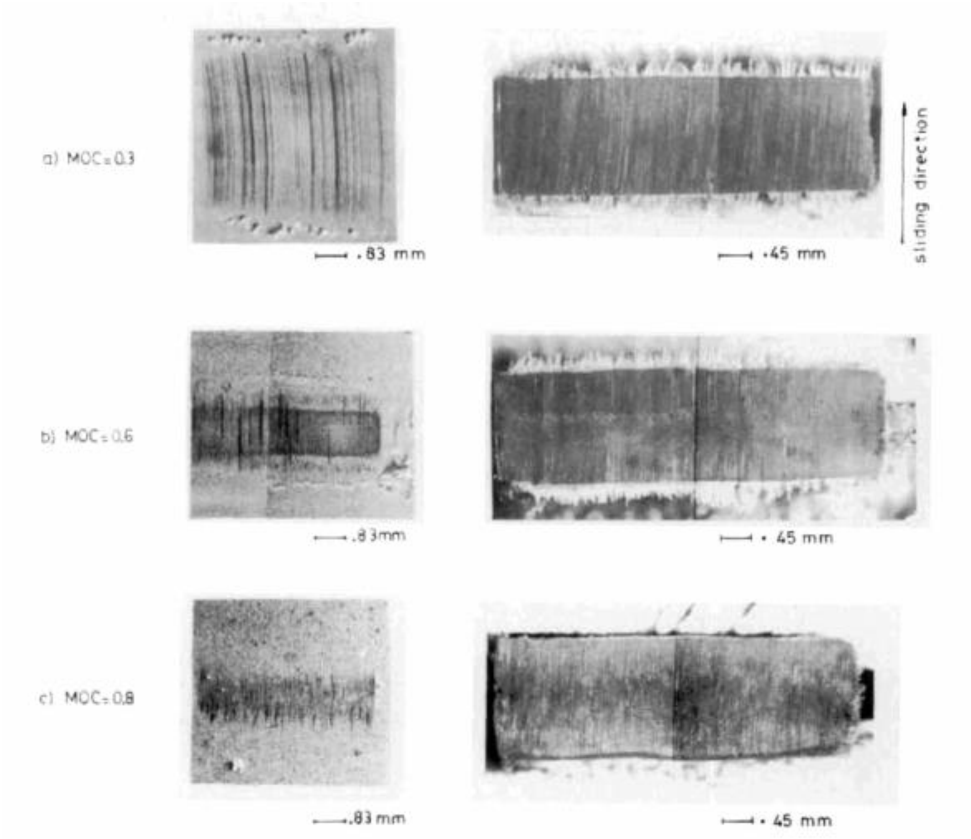

Figure 18 – Optical photomicrographs of the third body transfer layers of UHMWPE material under different MOC values. Images on the left represent the wear track upon the material and the images on the right are the wear tracks upon the pin (Abarou, et al., 1987).

By allowing the transfer layer to be formed over a large area, the load carrying capacity of the of the third body layer is increased which in turn decreases the wear of the material. Abarou *et al.* (1987) also reported that the centralised transfer layer formed in higher MOC values was credited to a mechanical action of cold rolling and this action in turn ruptures the molecular chains of polymers producing non-uniform and clustered transfer layers which are easily abraded.

To further understand this reciprocating motion wear rate phenomenon, Gawarkiewicz & Wasilczuk (2006) investigated the life durability of certain self-lubricating materials in small oscillatory motion and reported that the durability of such lubricants is affected by stick-slip motion occurring, since the real sliding distance will be smaller than the apparent sliding distance. This is due to part of the movement being carried out without sliding (during the stick phase) and in certain cases this sliding distance lost is attributed to the elastic shearing of the polymer material. Further noted by Qiu *et al.* (2011), as oscillation frequency or sliding speed increases the wear mechanism in self-lubricating bearings with a PTFE-glass fibre liner transitions from adhesive to abrasive and spalling wear.

The final stage of wear of a self-lubricating bearing consists of the breakdown of the third body transfer layer. This stage occurs when most of the solid lubricant has been consumed. During this stage, the third body layer cannot be maintained, a smooth sliding surface ceases to exist and in turn the coefficient of friction increases due to the lack of lubrication. The increased coefficient of friction is attributed to the increased levels of asperity exposure within the sliding surface. The sliding contact therefore progressively transitions from polymer-metal contact towards metal to metal contact causing abrasive wear to be the dominant wear mechanism.

During this stage, the rate of wear increases rapidly and is attributed to the rough sliding contact now present, while the temperature also increases at a high rate.

2.2.4 Parameters affecting performance

Evans (1981) described self-lubricating bearings as being most useful under certain operating conditions, including high stop-start operation along with oscillatory motions in which a rolling element bearing would not be able to develop a lubricating film and would therefore be in danger of rapid failure. Self-lubricating bearings are also preferred where extreme environmental conditions are present i.e. vacuum, along with applications where contamination is a possibility. Finally if a system can be greatly simplified by the removal of oil supply and filtration systems, then once more self-lubricating bearings are preferred. Environmental factors of all types can influence both the initial wear rate and in turn the lifetime of the bearing. Such factors include temperature, fluid / solid contamination and humidity.

Temperature effects during operation of a bearing can either be due to external factors such as ambient temperature or by-products of operation such as heat generation due to the relative sliding motion. A study carried out by Lancaster (1978) showed that at elevated temperatures the formation of a uniform third body transfer layer on the counterface became increasingly difficult, which was speculated to be linked to the weakened structure of the composite. Lancaster concluded that, as the elastic modulus of the composite decreases with increasing temperature, there will be greater penetration of the counterface into the composite leading to a greater degree of surface disruption, thus inhibiting the formation of a transfer layer. Subsequently, a different study (King, 1979) relating temperature effects to inorganic fibres and fillers was conducted, which complemented Lancaster's findings. It was found that the wear rates of PTFE composites increased most rapidly with temperature in the range of 20 -

150 °C when the fillers or reinforced fibres were inorganic. This increased rate of wear was attributed to the abrasive wear of the inorganic filler impeding transfer film formation on the counterface at elevated temperatures (King, 1979). Interestingly, King also concluded that the depth of wear which corresponds to the 'knee' remained independent of temperature effects. The 'knee' of a wear depth vs. time graph can be found if an imaginary construction line is drawn from the starting position of the steady-state wear rate section and extended to y axis at time=0 (h) point of the wear curve as displayed in Figure 19.

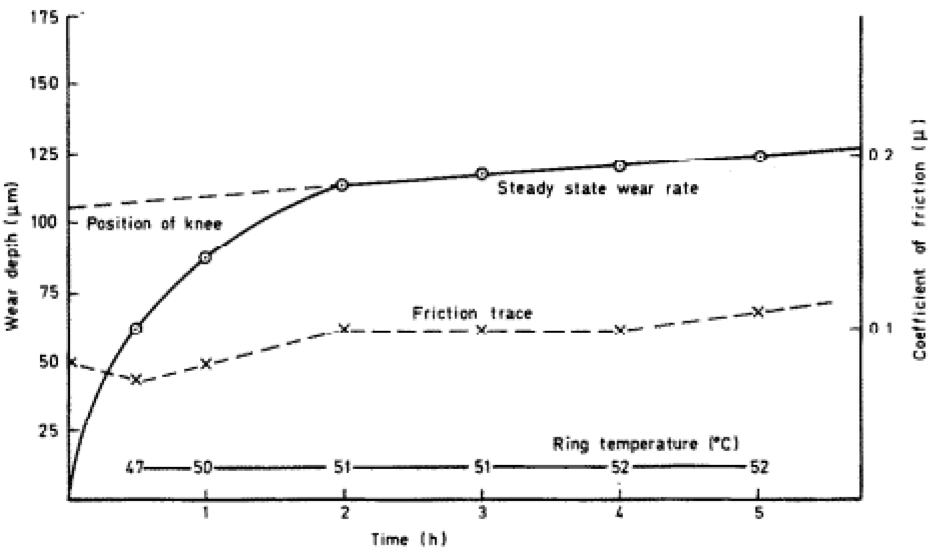

Figure 19 – Typical initial wear curve of a polymer material. The position of the 'knee' is graphically represented upon this curve (King 1979).

Therefore King's conclusions showed that even though the time taken to transition into the steady state section of the graph could vary (depending on environmental parameters), the final 'knee' wear depth at the plateau point will remain the same as shown in Figure 20, complemented by Figure 21 which details the materials under test..

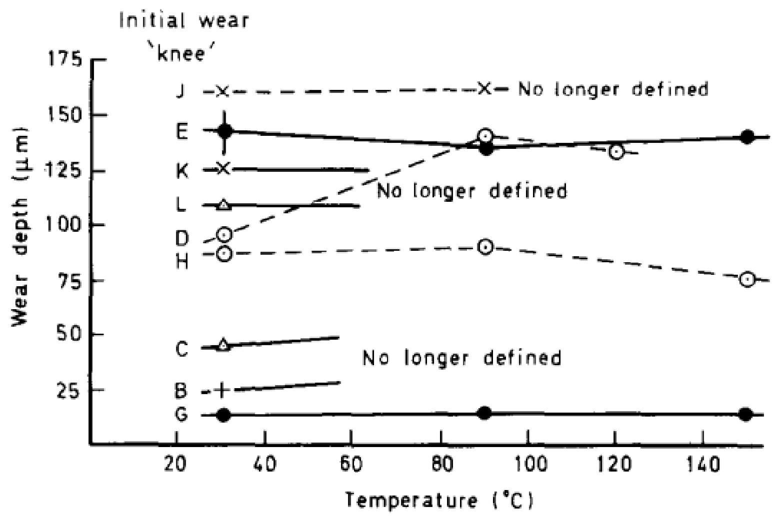

Figure 20 - Variation of the 'knee' wear depth with increasing temperature of different materials under test.

Code[a]	Material description	Elastic modulus (GPa)
Group 1 Interwoven fibre constructions		
B	PTFE/Nomex fibres with high temperature polyimide resin	1.65
C	As B but with lower temperature resin	1.70
E	PTFE/glass fibres with polyimide resin	2.20
G	PTFE/Nomex fibres with thin PTFE flock/phenolic resin overlay	2.50
K	PTFE/glass fibres in phenolic resin; PTFE fibres at surface	3.65
L	Similar to K but additionally some glass fibres at surface	4.30
Group 2 PTFE flock/granules in resin with fabric reinforcement		
A	PTFE flock in synthetic resin with Terylene fabric	1.63
D	PTFE flock in phenolic resin with Nomex fabric	2.20
H	Granulated PTFE in vinyl phenolic resin with Dacron fabric	2.65
J	Filled PTFE reinforced with bronze mesh	3.20
Group 3 Fibre-reinforced experimental constructions		
M		4.34
N		4.04
O	Woven PTFE/glass fibre constructions of different weaves laminated with phenolic resin	4.17
P		4.67
Q		4.61
R		5.79
S	As above but with polyester fibre instead of glass fibre	3.68

Figure 21 - Materials used by King (1979) within his 'knee' wear depth investigation with regards to temperature.

Fluid, along with hard particle contamination is the largest contributing factor to unpredictable bearing failure known to this day. Considering the normal flight conditions of an aircraft throughout its lifetime, many harsh environments are likely to be encountered, such as deserts and rainforests which both contribute to possible contamination of the bearing. When a foreign hard particle enters the bearing and deposits itself between the composite liner and the inner race, the localised stresses are greatly increased in that region due to an 'extreme' asperity being present. This will in turn score the composite liner, causing it to reach the glass fibre backing and at that point temperatures become significantly elevated, eventually leading to bearing failure.

An investigation into fluid contamination was conducted by Lancaster (1982), who concluded that there are two main reasons for the increase in wear in the presence of such contaminants. Firstly, the fluid prevents the formation of transfer films on both the counterface and the surface of the liner itself. Secondly, fluid penetrating into cracks within the liner composite leads to the development of hydrostatic stresses during contact, which alter the mechanical strengths and load carrying capabilities of the composite (Lancaster, 1982).

Relative humidity within the bearing can also be due to environmental effects or a by-product of operation during the bearing's lifetime. Geographical locations with high humidity levels such as rainforests cause 'swelling' of the liner material, which in turn creates high torque levels often above the optimum operating conditions of the bearing. Morgan & Plumbridge (1987) describe torque to be proportional to the modulus of elasticity and to the coefficient of friction of the polymer matrix, but inversely proportional to its thickness. An increase in torque, affects the tensile strength of the liner in a negative way with regards to performance, but also has some beneficial effects; if the increased torque is induced by an increasing humidity value, the liner composite becomes more densely packed due to expansion of the PTFE fibres and inhibition of the airgaps within the liner by moisture. This allows for greater compressive loads to be supported (Morgan & Plumbridge, 1987).

2.3 Condition monitoring techniques

The main drive of condition monitoring has always been, and still is, closely related to the maximising of asset operator's profits by ensuring a smooth operation and minimising the effects of machinery downtime. In the early 1970s condition monitoring was viewed as a 'gamble' by the majority of industry. This was due to the overall cost of adopting such techniques, along-side the personnel and expertise required for correct information interpretation and machinery diagnosis. However, throughout the development of condition monitoring, there has been a continual decrease in the overall cost of instrumentation driven by technological advancements, along with storage, processing and interpretation capabilities of useful data (Barron, 1996).

Structural Health Monitoring (SHM) and Health and Usage Monitoring (HUM) consists of an emerging field within mechanical engineering that is gaining interest from both academia and industry. Nowadays there are many kinds of sensors, meters, controllers and computational devices for conducting machine diagnostics. These can be used to acquire and analyse signals from a machine or process (Kumar, Makherjee, & Misra, 2013). To further expand, an effective condition monitoring system must be able to pinpoint a source of faulty operation, provide a quick response to an unusual occurrence and, vitally, the benefits of the applied systems must outweigh the costs of implementation of such a system. The benefits are not solely in the form of the reduction in maintenance or downtime but may also include safety improvements.

Having a clear understanding of the failure mechanisms and the parameters which affect the probability of failure, it is now possible to discuss how the health of a bearing in operation can be monitored and diagnosed as accurately as possible in order to minimise maintenance costs along with the avoidance of complete failure. Failures can be classified into two types, which condition monitoring tries to identify and these are labelled as 'hard' and 'soft' failures. 'Hard failures' by definition are catastrophic and result in a complete cessation of all operations associated with the particular failed component. In order to prevent such a high magnitude of downtime within the system, a prognostic stage must be present which monitors 'soft failures'. Such failures are defined as partial within the operating system, which in turn lower the performance of the system as a whole and which increase in amplitude or severity over the period of their lifetime (Davies, 1998). Referring back to Figure 21, if a failure occurs within the bearing, appropriate diagnostics can be carried out during the plateau stage and labelled as a 'soft failure', before it transitions into the critical failure region and becomes classified as a 'hard failure'. Explaining these three sections with the theme of condition monitoring in mind, the following stages can be labelled:

1) Wear-in stage: The probability of failure decreases over time to a constant level.
2) Constant failure rate stage: The probability of failure plateaus, meaning that the chance of failure is still present but its probability is relatively constant.
3) Wear-out stage: The component degrades rapidly due to its main functionality now being limited and therefore being operated outside its optimum conditions.

Condition monitoring is essential during the constant failure rate stage due to the unpredictability of the failure modes. Therefore it is at this stage where 'out of the ordinary' patterns within gathered data can be detected and interpreted to provide provisional warning to the operator. Techniques that are commonly used in order to detect and prevent damage include the monitoring of vibrations, oil debris, ultrasonic parameters, thermal bi-products and acoustic emission.

2.3.1 Vibration monitoring

The simplest bearing damage detection vibration method currently used is the monitoring of the Root Mean Square (RMS) value of a signal. The RMS value alone is not all that useful but when compared to a reference healthy value can provide an indication of a present fault within the system. Although useful, such an approach is limited to a very simple system configuration where no external information is present. Furthermore, this type of approach tends to be insensitive to bearing damage initiation and the RMS levels only tend to increase when the damage has entered a critical state (Downham, 1980).

Although the raw RMS signals are said to not be valuable prior to the failure becoming critical, Igba *et al.* (2015) devised a way to convert the RMS value into a useful delta RMS output, able to detect early bearing faults in wind turbine gearboxes. This model was named 'RMS deviation intensity' and its principle of opperatation is based on the relationship between two consecuitive RMS values. This technique was applied to wind turbine data aquired up to a year before the damage occurred as presented within Figure 22. The main disadvantage of this method, as reported by the authors, is the parameter's sensitivity to load changes and therefore it should be applied with caution and expert judgement (Igba, Alemzadeh, Durugbo, & Eiriksson, 2015).

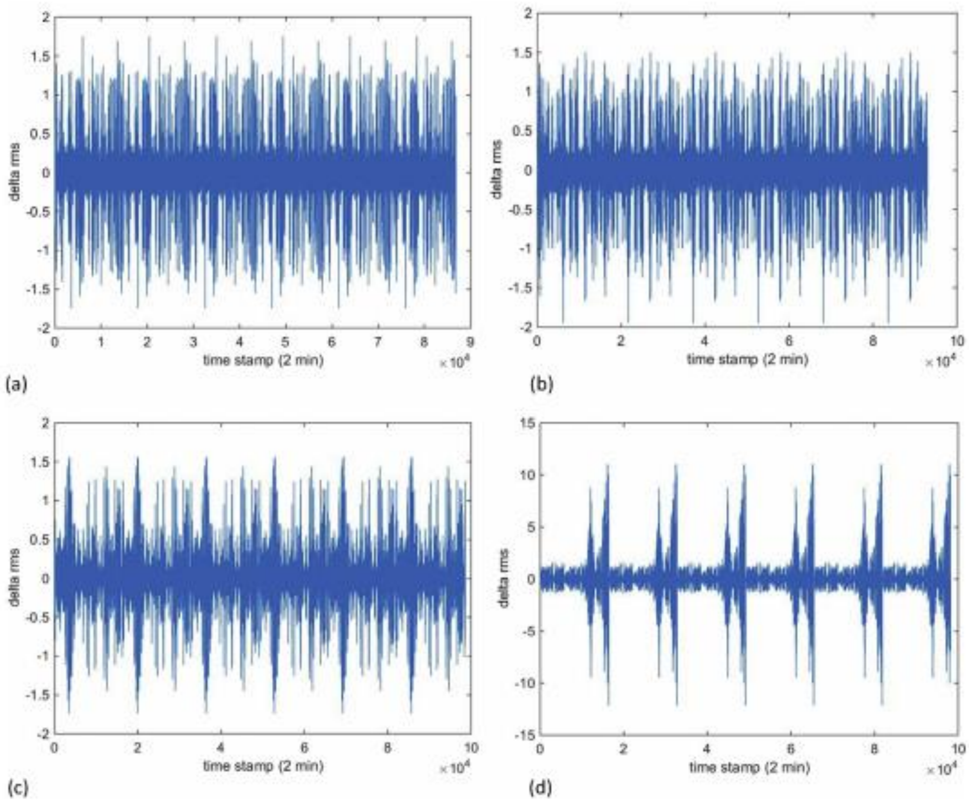

Figure 22 – Delta RMS plots (a) normal operation; (b) 6 months before failure; (c) 1 month before failure; (d) 1 week before failure (Igba, et al., 2015).

A further approach employed consists of the monitoring of the ratio of peak acceleration to RMS acceleration. When a fault is present within the bearing system, the peak levels of acceleration increase more violently than the corresponding RMS levels. This ratio is called the crest factor and, as opposed to the 'RMS deviation intensity' method, it is relatively insensitive to bearing speeds and loads. This method is predominantly used for the detection of minor defects, but as the defect size grows, the value of the crest factor decreases rapidly due to the increasing RMS value (Ingarashi, et al., 1980).

Finally, one of the most established techniques regarding vibration analysis is the monitoring of the Kurtosis parameter. This method involves the examination of the acceleration distributions via the application of the probability density distribution. A bearing in a healthy state is said to have a Gaussian distribution of accelerations. As damage is initiated inside the bearing, an introduction of higher levels of acceleration will be present within the vibration data and therefore the tails of the distribution start to become more prominent (Collacott, 1977).

2.3.2 Oil debris analysis

Oil and debris analysis are typically conducted through a spectroscopic analysis of different metallic elements present within a sample of the lubricant in use. This type of analysis technique is not applicable to self-lubricating bearings, due to the absence of oil within this type of bearing. A study conducted by Halme (2002), compared the conventional RMS technique with an oil debris method. It was concluded that the oil debris monitoring method was able to detect a bearing fault at a much earlier stage than the RMS method. The results for the spectoscopy analysis are shown in Figure 27 and it can be seen that significant changes to the particle sizes are detected within 9 hours of opperation.

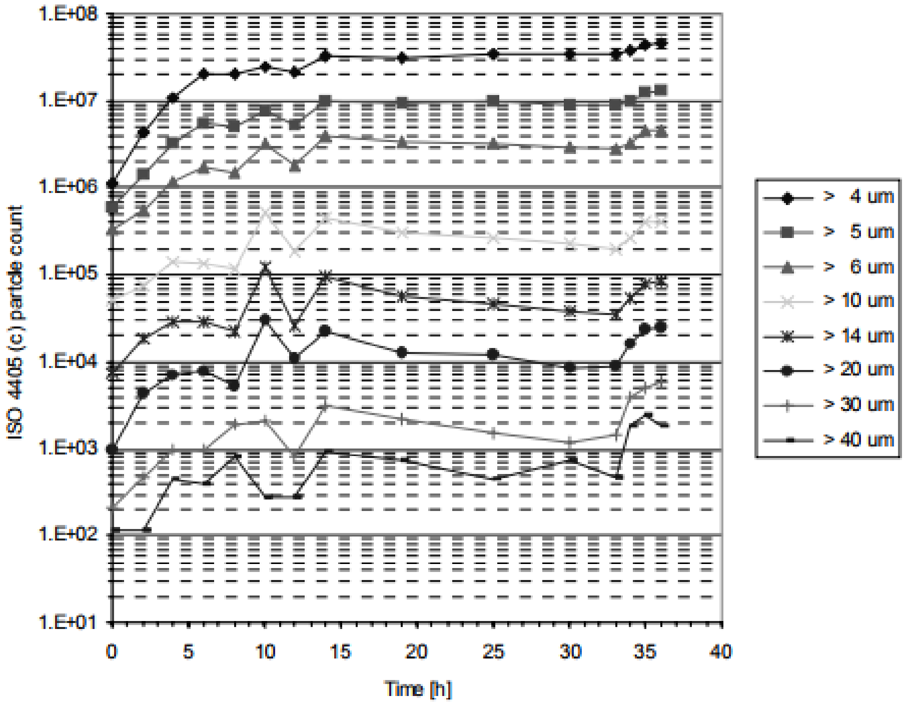

Figure 23 - Oil debris analysis with regards to particle size (Halme, 2002).

The RMS results from the same test are shown in Figure 28 and it is clearly seen that the raw RMS values do not detect any significant damage up to 5 hours prior to failure.

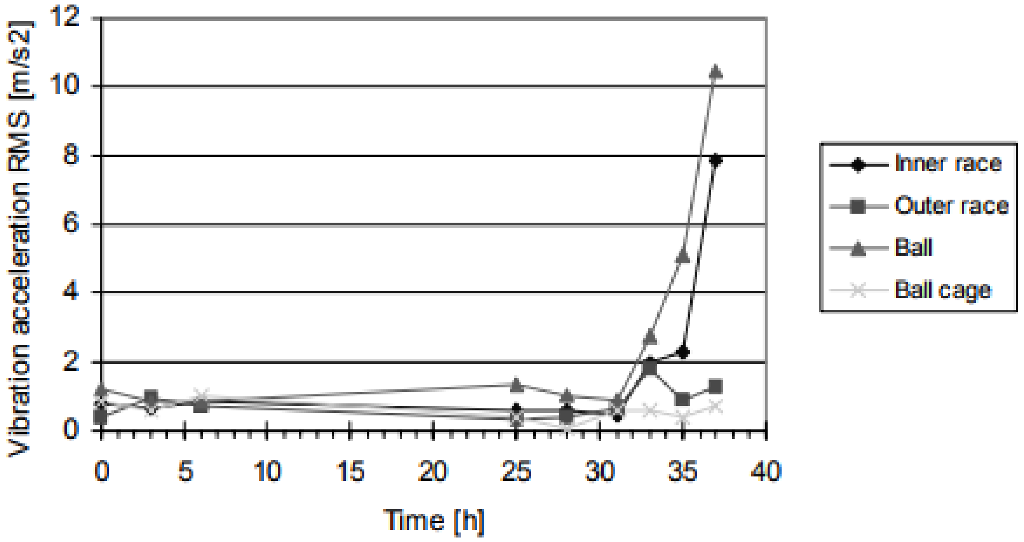

Figure 24 - RMS recorded in parts of the bearings composition (Halme, 2002).

2.3.3 Ultrasonic analysis

Ultrasound is defined as sound waves which possess frequency levels which lay between the 20kHz and 100kHz frequency range. During machine operations an ultrasound signature is emitted by each vibrating component and these can be detected and in turn compared to a healthy signal in order to aid damage detection and identification. This type of monitoring technique has the advantage of possessing a good signal-to-noise ratio, which allows it to be used by technicians to identify and locate bearing damage, hydraulic fluid or compressed air leaks and tank leaks (UESystems, 2018).

Kim *et al.* (2006) carried out an investigation into low speed bearings with the aim of using the ultrasound technique to detect bearing damage defects. This method was to be compared with the more established vibration alaysis methods of RMS, Crest Factor, Skewness and Kurtosis as previously discussed. The experment conducted involved the scratching of a mechanical defect upon a cylindrical roller bearing which was attached to a speed controlled shaft. The test aparatus is shown in Figure 25.

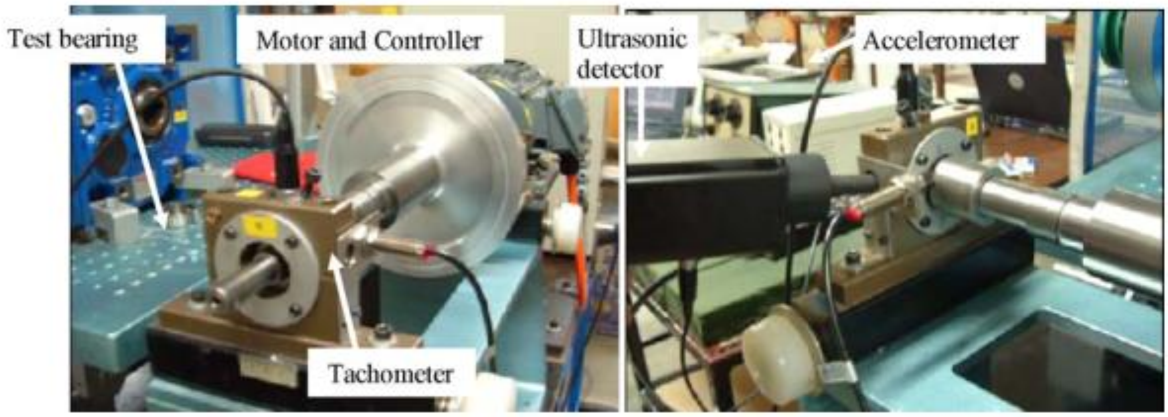

Figure 25 - Testing apparatus used to detect bearing damage (Kim, et al., 2006).

The raw signals obtained from the two monitoring methods are shown in Figure 26. As it can be seen both signals have distinct fault characteristics in the damaged bearing and are detected in both proposed techniques.

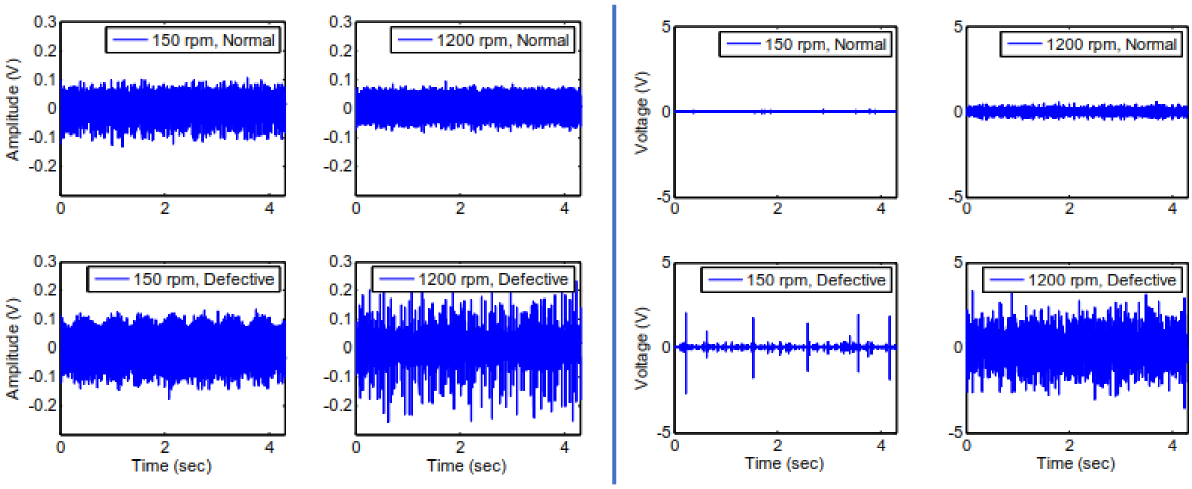

Figure 26 – Time waveforms of (left) acceleration signal and (right) ultrasound signals from a normal (upper row) and defect (lower row) bearing (Kim, et al., 2006).

All four of the detected signals were subjected to the analysis techniques of RMS and Kurtosis in order to view their difference. These are shown in Figure 27 and Figure 28.

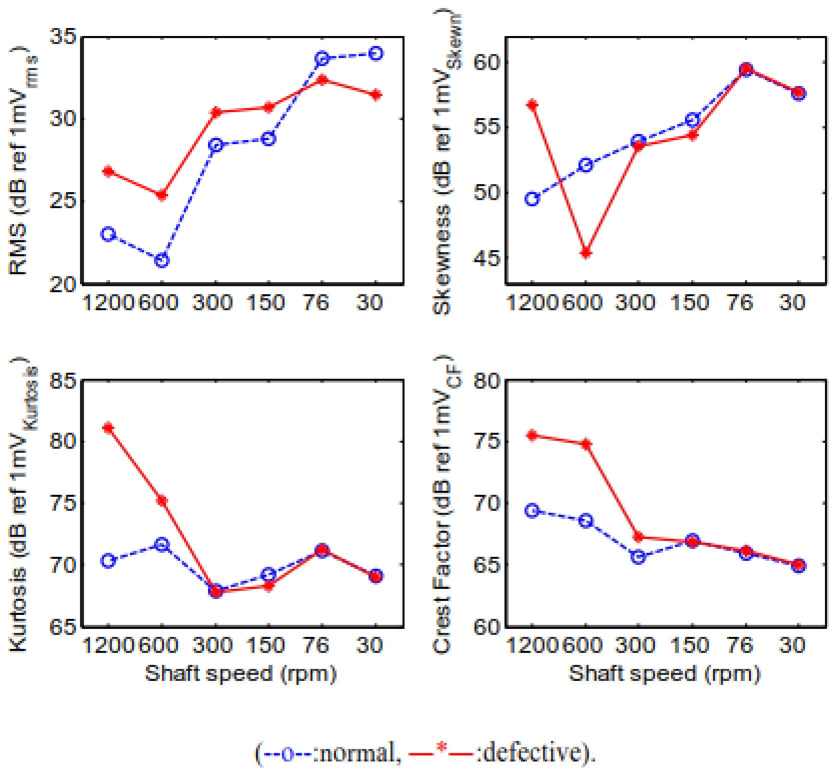

Figure 27 – Comparison from statistical parameters from vibration (Kim, et al., 2006).

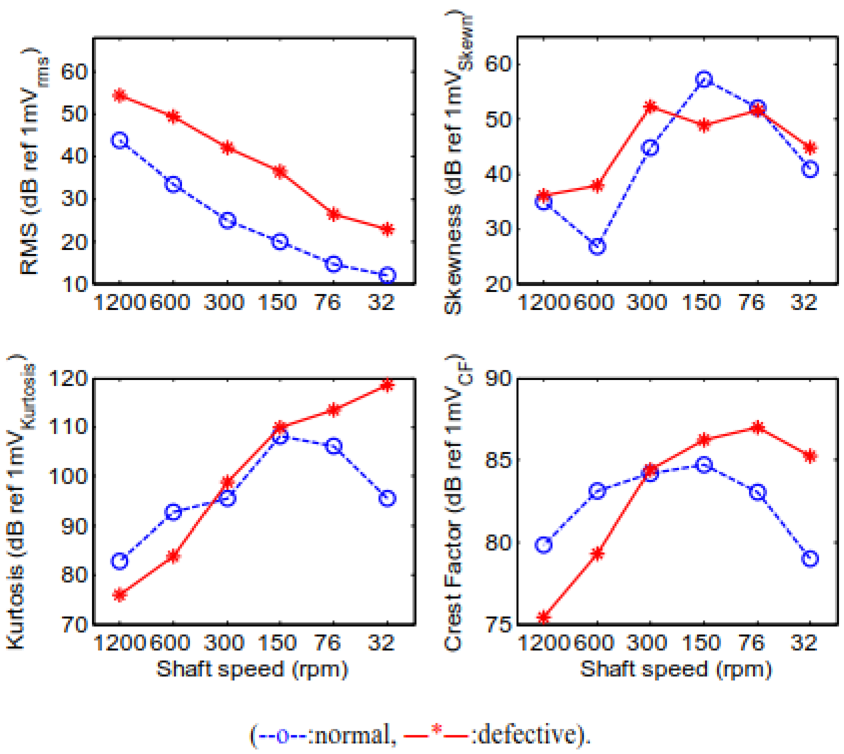

Figure 28 – Comparison from statistical parameters from ultrasound signal (Kim, et al., 2006).

As observed by Kim *et al.* (2006) the RMS values of the ultrasound signal almost linearly decrease with respect to shaft speed. This suggests that RMS is a good condition monitoring indicator and justifies the reason for the use of RMS as an example from ultrasound detector manufacturers.

The final comparison between the two signals was made with regards to the frequency content of the acquired signals. These can be seen in Figure 29.

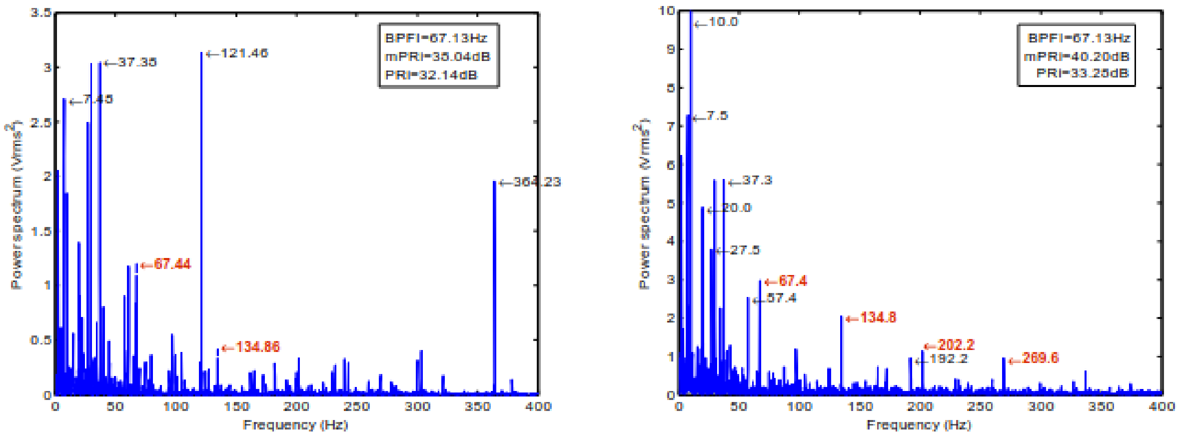

Figure 29 – Vibration power spectrum (left) and Ultrasound power spectrum (right) (Kim, et al., 2006).

The defect frequency was identified in this study to be 67.13Hz. The peak can be clearly identified in both the spectrograms but the ultrasound signal is able to identify the required defect frequency with a higher power value, along with its higher harmonics.

2.3.4 Thermal monitoring

Thermal monitoring of dynamic mechanical systems, is perhaps one of the most established techniques in industry. Consider, for example, the use of hot-axlebox detectors on the railway network, for identifying overheating wheel bearings on railway rolling stock. However, it is true to say that the temperature's slow response to damage makes it an undesired parameter for monitoring. It is said by many that temperature monitoring is not a sensible approach until the monitored component approaches its end of life where temperatures increase rapidly (Kurfess, Billingston, & Liang, 2006). One of the major disadvantages which arises with incorporating such signals comes in the form of fault identification. If a temperature increase is detected by a condition monitoring system, further investigation is required by an operator in order to determine and identify which machine part is at fault and responsible for such an increase (Zhou, et al., 2007). Zhou *et al.* (2007) describes the advantages and disadvantages of a wide range of bearing condition monitoring methods (Table 1).

Table 1 – Summary of different bearing condition monitoring methods (Zhou, et al., 2007).

	Monitoring Schemes	**Major Advantages**	**Major Disadvantages**
Extra Sensor Required (Sensor-based)	Vibration monitoring	Reliable; Standardized; (Related Standard: ISO10816)	Expensive; Intrusive; Subject to sensor failures
	Chemical analysis	Directly monitoring the bearing and its oil	Limited to bearings with closed-loop oil supply system; Specialist knowledge required
	Temperature measurement	Standard available in some industries (Related Standard: IEEE 841)	Embedded temperature detector required; Other factors may cause same temperature rise
	Acoustic emission (ultrasonic frequency)	High signal-to-noise ratio	AE sensor required; Specialist knowledge required
	Sound measurement (audio frequency)	Easy to measure	Background noise must be shielded
	Laser displacement measurement	Alternative way to measure bearing vibration	Laser sensor required; difficult to implement
Extra Sensor Not Required (Sensor-less)	Stator Current monitoring	Inexpensive; Non-intrusive; Easy to implement	Sometimes low signal-to-noise ratio; Still in development stage

2.3.5 Acoustic Emission monitoring

Acoustic Emission (AE) is described as the release of elastic waves when a solid is subjected to sudden internal stress redistributions (strain energy) within its internal structure. Such changes are said to be caused by crack formation and propagation, plastic deformation due to subjected loads, dislocation movement, twinning and phase transformation in certain materials (Huang, et al., 1998).

Dr. J. Kaiser, in Germany, appears to have produced the first investigation regarding acoustic emission in 1950, but before this critical date, literature on a phenomenon labelled as "tin cry" had appeared, dating back to 1928 (Spanner, 1974). Furthermore, the first recorded application of acoustic emission as a monitoring technique in the field of engineering, formed part of an investigation in 1963 into the 'structural health of a fibreglass rocket chamber during a hydrotest' (Green, et al., 1964).

This type of damage detection method was developed for non-destructive testing of static structures, but has since then been applied to health monitoring of rotating machines and bearings (Mba & Rao, 2006). Acoustic emission techniques in comparison to vibration monitoring methods have the advantage of being able to detect the growth of subsurface cracks and other failure mechanisms due to its sensitivity, whereas vibration monitoring is mainly focused on the detection of defects present at the surface of the material under test. Therefore, acoustic emission methods offer much earlier detection than vibration techniques in many cases. A study carried out by Tan *et al.* (2007), compared the acoustic emission and vibration monitoring techniques in spur gears where natural pitting was allowed to occur. The findings concluded that acoustic emission levels measured were linearly correlated with the gearbox pitting rates. Further, the acoustic emission technique was able to detect the pitting damage at

8% of the pitted area, as opposed to vibration measurements which did not detect pitting until it reached 20%.

With regards to applying acoustic emission condition monitoring techniques to bearings, and in general dynamic systems, a vast frequency analysis must be conducted if a single defect frequency is to be found. This will include the investigation and in turn isolation of all external factors which may be interfering with the signal strength and attenuation path. Such factors may range from rotating machinery noise to electromagnetic noise. All factors must be considered within a spectral analysis to understand and locate the source of a particular 'fault' within the bearing structure.

A large amount of work has been carried out on rolling element bearings, as summarised by Mba & Rao (2006), but publications regarding the detection of acoustic emission within self-lubricating bearings are still relatively rare. Despite the above, the techniques used, along with the most commonly measured AE parameters, remain the same and therefore must be mentioned. Regarding the AE parameters, the most commonly measured include: ringdown counts, events and peak amplitude of the received AE waves. These are graphically represented in Figure 30 (Research-Center, n.d.).

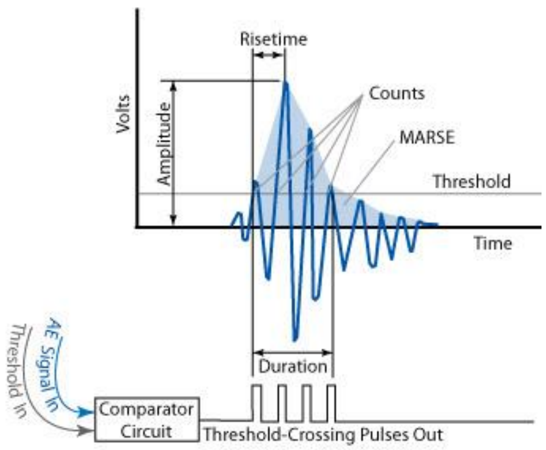

Figure 30 - AE signal characteristic parameters.

Ringdown counts signify the number of times the amplitude of the received signal exceeds a pre-determined threshold level, set by the operator, and this amplitude is in the form of a voltage output, produced by the receiving transducer (sensor). The ringdown counts are measured in time periods and a group of ringdowns form an ‘event’ which signifies a transient wave being present (Choudhury & Tandon, 2000). Choundhury & Tandon display the importance of the peak amplitude and count parameters by referring to a paper by Tan (1990) which suggests that the area under the amplitude time graph can be used to detect defects within rolling element bearings. Furthermore, during the operating lifetime of a bearing the AE bursts will alter and in the case of a defect being present these bursts will increase in amplitude. Depending on the size and nature of such defects within a bearing, the received signals from the transducer will consist of multiple amplitudes. If a signal during the failure period has a consistently repeated detection time interval, the frequency under which it is detected is referred to as a characteristic defect frequency. Techniques used to identify such frequencies include Fast Fourier Transforms (FFT), peak level R.M.S and shock pulse counting (Li & Li, 1995).

The use of acoustic emission detection in environments involving friction and wear has shown signs of promise in studies focusing on metal cutting and forming processes (Jiaa & Dornfeld, 1990). In an investigation aimed at various different types of strain energy dissipation events in metal to metal sliding contacts, Rigney and Hirth (1979) identified three certain events:

i. Plastic deformation which was linked to the material’s surface geometry asperities and thermoelectricity.
ii. Stress-induced phase transformation and twinning.
iii. Dislocation motion and dislocation-dislocation interactions.

Further Acoustic Emission sources from friction and wear processes have been identified which include:

i. Crack nucleation and propagation. (Tetelman, 1972) (Sano & Fujimoto, 1979)
ii. Impulsive shock in the case of asperity collision and debris. (Sayles & Poon, 1981)
iii. Microvibration due to slip conditions. (Bowden & Leben, 1939), (Dornfeld & Handy, 1987)

Focusing on self-lubricating bearings, Belyi *et al.* (1981) devised an experimental procedure where counterfaces with different surface roughness were used to wear polymer samples in a conformal cylindrical loading contact. Their findings recorded the acoustic emission intensities with each of the selected polymers tested upon two counterfaces with different surface roughnesses. It was concluded that, under the abrasive wear of the liner caused by the rougher of the two counterfaces, higher values of AE intensities were recorded when compared with the adhesive failure modes provided by the smoother counterface. Under the same type of wear, it was also noted that as the elastic modulus of the different polymers was increased, the AE intensity also increased. The materials under test included low density polyethylene (LDPE), polytetrafluoroethylene (PTFE) and polymethylmethacrylate (PMMA).

In terms of the analysis of such AE signals, El-Gharmy *et al.* (2003) reported that acoustic emission signals in the frequency domain can be extremely useful for diagnostics, especially in rotating systems but during reciprocating motion, the signal signature is given in terms of pulses whose fundamental frequencies remain the same and therefore a time-domain analysis may identify damage parameters which would not normally be detected using alternative methods. Subsequently, Liao *et al.* (2011) conducted a study on the stick-slip characteristics of the reciprocating O-Ring Seals used in reactor coolant pumps. The main focus of the investigation was to establish, if any, a correlation between the acoustic emission generated by stick-slip and the coefficient of friction of these rubber seals. A very strong correlation was found between the two parameters under investigation, as shown in Figure 31, in multiple tests using stroke incremental stroke lengths and therefore led to the conclusion that the AE energy produced during oscillatory motion could be attributed to the coefficient of friction at that particular moment in time.

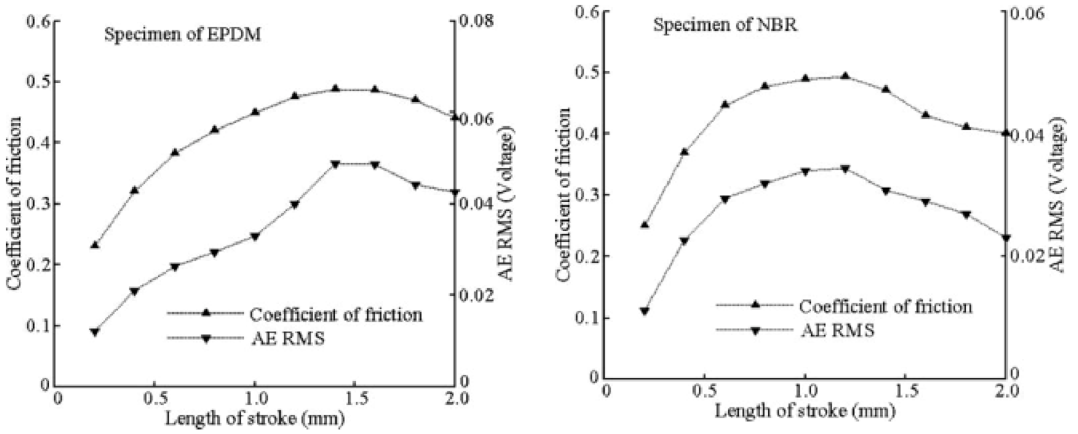

Figure 31 - Coefficient of Friction & AE RMS values vs reciprocation stroke length ofeEthylene propylene diene rubber (left) and nitrile-butadiene rubber (right).

Therefore, if any unwanted friction was being produced by the O-Seal during its working life, it would be able to be detected by the AE sensor and therefore replaced before failure, leading to a healthier operational life of the system as a whole.

2.4 Conclusion

A description of the history and evolution of tribology and self-lubricating technology was summarised, with the aim of giving the reader a good understanding of the current state-of-the art industrial self-lubricating products and their tribological operations. In turn, the condition monitoring techniques currently used within industry and developed within academia were summarised and examples of each was given in relation to bearing operations. The listed techniques are predominantly used within rolling element bearings but in some cases have the ability to be translated into a condition monitoring technique for self-lubricating bearings.

The following chapter aims to describe the development of a test-bench, which acted as a platform for implementing relevant condition monitoring techniques. Such techniques were intended to be applied to life-testing of SKF developed self-lubricating materials. Further, all other test benches which were utilised throughout the PhD programme are described in moderate detail in order to give the reader an understanding of their operations.

Chapter 3: Overview of experimental test facilities

3.1 Introduction

The primary focus of this chapter is to describe the test rigs and benches used for data collection within this thesis. In order to create a robust condition monitoring algorithm, a range of data from different types of test were used. For this reason, the test benches used throughout the research programme varied from fundamental coupon test benches to full scale bearing test rigs.

The most fundamental testing apparatus which was utilised consisted of a Cardiff University developed, reciprocating wear test bench. Due to its simplicity, sensing and high frequency recording capability, fundamental signals were able to be investigated without affecting the signals with large quantities of mechanical noise. The principle of operation consisted of a stationary hemispherical pin, in contact with a reciprocating flat coupon. The test bench is further discussed in section 3.6.

In order to generate a continuous stream of comparative data across multiple samples, a second test bench was developed and enhanced during the research programme. This test bench was named 'Rig Q', due to its capability of testing four bearing liner coupon samples simultaneously and therefore under the same environmental conditions. This test bench had the largest versatility with regards to sensing and mechanical alterations. Rig Q features four reciprocating cylindrical counterfaces in contact with stationary flat coupon samples. This is further described in detail in sections 3.2 – 3.4.

Through the use of the accelerated wear condition test benches described above, a large database was created, where the fundamentals of bearing liner wear could be investigated. In order to investigate how these results compare to the operation of actual bearings, a full bearing test bench within SKF Clevedon was made accessible to the author, with the ability to expand its signal sensing capability.

These test benches are now discussed in further detail in turn.

3.2 Rig Q - Purpose

In order to develop a large data set of the required monitoring physical parameters, a test bench had to be constructed, which would also allow further understanding of the liner material. The original design of the test bench was done by a former Cardiff University PhD student, Dr Russel Gay, together with Dr. Alastair Clarke, as part of a Knowledge Transfer Partnership (KTP) project. The test bench was named ‘Rig Q’ by the industrial sponsor (SKF), due to the bench’s ability to test 4 (Quattro) samples simultaneously. Initially, the test bench served the primary function of collecting preliminary data in order to investigate the wear and temperature patterns presented within literature. As the project progressed, further parameters needed to be monitored and the test bench underwent major modifications by the author which are explained within this chapter. The original CAD model of the test bench as built is shown in Figure 32.

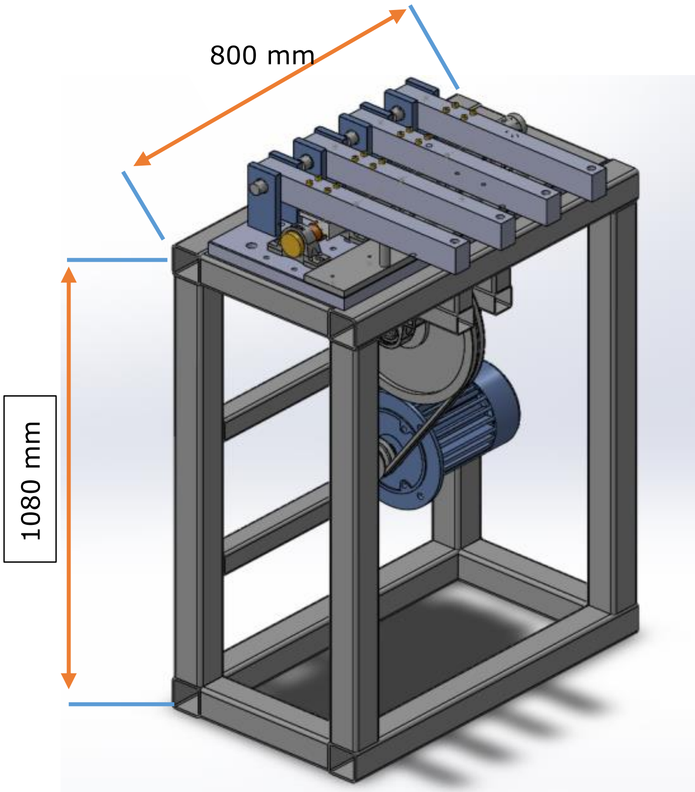

Figure 32 - Original CAD design for the test bench - Rig Q. Designed by Dr Russell Gay and Dr Alastair Clarke.

The principle of operation of Rig Q, was designed around the test bench's ability to test four liner samples at once, originally for rapid screening of new liner materials but also, fortuitously for this work, the four nominally identical test coupons may be thought of as representing the system of pitch control bearings located on a rotorcraft's main rotor and acting as critical components for a functioning cyclic / collective system. Each sample tested was subjected to accelerated conditions through the use of a non-conformal contact giving initially highly amplified pressure distribution values (to a certain extent this effect is reduced as the test progresses and the liner wears such that the contact gradually becomes more conformal).

A sample of the self-lubricating liner material was bonded onto a flat metal backing sample which represents the outer ring of the original bearing. The inner ring or ball was represented by a cylindrical counterface made from 440C hardened steel with a Brinell hardness of 269

(Rc29). The counterfaces have had their sliding surfaces super-finished to an Ra value of approximately 0.05 µm. The material properties of the counterfaces are designed to match those of the bearing inner ring. Although this accelerated coupon testing method was preferred, Rig Q was originally designed to also have the geometrical capability of testing full-sized pitch link bearings. In order to apply representative operating conditions to the test bench, the SAE standard AS81819 Aerospace (2001) was followed. This standard states that the bearing's motion must consist of an oscillatory 5Hz motion through a reciprocating angle of ±10°. Typical contact pressures between the inner and outer ring in main rotor applications, are between 10 – 20 MPa, as illustrated by Figure 33.

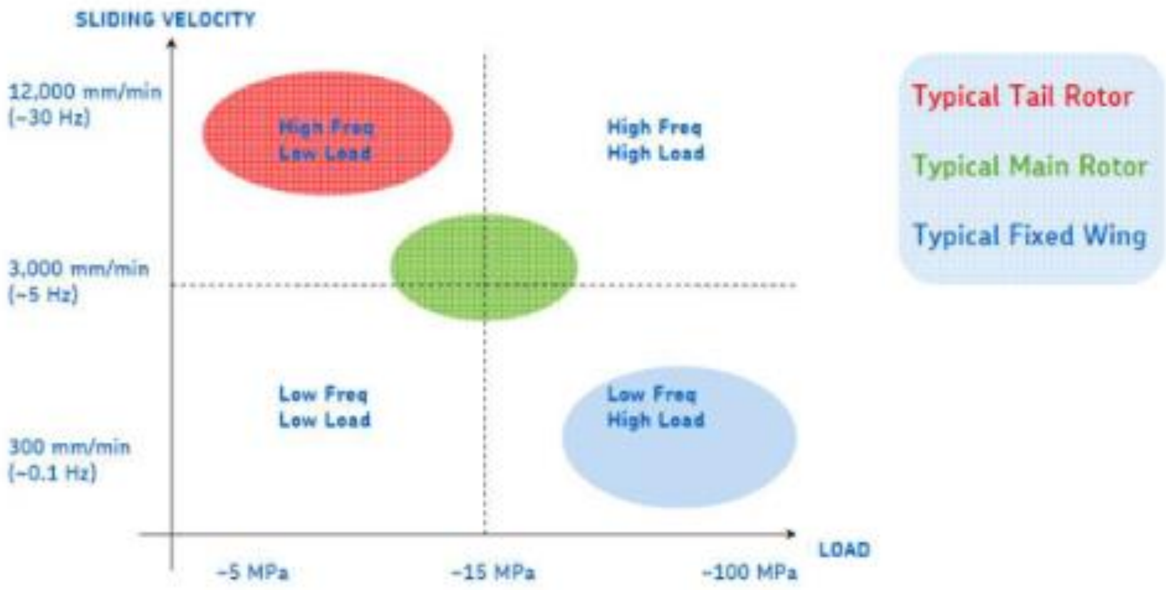

Figure 33 - Applications and operating parameters of self-lubricating plain bearings (Bell, 2009).

A schematic representation of the load application and reciprocating nature of Rig Q is shown in Figure 34.

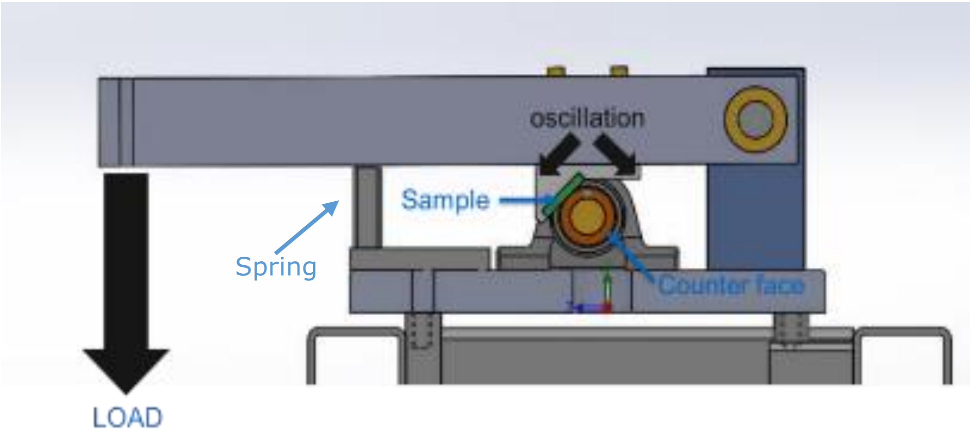

Figure 34 - Example of the oscillation movement to provide a reciprocating line contact (Jenkins, 2015).

Due to the nature of the contact between the liner sample and the counterface, the contact pressures stated in Figure 33 represent an average value throughout the length of the test. Initially the contact pressure values are very large, due to the small contact area formed during a line contact scenario. As the liner sample wears and enters the plateau wear rate stage, the contact becomes more conformal due to liner wear. This increases the contact area between the mating sliding surfaces and therefore the required main rotor pressure values are achieved.

Many researchers have raised significant doubts regarding the performance of self-lubricating materials when subjected to such accelerated conditions. Lancaster (1981) stated that in a reciprocating line contact there exists a significant amount of elastic penetration by the reciprocating component, in this case the counterface, which causes a very thin surface layer of the liner to be subjected to cyclically reversing shear stresses along with tensile and compressive stresses. This type of loading upon the liner-matrix causes the wear-in period to be extended through extreme wear aggression, which translates to the prolonged establishment of a third body transfer layer upon the counterface. Therefore, a larger volume of the consumable self-lubricating material is required in order to reach the second phase of liner wear, the ‘plateau’. This type of wear mechanism hinders the importance and impact of critical parameters which affect the wear-in phase of the bearing liner such as contamination, temperature, speed and counterface roughness. Anderson (1982) backed up Lancaster's theory by stating that there are some dangers when an accelerated reciprocating line contact test is adopted. This is due to the introduction of certain wear mechanisms which would not normally be present in a practical situation and therefore results acquired via accelerated tests are not recommended to be extrapolated for practical situations but should, in principle, be able to establish trends relating wear to the controlling variables such as temperature, humidity, contamination etc. (Lancaster, 1978). Noting the potential drawbacks of the accelerated line contact approach, it is important to understand that for the purpose of the PhD program, the author was not focused upon the absolute values of the physical parameters recorded throughout the testing. This will be explained in later chapters when the comparative nature of the proposed condition monitoring system is introduced.

3.3 Rig Q – Original design

3.3.1 Mechanical components

Throughout the duration of the project, the test bench underwent numerous mechanical alterations for multiple reasons, which will be discussed within this chapter. The original inherited design will be discussed first, followed by a detailed description of the alterations carried out by the author.

The original Rig Q design can be seen in Figure 32. The test head is mounted on a mild steel box section frame, which was chosen by the designers to provide a rigid structure on which the motor, drive system and test head can be mounted. In order to achieve reciprocating motion of 5Hz and ±10° reciprocation angle as determined by SAE standards, the rotational motion of the three phase motor at a continuous 25 Hz (1500 rpm) had to be transformed into a 5 Hz reciprocating motion at the main shaft, which was achieved in stages. Initially, motion was transferred from the motor to an intermediate shaft via twin rubber V belts and pulleys. The belts had to be in tension to allow the friction forces to be sufficient in order to prevent slipping which would result in loss of power. Drive was transmitted from the intermediate shaft to a spindle via a timing belt. The spindle was connected to the main shaft of the test rig (on which the counterfaces were mounted) by a crank mechanism which provided the required ±10° reciprocation motion. The drive train system is shown in Figure 35.

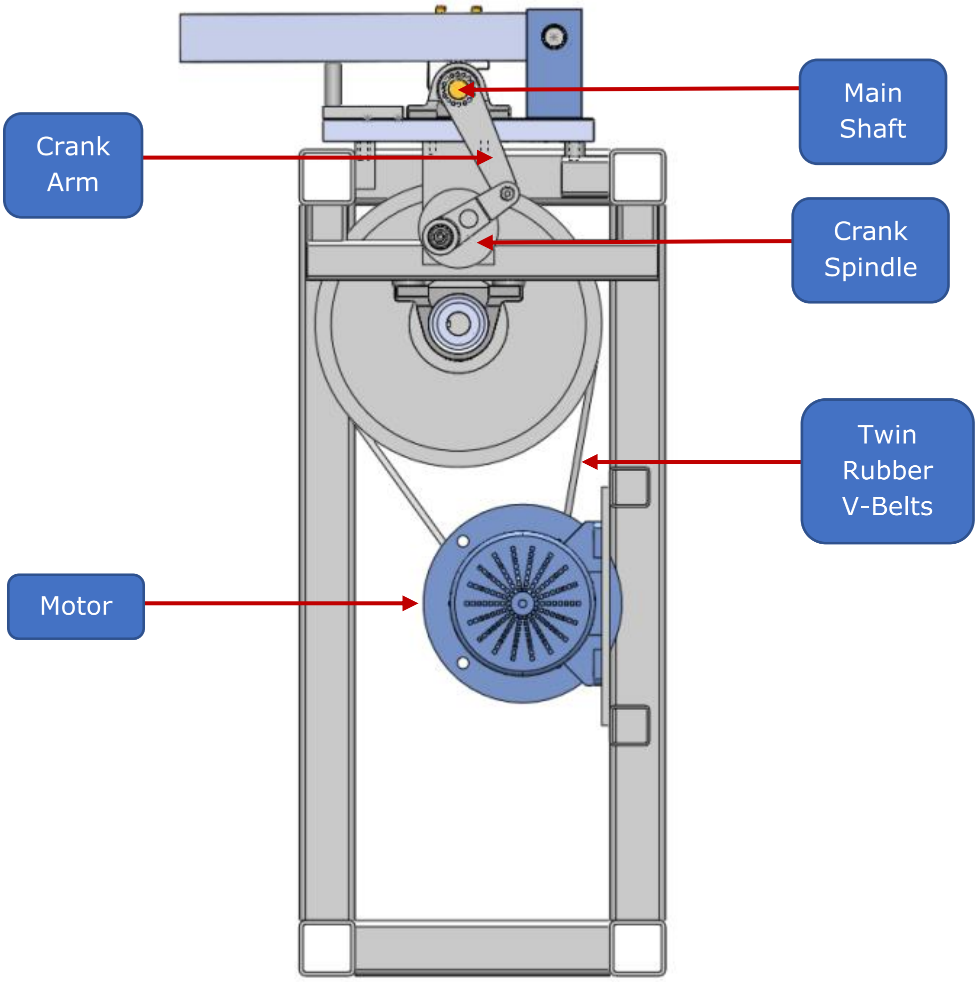

Figure 35 - Drivetrain system of Rig Q.

The liner sample, mounted to a plate, was held in a sample holder which in turn was attached to the loading arm itself, as illustrated in Figure 34. The loading arm was pivoted on a self-aligning self-lubricating spherical bearing, which was held on a pin which passed through the inner ring of the bearing and through the machined holes on each of the arm mounting uprights attached to the base plate. The sample holder was designed so that the sample made contact with the counterface at a 45° angle in order to provide a further self-aligning method between sample and counterface.

Regarding the fitting of the counterfaces upon the main shaft, a series of matching holes on the shaft and the counterfaces were drilled, with tight tolerances in both, to prevent unwanted stresses created on both components when the reciprocating motion was present. These stresses are mainly caused when the oscillatory motion is at its extremes, indicated by a direction change i.e. at the extremes of +10° and -10°. The counterfaces were bolted to the shaft to allow for easy replacement and also to allow for the rotation of the counterfaces. During operation only some 20° of the circumference of the counterface was in contact with the sample. To maximise the lifetime and efficiency of the resources allocated to this project, the main shaft was designed to allow the counterfaces to be rotated by 45° after each test, achieved by drilling and tapping 8 holes located at the connection between the main shaft and crank arm. After a test had been completed, the exposed section of the counterfaces in contact with the liner material were coated with a third body PTFE layer. Following a test, the main shaft was unbolted from the crank arm and rotated through 45° to the next position which exposed an undamaged section of the counterfaces ready for a new test to be conducted.

As seen within Figure 34, the point of load application on Rig Q was designed to be located at the end of the loading arm. The load was applied via the suspension of masses which through the leverage factor would allow for the required contact pressure to be achieved between sample and counterface. When testing four samples simultaneously, it is highly unlikely that all four samples will reach end of life at exactly the same time. Therefore, the loading system needed to be able to unload each arm when some pre-determined condition was reached, whilst allowing the testing of the remaining samples to continue. The design had to meet the following requirements:

- The load had to be able to be safely separated from the test bench when a sample has worn through onto the metal backing.
- The load had to be able to be varied between experiments, and potentially between arms during the same experiment.
- The load at each arm must had to be able to be removed individually.
- When the load had to be removed, the contact between sample and counterface had to be broken by some means in order to preserve the specimens whilst the testing of the remaining samples continued.

Following these considerations, an electromagnet was used for holding and releasing the applied masses. The electromagnet was bolted to the unsupported end of the loading arm and masses were suspended from it. The electromagnets had a rated loading capacity of 360kg, but these ratings were only achieved when load was applied directly perpendicularly to the face of the magnet. If there was any component of the load acting parallel to the face of the magnet due to even a slight misalignment, it was found that the masses had to be detached from the loading arm at much lower loads. Therefore a new design was proposed where an armature plate was used as an intermediate attachment point between the suspended masses and the electromagnet itself, with the loads applied using a ratchet strap attached to the armature plates via a "U" bolt. The use of ratchet straps also had health and safety advantages, since they allowed the masses to be lifted off the ground with minimal effort, therefore minimising the risk of injury. The arrangements are shown in Figure 36.

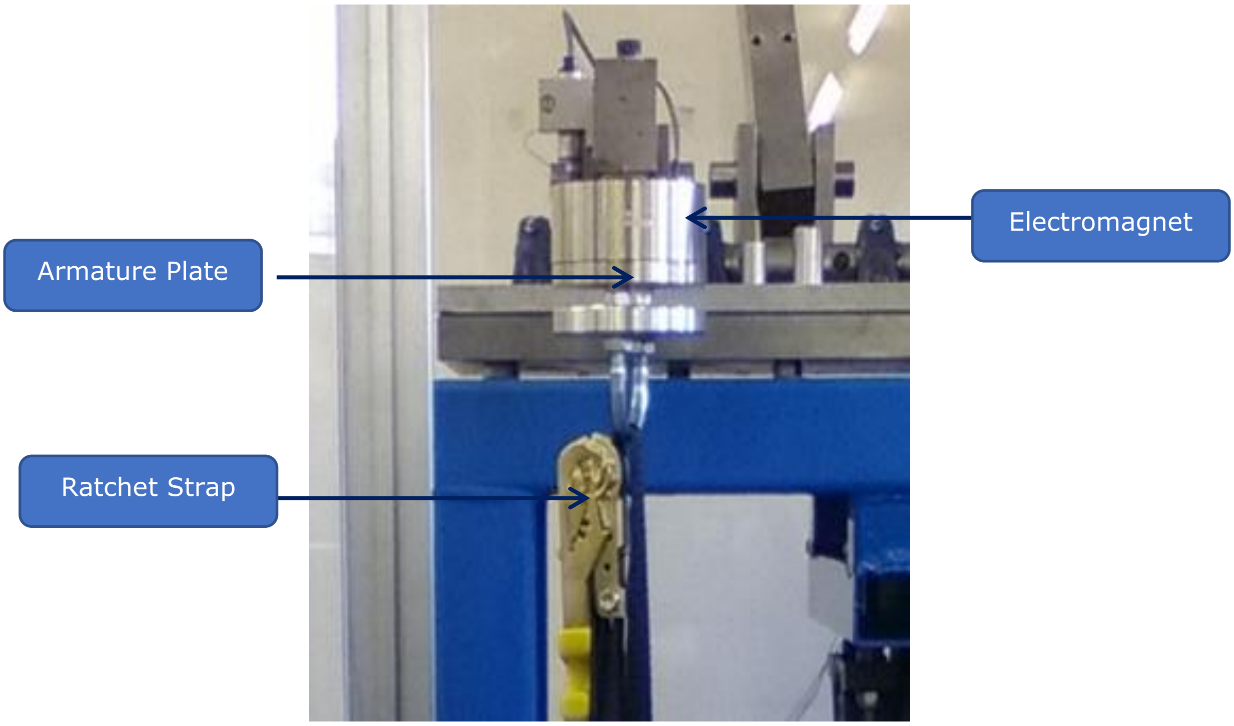

Figure 36 - Labelled image of the loading mechanisms incorporated.

In Figure 36, it can be seen that the mechanical arm on the left appears angled. The explanation of this purposeful misalignment of the arm, was due to the face that the spherical plain-bearings were located at the pivot point of the arm. These bearings allowed the mechanical arm to have a certain degree of freedom in order to self-align the flat sample with the steel counterface and therefore provide a uniformly loaded sliding contact area.

When one of the four samples had worn through, it was programmed via LabVIEW to trigger the release mechanism of the electromagnet to disengage the applied load from the contact. To separate the sample from the counterface, a coil spring was mounted between the loading arm and the baseplate in order to overcome the vertical forces created by the mass of the mechanical arm and magnet once the applied masses had been released. This lifted the sample just clear of the counterface, allowing the test to continue until all samples had reached the end of their life.

3.3.2 Components under test

For the experimental procedures planned, the composite wear liner material was adhesively bonded onto a metal backing, which in turn was fitted within the sample holders located on the underside of the loading arms. Figure 37 shows a healthy and worn liner sample and shows the nature of the line contact present between counterface and sample.

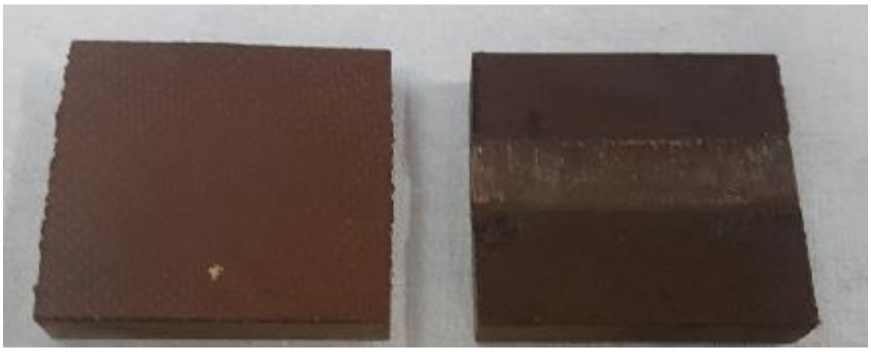

Figure 37 - Healthy sample (left), Worn sample (right).

The orientation of the fabric liner bonded on the metal backing, plays a very significant role when the liner is subjected to reciprocating conditions. When the liner is prepared, it is important to orientate the glass fibres at a 45° angle to the nominal contact line. If the glass fibres are parallel or perpendicular to the contact line, the wear rates of the product are increased significantly. Furthermore, it is of vital importance for the load to be removed quickly when the metal backing is reached at the point of complete wear, in order to protect the sample holders from further damage.

The counterfaces which were used throughout the testing period, consisted of steel cylindrical components which were initially heat treated and ground to achieve a required 0.4 µm Ra and further superfinished to reduce this Ra value to approximately 0.05 µm. The counterfaces therefore closely replicate the material which forms the inner-ball of self-lubricating bearings. Figure 38 illustrates a damaged and a healthy counterface.

Figure 38 - Healthy counterface (top) vs Damaged Counterface (bottom)

Figure 39 shows a cross-section view of the two mating components responsible for creating the accelerated wear conditions, consisting of a flat liner sample and a cylindrical counterface.

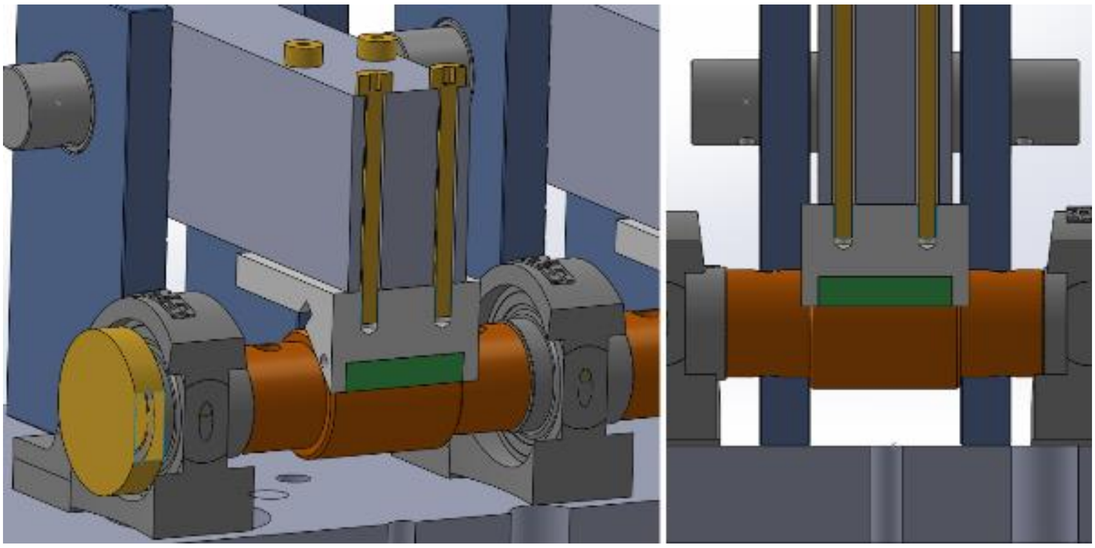

Figure 39 - Illustration of line contact created between sample (Green flat section) and Counterface (Orange cylindrical section)

3.3.3 Instrumentation

The following section describes the instrumentation fitted to the test bench in order to acquire data for subsequent analysis. The main parameters which were monitored included temperature, humidity and wear depth of liner.

3.3.3.1 Temperature

Regarding the measurement of temperatures, a number of type J thermocouples were chosen and located at various locations. Type J thermocouples were chosen due to their wide operating temperature range along with their low cost.

These thermocouples were to be placed strategically around the test-bench in order to monitor the temperature changes at relevant locations. The following were chosen to be monitored:

- Ambient room temperature e.g. out of case temperature
- Motor temperature, to allow for motor cut-off in the event of a fault occurring
- Sample temperatures, in order to be used for analysis and algorithm development

In order to allow for the acquisition of the temperature data, a PCB with a monolithic amplifier with cold junction compensation as shown in Figure 40 was used. The output signals were then passed into a NI 6008 USB DAQ which was responsible for digitising them and interacting with LabVIEW.

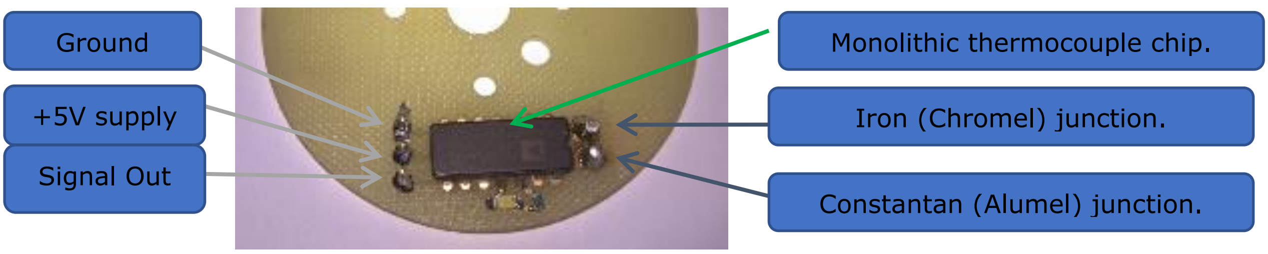

Figure 40 - Labelled image of inherited temperature logging device.

In order to locate the thermocouples, small holes were drilled on the side of the metal backing, of the samples and the thermocouple wire tip was cemented into place using special thermocouple cement which possesses high thermal conductivity (Figure 41).

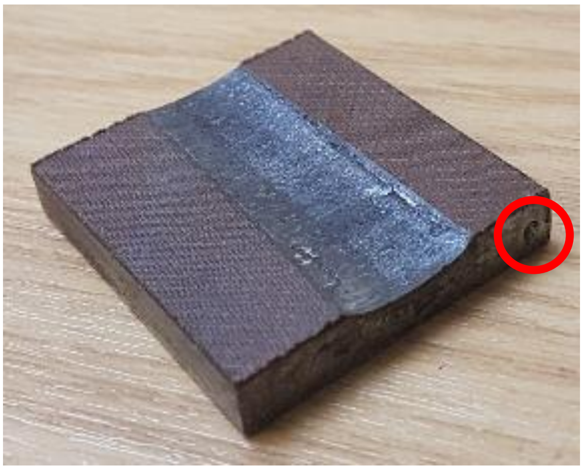

Figure 41 - Location of the proposed thermocouple location marked in a red circle.

This sensor location was deemed inadequate due to its substantial distance away from the sliding contact. The author's modifications to this design are discussed later in this chapter.

3.3.4.2 Humidity

Humidity sensors were to be included on the test bench due to the literature available regarding the effect of humidity upon the liner material. Morgan & Plumbridge (1987) recorded the differences of the liner's ultimate strength by subjecting the liners to different percentage levels of humidity before carrying out compressive and tensile tests upon them. They reported that by reducing the relative humidity from 80% to 20%, there was an increase in ultimate tensile strength of approximately 25%.

Although fitting humidity sensors was seemed ideal, the location of these sensors on the test bench proved to be less straight forward. Due to the open-top nature of the test bench, it was not possible to regulate humidity and therefore it was decided not to monitor it. To achieve humidity control would require the rig to be fitted within an environmental chamber, which was outside the scope of this project. An alternative of fitting humidity sensors close to the samples under test was considered but later discarded.

3.3.4.3 Wear

One of the most important parameters to be monitored throughout a test was the wear which occurs when the liner material is consumed throughout a test. The instrumentation used in order to record this physical parameter was a Linear Variable Differential Transformer (LVDT). In order to measure the wear of the liner, the LVDTs had to be mounted somewhere along the length of the loading arm to measure the distance between the loading arm and the baseplate, using an external mount which bolted onto the side of the loading arm. Figure 42 shows the components used as part of the wear measurement system.

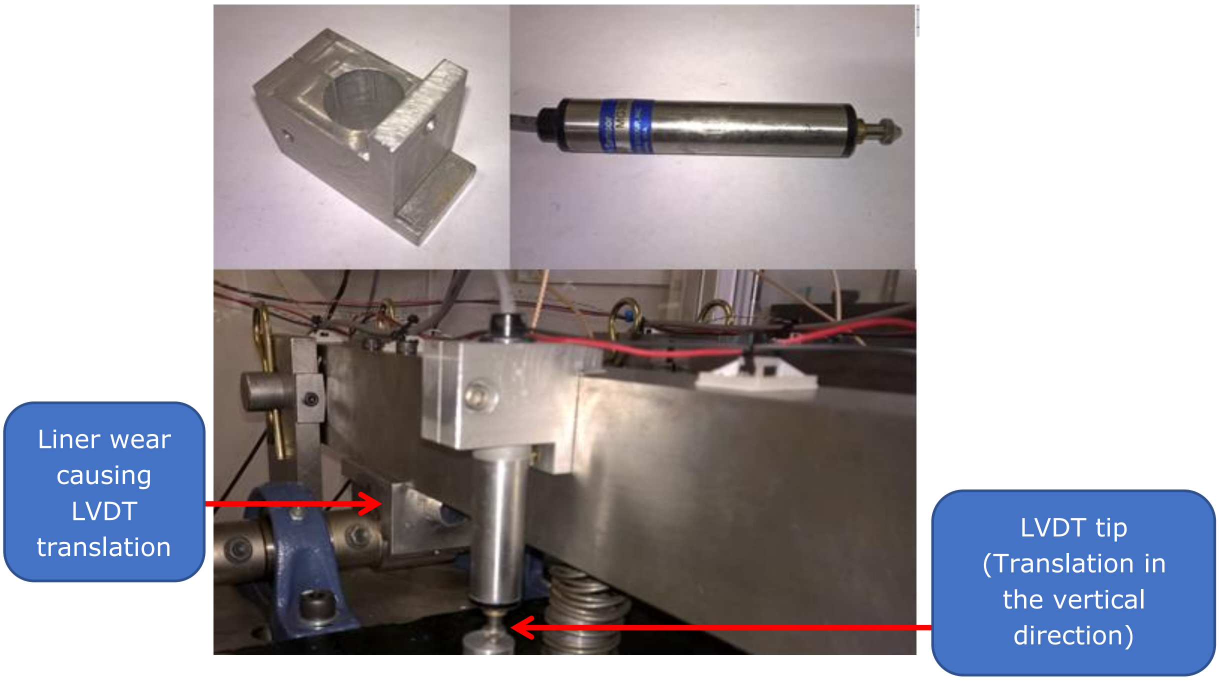

Figure 42 - LVDT mount (top left), LVDT sensor (top right), wear measurement system mounted on the loading arm (bottom).

It is evident that the wear measurement recorded would not be the absolute value of wear, due to the position of the LVDT. Therefore a translation function had to be incorporated within the LabVIEW data acquisition system in order to record the required wear data for subsequent analysis.

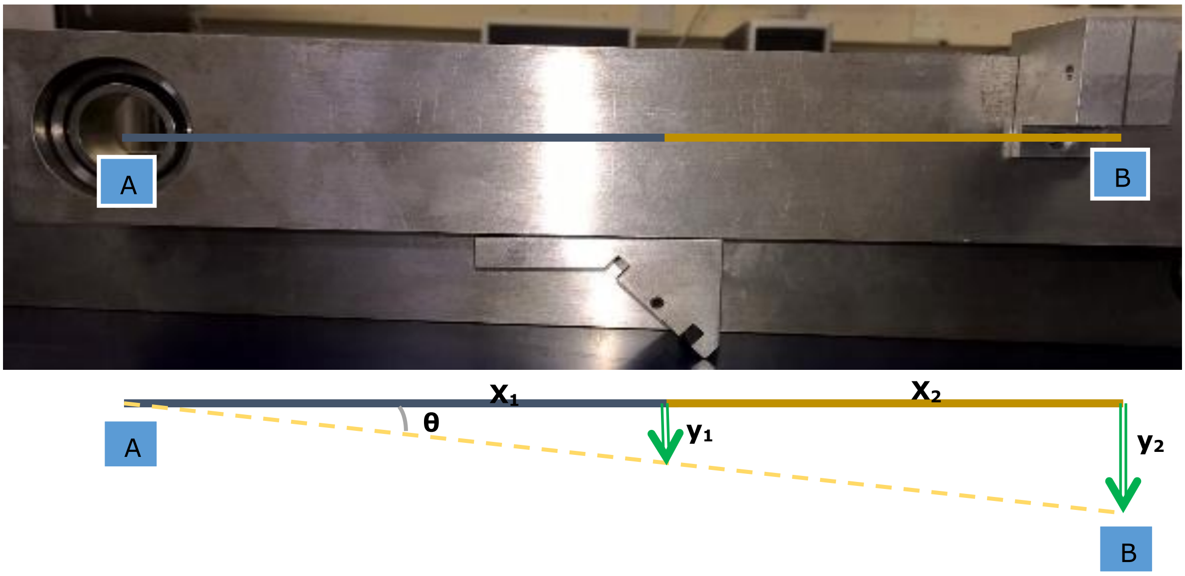

Figure 43 - Translation function schematic. Pivot point marked as 'A' and LVDT displacement point 'B'.

Figure 43 shows the position of the LVDT relative to the sample. The lengths x_1 and x_2 were 140 mm and 130 mm, respectively. The displacement of y_1 in relation to y_2 was calculated by utilising similar triangles as follows::

$$\frac{y_1}{x_1} = \frac{y_2}{(x_1 + x_2)} \tag{1}$$

$$y_1 = \frac{y_2 \cdot x_1}{(x_1 + x_2)} \tag{2}$$

Knowing the values of $x_1$and x_2 the equation can be simplified to:

$$y_1 = 0.5185 \cdot y_2 \tag{3}$$

Although the value of y_1 represents the vertical displacement of the sample holder, it does not represent the wear depth of the liner due to the sample under test being oriented at a 45° angle relative to the loading arm. Therefore a further calculation was required as follows:

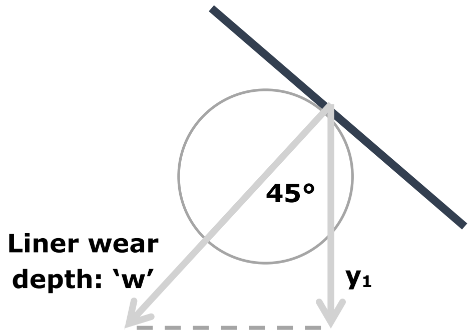

Figure 44 - Schematic of flat sample in contact with cylindrical counterface.

$$\mathrm{w} = \frac{y_1}{\cos 45} \tag{4}$$

$$\mathrm{w} = \frac{0.5185 \cdot y_2}{\cos 45} \tag{5}$$

$$\mathrm{w} = 0.73338 \cdot y_2 \ (mm) \tag{6}$$

Therefore, to conclude, there was a ratio of 1:0.733 between the displacement measured by the LVDT and the liner wear depth.

3.3.4.4 Magnet Release

The final piece of inherited hardware was a quick release mechanism for the electromagnet units, in order to disengage the load from the sample when both a 100°C temperature and 0.3mm of wear had been recorded by the acquisition system, indicating the end of the test. Initially when the test bench was designed, it was intended to use much smaller masses than those which the author used, and these smaller masses were considered during electromagnet power rating selection. Once it was realised that the original masses were not sufficient enough to provide an accelerated test, much heavier and physically larger masses were introduced. This in turn affected the electromagnet specifications and therefore more powerful magnets had to be purchased. This is further described within Section 3.4.2

3.4 Rig Q - Design alterations

Throughout the PhD programme, multiple areas for improvement to the design of Rig Q arose but, due to time constraints, only those which were of a critical nature were considered and implemented upon the test bench. The following section describes these modifications in detail and also contains a future considerations section which lists further improvements for implementation during further research projects using Rig Q.

3.4.1 Mechanical components

The first complication which arose during the course of the project was the unexpected requirement to increase the load in order to allow for accelerated test conditions to occur. As previously mentioned, the electromagnets had to be replaced with ones of higher power rating. Due to the increase in the applied mass, the physical size of the masses increased. Figure 45 shows the original and the current masses used for suspension.

Figure 45 - Original proposed mass of 20Kg (left) & currently used masses of 60kg (right).

This increased size, unfortunately caused the available spacing between each of the loading arms to be insufficient when all the weights were suspended. Alongside this, when all the newly required masses were suspended from all four loading arms the test bench became unstable due to its high centre of gravity and the overturning moment created by the overhanging masses.

The solution to both of these problems involved major alterations to the mechanical design of Rig Q. In order to stabilise the test bench, two of the four arms were reversed and therefore acted as counterweights to the opposing arms. This required modifications to the test head baseplate, to allow for the new mounting points of the uprights of the reversed arms. To stabilise it further, the legs of the test bench were extended and a 'dropping plate' was welded onto these extensions. The dropping plate was incorporated in order to minimise the damage caused to the floor of the laboratory by the newly increased masses when they were released by the electromagnets. This solution provided both the space and stability required, in order to carry out the required experiments in a safe manner. Figure 46 shows the revised CAD model which incorporates the mechanical design alterations.

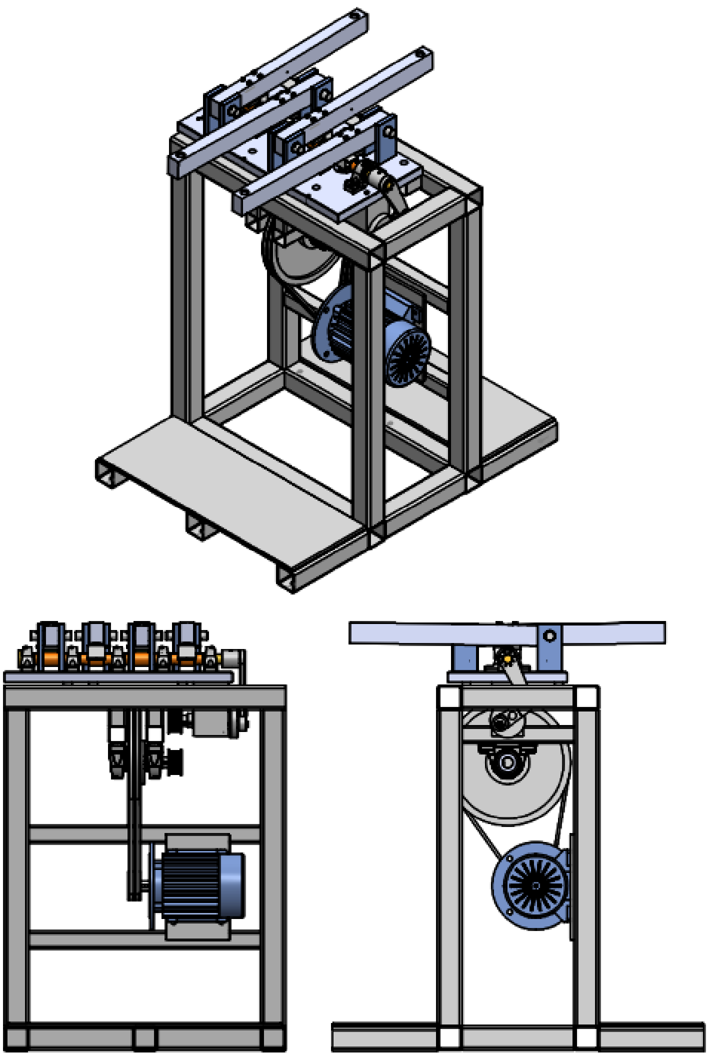

Figure 46 - Current four arm design of Rig Q.

After a shakedown test was performed, a misalignment issue was noticed in most test samples and this was deemed to be due to the way in which the electromagnets were attached to the loading arms. The electromagnets at the time were chosen to be attached to the loading arms via a large bolt, which passed through an over-sized hole in the arm. Whenever the bolt was not perfectly located in the centre of the oversized hole by the operator, the load imbalance caused one side of the sample to be in heavier contact with the counterface than the other, as seen in Figure 47.

Figure 47 - Properly aligned (left) vs poorly aligned (right) samples due to load distribution.

In order to minimise the geometrical variation of the location of the required loading point, a self-aligning mounting method was designed, as seen in Figure 48, which allowed for a custom machined bolt to freely pivot within the ball-cup joint and therefore produce even loading.

Figure 48 - Components of weight aligners (left), assembly (right).

3.4.2 Instrumentation & LabVIEW

Initially the monolithic amplifiers were inherited from a previous, unrelated, project and were mounted on a disk shaped printed circuit board in groups of two. This type of configuration was not desirable due its geometry, along with the planned expansion of the test-bench towards a 12 thermocouple channel configuration. This expansion was due to the desired temperature monitoring of extra components such as the motor, allowing for an automated cut-off of the test bench operations if this temperature exceeded a manually set threshold of 50 °C. This was incorporated into the LabVIEW control system architecture. The solution to this, was to create a new PCB in order to amplify up to 12 type J thermocouples and the result was a well packaged and clean interface for the thermocouple amplifiers, as shown in Figure 49.

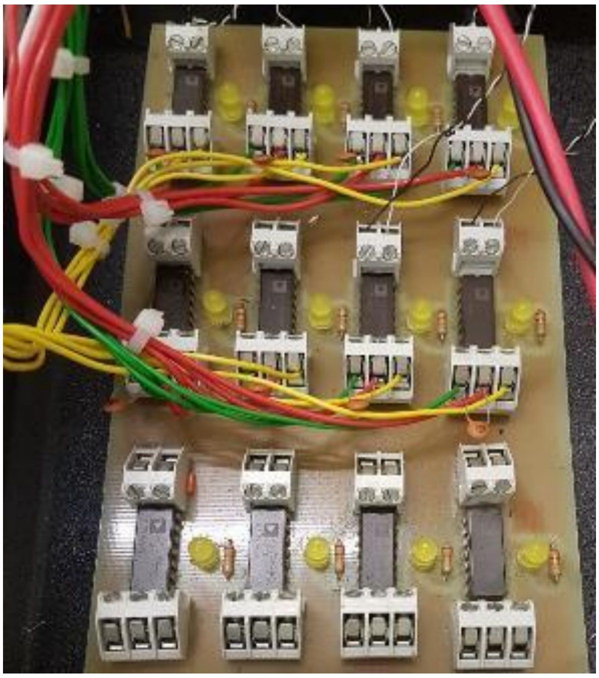

Figure 49 - Configuration of thermocouple board for easy thermocouple access and replacement.

The next problem was due to the increased size and therefore power requirements of the electromagnets. When operating the original electromagnets, the current supplied from a USB DAQ 6008 was sufficient enough to trigger the original relay in order to cut the circuit and stop the current flow to the component. As new and more powerful components were used, this current from the DAQ was not sufficient and the circuit could not be broken. Initially a 6111 USB DAQ board was used under loan from Cardiff University's electronics workshop which provided enough current from its output channels to trigger the new relay. Although this was deemed suitable in the short term to allow testing to proceed, a longer term solution was implemented by introducing an additional relay switch to the system which was driven by the weak 5V signal generated from the inherited NI6008 DAQ.

In order to allow the collection of data through the NI DAQ boards, a LabVIEW programme had to be developed. The interface was designed to incorporate all the required functions from the test bench in order to achieve full automation during the length of the test. A flowchart representation of the Rig's operations is shown in Figure 50.

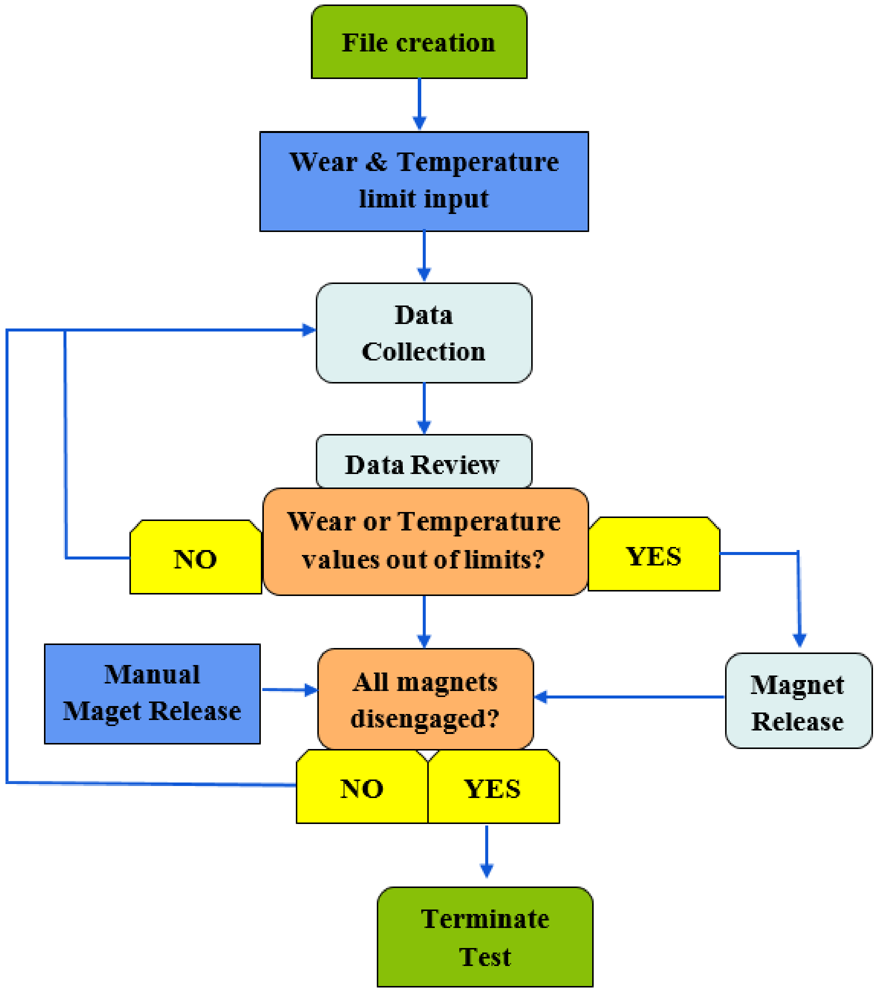

Figure 50 - Flowchart of the LabVIEW operations.

3.4.3 Future design considerations

The following section focuses on the mechanical alterations proposed by the author, in order to address a number of undesirable features of the current iteration of the test-bench. Figure 51 numbers the alterations in order to provide a reference for discussion.

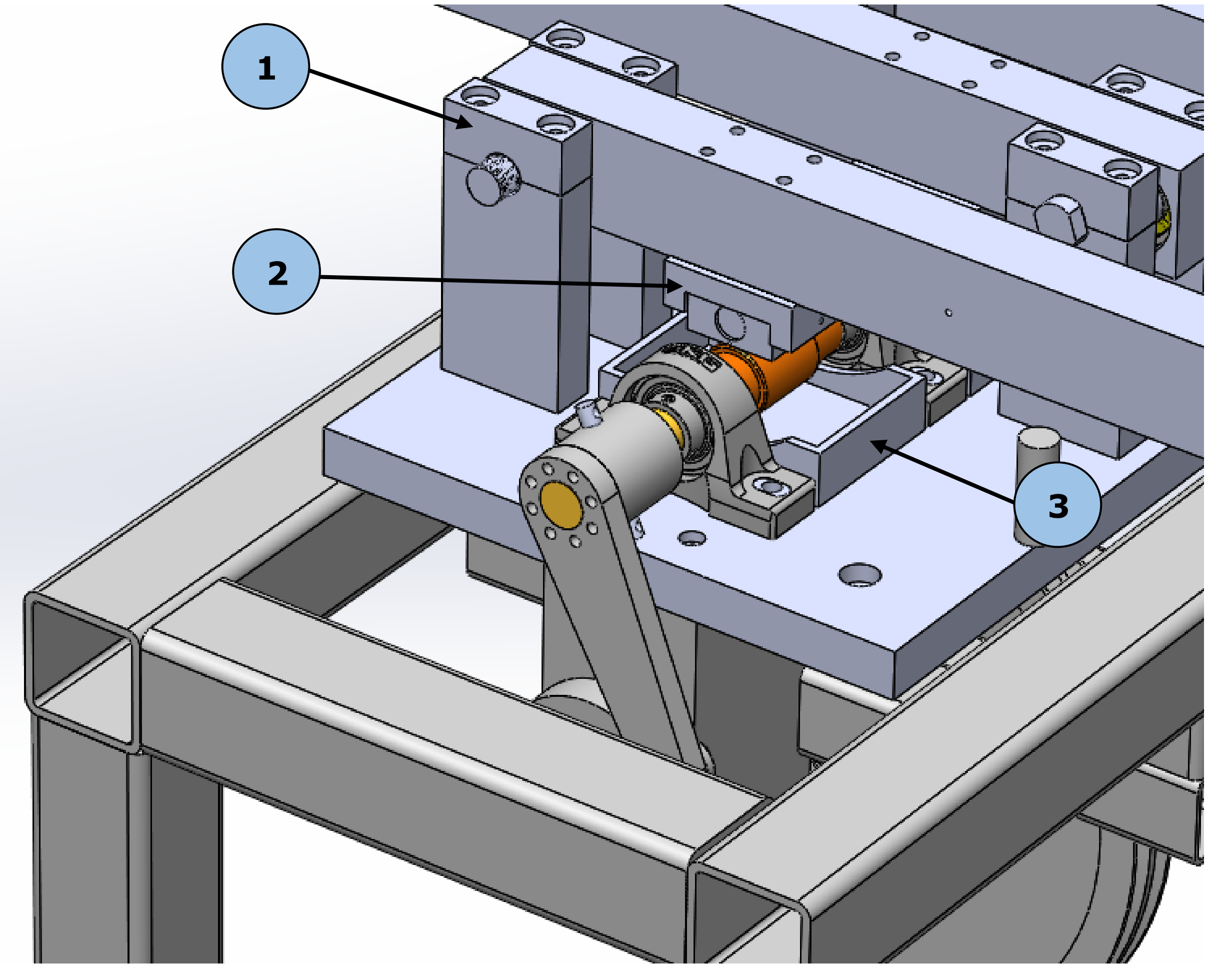

Figure 51 - Design alterations proposed for Rig Q: 1) Arm uprights, 2) Sample holder, 3) Catch tray.

The uprights responsible for locating the loading arms are proposed to be altered in order to ease the mechanical arm installation or removal when the test bench is in need of disassembly. The current uprights only incorporate a tapped hole on the face contacting the baseplate, therefore in order to remove the mechanical arm, the operator must unwind the required screws from the underside of the baseplate. This can prove to be very tedious due to the poor access to these fasteners underneath the test bench. The proposed design is to include a further two tapped holes per upright to be created, in order to remove the mechanical arm from a more comfortable position.

A geometric alteration to the sample holder is proposed by the author in order to reduce the load required to achieve similar contact pressures. Currently the sample subjected to wear comes into contact with the counterface at a 45° angle. The proposed design moves the test sample to the top of the counterface, therefore reducing the mass required to achieve the same nominal contact pressure, as seen in Figure 56.

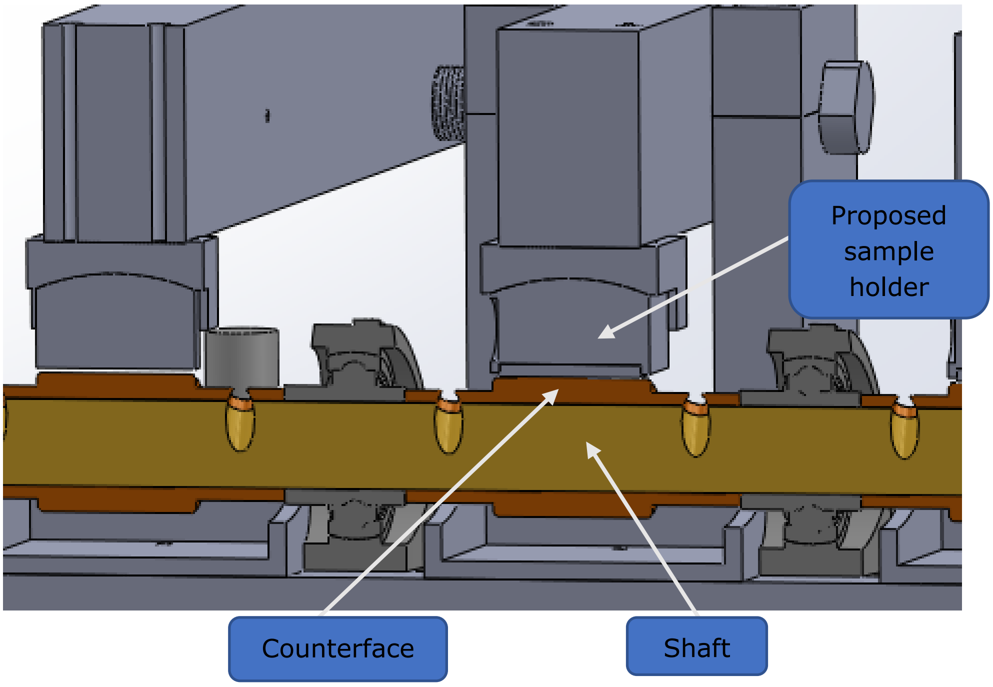

Figure 52 – Annotated section view CAD image of the proposed sample holder design.

Finally, the catch trays are proposed by the author in order to aid future debris analysis. Currently, there is no allocated space for the collection of the third body particles rejected from the sliding surfaces and these can be of scientific value.

3.5 Rig H

Rig H (Figure 53 - Figure 59) is a full-size bearing test bench, designed and developed in SKF Clevedon.

Figure 53 – Full Bearing test, Rig H, with two test sides (right and left).

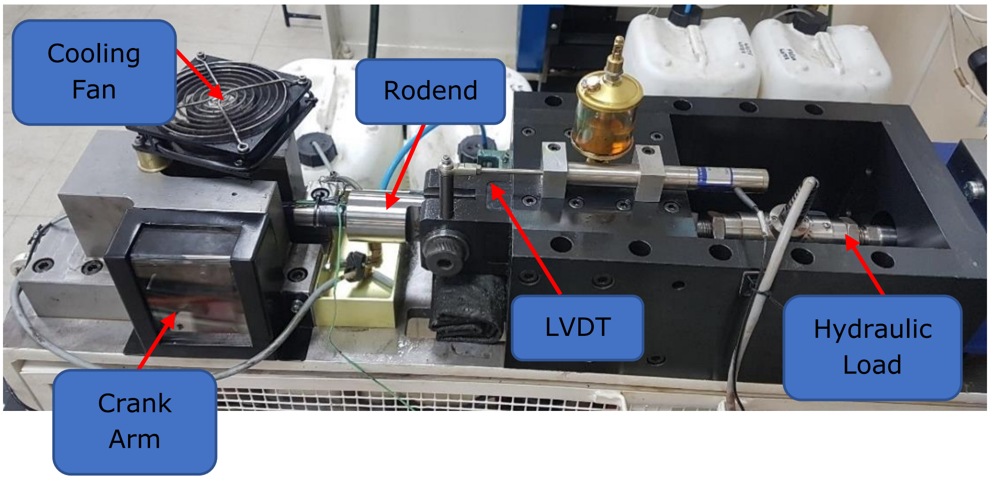

Figure 54 – Rig H test head with labelled components.

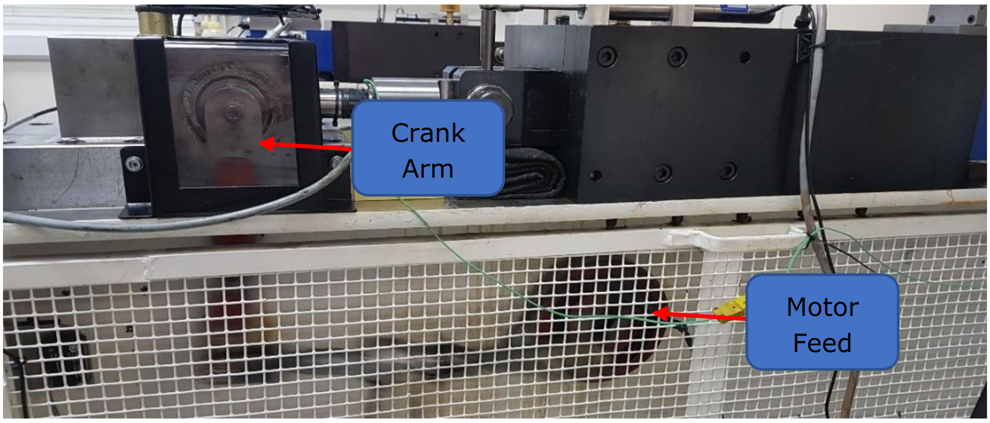

Figure 55 – Rig H, creation of the required reciprocation motion.

Within this project Rig H was utilised to observe how the condition monitoring techniques developed by the author, based on coupon testing carried out on Rig Q, translated into full bearing tests. The test bench is able to test up to two bearing samples simultaneously and independently. The load is applied by hydraulic actuators and three test standards can be achieved, two following the AS81819 test procedures and one following the ETI 24 test procedure (AMPEP, 2001). The first of the AS81819 tests involves the application of a cyclic load of ±2300 lb (± 10 kN) about the 0 lb position at a frequency of 5 Hz. The load is applied in a sinusoidal form such that the maximum load and maximum test bearing rotational speed occur at the same time (0° rotation) (SKF, Internal Communications., 2013) (Figure 56).

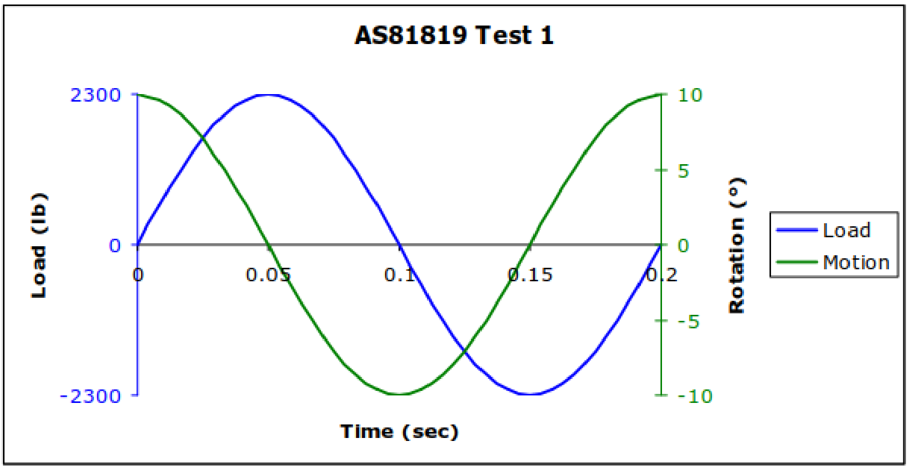

Relationship between cyclic load and oscillation angle during one cycle	Frequency (Hz)
0Lb → +2300LB → 0LB → -2300LB → 0LB +10° → 0° → -10° → 0° → +10°	5

Figure 56 – Description of Rig H's test 1 – AS81819 (SKF, 2013).

Test 2 applies a cyclic load of ±2300 lb (± 10 kN) about the 2300 lb (10 kN) position at a frequency of 5 Hz. The load is applied in a sinusoidal form such that the maximum load and maximum test bearing rotational speed occur at the same time (0° rotation) (Figure 57).

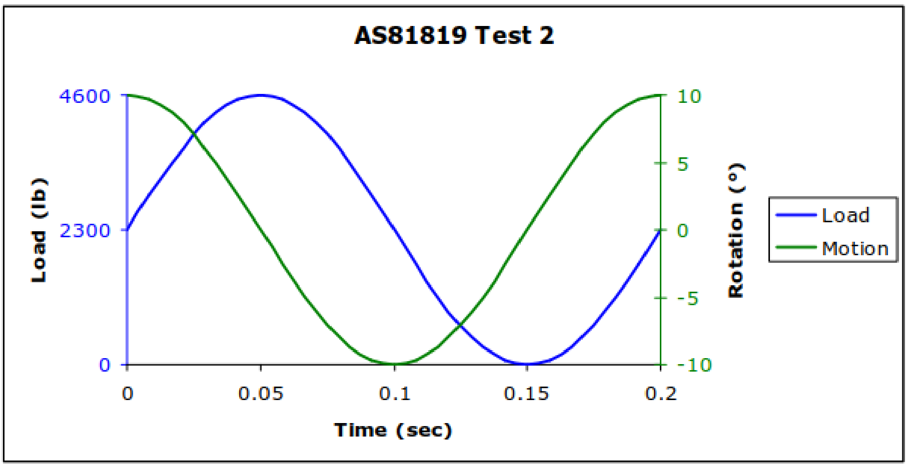

Relationship between cyclic load and oscillation angle during one cycle	Frequency (Hz)
+2300Lb → +4600LB → +2300LB → 0LB → +2300LB +10° → 0° → -10° → 0° → +10°	5

Figure 57 - Description of Rig H's test 2 – AS81819 (SKF, 2013).

The final testing procedure involves an application of a cyclic load of ±540 lb (2.4 kN) about the 0 lb position at a frequency of 6 Hz. The load is applied in a sinusoidal form such that the maximum load and test bearing rotational speed occur at the same time (0° rotation).

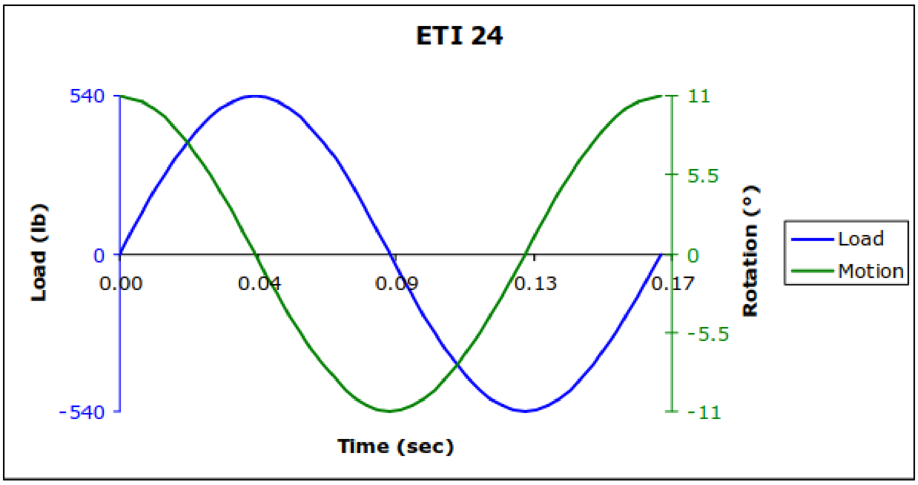

Relationship between cyclic load and oscillation angle during one cycle	Frequency (Hz)
0Lb → +540LB → 0LB → -540LB → 0LB +11° → 0° → -11° → 0° → +11°	6

Figure 58 - Description of Rig H's test 3 - ETI 24 (SKF, 2013).

All three test standards focus on a rotorcraft's main rotor conditions but the most commonly used within SKF is Test 1 of the AS81819 standard. It is important to note that the specifications for Tests 1 and 2 were created by an external committee and Test 3 was created internally.

In order to achieve these test conditions, Rig H's control system has two main primary functions which consists of:

1. Phasing the load to the motion using a signal from rotary controls.
2. Periodically pausing the motion to take a loaded static displacement measurement.

Although both desirable, the latter feature is of most relevance to this project. While in operation the control system of the test bench is responsible for the data acquisition of multiple parameters. Some of these include temperature, dynamic displacement and static displacement. All of the above features can be viewed within an annotated test bench results example in Figure 63.

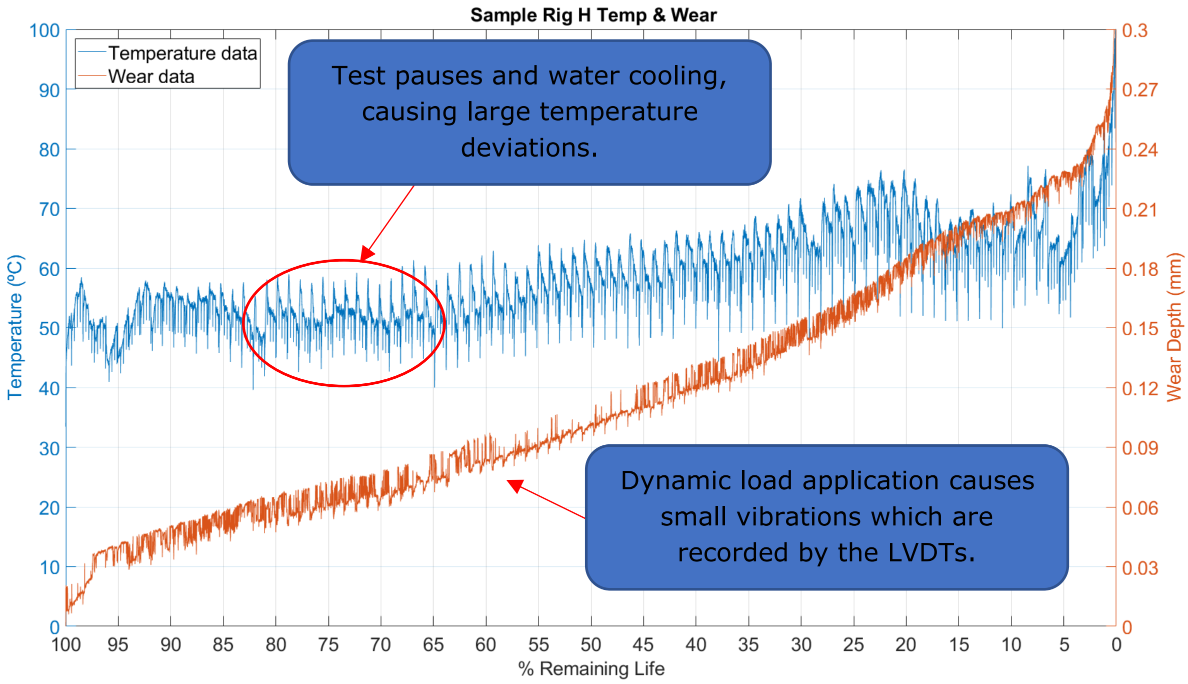

Figure 59 - Example of test results from Rig H.

3.6 Reciprocating wear test bench

This particular test rig was designed and manufactured within Cardiff University and is used for rapid wear testing of a range of samples, following the ASTM G133 standard (ASTM, 2016). It was of interest to this project due to its reciprocating motion. As discussed in chapter 6, this configuration allowed the author to directly relate or eliminate some of the phenomena of the acoustic emission effects and trends observed during tests on Rig Q. The principal of operation is based on its reciprocating nature and its ability to provide large loading pressures upon the sample under test via the use of small contact areas. The samples are the flat components under test and the equivalent 'counterface' is the steel ball. The component which reciprocates, is the flat sample which is clamped in position on a reciprocating plate and the load is applied in a directly vertical manner through the use of masses. Figure 60 shows a CAD model and an actual image of the test bench (Bertera, et al., 2015).

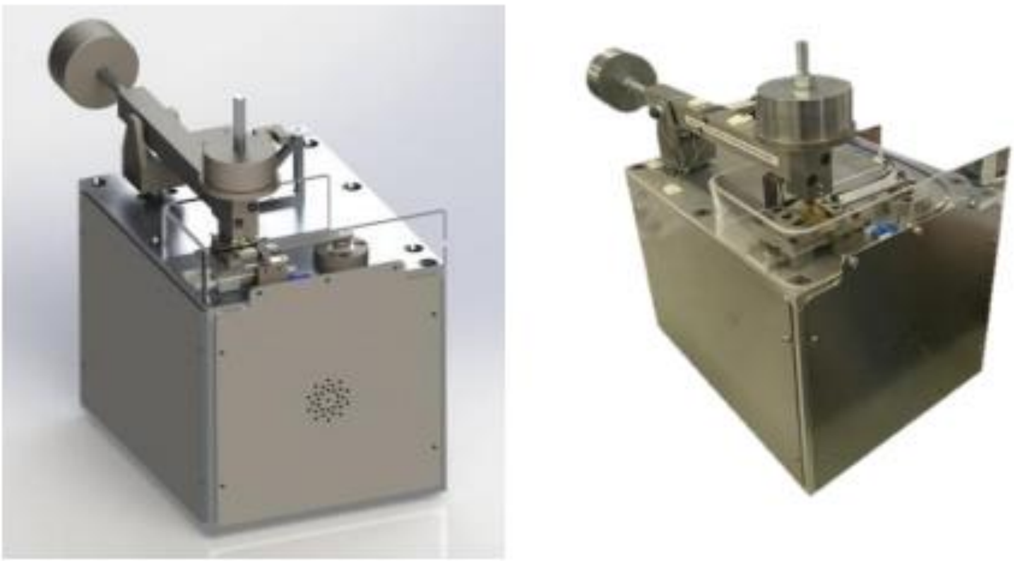

Figure 60 - CAD image (left) and actual image (right) of Cardiff Universities reciprocating test bench.

In order to follow the ASTM G133 -05 standard, a stroke length of 10mm at 5Hz was chosen. This particular test bench was capable of recording a number of variables, such as the sample temperature, wear depth and coefficient of friction. Sample temperatures were measured via an intrusive thermocouple located near the contact zone between sample and pin and the wear depth of the test was measured via the use of an inductive sensor, located between the baseplate of the test bench and the loading arm. Finally, the coefficient of friction was measured via the use of a load-cell which was attached to the loading arm as shown in Figure 65.

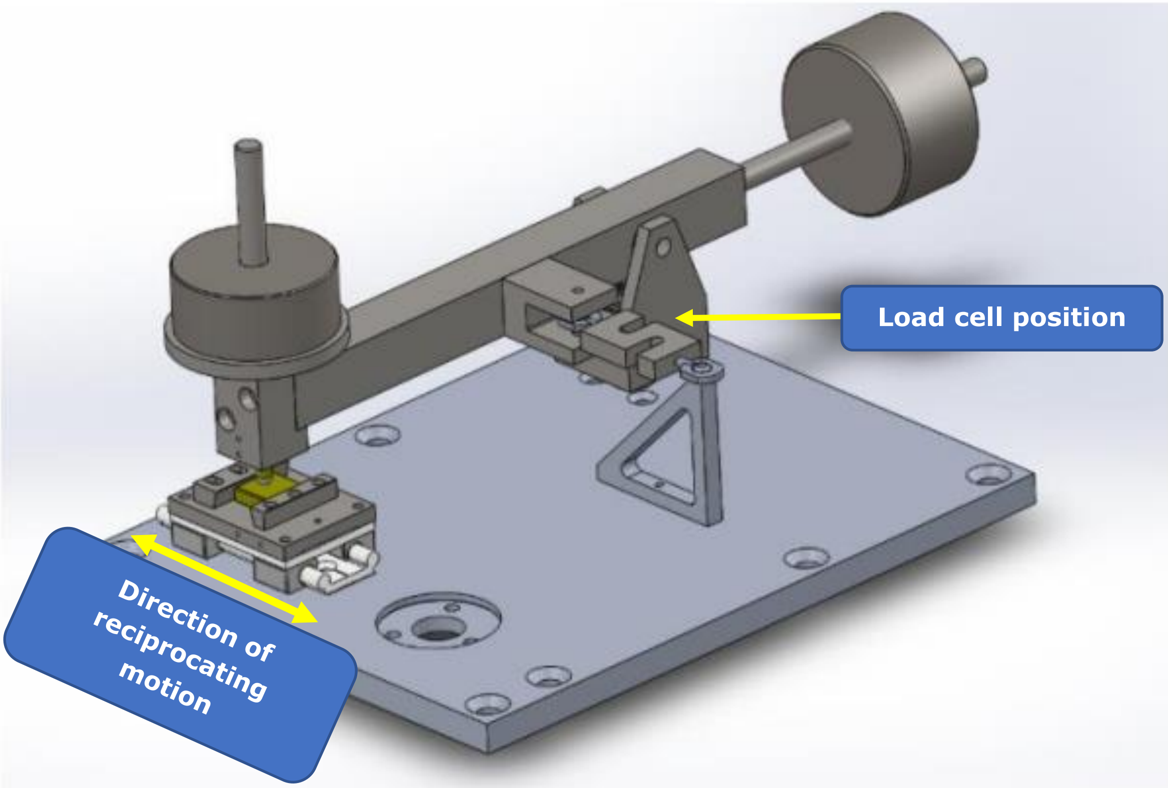

Figure 61 - Load cell location and reciprocation direction of the CU reciprocating test bench.

Having described the various testing facilities used during this project, the next chapter presents the largest group of results obtained, from Rig Q.

Chapter 4: Rig Q – Test results

4.1 Introduction

This chapter provides an understanding of the raw temperature and wear data collection throughout the testing phase of the research programme. During the presentation of the raw data, references to the literature are also made, where relevant. The testing methodology of Rig Q is described in further detail and post-testing investigations are also introduced. These investigations mainly focus on the third body transfer films produced during the wear cycle of the liner.

4.2 Test procedure

4.2.1 Contact pressure progression

Within Chapter 3, the loading conditions of Rig Q were briefly described. It was stated that in order to achieve accelerated wear conditions, the contact between the two sliding surfaces had to be created as a line contact. Although this type of contact was deemed valid for the nature of coupon testing, an inherent contact pressure variation occurs during the wear of the materials under test. As the self-lubricating liner began to wear, a larger proportion of the liner composite came into contact with the cylindrical counterface, therefore decreasing the contact pressure. In order to quantify this variation, the Hertzian contact pressure between the two sliding surfaces was initially calculated and the pressures were in-turn calculated at incremental wear depths up to the point where metal to metal contact was reached (0.28mm).

To calculate the initial contact pressure between the liner composite and the steel counterface, the Hertzian contact pressure was calculated by assuming the contact geometry resembled a flat on cylinder type interface. To do so, the following equations were utilised:

$$b = \sqrt{\frac{4 \cdot F \cdot \left(\frac{1-v_1{}^2}{E_1} + \frac{1-v_2{}^2}{E_2}\right)}{\pi \cdot L \cdot \left(\frac{1}{R_1} + \frac{1}{R_2}\right)}} \tag{7}$$

$$P_{max} = \frac{2 \cdot F}{\pi \cdot b \cdot L} \tag{8}$$

$$P_{mean} = \frac{\pi \cdot P_{max}}{4} \tag{9}$$

Table 2 explains the notation of equations 7-9.

Table 2 – Notation used within the Hertzian contact pressure calculation procedure.

Notation	Meaning	Value	Units
b	The half-width of the Hertzian contact between the counterface and the liner composite.	Calculated	m
F	Force applied at the contact area.	1678.54	N
v_1	Poisson's ratio of the steel counterface.	0.28	Dimensionless
v_2	Poisson's ratio of the liner composite.	0.40	Dimensionless
E_1	Modulus of elasticity of the steel counterface.	200×10^9	N/m^2
E_2	Modulus of elasticity of the liner composite.	2.266×10^9	N/m^2
L	Length of contact between the counterface and the liner composite.	0.04	m
R_1	Radius of the counterface.	0.019525	m
R_2	Radius of the liner composite.	Infinite	m
P_{max}	Maximum Hertzian contact pressure.	Calculated	N/m^2
P_{mean}	Average Hertzian contact pressure.	Calculated	N/m^2

The load applied to the contact zone, as stated in Table 2, was calculated through considering static equilibrium of the loading arm about the pivot point, along with considering the angle at which the sample comes into contact with the counterface. These values are presented in Table 3.

Table 3 - Loading conditions of Rig Q at the liner composite - counterface interface.

Loading Properties	
Load applied (Kg)	**Vertical Force Applied at Sample (N)**
80	3195.257143
Load applied (N)	**Angle of contacting force (degrees)**
784.8	45
Distance between Sample Contact and Arm Pivot (m)	**Force applied perpendicular to the sliding contact (N)**
0.14	1678.538837
Distance between loading point and Arm Pivot (m)	
0.57	

The value of the mean Hertzian contact pressure was calculated to be 33.53 MPa with a half width contact ‘b’ of value 0.000626 m. The half-width value was in turn used to calculate the initial deformation of the liner composite and counterface, prior to any reciprocating wear motion being initiated. Taking Figure 67 as reference, it can be seen that with a width of ‘b’, the deformation which occurs at the interface between the liner and the counterface is ‘r’.

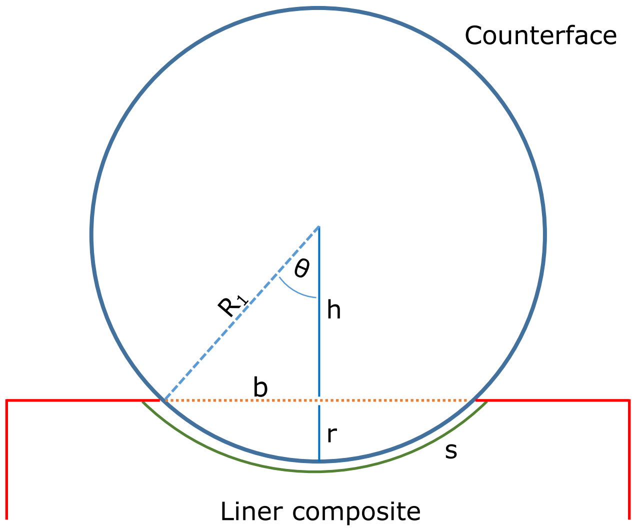

Figure 63 - Schematic of the steel counterface being in contact with the liner composite.

To calculate the value of r Pythagoras’s theorem is used to find ‘h’ and then subtract it from the value of R_1 which equated to the radius of the counterface. This value was found to be 1.002×10^{-5} m or 10.02 µm.

In order to calculate the contact pressures at the remaining wear depths, this value was subtracted from the maximum wear of 0.28mm and then divided into 27 increments of roughly 10 µm of wear. In order to find the area over which the force was acting upon, the length noted as ‘s’ on Figure 67 was calculated and multiplied by the contact length of 0.04m. The results of the contact pressure progression can be seen in Figure 64.

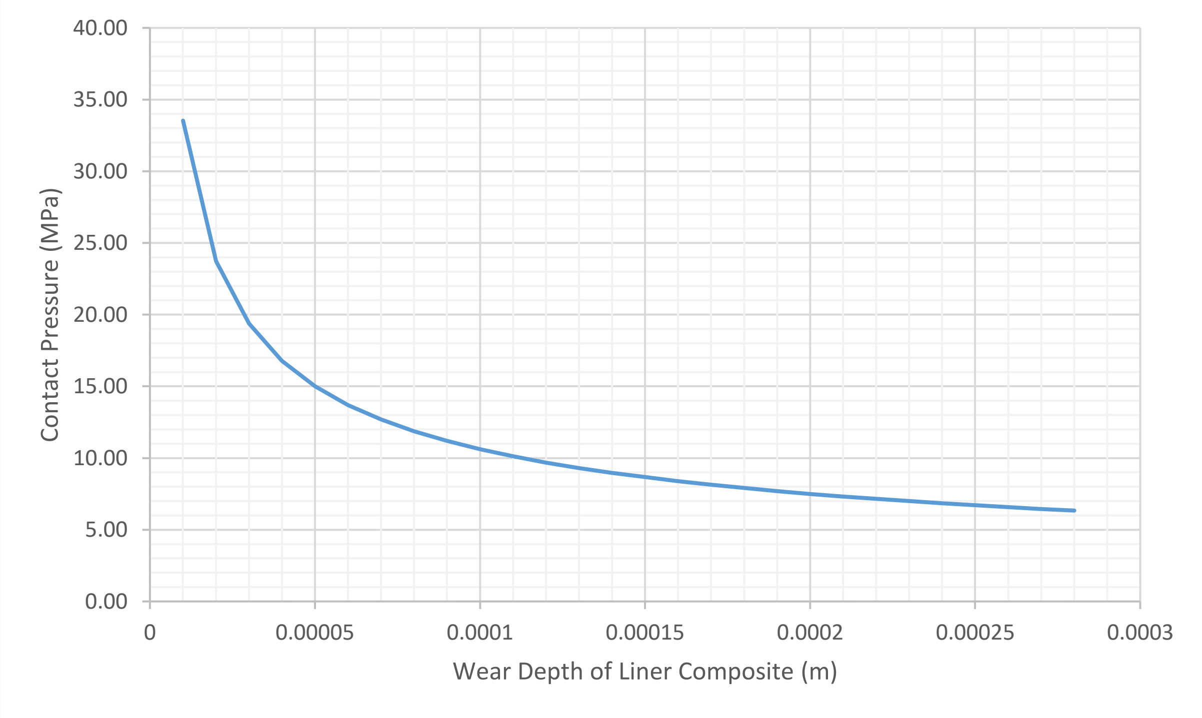

Figure 64 - Contact pressure progression vs liner wear depth.

Referring back to Figure 33 (Page 62), it can be seen that the majority of the contact pressures throughout the test lay within the preferred range for this type of main rotor testing, with exception of the very high initial contact pressures present at the test initiation phase, where the contact area between the liner and counterface is very small.

4.2.2 Speed of reciprocation and sliding distance

Due to the reciprocating nature of Rig Q, the angular velocity of the counterface in contact with the liner composite, varies with respect to the reciprocating angle at that particular time. The maximum angular velocity which can be achieved from Rig Q can be calculated by

Equation 10.

$$\omega = 2 \cdot \pi \cdot (RPS) \tag{10}$$

Where RPS stands for revolutions per second. The revolutions per second of the test bench is equivalent to the reciprocation speed of 5Hz and therefore the maximum value of the angular speed is 31.42 rad/s. Now that the maximum value of the angular velocity is found, the variation of the angular speed throughout the reciprocation cycle of ±10º can be calculated. For the purpose of this study, the position of the counterface at its extreme reciprocation angle was given the values of 0,10º and 20º. Figure 65 shows a simulated curve, which illustrates that the maximum angular velocity of the counterface is achieved at the half-way point of its reciprocation at the angles of 5 º and 15 º. It is important to note that this does not represent the crank arm movement of the test bench but is used for illustrative purposes.

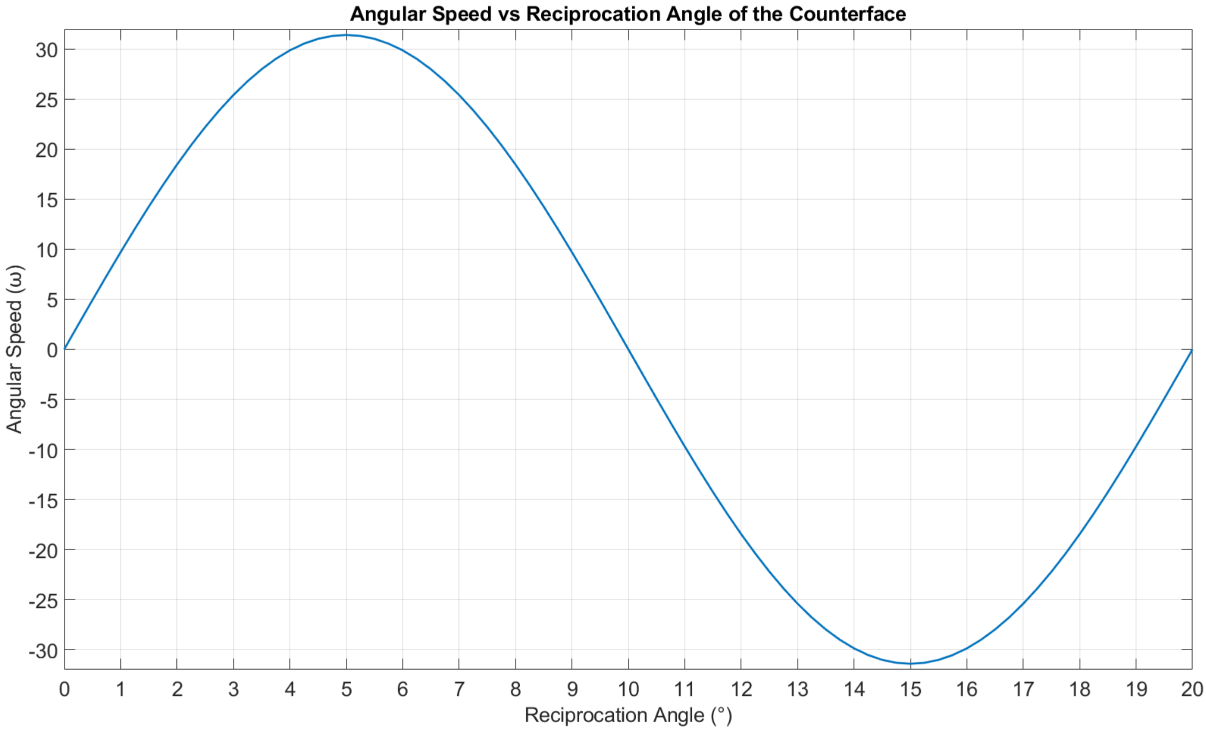

Figure 65 - Angular speed variation of the counterface with respects to reciprocation angle.

In order to calculate the sliding distance between the counterface and liner composite, Figure 67 must be revisited. During a single reciprocation, completion of ±10º the length of the liner in contact with the counterface equates to two times the arc length value of the segment. Once again, by working from a minimum wear depth of 10µm and increasing by 10µm intervals, the sliding distance variation of this type of accelerated test was calculated.

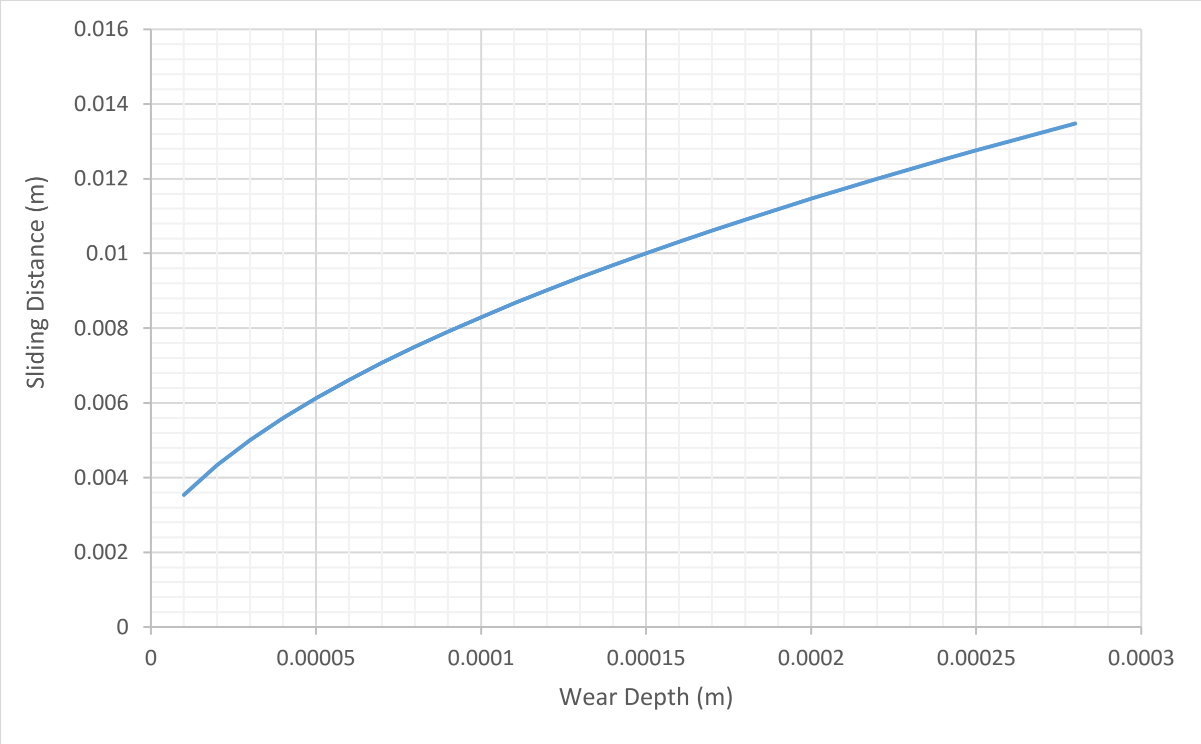

Figure 66 - Sliding distance of a single complete reciprocation of the counterface with respect to wear depth.

4.2.3 Surface properties of the liner composite and counterface

As a reminder to the reader, the parameters which affect the laminating process include the temperature of the press' heating elements, the pressure used, the kiss and dwell time of which the heating elements hover very closely to the pre-preg and fabric and finally, the amount of time of which the press applied the load upon the two material sheets. The final product takes the form of a single combined sheet (

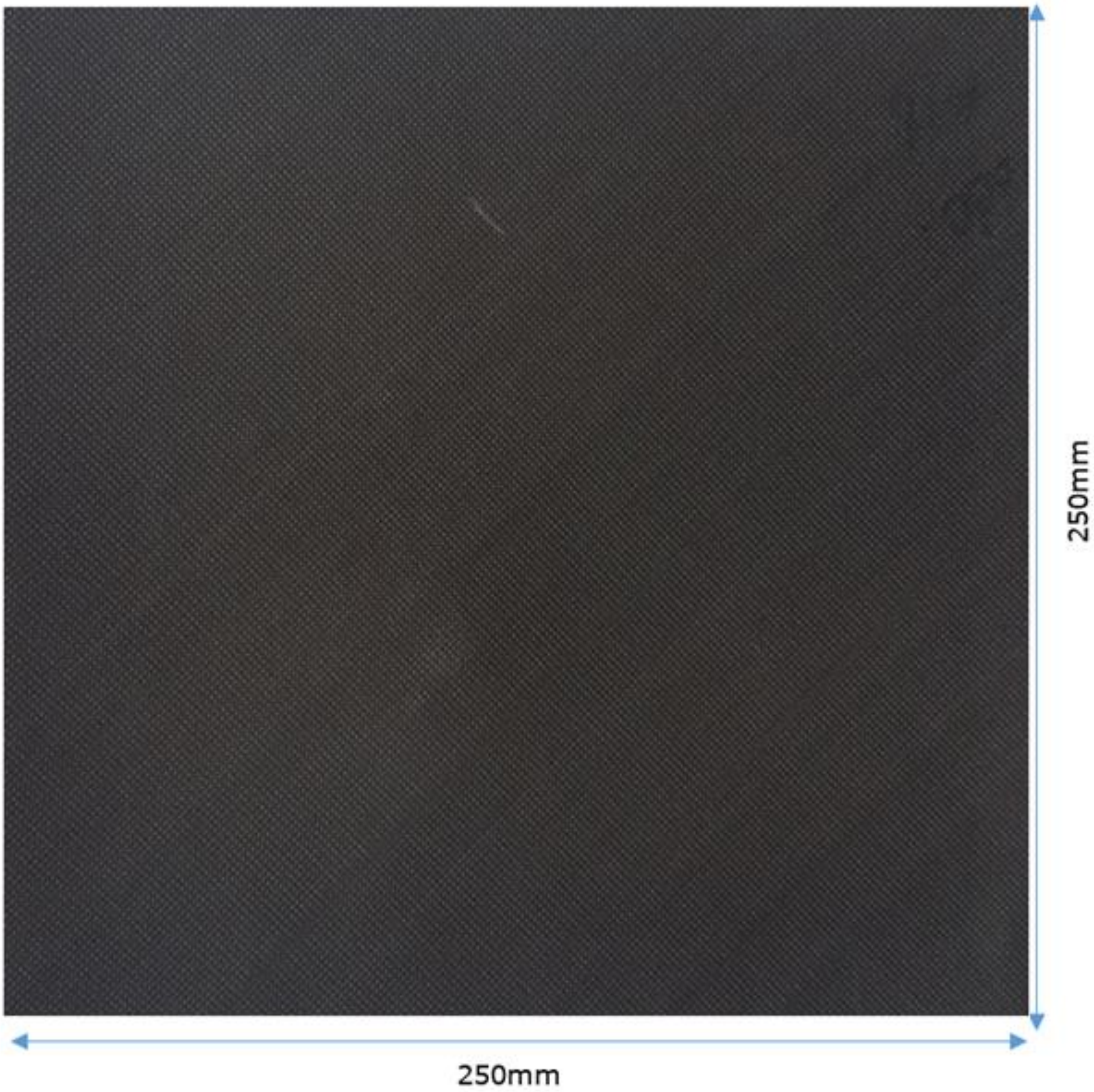

Figure 67), which can then be cut into the required geometry and in turn fitted to the inner side of the outer race of the bearing.

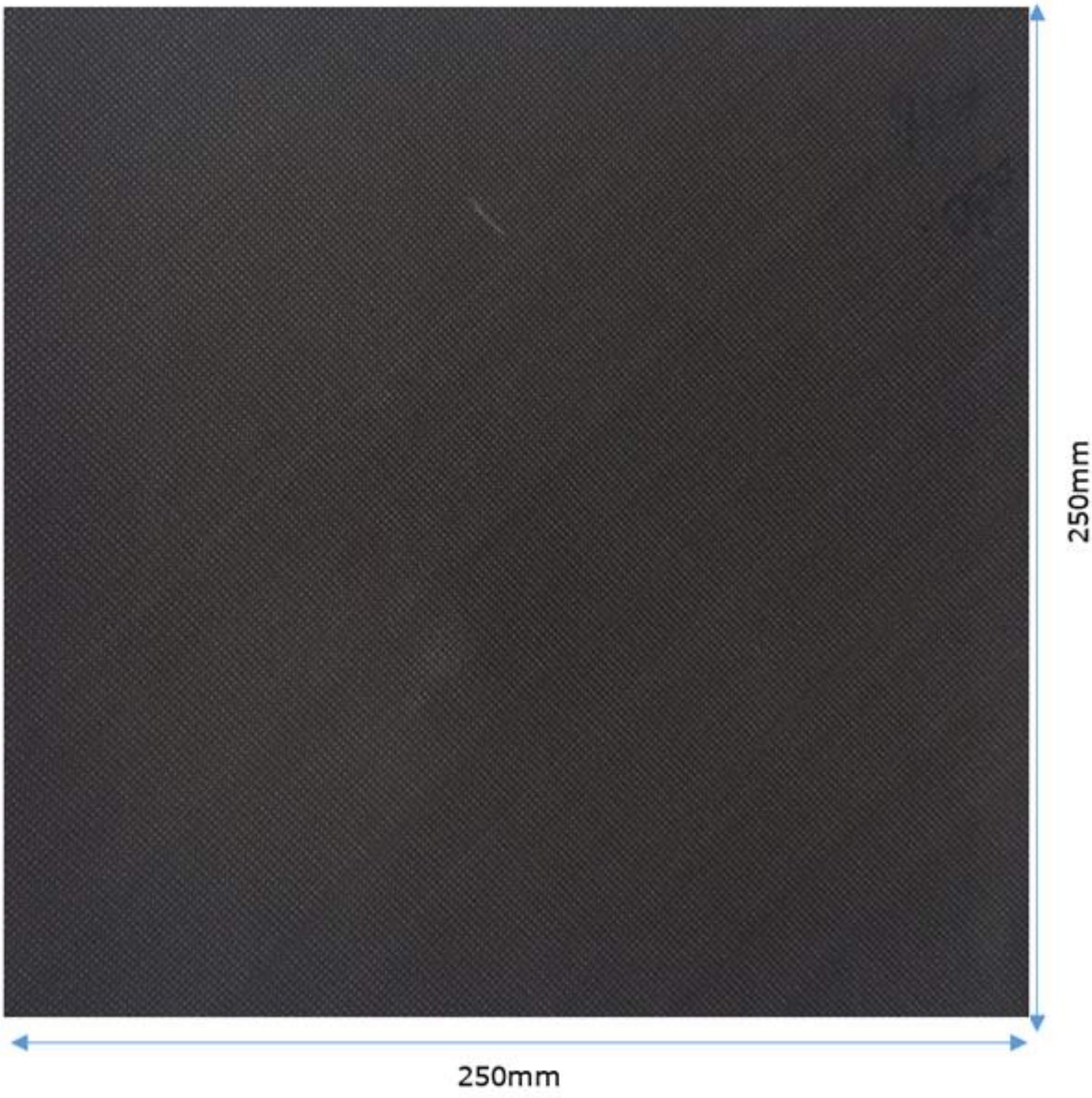

Figure 67 - Image of a laminated X1 liner.

Although visually, the glass fibres can be seen on

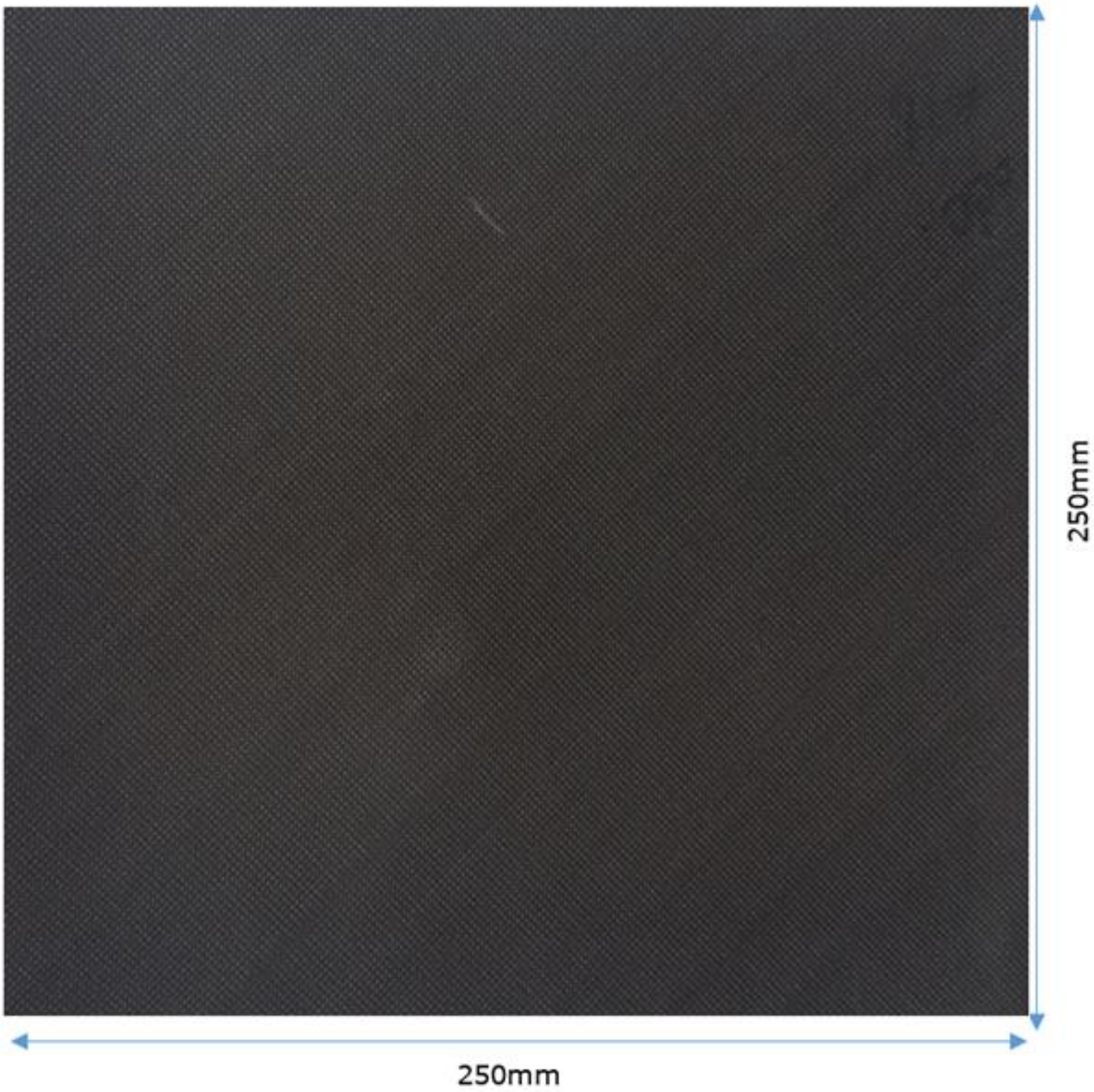

Figure 67, a three-dimensional surface profilometer measurement was conducted using a Taylor Hobson Form Talysurf in order to investigate the material properties in more detail and this is shown in Figure 68.

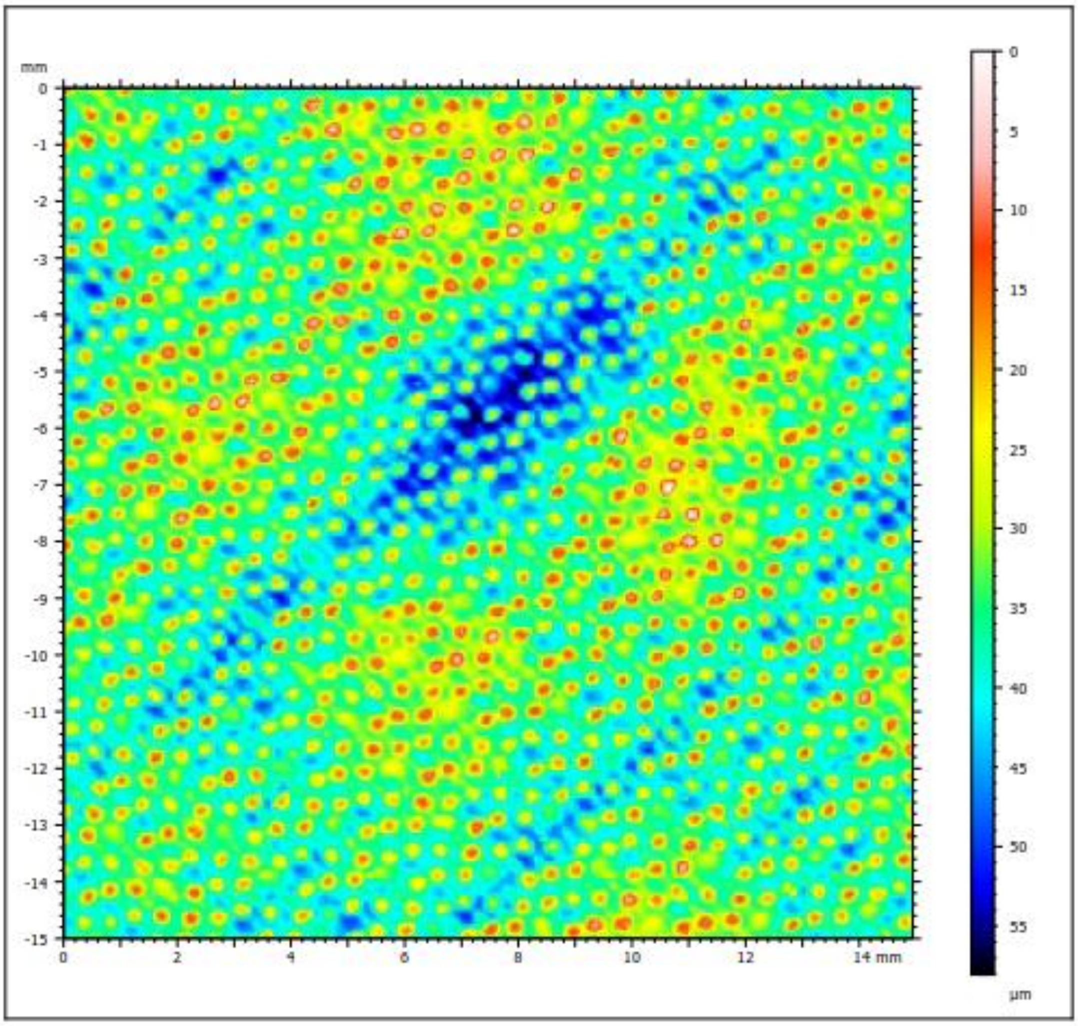

Figure 68 - Talysurf image of the X1 liner.

Within Figure 68, the weave direction composition of the liner composite becomes clearer with the scale being viewed in depths. In order to further investigate the surface roughness of the liner, a section 2D scan was taken as shown in Figure 69 and further visualised via 3D mapping with an accented peak percentage of 20% (Figure 70).

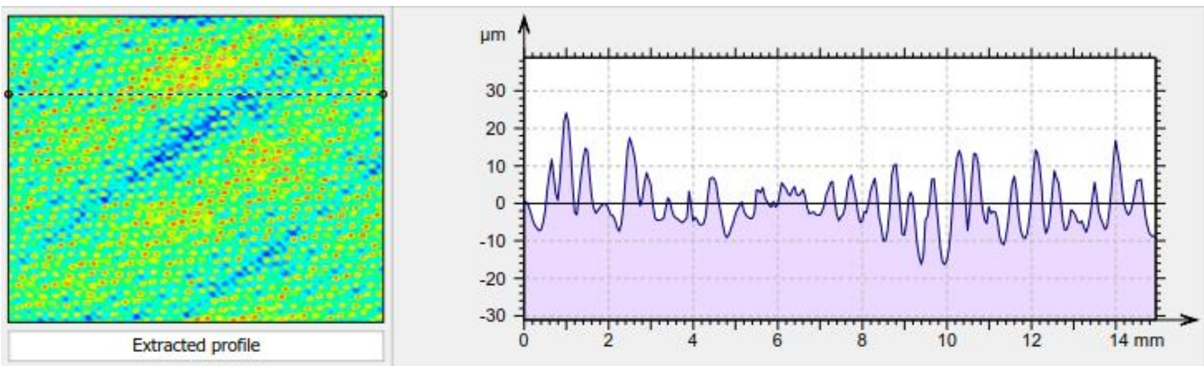

Figure 69 - Extracted profile of a section of the liner composite.

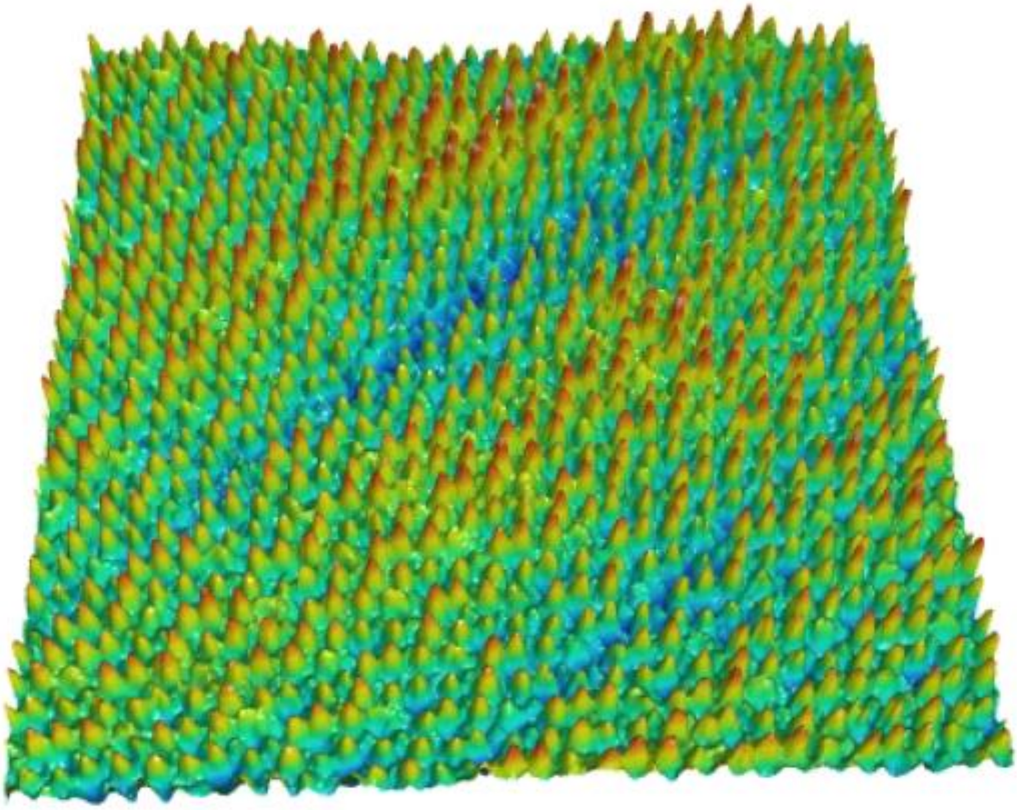

Figure 70 - 3D visualisation of the liner composite with exaggerated peak amplitudes.

Further, an optical microscope was used in order to view the weave structure (Figure 71).

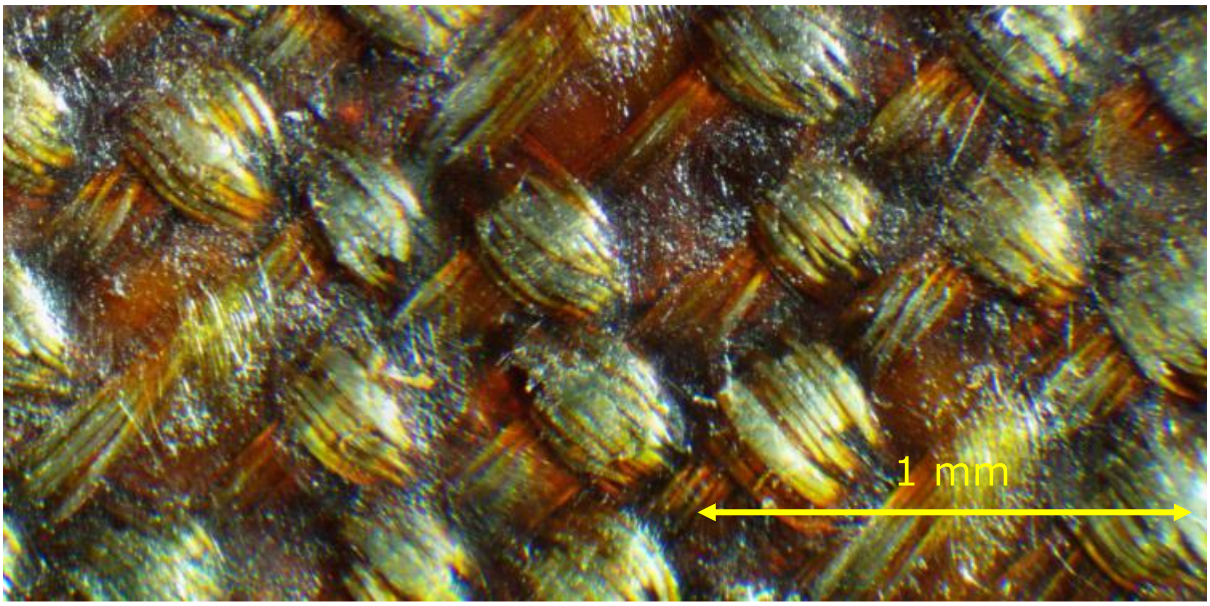

Figure 71 - Weave structure of the liner composite under a microscope.

The reflective substance which can be seen filling the spaces between the PTFE and glass fibre strands is the phenolic resin which penetrated through the liner fabric during the laminating process.

The counterfaces were also measured using the profilometry equipment in order to get a complementary understanding of the sliding contact zone of the test. Due to the cylindrical geometry of the counterface, a curved scan was taken (Figure 72 a), then levelled in sections in order to produce a flat representation of the surface (Figure 72 b) and finally a 2D scan of the counterface was conducted in order to understand its roughness value Figure 73.

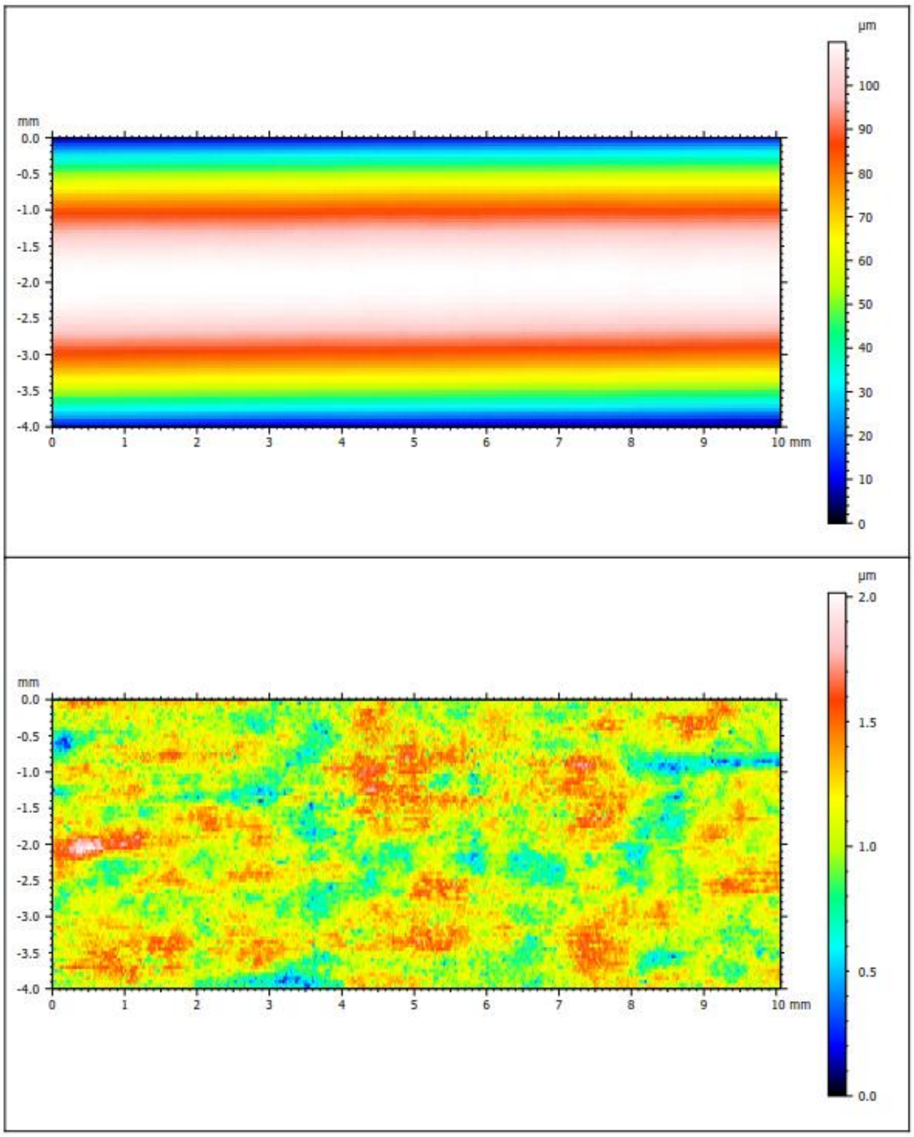

Figure 72 - Talysurf scan of the cylindrical counterface (a)(top) and levelled surface (b)(bottom).

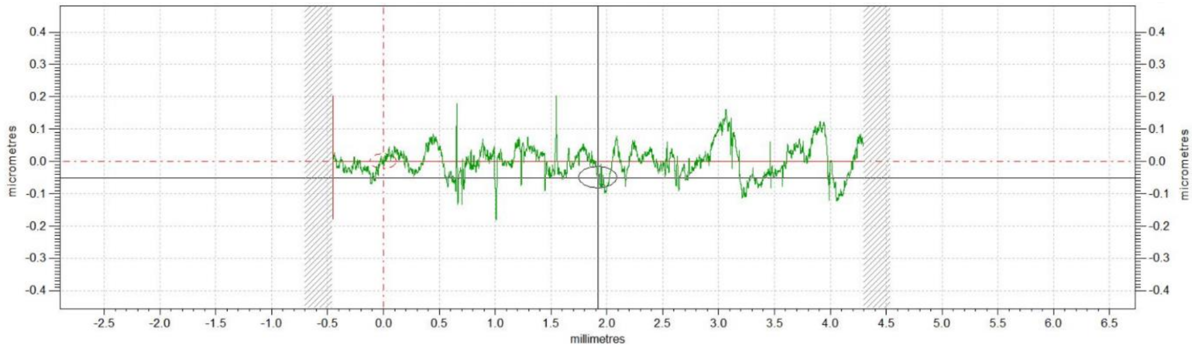

			Slope	-0.3483	°
Ra	0.0381	µm	Rq	0.0488	µm
Rp	0.0912	µm	Rv	0.0833	µm

Figure 73 - Roughness of the super finished counterface (Ra 0.0381 µm).

Optical microscopy was once again used, in order to view the counterface’s sliding surface.

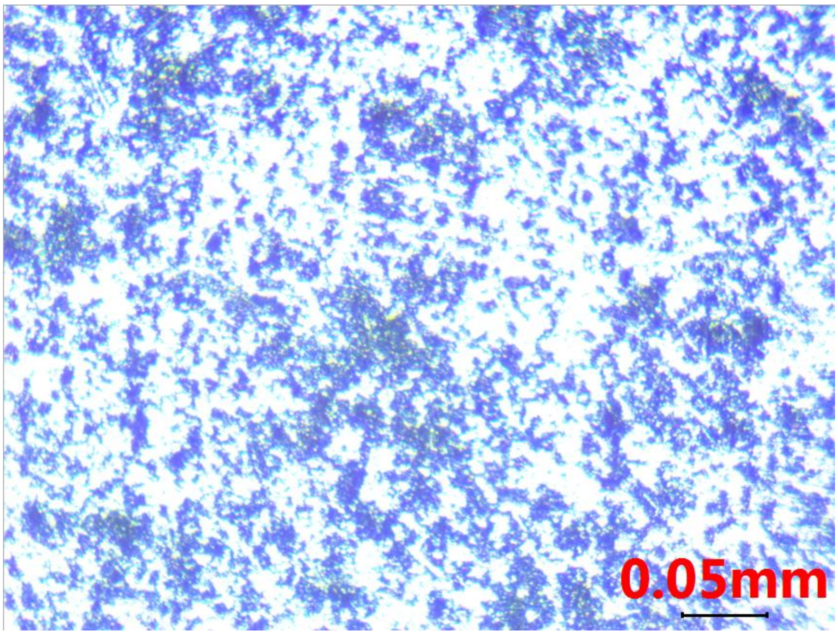

Figure 74 - Optical microscopy of the counterface's surface.

As it can be seen within Figure 74, there is little evidence of machining marks and the surface appears relatively isotropic which provides us with visual information regarding its super-finished nature.

4.3 Results

The raw temperature and wear results of all of the tests conducted during the research programme are described herein. Chosen samples and counterfaces will also be analysed in more detail, to aid the description of how a third body transfer layer is able to be established upon the counterface's sliding contact region.

4.3.1 Temperature and wear vs time

During the pre-development phase of the test bench, the inherited test bench had to undergo a number of shakedown tests, where only two of the four possible arms were loaded. The arms were loaded with 60kg and the crank reciprocation speed was kept at a constant of 5Hz with a reciprocation angle of ±10º. Although the full main rotor representation configuration (4 arms) was not able to be achieved, the data was still collected and is presented in Figure 75 and Figure 76.

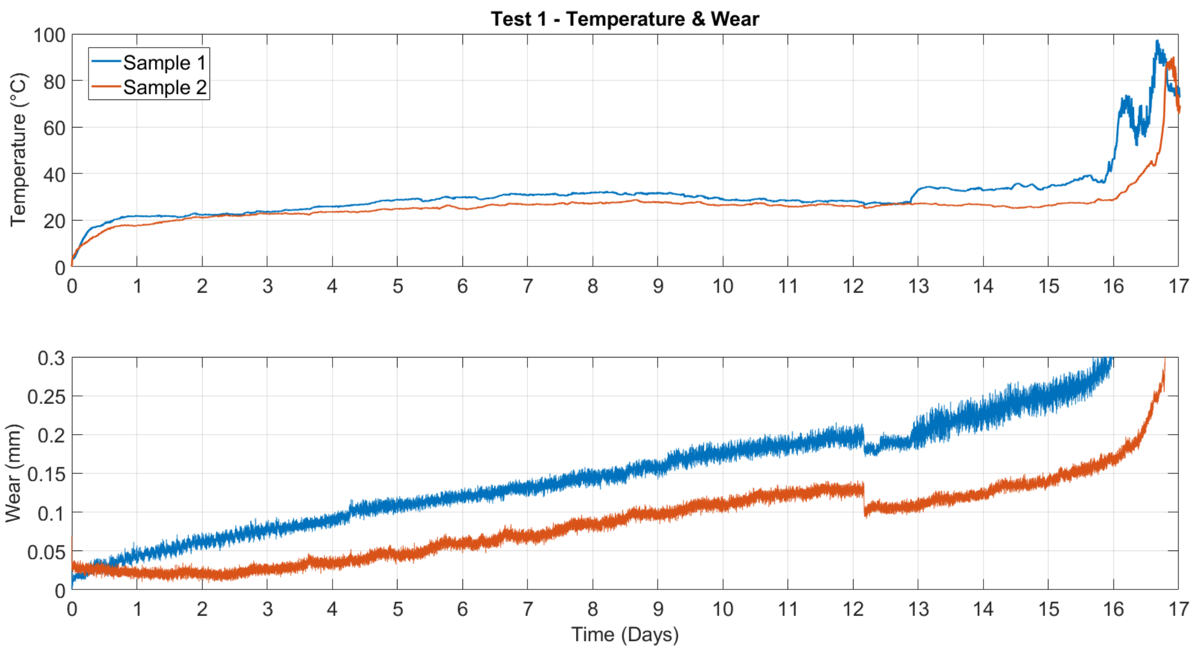

Figure 75 -Temperature and wear data from the first test conducted on Rig Q.

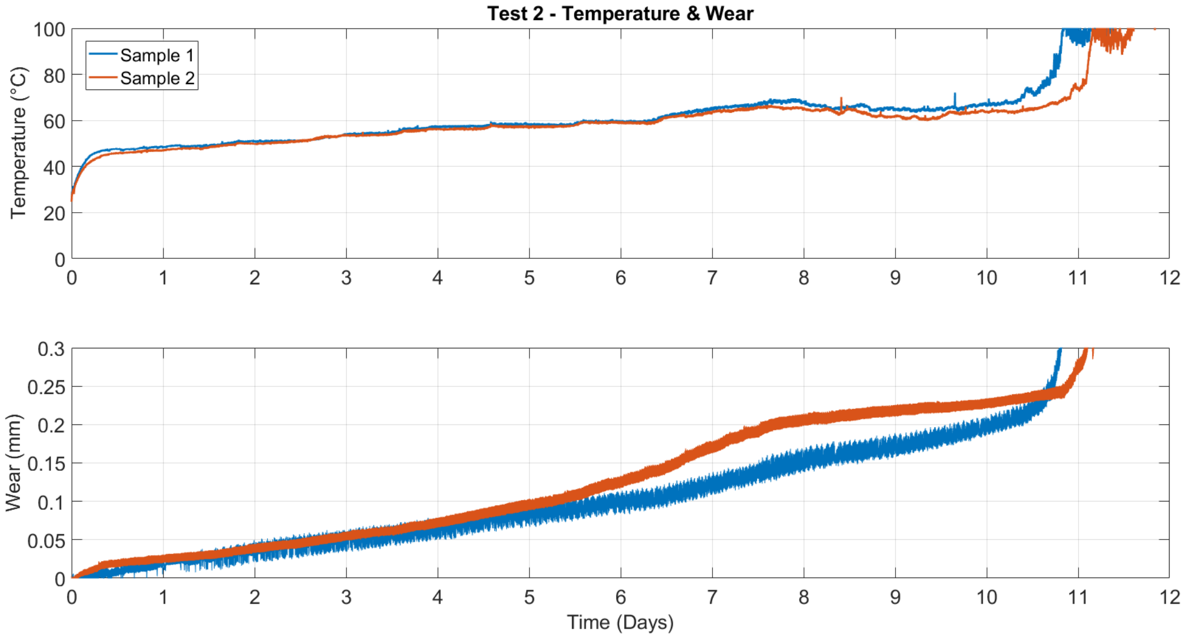

Figure 76 - Temperature and wear data from the second test conducted on Rig Q.

From Figure 75 and Figure 76 it can be seen that the samples under test have a relatively small spread in terms of time to final failure. Failure in these two experiments was either defined by reaching a wear depth of 0.3mm, which exceeds the 0.26mm thickness of the liner material, or, in the case of LVDT noise, a temperature cut-off was introduced at around 120ºC.

It is also important to note that the temperature and wear curve characteristics of the shakedown test results match those of literature. Such include a relatively short bedding in period consisting of roughly half a day, followed by a long stage of steady state wear at a relatively constant rate until the final failure, after the backing material is reached and the transfer layer breaks down.

After the completion of the two shakedown tests, the development of the test bench to the new loading arm configuration and geometry extension was finalised prior to conducting further experiments. This mechanical arm configuration change is described in section 3.4.1. The following results (Figures 81 – 85) were conducted with a 60kg weight attached to the loading arms and once again the crank reciprocation speed was kept at a constant of 5Hz with a reciprocation angle of ±10º.

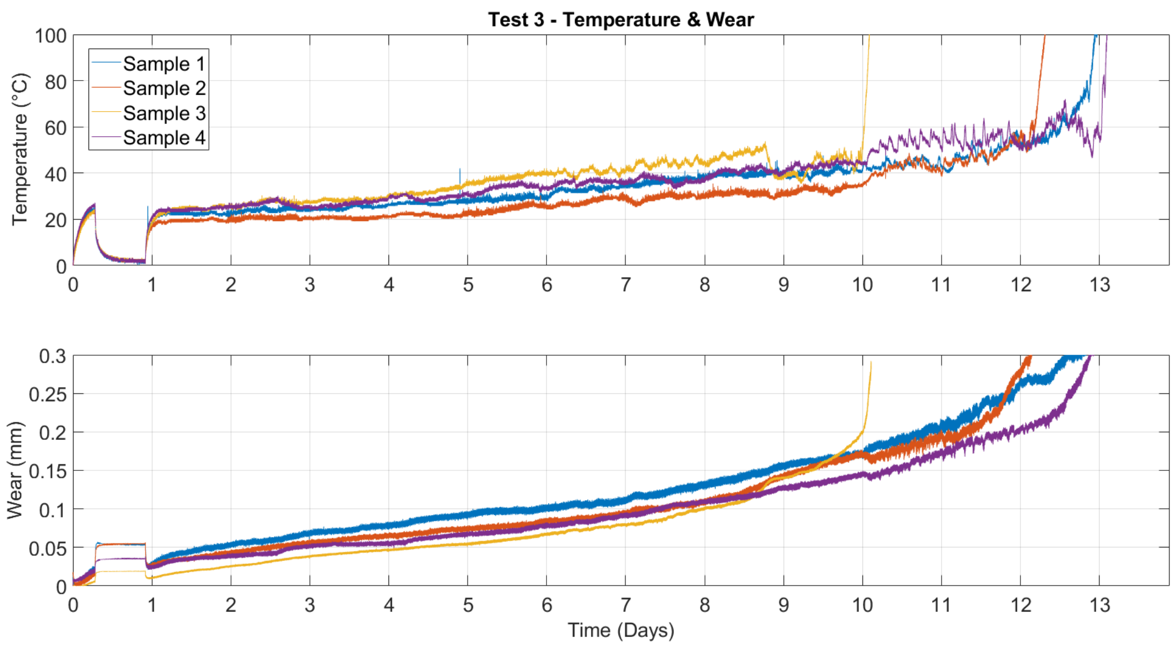

Figure 77 - Temperature and wear data from the third test conducted on Rig Q.

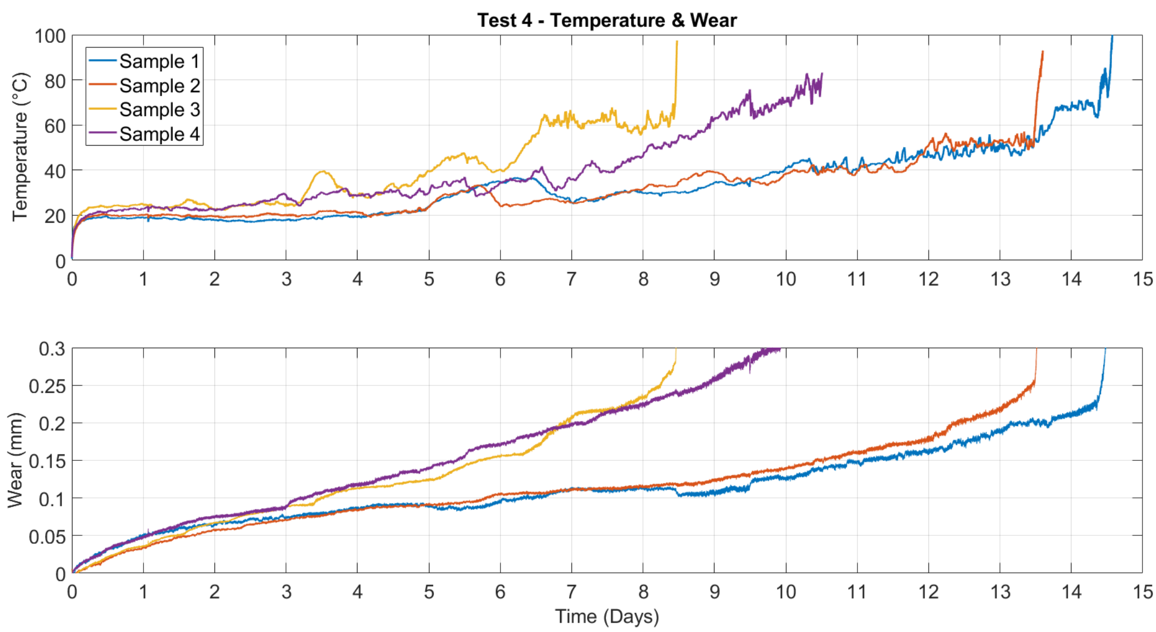

Figure 78 - Temperature and wear data from the fourth test conducted on Rig Q.

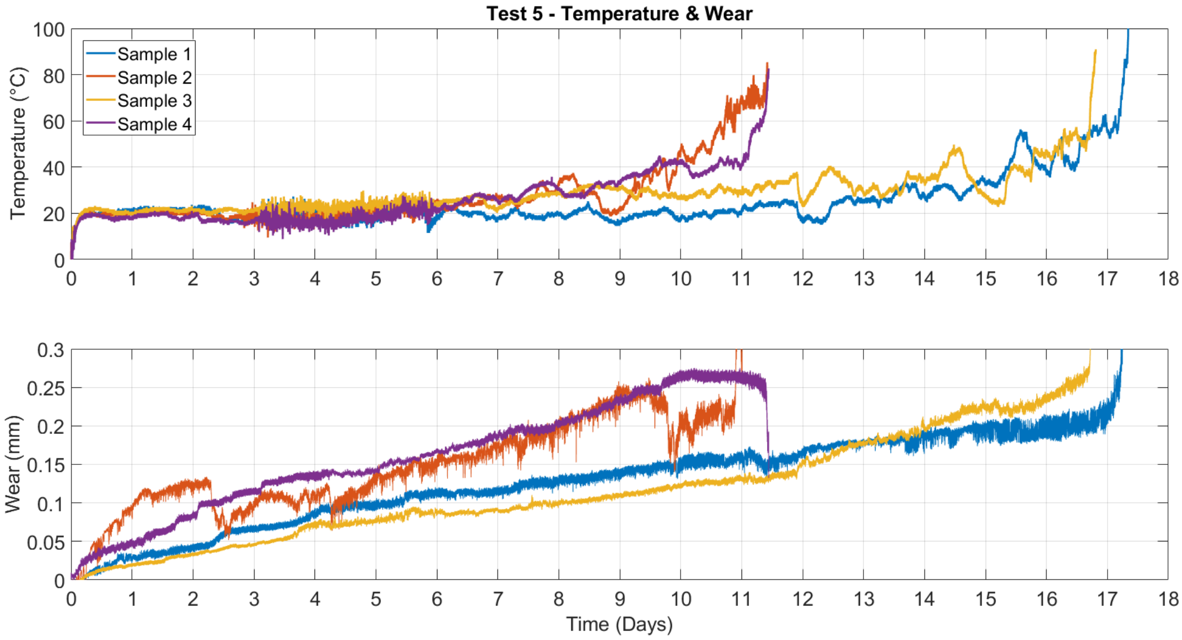

Figure 79 - Temperature and wear data from the fifth test conducted on Rig Q.

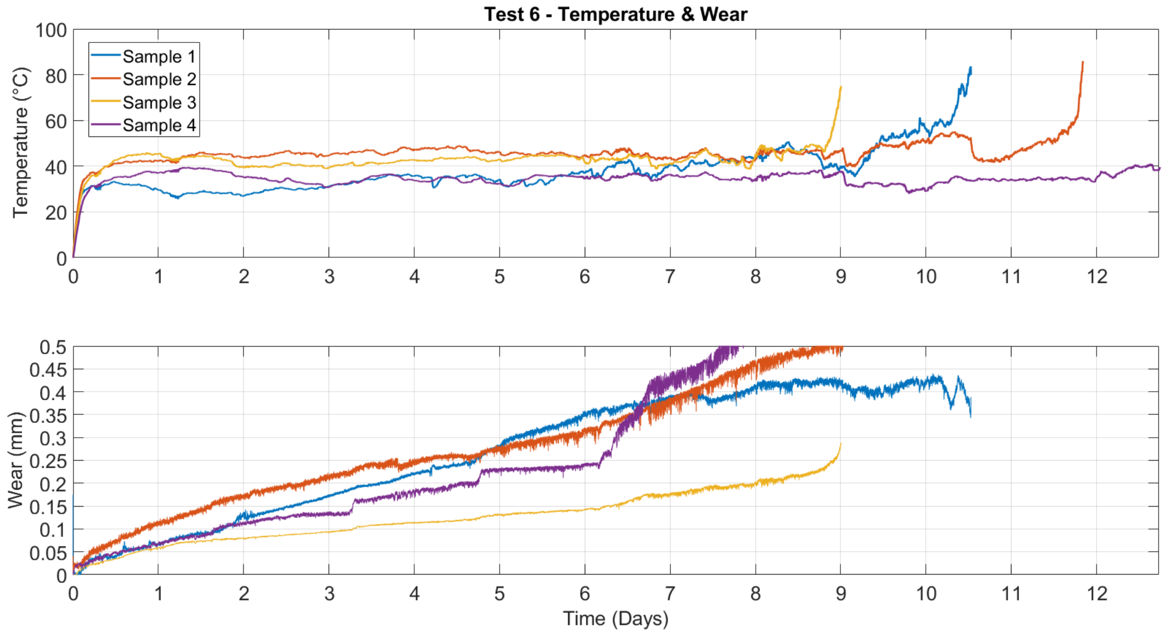

Figure 80 - Temperature and wear data from the sixth test conducted on Rig Q.

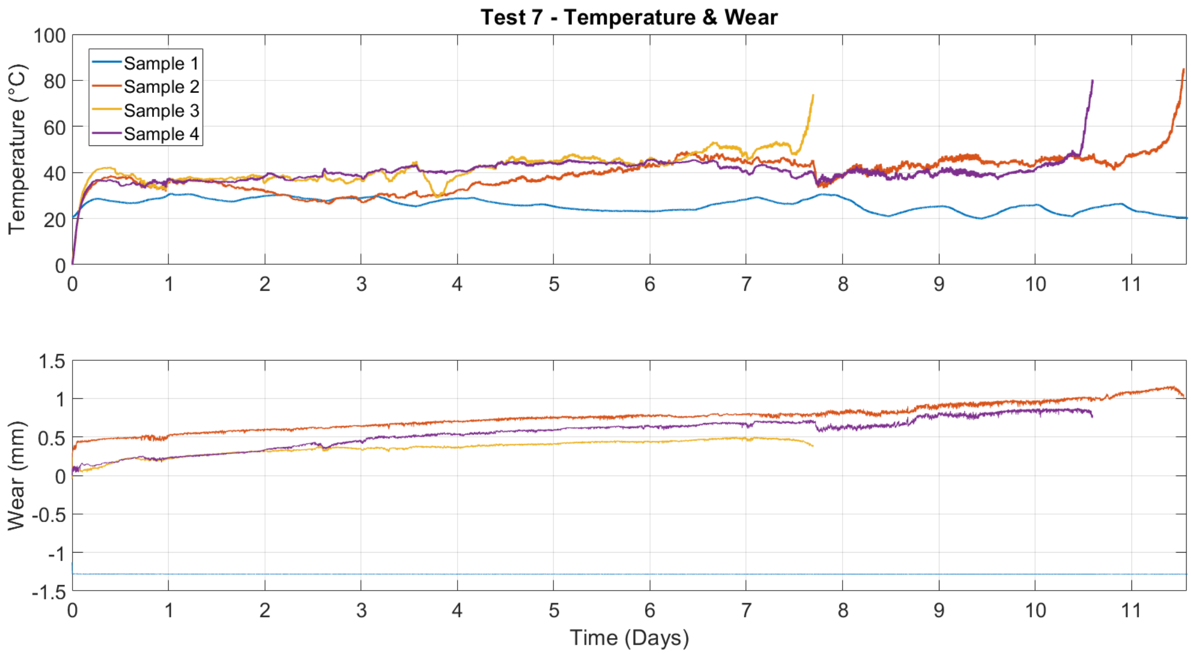

Figure 81 - Temperature and wear data from the sixth test conducted on Rig Q.

To note, all of the above temperature data were normalised against the atmospheric temperature recorded during the tests. This allowed for the removal of any environmental fluctuation effects caused by day and night temperature differences within the laboratory. Having displayed the test results in full, some general observations were made regarding the temperature and wear behaviour of the materials under test.

Before doing so, it is important to describe some of the unwanted features produced during testing. Firstly, within the initial shakedown test (Figure 75) an LVDT slip can be observed in the wear data between days 12 and 13 and unfortunately the cause of this was not discovered. Within days 0 and 1 of test 3, it can be seen that a large temperature drop and region of no wear occurs. This was due to the inadvertent pausing of the test bench by an electrical supply interruption to the laboratory. Electrical noise was also an issue within Figure 79 as seen by the region of high temperature volatility between day 3 and 6. This was credited to electrical maintenance works which were occurring in the building at the time of testing. Furthermore, a temperature instrumentation issue presented its self in the form of a detached thermocouple in Figure 81, sample 1. Finally, the largest issue with the testing on Rig Q came in the form of the LVDT results. Due to the high vibration levels in the test bench and the ability of the arms to drift for alignment purposes, the LVDT results sometimes became redundant. An example of this issue can be seen on sample 4 of Figure 78, samples 2 and 4 of Figure 79, samples 1,2,4 of Figure 80 and all samples of Figure 81. Although the wear data were not able to be considered, the temperature data remained valuable to the author.

Further, due to the previously discussed misalignment issues (Figure 47, Page 78), some samples within a test fail at a much higher wear rate. This was attributed to the uneven load distribution upon the sample under consideration, which causes the contact pressure on one side of the wear scar to be of a higher magnitude when compared to the opposite. Examples of such behaviour can be seen by sample 3 in Figure 77, samples 2 & 3 in Figure 78, samples 2 & 4 in Figure 79, samples 3 in Figure 80 and sample 3 in Figure 81.

4.3.2 Phases of wear and effects on temperature

The wear-in phase of the two materials under sliding contact was defined as the time taken to reach a temperature equilibrium during the wear process. This effect can be seen as a rapid temperature increase at the start of each wear process and it is credited to a number of parameters. The first parameter involved the very high initial pressures which occur due to the geometry of the sliding contact. As the material begins to wear-in a higher degree of conformity is achieved between the sliding surfaces and therefore the contact pressure rapidly decreases. Secondly, the absence of a third body transfer upon the counterface plays a vital role in producing this initially rapid temperature increase. To begin with, the sliding contact behaves abrasively, since the asperities of the counterface remain intact. As a third body transfer layer is built up upon the counterface, these asperities which contributed to the abrasive wear begin to be filled in by PTFE wear debris and therefore their amplitude is decreased (Lancaster, 1982). The point at which an equilibrium is reached between the destruction and construction of this third body layer, is called the ‘knee’ of the wear process and signifies the start of a constant wear rate process (King, 1979).

Once the point of steady wear is reached, the temperatures also reach a plateau. Under the experimental loading and sliding speed conditions described within section 3.2, the temperature plateau region had a range between roughly 20ºC and 40ºC above ambient temperature. This region represented the PTFE rich area of the liner composite and ranged persisted between wear depths of 0.025mm and roughly 0.15-0.18mm. The upper value of 0.15-0.18mm assigned to this range represented a material composition change within the liner. At this point, the PTFE rich region begins a transition into the glass fibre backing material region of the liner which does not contain PTFE. When this change occurs, the temperature and wear characteristics begin to behave differently.

The final phase of wear as described in section 2.2.3, involves the failure region of the material under test. At a wear depth of approximately 0.15-0.18 mm, where the material composition changes, the wear depths and temperatures begin to increase rapidly. This was believed to occur due to the abrasive wear nature of the glass fibre rich region. At this stage, the friction coefficients are believed to rapidly increase and therefore higher temperatures are produced by the wear region. When a liner sample is fully worn and therefore metal to metal contact is reached, an extremely rapid growth of both temperature and wear depths is produced. This signified the end of the test for that particular sample.

4.3.3 Wear scar inspection

In order to understand the surface properties of the samples during their wear process, sample 3 of test 7 was removed at a wear depth of 0.1mm. The wear scar is visually presented in Figure 82.

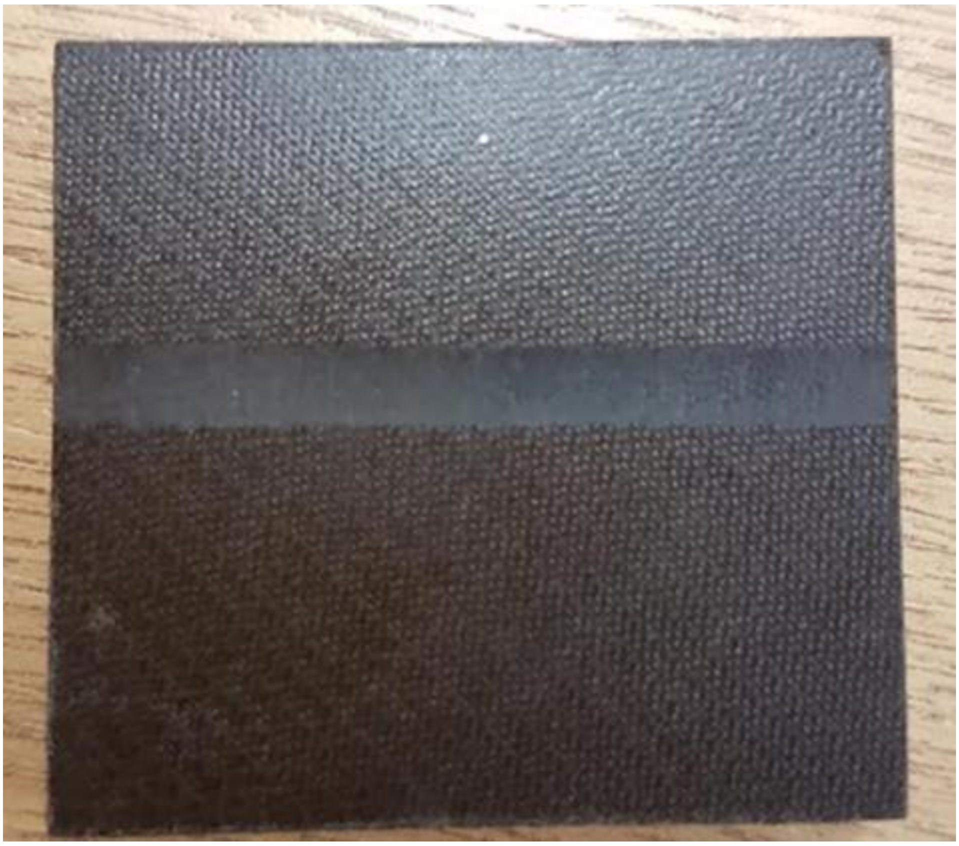

Figure 82 - Wear scar of a 0.1mm depth.

In order to understand the composition and wear behaviour of the sliding contact at the time of removal, the wear scar was inspected by an optical microscope. The results are shown in Figure 83, where a comparison was made between a healthy sample, prior to being subjected to load, the 0.1mm worn liner sample under investigation and finally a liner sample which has undergone full metal to metal contact at 0.5mm of wear. As seen by Figure 83 (b) the section where the wear scar occurs appears to have undergone a large amount of physical deformation. The fibres appear to be compressed and stretched out across the contact zone and in certain zones the fibres cannot be distinguished.

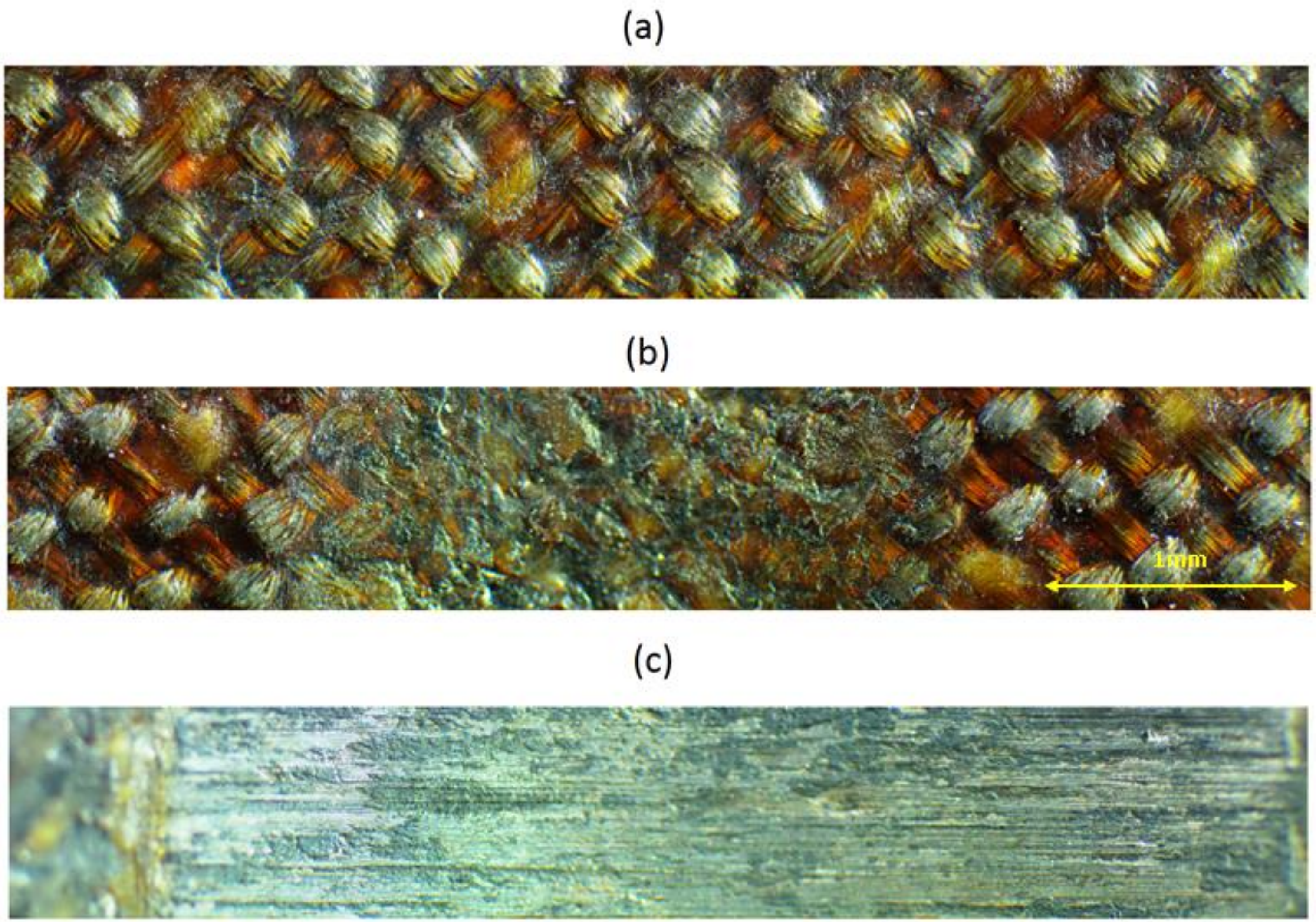

Figure 83 - Progression of wear scar from (a) healthy, (b) 0.1mm worn, (c) 0.5mm worn.

4.3.4 Counterface third body transfer layer investigation

Alongside the inspection of the liner composite's wear scar, a series of scans were conducted upon the mating counterfaces of the liner sample. Optical microscopy proved difficult for such a cylindrical geometry due to the inability of the lenses to focus on such a curved surface. Nevertheless, a series of images were obtained which show the third body transfer layer build-up upon the counterface, but the resolution of these images was not ideal. It is believed that within Figure 84 (a) the heavily reflective points represent the peaks and the darker regions the valleys of the asperities. This is due to the light source being applied at an angle almost parallel to the counterface's surface, therefore a shadow would have been cast on the troughs.

As the wear progresses and a transfer film is slowly built up upon the counterface, the darker regions of the sliding contact begin to decrease and a more speckled light pattern becomes visible (Figure 84 (b)). This is believed to occur due to the filling of the asperities with PTFE and therefore the surface roughness of the sliding contact would become less. A smoother surface tends to reflect a larger portion of the subjected light and this was recorded by the microscope.

Finally, as metal to metal sliding contact is achieved between the liner sample and the counterface, the contact zone begins to become abrasive and therefore the asperity peaks start becoming flat. When the sliding contact begins to approach a fully flat geometry, the nature of the contact zone begins to convert from abrasive to adhesive. This is attributed to the highly reflective surface observed within Figure 84 (c).

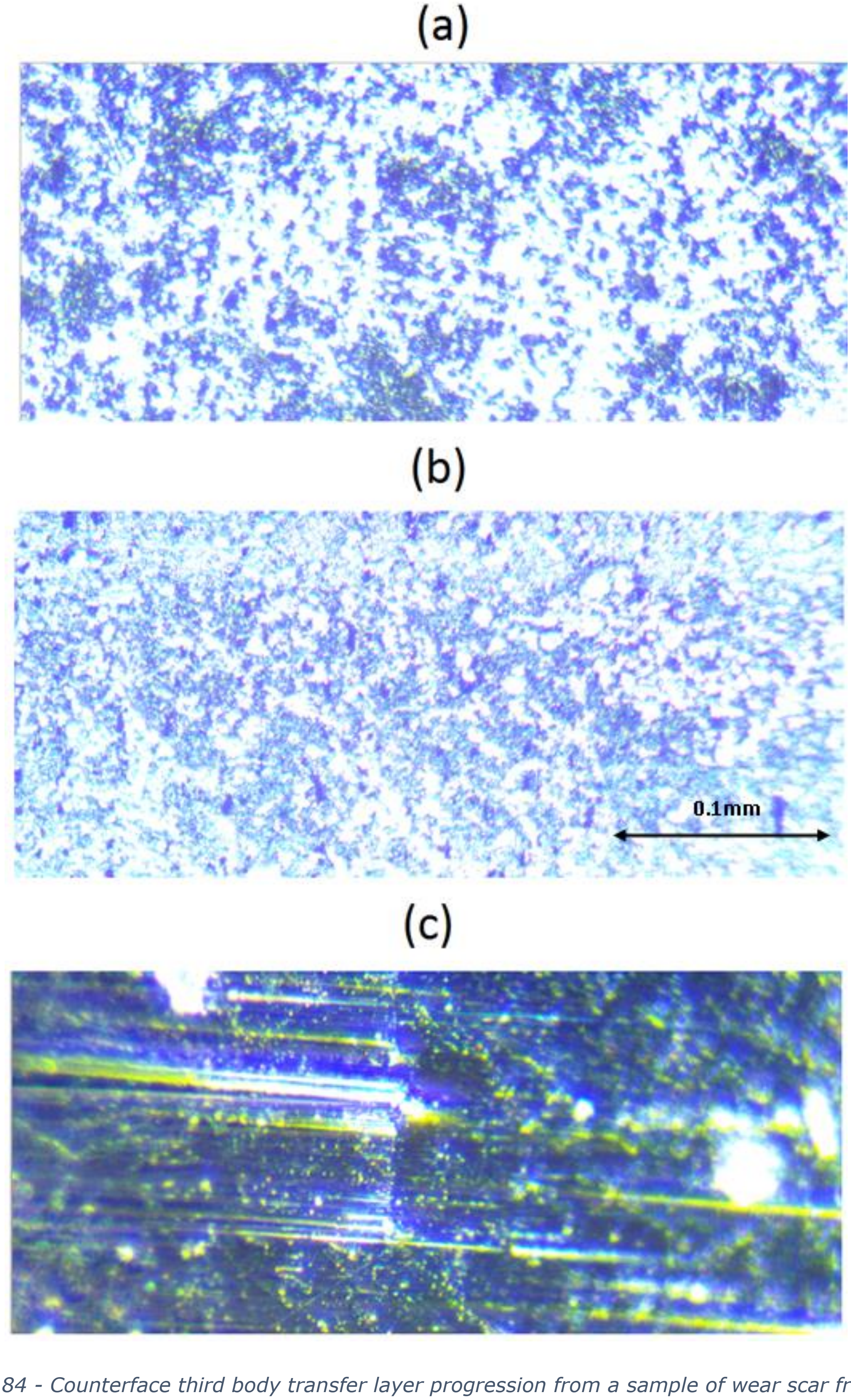

Figure 84 - Counterface third body transfer layer progression from a sample of wear scar from (a) healthy, (b) 0.1mm worn, (c) 0.5mm worn.

4.4 Conclusion

Within this chapter, a summary of the test results was presented which allows the reader to understand the nature of the test bench's testing procedure. The results showed trends which matched with what was expected to be seen from literature and finally, issues with the test bench were highlighted and taken into consideration when inspecting the results.

Having described all of the above, the next two chapters describe the development of a conditioning monitoring technique for bearing liner damage detection, which focus on the utilisation of raw temperature data.

Chapter 5: Test bench results - Temperature

5.1 Introduction

This chapter aims to explain the analytical techniques employed throughout the course of this research to analyse temperature response, including conventional methods and analysis techniques developed specifically for this research. In this and the following chapters, the test results are considered in turn, depending on the physical parameters being monitored and the test-bench used for data collection. The two measured parameters which were considered for the purpose of the project were temperature and acoustic emission.

Initially, a study was conducted in order to evaluate which parameters were suitable for monitoring in the rotorcraft main rotor pitch control application. In order for a signal to qualify for measurement, it had to be realistic with regards to its extrapolation from laboratory conditions and onto the real-life application. This selection process was conducted through a workshop exercise with the help of the industrial sponsor (SKF) supervisors, along with the academic supervisors from Cardiff University. Due to the nature of the application, the following parameters had to be considered when deciding on the most appropriate parameters to be measured:

- Geometric restrictions of the main rotor with regards to sensor integration – substantial modifications to the rod ends were not permitted.
- Possible mass of the data-logging system for the selected parameter.
- Energy requirements of the data-logging system had to be minimised.
- Intrusiveness of the integrated hardware to produce the chosen signal had to be minimal.

The physical parameter which best fitted all of the above criteria was temperature. The potential mass and volume of the data-logger can be very low and off-the-shelf solutions were found with mass and volume similar to a quarter dollar coin (approximately 25mm diameter) (PhaseIVEngin, 2018).

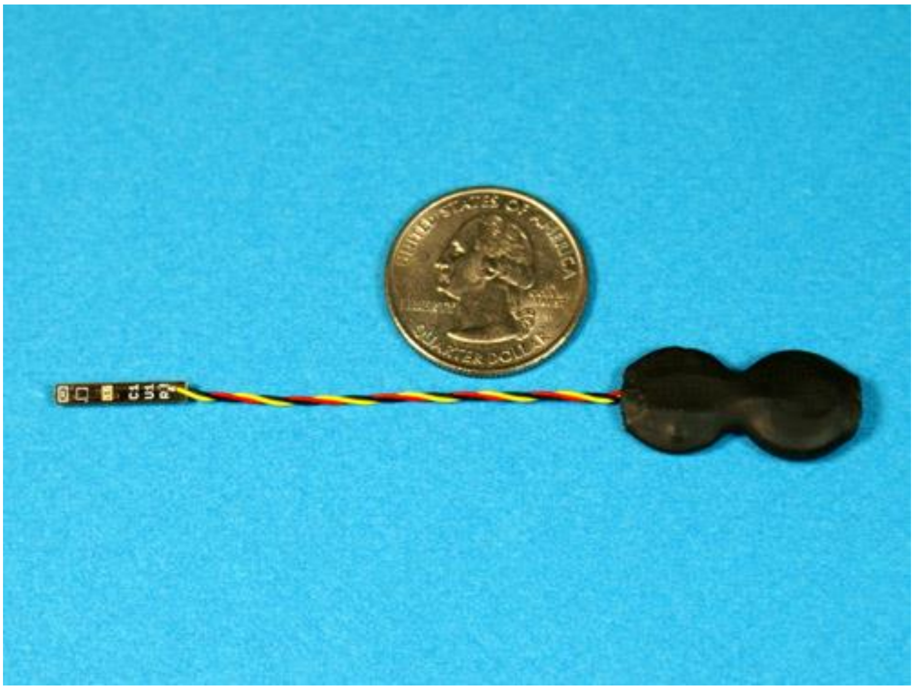

Figure 85 - Miniature temperature logger from PhaseIVEngin. (https://www.phaseivengr.com/product/temperature-thin-micro-t-rfid-data-logger-150c-miniature/)

Furthermore, the energy requirements of such data loggers, were of a small magnitude and the sensors were proven to function in full-scale bearing tests with a non-intrusive nature. This type of non-intrusive nature was the most desirable to the industrial partners, who wished to avoid altering bearing manufacturing processes which would require further requalification of the altered parts for flight. Furthermore, this non-intrusive nature of such instrumentation was desirable due to its ability to be retro-fitted onto existing bearing components.

To test the feasibility of the non-intrusive temperature sensors, an experiment was conducted on Rig H in order to investigate the temperature variation between the outer ring of the bearing component and the surface of the rod-end in which the bearing was installed. Figure 86 shows the configuration of the thermocouples which were located in strategic points on the rod-end system. The fan seen at the top of the assembly in Figure 87 is incorporated in order to allow for the replication of the wind effects expected to be seen during flight stated within the SAEAerospace (2001) standard.

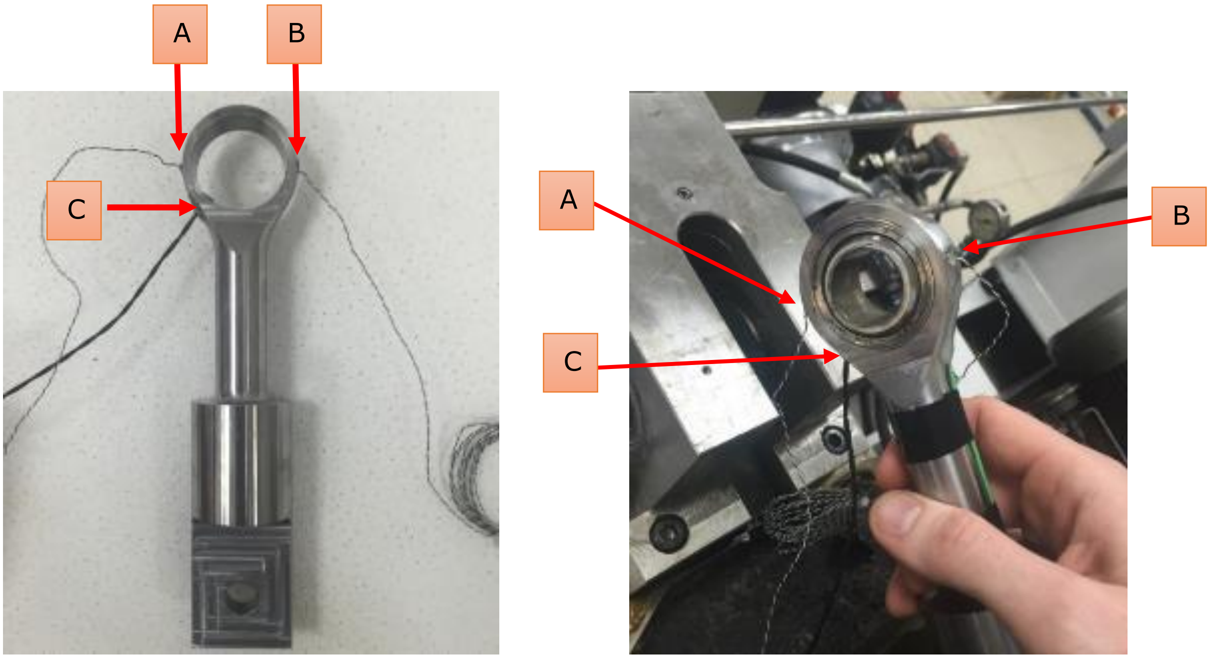

Figure 86 - Thermocouple location on Rig H rod-end. Without the assembled bearing (left) full assembly (right). A) Non-intrusive fan facing thermocouple, B) Non-intrusive fan shielded thermocouple, C) Intrusive flathead thermocouple.

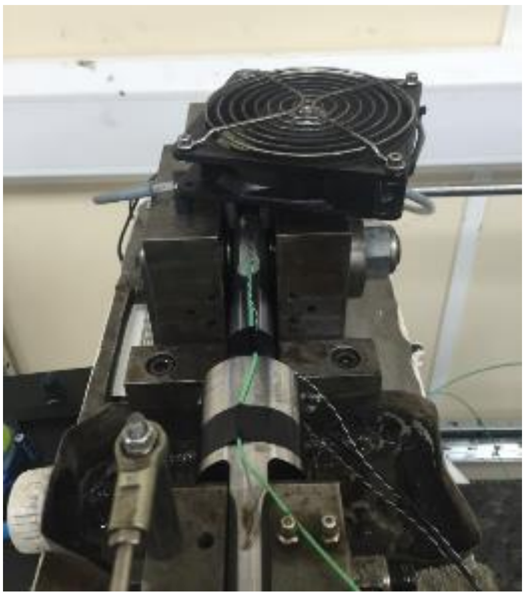

Figure 87 - Rig H rod-end assembly fitted onto the test rig.

Figure 88 shows the results from the three externally placed thermocouples along with the conventional thermocouple used by SKF. The x axis labelled as '% Life' denotes the percentage of wear life of the bearing under test with respect to time.

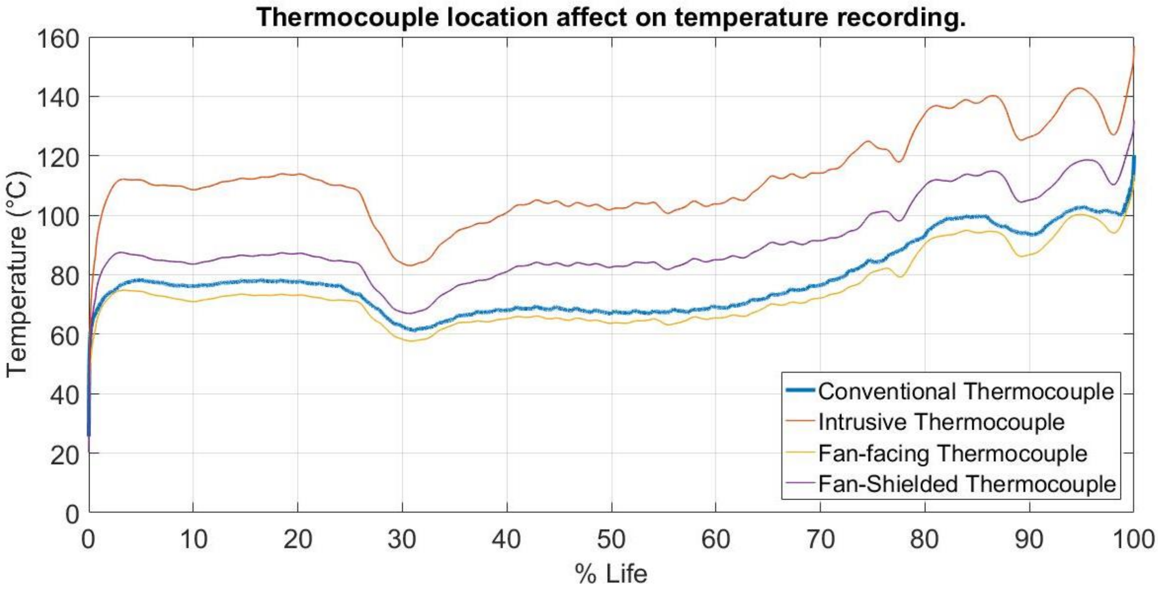

Figure 88 - Comparison of temperature data from previously stated thermocouple locations on a full-bearing test on rig H.

The analysis techniques used during this project place importance on temperature *trends* rather than the absolute values, due to the comparative nature of the developed algorithm. Therefore, it can be clearly seen that the non-intrusive thermocouple temperature data had a strong positive correlation with the intrusive flathead thermocouple data. To confirm this correlation, the external thermocouple temperatures are plotted vs. the conventional thermocouple used normally in Figure 89. It was concluded that as far as laboratory conditions are concerned, temperature was a very desirable parameter to be monitored in future tests.

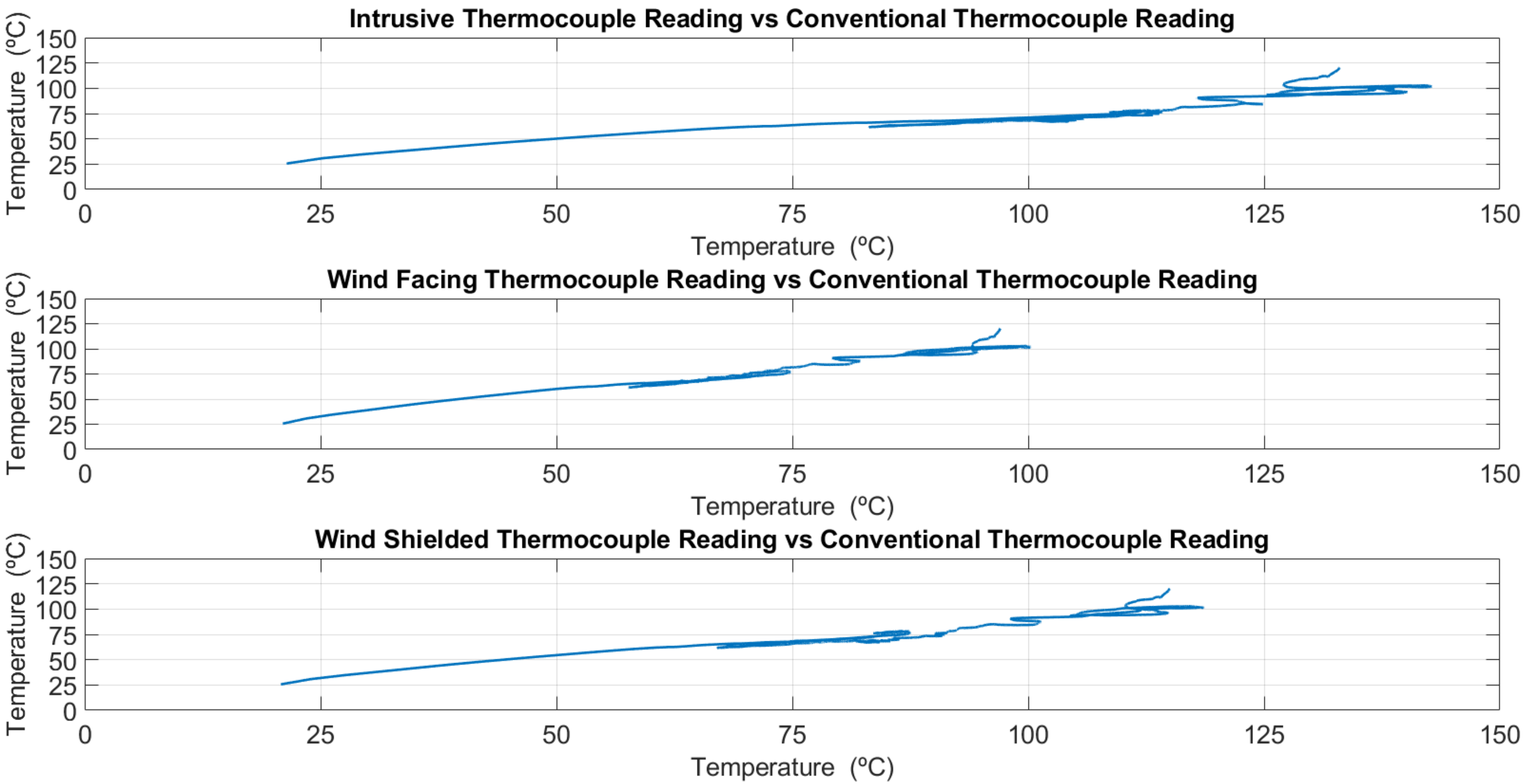

Figure 89 - X-Y plots of external thermocouple locations vs a conventional thermocouple location.

The second parameter which was selected to be monitored was acoustic emission. Acoustic emission was a very desirable parameter, due to its ability to aid the understanding of certain tribological phenomena during the degradation of the liner material.

5.2 Statistical process control charts

The following sections will explain how the thermocouple data obtained from the third test (see section 4.3.1) conducted using Rig Q, was analysed in order to provide a condition monitoring technique in an attempt to identify the onset of liner failure in advance of the final, catastrophic failure. The aim was to develop a technique which was essentially comparative in nature, in order to effectively eliminate environmental effects acting upon the rotorcraft main rotor bearing system. As the rotorcraft is in flight, all of its 4 pitch control bearings are subjected to both equal loading and environmental effects. Providing a reference signal for the purposes of condition monitoring, for every possible flight and environmental condition, would be nearly impossible. Therefore, by comparing the monitored parameters of each bearing within the pitch control system to its 3 neighbours, a fault can be said to be detected when a deviation in that particular parameter occurs on one of the bearings. This method assumes that it is statistically improbable that all bearing components will fail at identical times, or deteriorate at exactly the same rates.

Statistics, as a field, can be defined as a mathematical science concerned with the collection, analysis, interpretation or explanation and representation of data (Watkins, 1994). This chapter focuses on the importance of statistics in the process of fault identification within a system of identically, or at least very similarly, loaded components. The particular method which was used for this purpose of fault detection, was cross sample correlation.

Statistics are widely used within the condition monitoring field in order to predict the failure, or current health state of a system or component. Examples include machine tool condition monitoring through the use of statistical quality control charts (Jennings & Drake, 1997) and statistical condition monitoring via the analysis of vibration signals (Zhang, *et al.*, 2004). Figure 94 shows the data-set selected for this type of comparative analysis to be applied. Note that the word sample which appears on the legend in Figure 94, represents each bearing liner coupon.

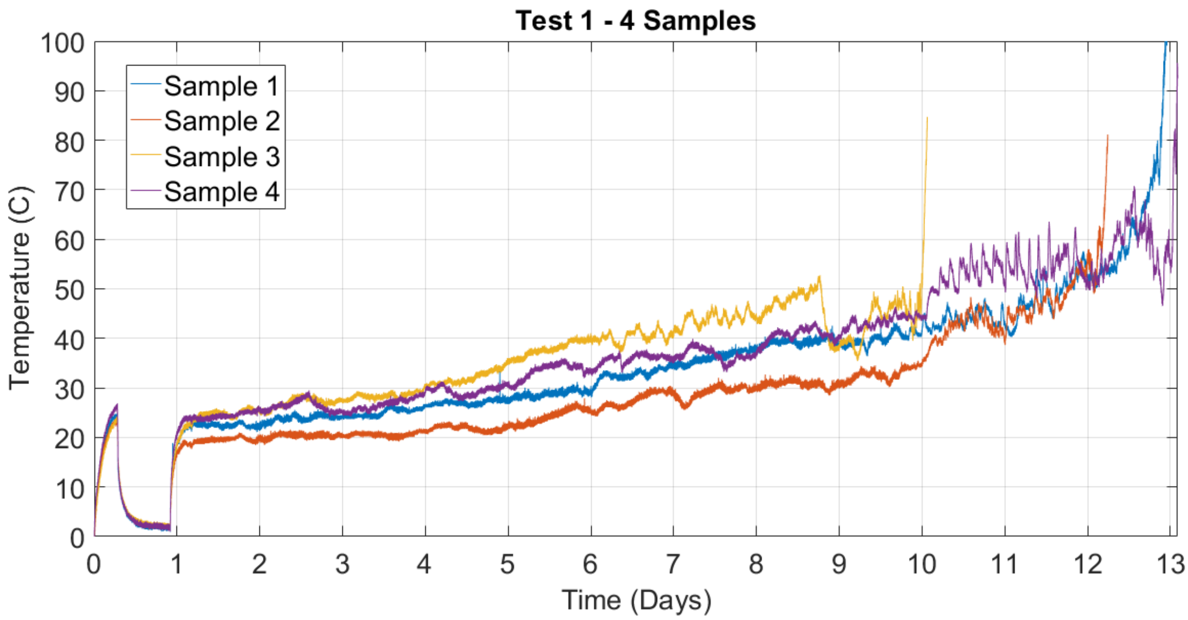

Figure 90 - Temperature rise above ambient vs time (Rig Q – First test of the 4 arm configuration).

Within Figure 94, as described in Chapter 4, a sudden drop in the temperature data can be observed between Day 0 and Day 1 due to an electrical cut-out of the laboratory which forced the test-bench to stop and therefore allowed for the cooling down of the sliding surfaces. Instead of seeing this data set as corrupt and faulty, the sudden temperature drop can be said to simulate a period of rest as would happen in real-life conditions when the rotorcraft is grounded. This will be discussed further within the chapter. Figure 94 shows that the temperature data for each sample stops when a large temperature increase occurs. The test bench control system is designed in such a way that when a certain temperature threshold is reached, the sliding contact between counterface and coupon is disengaged and therefore the test stops for that specific sample. This is due to the liner reaching a wear depth of 0.3mm by which point the sliding contract between the liner and counterface had reached metal to metal conditions. Finally, the temperature presented in Figure 94 is the value of the temperature rise of each sample above ambient, which consists of the actual sliding contact temperature at the point of measurement, minus the atmospheric temperature throughout the test. This allowed the data to be de-trended, to remove any effects of ambient temperature fluctuations. Both sets of temperatures prior to and after de-trending can be seen in Figure 91.

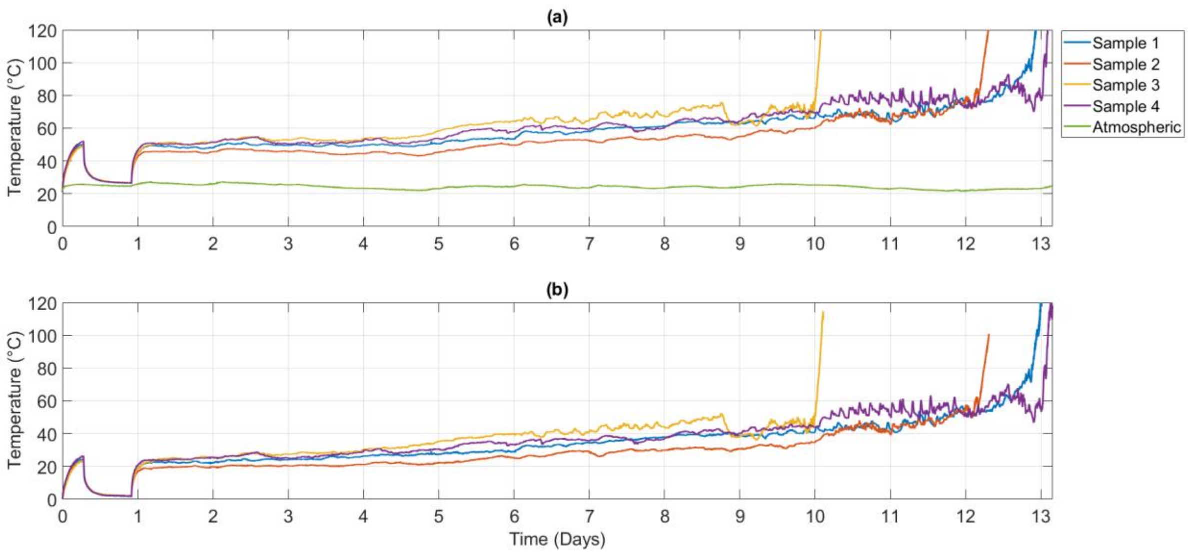

Figure 91 - Temperature data (a) Raw, (b) Detrended.

In order to complement the temperature data, the wear data measured by the LVDTs located upon each of the mechanical loading arms on Rig Q for that particular test, are presented in Figure 92.

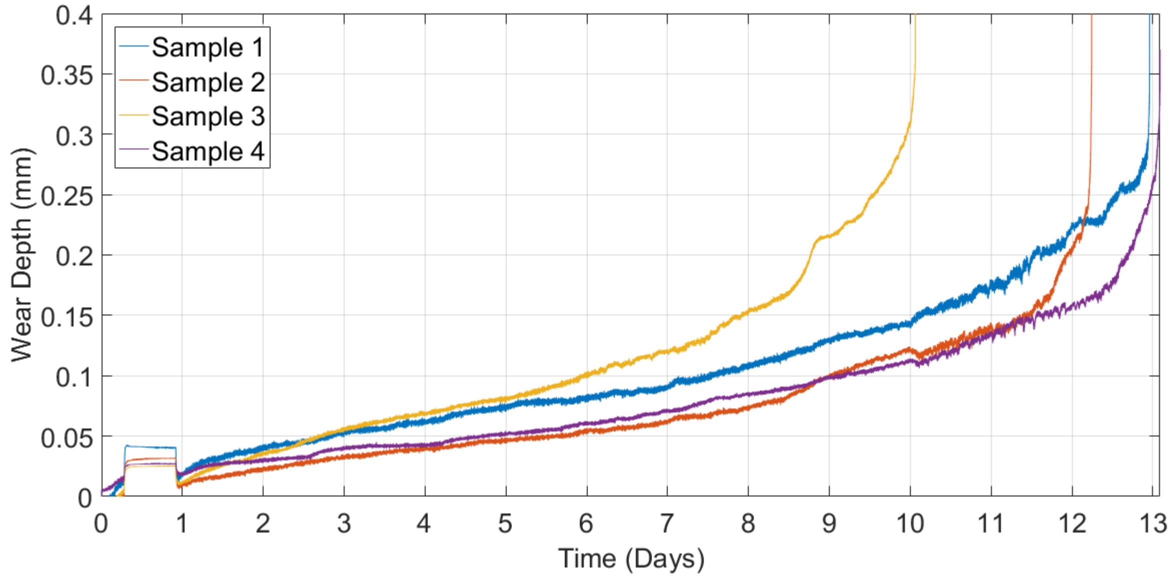

Figure 92 - Rig Q wear data.

5.3 Exponential Weighted Moving Average (EWMA) chart

Various techniques were investigated when trying to develop a comparative condition monitoring methodology, but the majority focused upon a residual analysis method. This type of method looks at the numerical value of the remainder when two data sets are subtracted from each other. When this occurs, a de-trended temperature data set is presented in Figure 93.

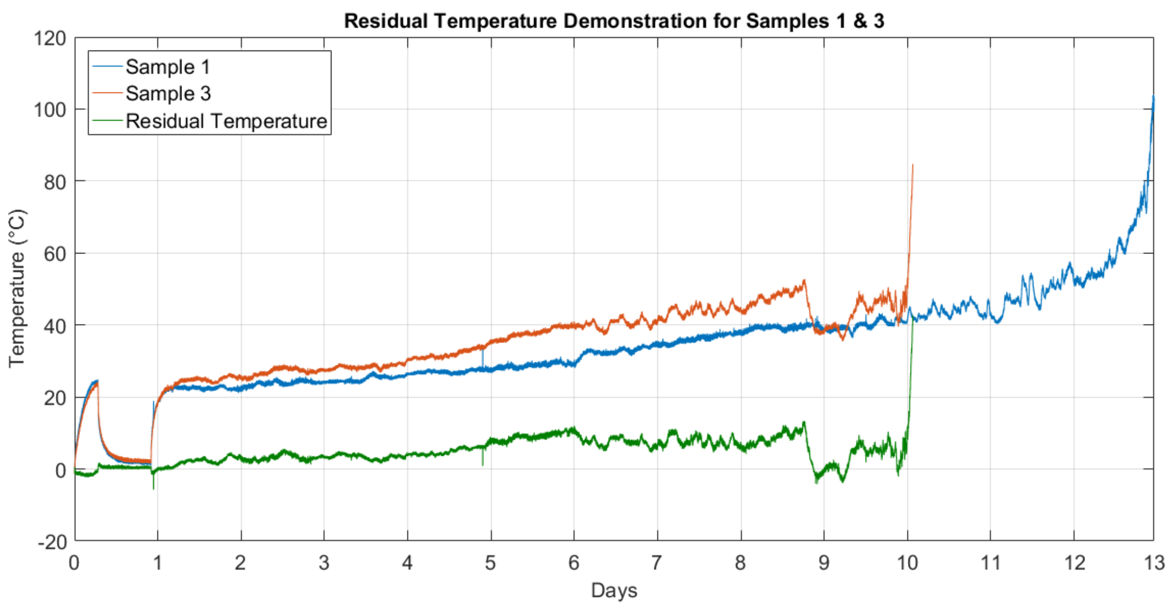

Figure 93 - Residual Temperature Demonstration.

Samples 1 and 3 were chosen due to their large temperature variability and therefore ability to clearly demonstrate the methods. As the wear process reaches its latter stages, it can be seen that the residuals reach a point of volatility and this was the temperature feature that was investigated in order to provide an early warning of bearing failure.

Within literature there are various techniques which are aimed at process control methods in industrial manufacturing processes, and these fall under the category of statistical process control (Oakland, 1996). For example, the length of manufactured rods from a process can be monitored and compared to a perfect standard, as described by the process creator. If the residual between the two measurements infringes certain control limits, set by the operator, an alarm point will be created which indicates that the process is starting to become out of control. This would allow the operator to investigate the reason behind the deviation and therefore minimise the downtime for maintenance of the machinery if a fault was found within the process.

To implement this method, a simple Matlab code was created which creates and applies control limits from a healthy / steady state region of the temperature curve. If the residual value goes above or below the created control limits, then an alarm point is raised and plotted. Figure 94 below shows this technique being applied on the residual temperature data from Figure 94.

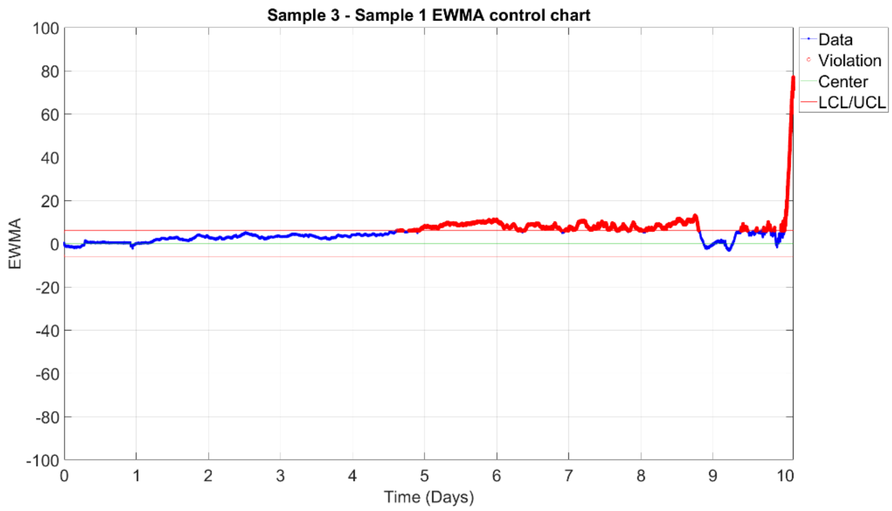

Figure 94 - Exponentially Weighted Moving Average control chart for damage detection.

At this point it is important to explain the method behind the calculation of the residual temperature that can be seen plotted. To allow the detection of a violation in real-time, a method called the exponentially weighted moving average (EWMA) was employed. The principle of operation behind this method, is the pre-assignment of a weighted value of the currently considered data point throughout the process in comparison to the historical mean of the built up residual data. Therefore the exponentially weighted moving average chart is a type of moving mean chart, which gives weighted importance to the last point of observation, depending on the assigned weighting constant, in which an 'exponentially weighted mean' is calculated each time a new result becomes available (Oakland, 1996) and is calculated as follows (Equation 11):

$$New\ Weighted\ Mean = (a \cdot new\ result) + ((1 - a) \cdot previous\ mean) \quad (11)$$

The constant 'a' is said to be a smoothing constant which determines the relative importance of the most recent observation in calculating the weighted mean. It is important to note that the 'new result' value within Equation 11 is the next temperature point under consideration. Most process operators use a value of a = 0.2 as a standard and for the purpose of the preliminary control chart created above, the standard value of a = 0.2 was employed (Oakland, 1996). The previous mean in this case is the average value of all the data points considered up to the point of the current observation. The biggest challenge in using this method is in defining the period in which the upper and lower control limits are calculated. These periods are essentially individually data-set dependant, as there are no existent data sets of such application. Therefore the control limits had to be created from the self-contained data. The control limits were calculated from the residual temperature data, in the region between day 0 and day 1. The upper control limit (UCL) was set as five times the standard deviation of the residual temperature between day 0 and day 1 and the lower control limit (LCL) as the mirror opposite about the line of the centre (Oakland, 1996). During this process, a second set of limits can be introduced within a process which involve action limits. Action limits are described by Stapenhurst (2005) as critical threshold values which, when exceeded, action must be taken prior to the process reaching the control limits. These action limits equate to ±3 standard deviations about the mean line. Although for this instance the calculation of limits were equal and opposite about the mean, there is no restriction towards using different upper and lower limit values. The centre was defined as the mean value of the chosen region selected. Therefore this method required a large amount of data, roughly 43200 data points, before the control limits were established and the length of period, approximately one day of data, required further investigation. This method was in turn applied to each possible combination of temperature results and plotted up to the failure point of each sample under consideration. Such results can be seen within

Figure 95 -Figure 106.

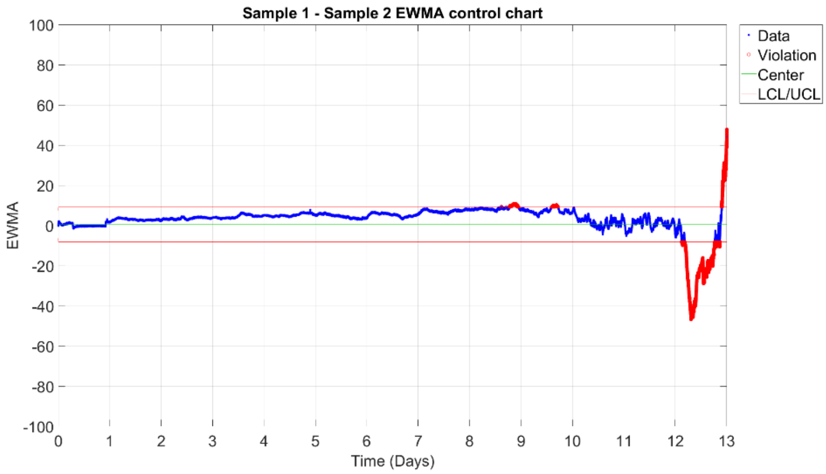

Figure 95 - EWMA chart: Sample 1 vs Sample 2 under consideration.

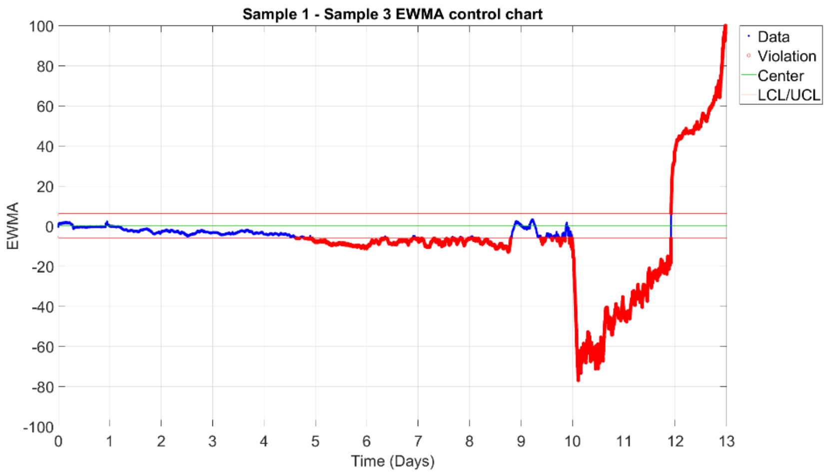

Figure 96 - EWMA chart: Sample 1 vs Sample 3 under consideration.

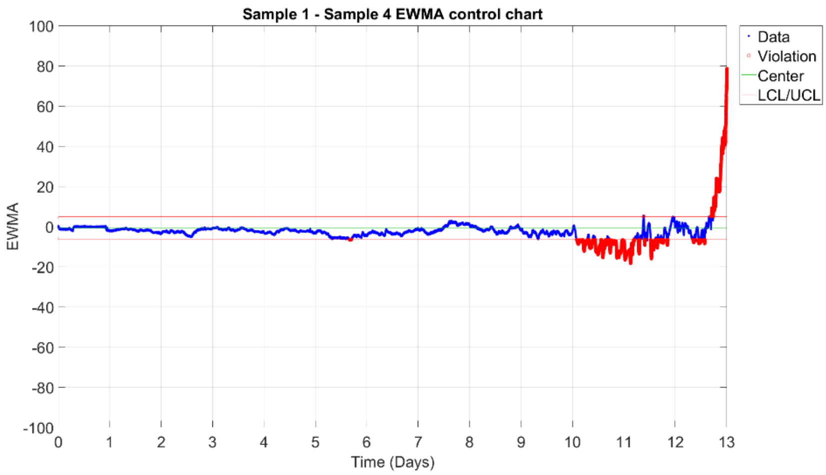

Figure 97 - EWMA chart: Sample 1 vs Sample 4 under consideration.

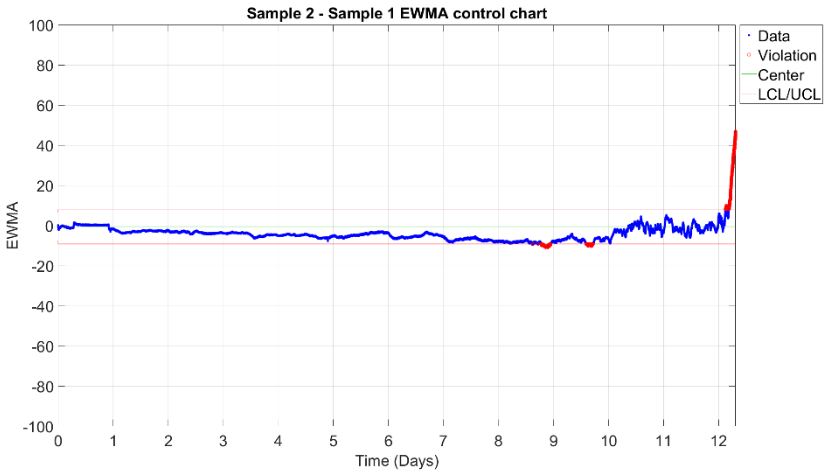

Figure 98 - EWMA chart: Sample 2 vs Sample 1 under consideration.

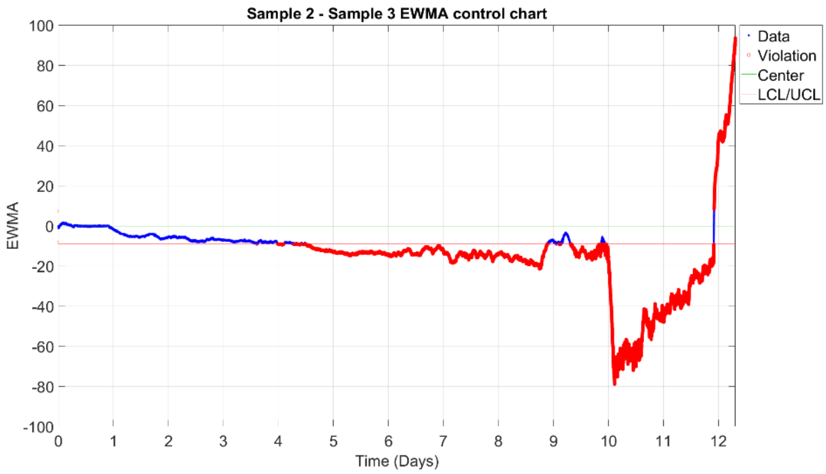

Figure 99 - EWMA chart: Sample 2 vs Sample 3 under consideration.

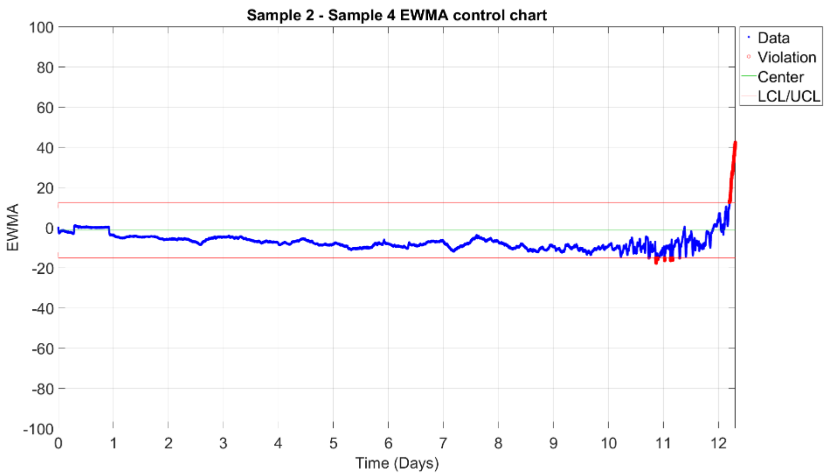

Figure 100 - EWMA chart: Sample 2 vs Sample 4 under consideration.

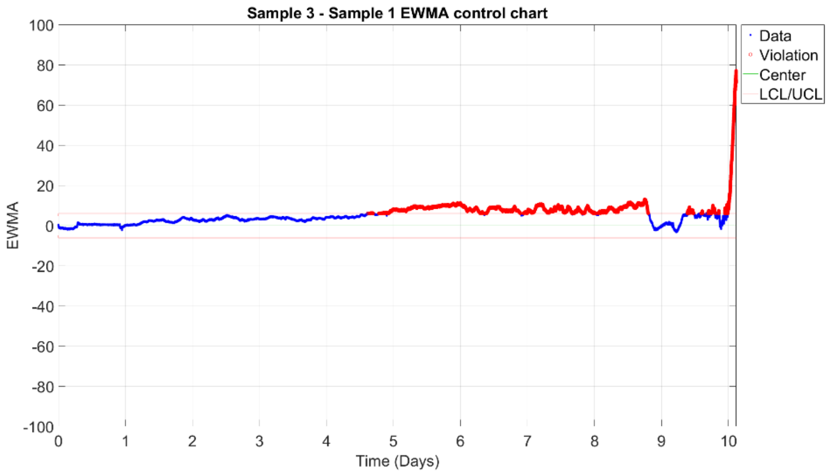

Figure 101 - EWMA chart: Sample 3 vs Sample 1 under consideration.

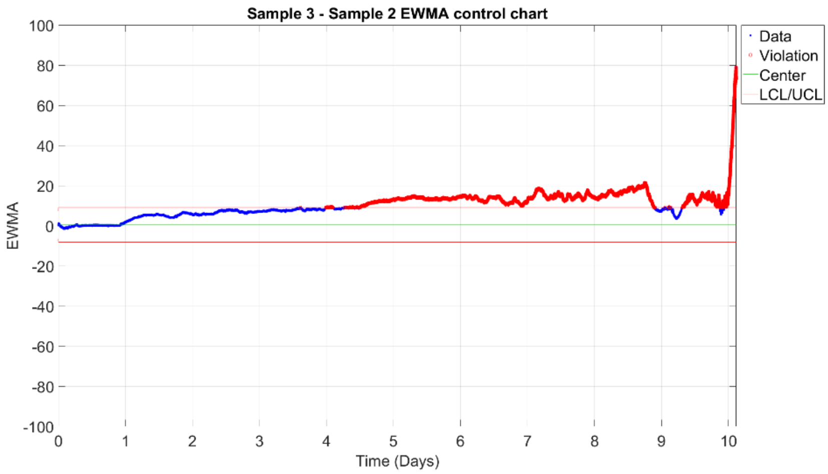

Figure 102 - EWMA chart: Sample 3 vs Sample 2 under consideration.

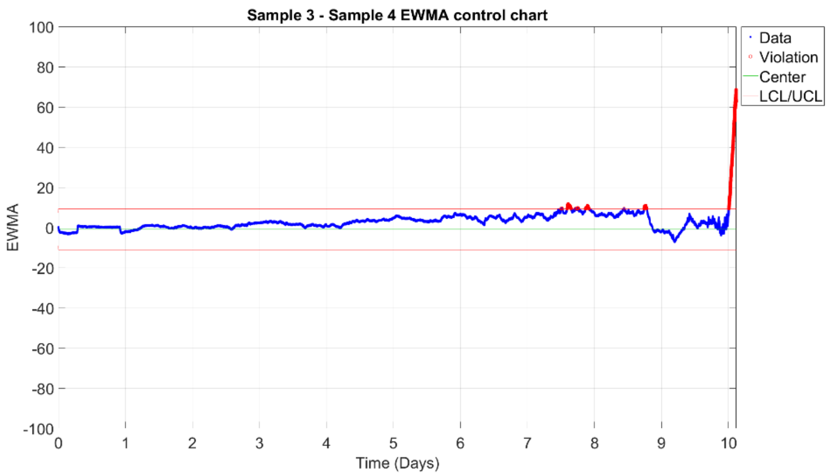

Figure 103 - EWMA chart: Sample 3 vs Sample 4 under consideration.

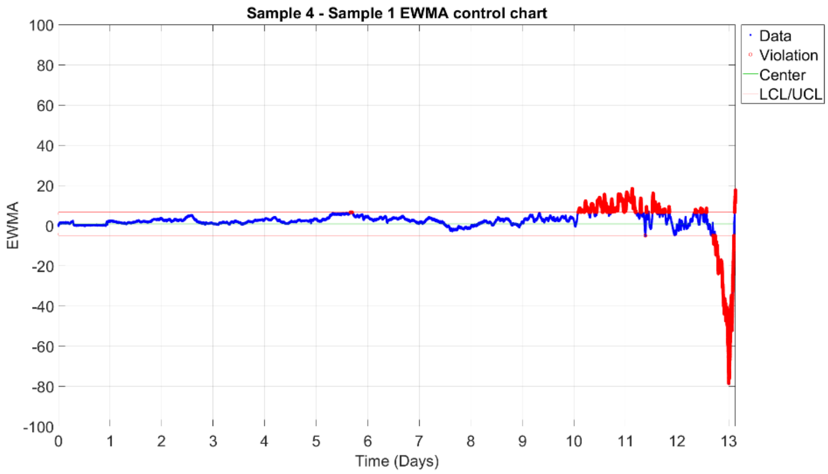

Figure 104 - EWMA chart: Sample 4 vs Sample 1 under consideration.

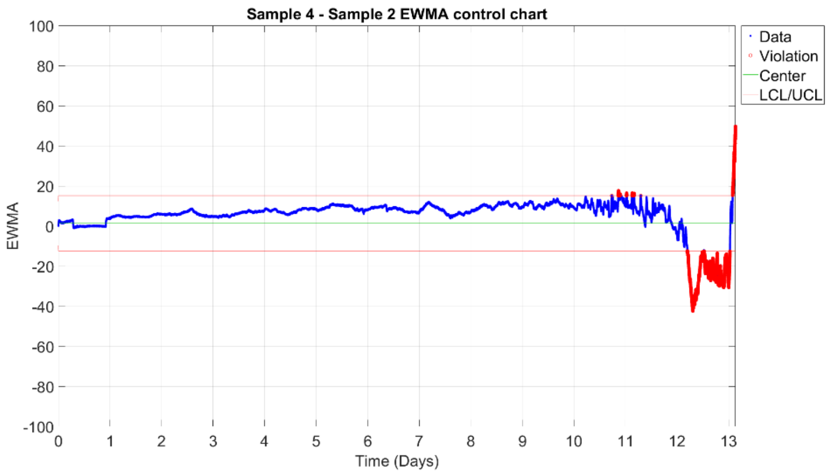

Figure 105 - EWMA chart: Sample 4 vs Sample 2 under consideration.

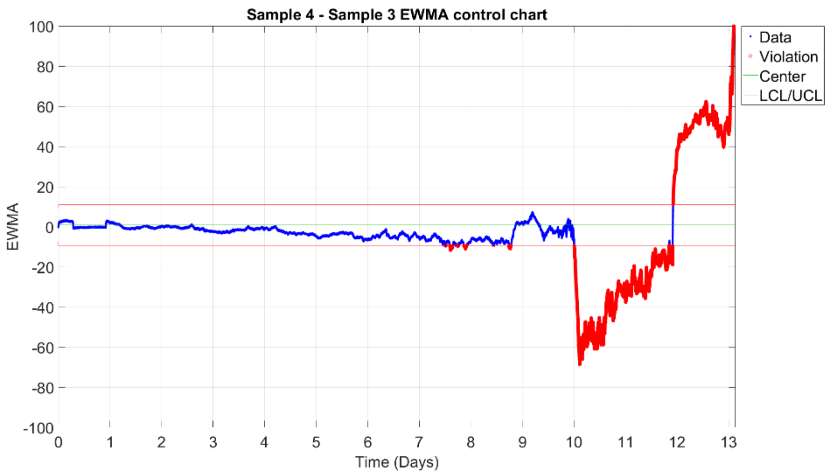

Figure 106 - EWMA chart: Sample 4 vs Sample 3 under consideration.

Figure 95 - Figure 106 show the maximum possible combination between the four samples that can be processed using the EWMA method for the temperature data set presented in Figure 94. It is important to note that some of the graphs above are mirror opposites about the centre line and therefore were not required to be presented. For example the EWMA chart of sample 1 and sample 2 is the mirror opposite of the EWMA chart of sample 2 and sample 1. These were presented in order to allow the reader to inspect the findings in an easier way. It is important to note that the time axis were cropped to the point of failure for each sample under consideration. For example within Figure 95, the time axis is tailored for sample 1's failure time (13 days) and within Figure 98 the failure time was adjusted for sample 2 (12.3 days).

During the implementation of this method upon a real-life application, the algorithm responsible for the comparison between the four bearings within the main rotor system would be responsible for flagging any anomalous patterns to the operator. In this case it can be visually seen that sample 3 exhibits anomalous behaviours very early on in its operation when comparted to the running temperatures of samples 1 and 2. At this stage, a flag would have been made for the potentially damaged bearing and an inspection interval would have been planned. The early predictions made from the algorithm can be seen to be accurate for this instance, as sample 3 was the first liner composite sample to fail with an unpredictable pattern as seen within Figure 94.

Although the above example was a very good fit for the demonstration of such technique, a case where the algorithm can yield a false alarm comes in in the comparison between samples 1 and 2 in Figure 95. An early warning was given during the test in between days 8 and 10 and after these violations the system becomes stable once more. These can be either interpreted as false indications or considered as potential signs of damage. Due to time constraints this subject was not investigated further.

As discussed Figure 95 - Figure 106 were created using an EWMA control chart method where the upper and lower control limits were calculated by using a period of existing data and equated to ±5 standard deviations about the centre line. As it can be seen within Figure 94, the period considered for this calculation included a stop in the test where the liner samples underwent a cooling down and reheating period. It was believed that the results from the EWMA charts could become unrepresentative if a cooling and heating period was to be considered. In order to investigate this speculation the temperature data-set in Figure 94 had its cooling and recovery period between days 0.2 and 1 cropped out. The results can be seen in Figure 107.

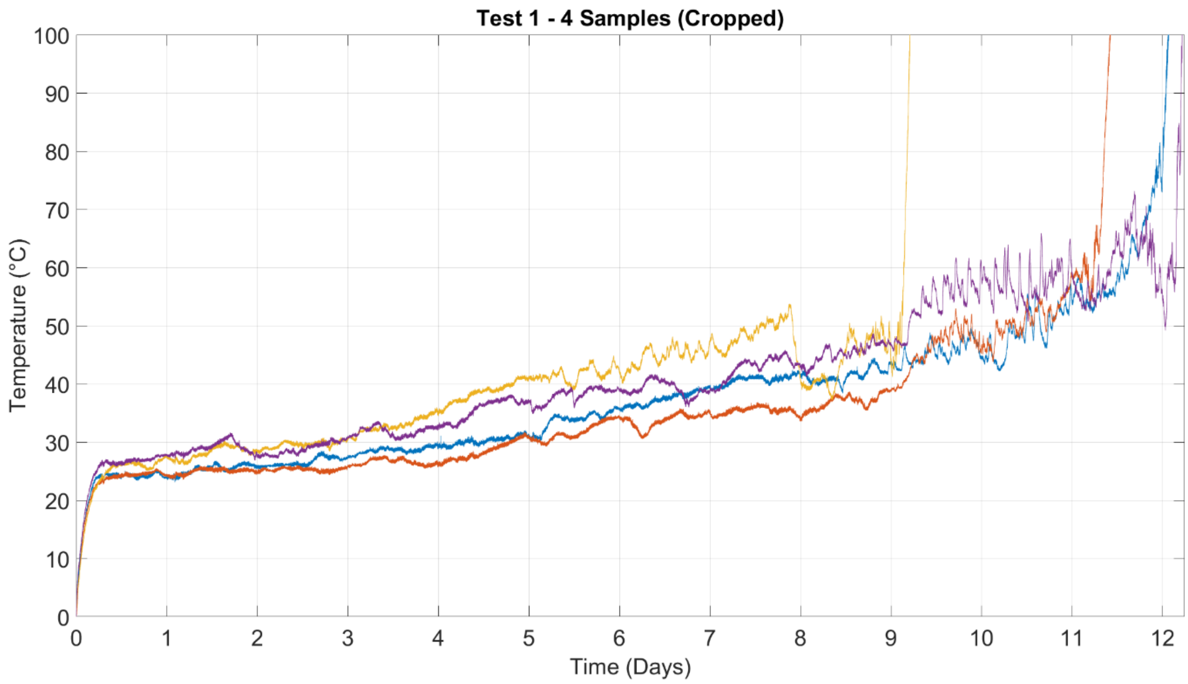

Figure 107 - Test 1 with its cooling and recovery period removed.

The EWMA charts were in turn re-created (Figure 108 - Figure 119) by using the data within Figure 107 with the same period of 43200 data points used to calculate the UCL and LCL thresholds.

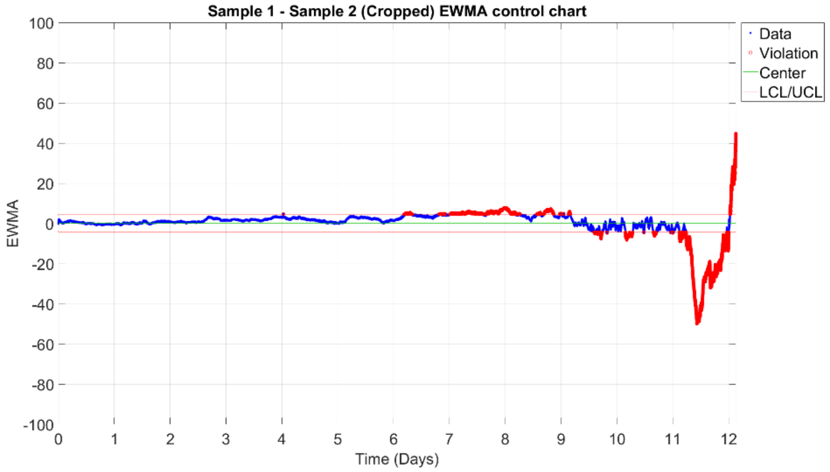

Figure 108 - EWMA chart: Sample 1 vs Sample 2 with cooling and recovery period removed under consideration.

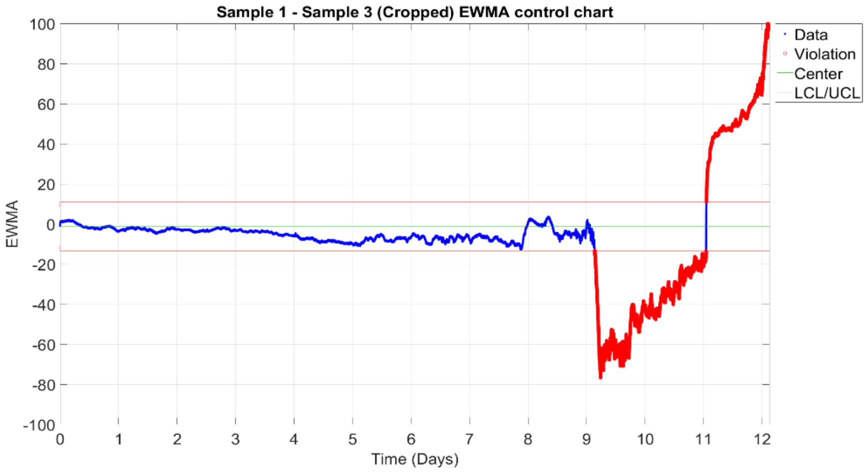

Figure 109 – EWMA chart: Sample 1 vs Sample 3 with cooling and recovery period removed under consideration.

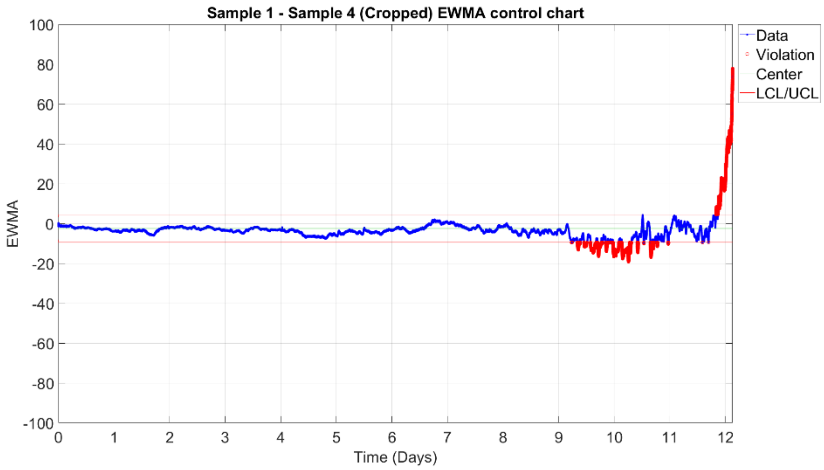

Figure 110 - EWMA chart: Sample 1 vs Sample 4 with cooling and recovery period removed under consideration.

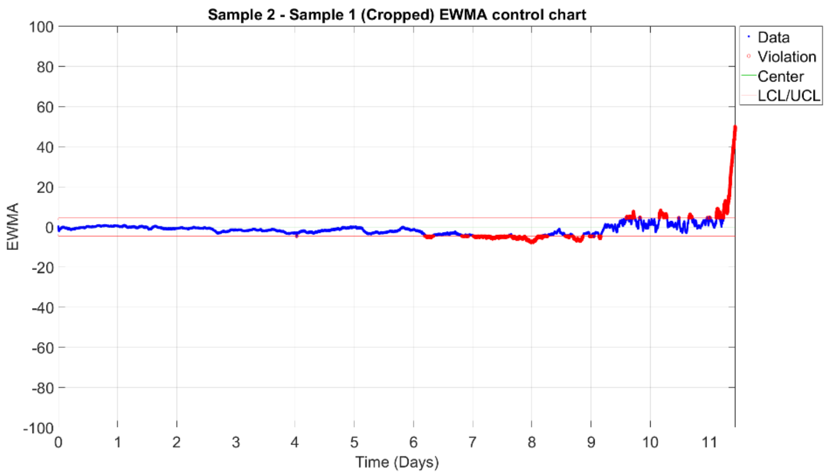

Figure 111 – EWMA chart: Sample 2 vs Sample 1 with cooling and recovery period removed under consideration.

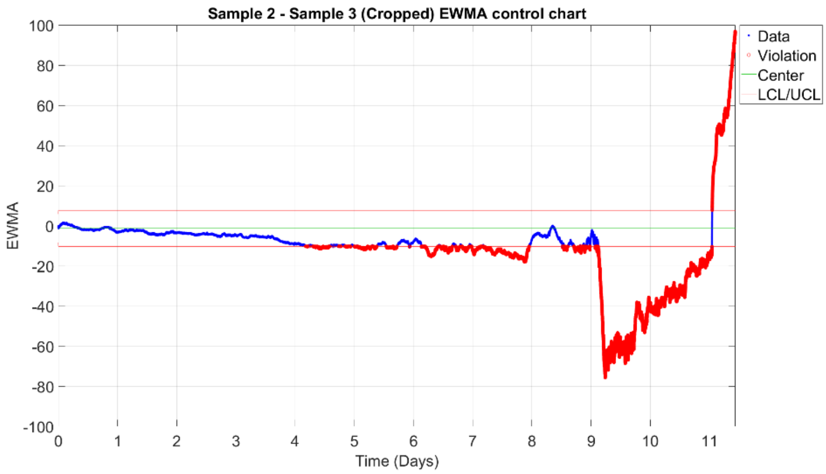

Figure 112 – EWMA chart: Sample 2 vs Sample 3 with cooling and recovery period removed under consideration.

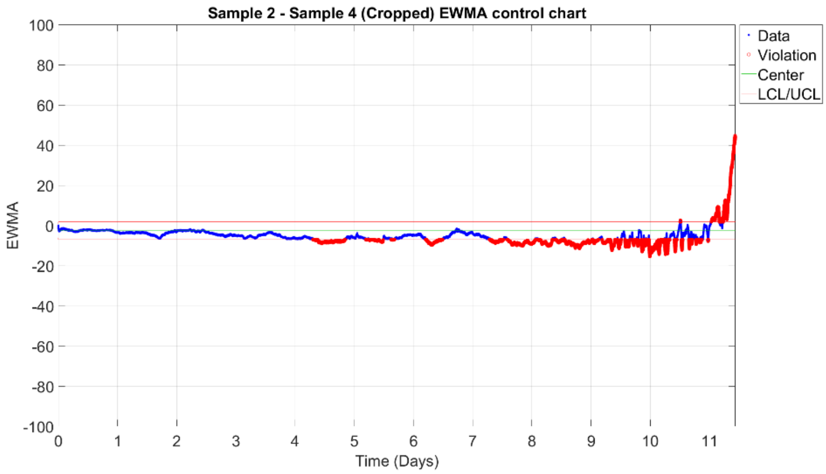

Figure 113 - EWMA chart: Sample 2 vs Sample 4 with cooling and recovery period removed under consideration.

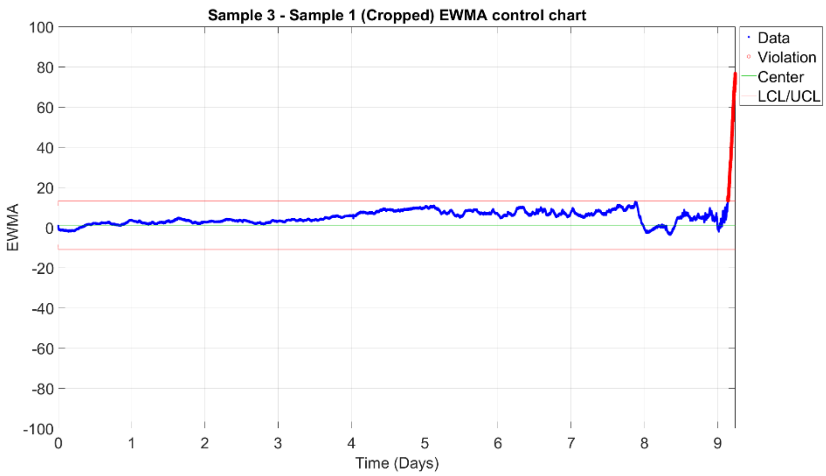

Figure 114 – EWMA chart: Sample 3 vs Sample 1 with cooling and recovery period removed under consideration.

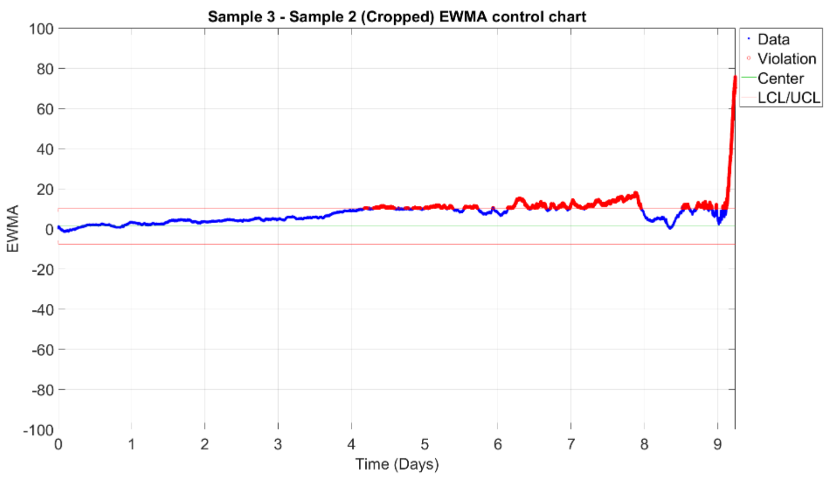

Figure 115 – EWMA chart: Sample 3 vs Sample 2 with cooling and recovery period removed under consideration.

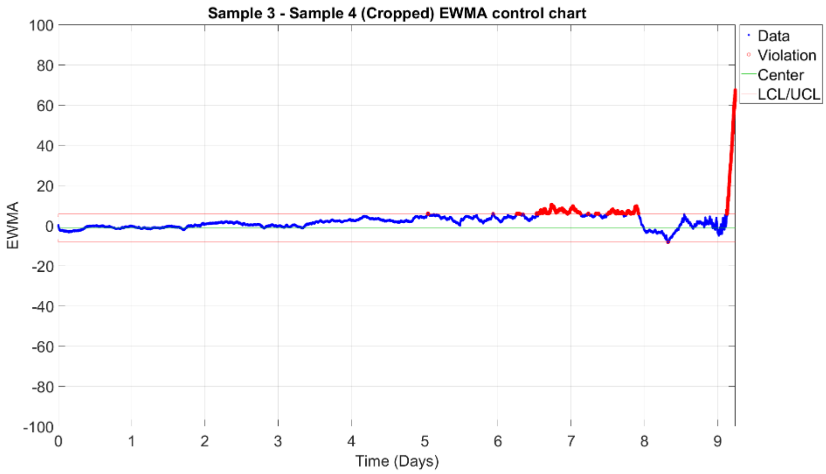

Figure 116 - EWMA chart: Sample 3 vs Sample 4 with cooling and recovery period removed under consideration.

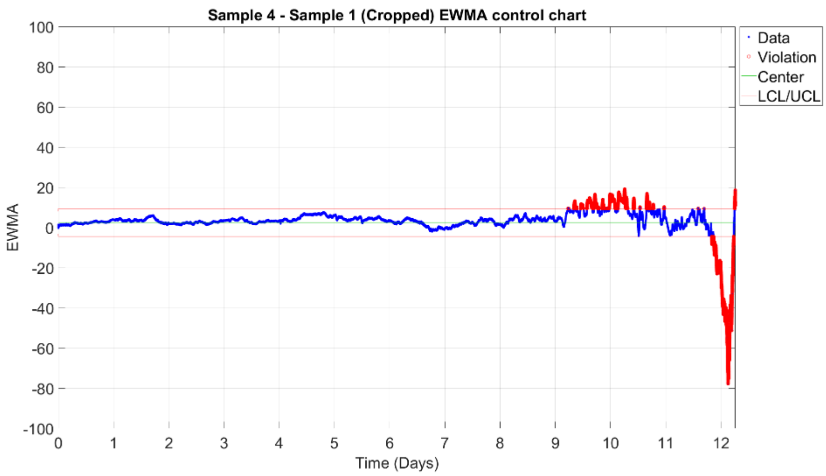

Figure 117 – EWMA chart: Sample 4 vs Sample 1 with cooling and recovery period removed under consideration.

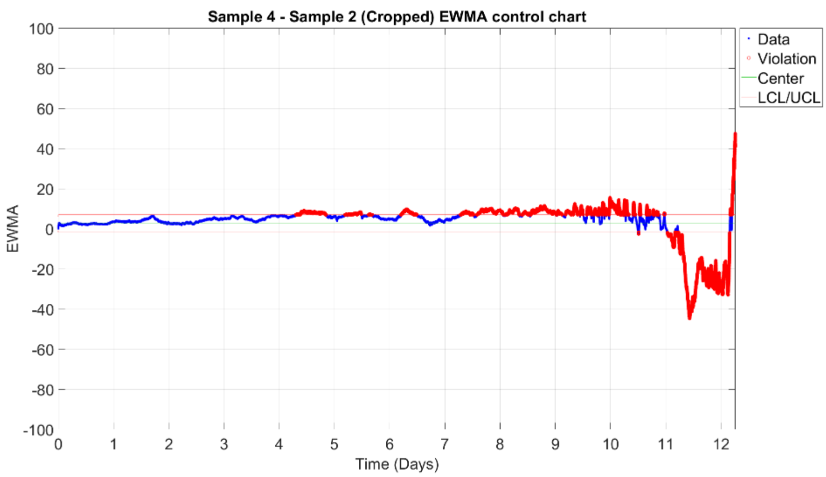

Figure 118 – EWMA chart: Sample 4 vs Sample 2 with cooling and recovery period removed under consideration.

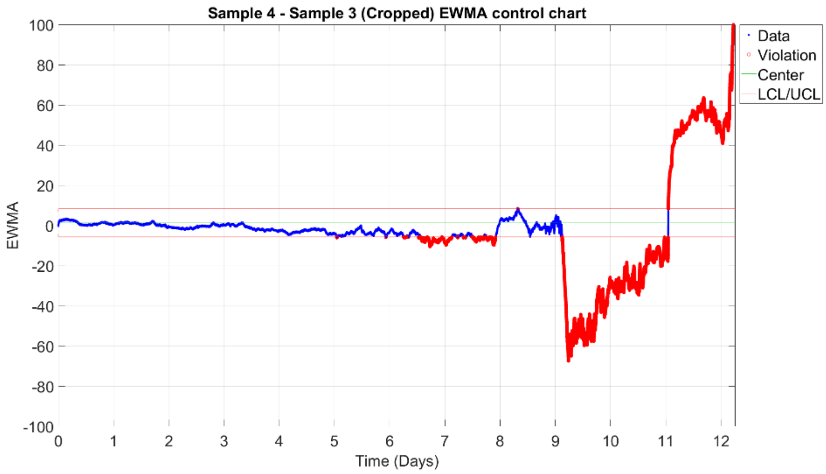

Figure 119 - EWMA chart: Sample 4 vs Sample 3 with cooling and recovery period removed under consideration.

By disregarding the cooling and recovery period when calculating the control limits for the EWMA charts, clear differences can be seen in the resulting violations. The algorithm became more sensitive to the comparisons between samples 1-2, 2-4 and 3-4, less sensitive between samples 1-3 and 2-3 and finally no effect was seen when considering samples 2-4. The reason for this seemingly random effect on the comparison pairs, is thought to be the temperature range which occurred at the initial period where the UCL and LCL values are calculated. As the cooling and recovery period was removed, new values of temperature differences became relevant to the control limit calculation and therefore affected the limits.

In order to investigate the tribological behaviour of the liner composite which causes the violations exhibited by Figure 108, Figure 119, wear was plotted with the corresponding temperature cooling and recovery period also removed (Figure 120). The data set of which the cooling and recovery period was removed was chosen due to its closer similarity to a real-life situation, where the algorithm is envisaged to consider temperature data only when a plateau temperature phase of the bearing system has been reached.

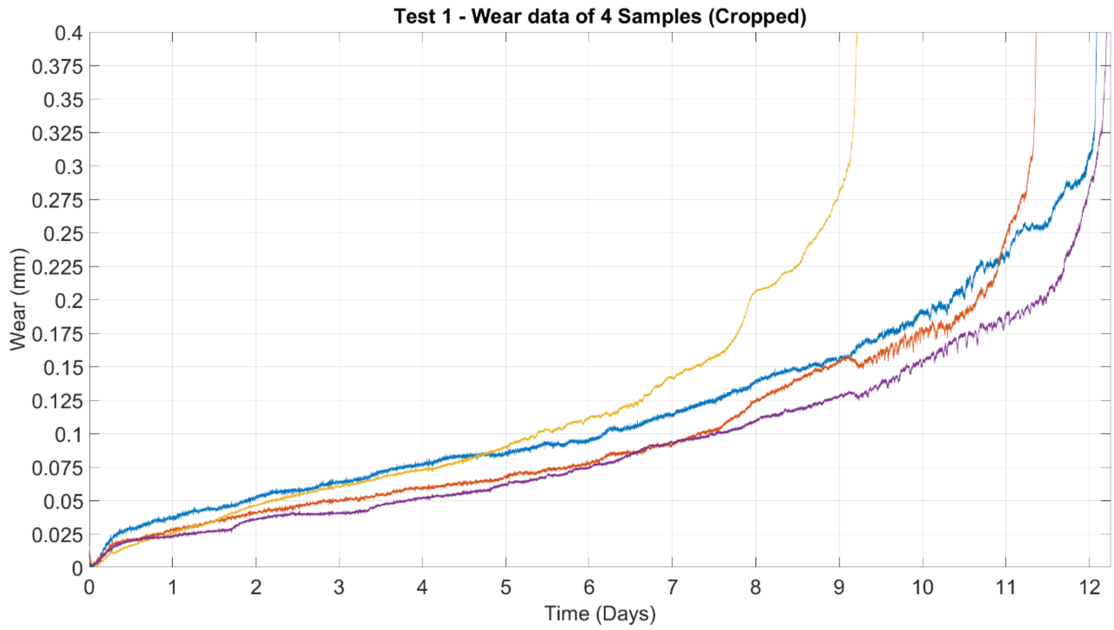

Figure 120 - Wear data with cooling and recovery period removed.

Table 4 shows the time at which a significant number of violations occurred in each EWMA chart, compared to the corresponding wear depth of the liner composite at the same time. In order for a violation cluster to be deemed significant, ten consecutive points on the plot must lay outside either the UCL or the LCL (Oakland, 1996).

Table 4 –Time-of-detection wear data of samples 1-4.

Sample Comparison. (a – b)	Time of Violation Custer occurrence (Days)	Corresponding Wear Depth of Sample 'a' (mm)	Corresponding Wear Depth of Sample 'b' (mm)
1 – 2	6.25	0.1	0.075
1 – 3	9.15	0.16	0.275
1 – 4	9.25	0.17	0.125
2 – 3	4.2	0.05	0.075
2 – 4	4.3	0.065	0.06
3 – 4	6.4	0.12	0.075

This time, each sample was considered once per pair, in order to avoid repetition of results. In order for this method to be evaluated, the time of detection and corresponding wear depth of the samples was compared to the current replacement criteria of a pitch control self-lubricating bearing of 0.12 mm. It was found that the algorithm detected signs of damage correctly 66.6% of the time and failed to detect damage prior to the replacement criteria 33.3% of the time. It was also noted that in one occasion, the algorithm failed to detect signs of damage upon sample 3, until the wear depth had reached a value of 0.275mm, meaning the contact was already on metal to metal. As imagined, this could be catastrophic in a real life application.

Considering all of the positives and negatives of the EWMA method, it was decided to proceed with researching the topic further, with a focus on understanding how the parameters and control limits of the EWMA method can be manipulated to in order to achieve a higher degree of accurate detection.

5.4 Tailored Exponentially Weighted Moving Average (EWMA) charts

Due to the issues raised by the preliminary EWMA charts, it was decided that further investigation was necessary in order to understand the sensitivity of the code to the values of certain parameters:

1. The effect of the length of the data-set assigned as a healthy period.
2. The effect of changing control limits during the process.
3. The effect of altering the smoothing constant 'a'.

For the purpose of this investigation the two data sets selected were Sample 1 and Sample 4 without the inclusion of the cooling and recovery period (Figure 107). These were selected due to their similarity in their time of failure and therefore these would provide the algorithm with most challenge of the available data sets. In order to decrease the running time of the Matlab code, the data sets were down-sampled by a ratio of 1:100. In order to evaluate if this down sampled data set could affect the results of the algorithm, a resolution study was conducted. The study calculated the temperature difference between two consecutive points and returned a percentage of sample differences which exceeded 1°C. A visual representation of the original vs down-sampled data sets is seen in

Figure 121.

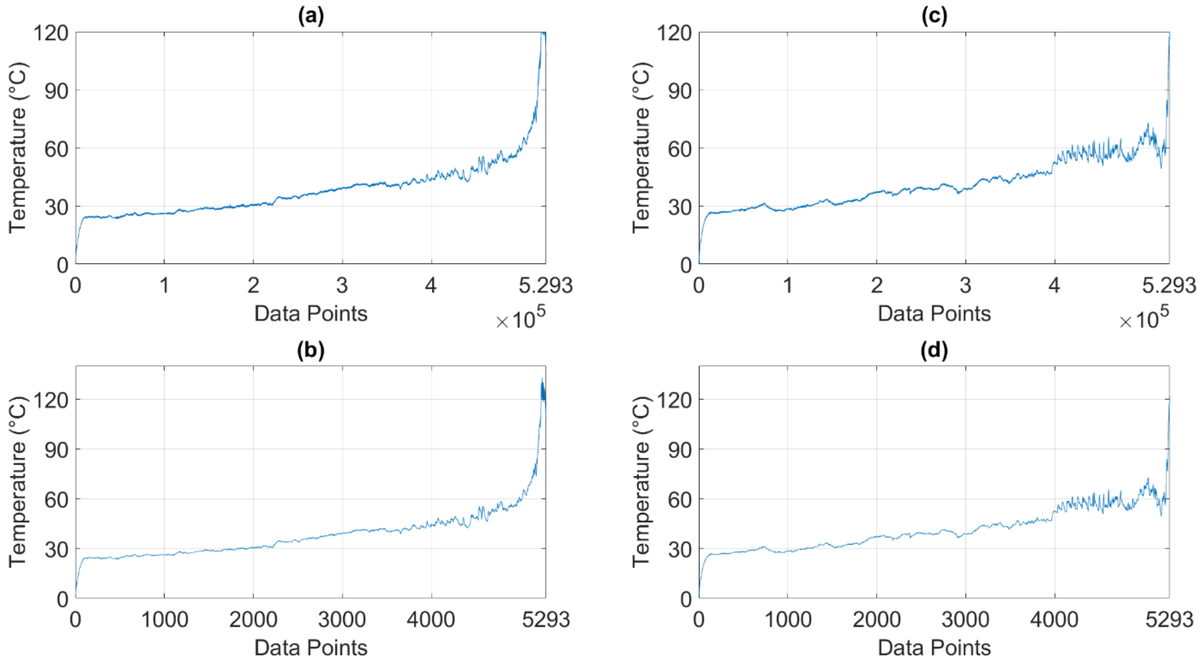

Figure 121 – Visual comparison of (a) Sample 1 original data vs (b) Sample 1 sampled data and (c) Sample 4 original data vs (d) Sample 4 original data.

Within the original data, 89.09% of consecutive data point differences were below 1°C for sample 1 and 91.33% for sample 4. After sampling had occurred, these percentages dropped to 88.48% for sample 1 and 90.71% for sample 4. Therefore it was concluded that the effect of the down sampling was negligible.

5.4.1 The effect of the length of the data-set assigned as a training period

Initially the length of the data window which defines the healthy period was considered. To recap, this healthy period was used in order to calculate the upper and lower control limits of the EWMA charts. The window lengths which were chosen consisted of 20, 40, 80, 160, 320 and 640 out of the total 5293 data points which represents the final failure point at 12.2 days of sample 4. These equate to approximately 0.04, 0.08, 0.16, 0.32, 0.64 and 1.28 days respectively. To keep the rest of the parameters stationary, the default 'smoothing value' of 0.2 was chosen for this investigation. Figure 122 - Figure 127 display the effect of this parameter alteration as a change in the number of the cumulative sum of violations.

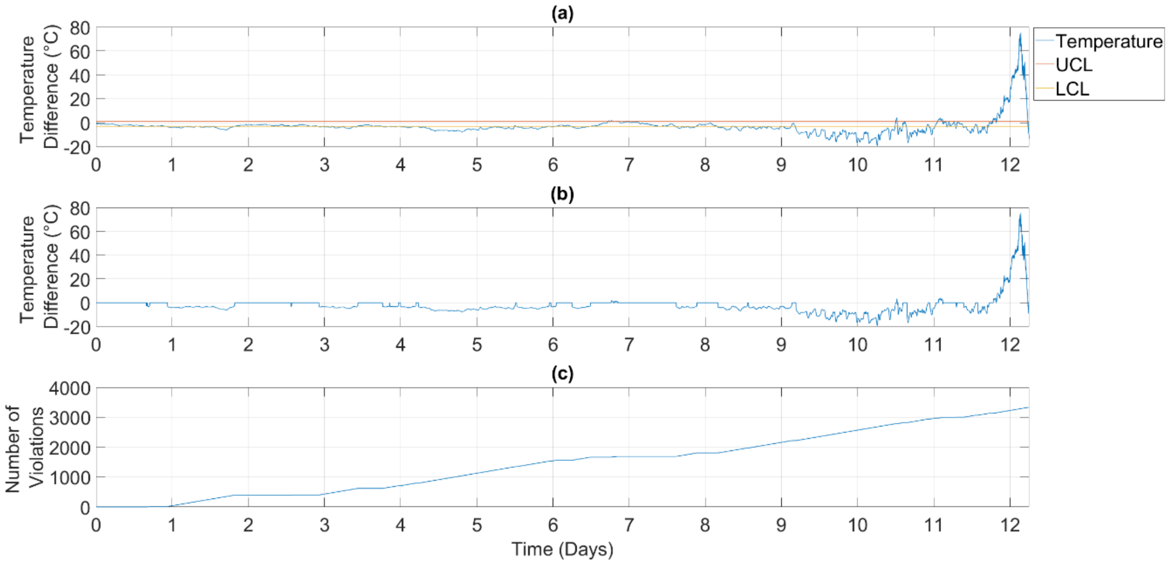

Figure 122 - Violation number for 'smoothing factor' 0.2, window size of 20 data points and stationary calculated limits: (a) Residual Temperature, UCL and LCL representation, (b) Temperature at the point of violation, (c) Cumulative sum of violations detected.

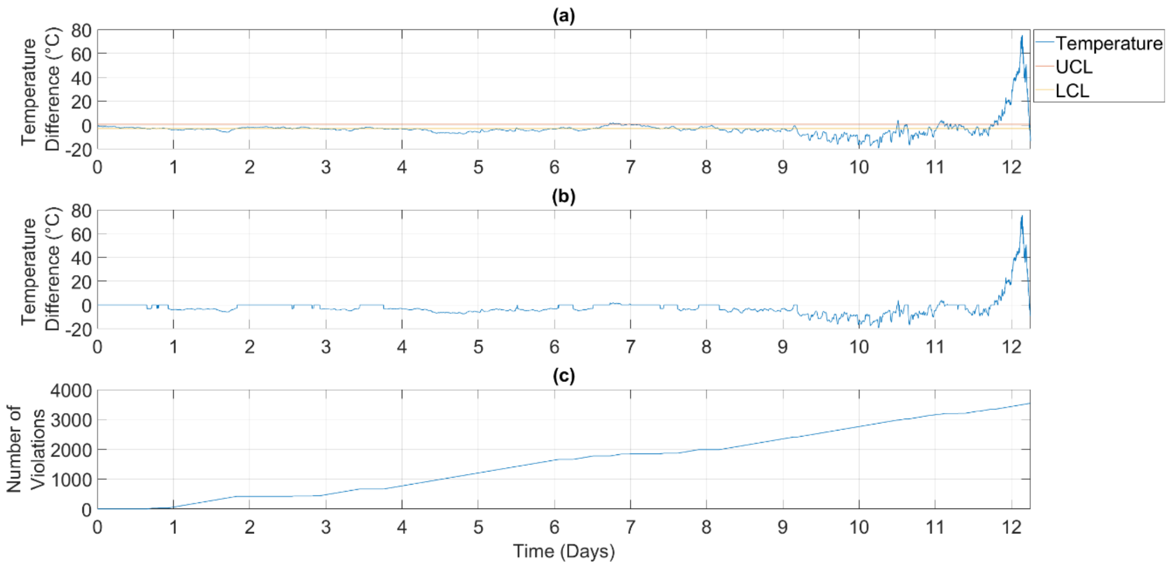

Figure 123 - Violation number for 'smoothing factor' 0.2, window size of 40 data points and stationary calculated limits: (a) Residual Temperature, UCL and LCL representation, (b) Temperature at the point of violation, (c) Cumulative sum of violations detected.

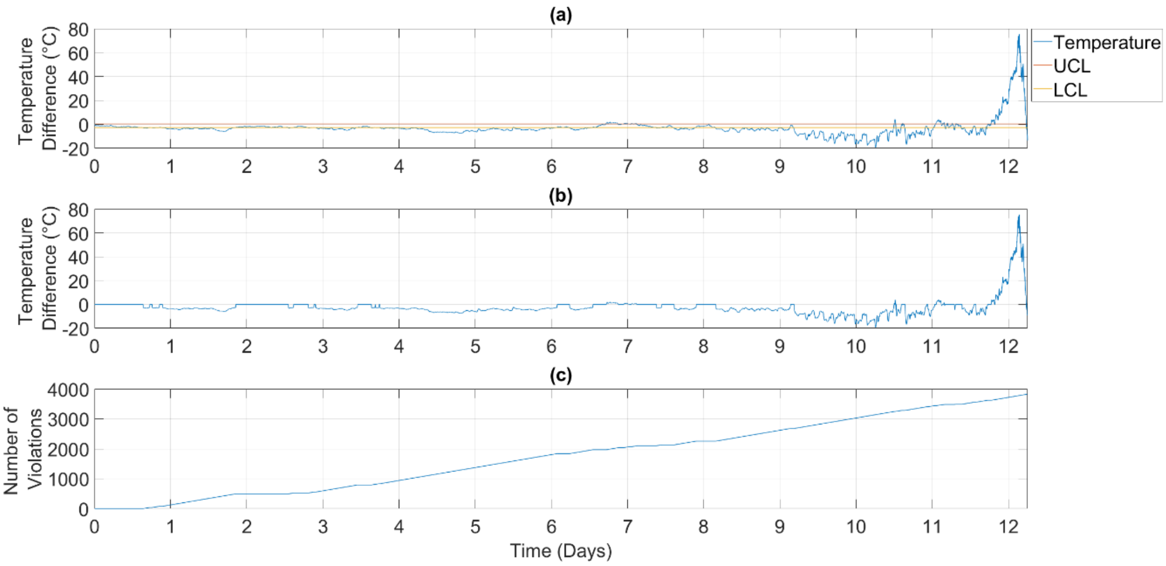

Figure 124 - Violation number for 'smoothing factor' 0.2, window size of 80 data points and stationary calculated limits: (a) Residual Temperature, UCL and LCL representation, (b) Temperature at the point of violation, (c) Cumulative sum of violations detected.

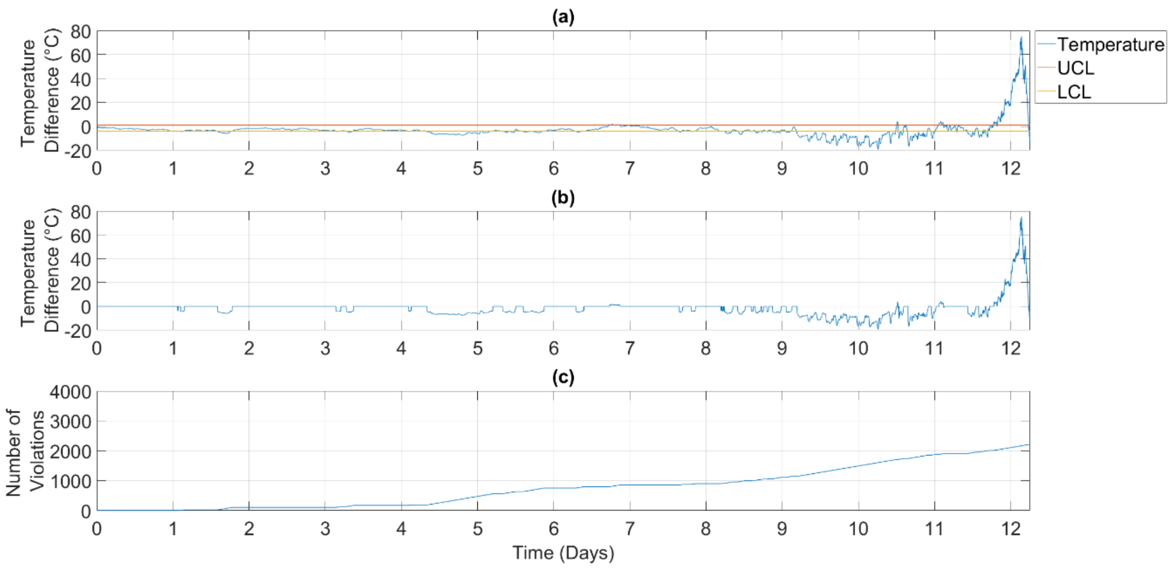

Figure 125 - Violation number for 'smoothing factor' 0.2, window size of 160 data points and stationary calculated limits: (a) Residual Temperature, UCL and LCL representation, (b) Temperature at the point of violation, (c) Cumulative sum of violations detected.

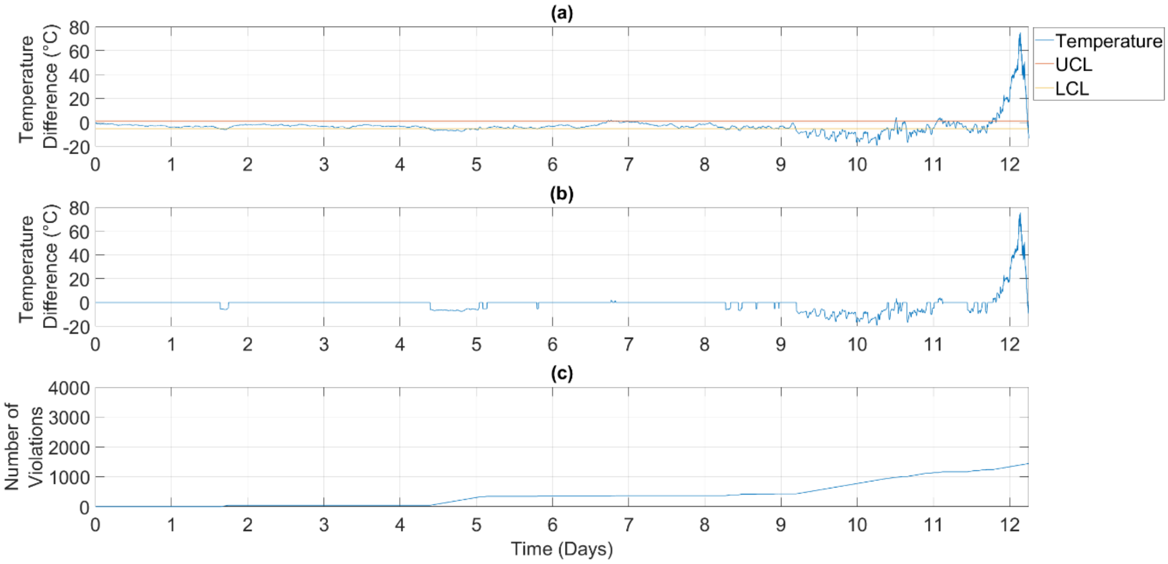

Figure 126 - Violation number for 'smoothing factor' 0.2, window size of 320 data points and stationary calculated limits: (a) Residual Temperature, UCL and LCL representation, (b) Temperature at the point of violation, (c) Cumulative sum of violations detected.

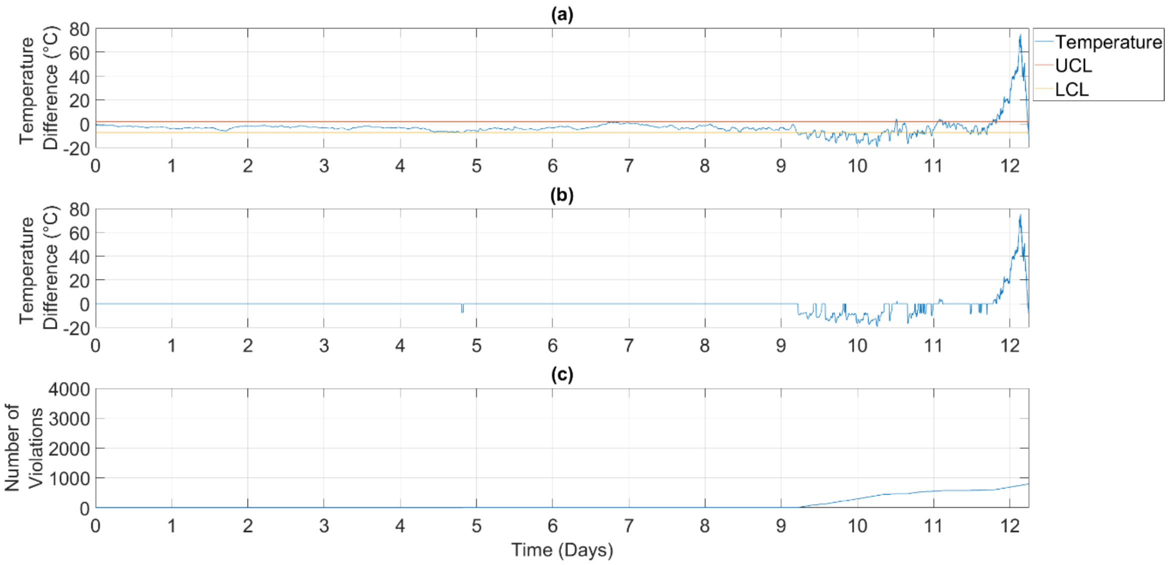

Figure 127 - Violation number for 'smoothing factor' 0.2, window size of 640 data points and stationary calculated limits: (a) Residual Temperature, UCL and LCL representation, (b) Temperature at the point of violation, (c) Cumulative sum of violations detected.

It can be observed from the figures, that as the defined healthy period is increased, the cumulative number of violations decreases drastically. This could be seen as a negative aspect of the algorithm, due to its apparently decreased sensitivity but in fact this proved to be the opposite. The total number of violations had indeed decreased but the majority of the remaining violations occur at the region where the two temperature data sets had begun to deviate, after approximately 9 days of testing, which is shown by the large variation in the residual temperatures, indicating one sample wearing more rapidly than the other. Table 5 shows the percentage of violations of each window width which occurred before the time of temperature separation.

Table 5 - Percentage of violations detected prior to the day of separation (9.2 Days).

Window Width	Number of Violations Prior to Temperature Separation	Number of Violations After to Temperature Separation	Total Violations Detected	Percentage of Violations Prior to Temperature Separation
20	**2249**	**1084**	**3333**	**67.48**
40	**2439**	**1099**	**3538**	**68.94**
80	**2710**	**1116**	**3826**	**70.83**
160	**1172**	**1041**	**2213**	**52.96**
320	**456**	**686**	**1442**	**31.62**
640	**26**	**769**	**795**	**3.27**

As seen within Table 5, using a large dataset to calculate the UCL and LCL yields the best results as a larger range of temperatures are allowed to be considered from the healthy period of the bearing's life. Therefore, the number of data points considered for the calculation of the UCL and LCL dictates the sensitivity of the overall technique. The larger the data point window considered for the calculation, the more lenient the UCL and LCL would be. The opposite occurs when considering a shortened data point window, resulting in 'tighter' upper and lower control limits.

Having identified the preferred training window size of 640 data points, the code was then applied to the data set which yielded the largest deviation. Samples 1 and 3 were chosen in order to observe how the method behaves when a premature failure occurs in one of the bearing liners, as opposed to the relatively similar sample 1 and 4 data. The data were analysed up to the point of failure of sample 3 due to the comparative nature of the code, with the results shown in Figure 128.

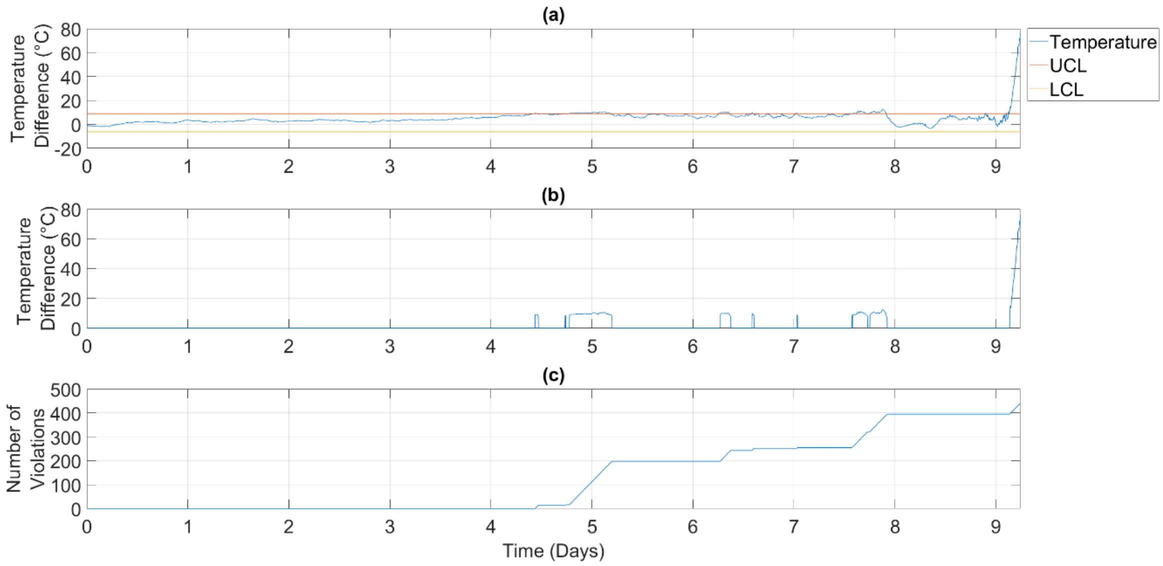

Figure 128 - Violation number for 'smoothing factor' 0.2, window size of 640 data points and stationary calculated limits: (a) Residual Temperature, UCL and LCL representation, (b) Temperature at the point of violation, (c) Cumulative sum of violations detected.

It can be seen that the algorithm has been able to establish when a large enough temperature variation occurs. This sample temperature separation period occurs approximately 4 days into the test and could be visibly seen when inspecting Figure 128, and more specifically considering the gradient at which each temperature curve is increasing. It can be seen that the temperature gradient of Sample 3 was increasing prematurely to that of Sample 1 which was due to abnormal wear behaviour.

Although this type of damage detection seems promising, the main issue lies within the determination of the healthy period over which the Upper Control Limits (UCL) and Lower

Control Limits (LCL) are calculated. In a real application, this type of control chart analysis would require the gathering of multiple data sets in order to further investigate the most appropriate length of training data for the calculation of such limits.

5.4.2 The effect of changing control limits during the process

Although the figures in section 5.4.1 showed the method's ability to detect deviations in temperature between samples, the challenge which was considered next consisted of reducing the significance of violations in the initial wear-in period of the bearing liner, since their importance is not of the same magnitude as the violations occurring in the latter stages of bearing liner wear. In order to provide a system which accounts for the high number of initial violations and avoids false alarms, a method which recalculates the upper and lower action limits, at the point of violation, was created.

A rolling window of a particular length was applied to the residual temperature data between samples 1 and 4, as used previously. This window length was initially used to calculate the UCL and LCL and only when a violation occurred the action limits were recalculated. In essence, if no violations occurred, the UCL and LCL would remain stationary. In turn, the control limits were recalculated by using the data prior to the point of violation. The length of data that was considered in the UCL and LCL recalculation, consisted of the length of rolling window applied initially. Since the control parameters were being recalculated each time a violation occurs, the violations themselves could not be used as an indicator of damage, therefore the rate at which the violations occur was the indicator. The value of this rate of violation occurrence which would signify signs damage was to be determined.

In order to isolate the effect of the rolling window upon the sensitivity of the damage detection control chart, the value of the smoothing constant ‘a’ was kept at the default value of 0.2. Also, to understand how the damage detection sensitivity alters with this technique, the values of 20, 40, 80, 160, 320 and 640 out of the total 5392 data points for the rolling window, were used as before (Figure 129 - Figure 134).

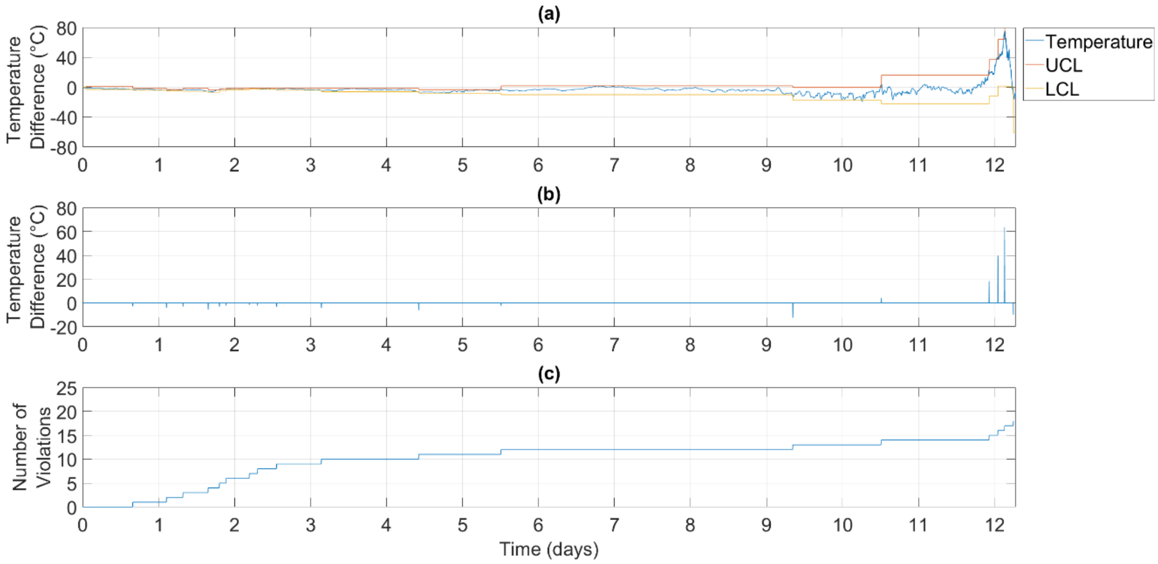

Figure 129 - Violation number for 'smoothing factor' 0.2, window size of 20 data points and non-stationary calculated limits: (a) Residual Temperature, UCL and LCL representation, (b) Temperature at the point of violation, (c) Cumulative sum of violations detected.

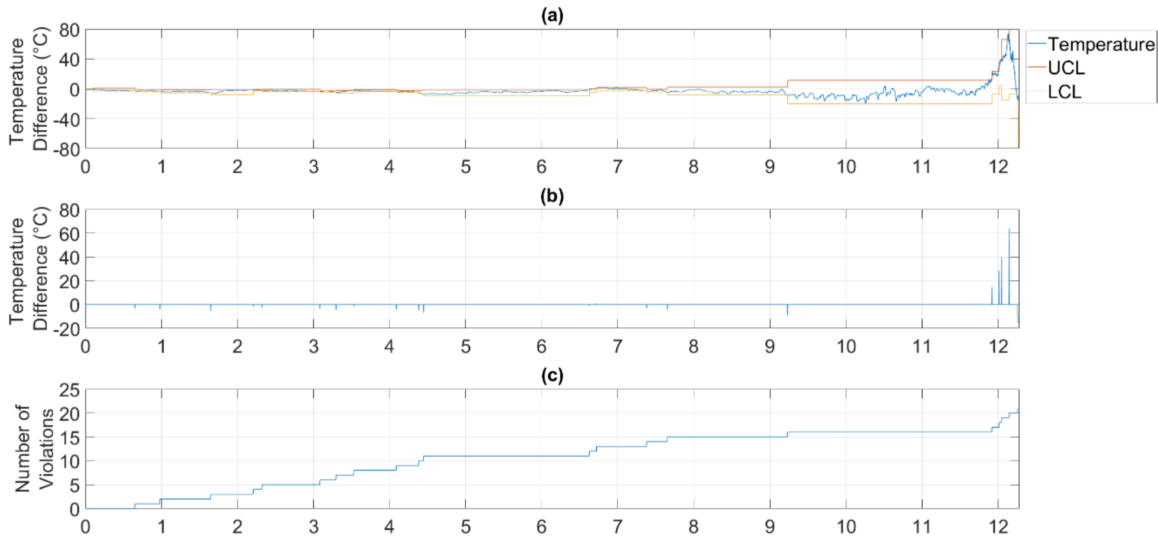

Figure 130 - Violation number for 'smoothing factor' 0.2, window size of 40 data points and non-stationary calculated limits: (a) Residual Temperature, UCL and LCL representation, (b) Temperature at the point of violation, (c) Cumulative sum of violations detected.

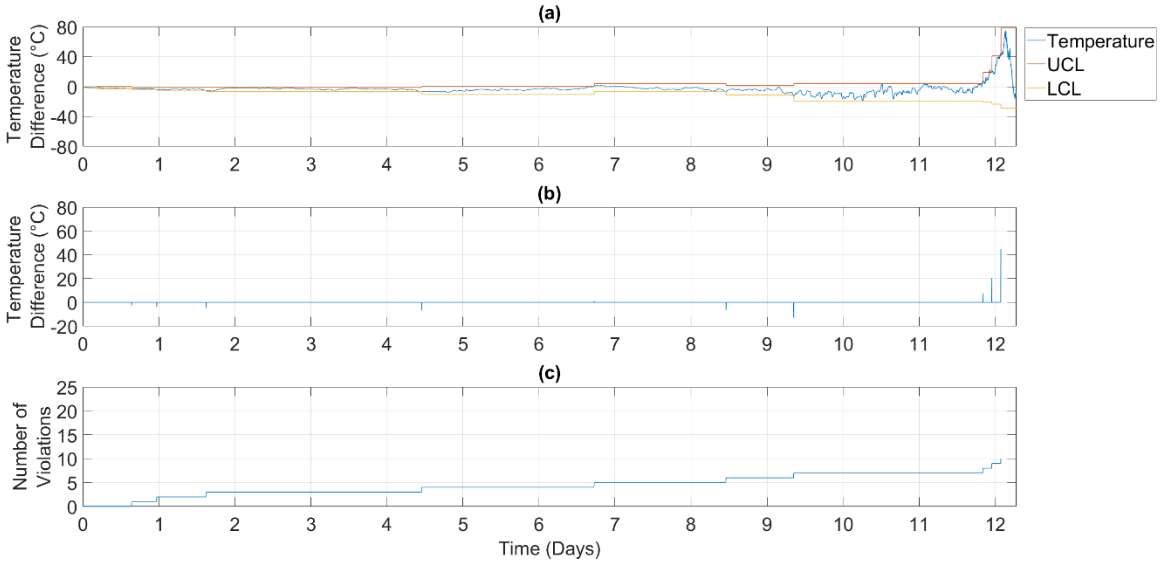

Figure 131 - Violation number for 'smoothing factor' 0.2, window size of 80 data points and non-stationary calculated limits: (a) Residual Temperature, UCL and LCL representation, (b) Temperature at the point of violation, (c) Cumulative sum of violations detected.

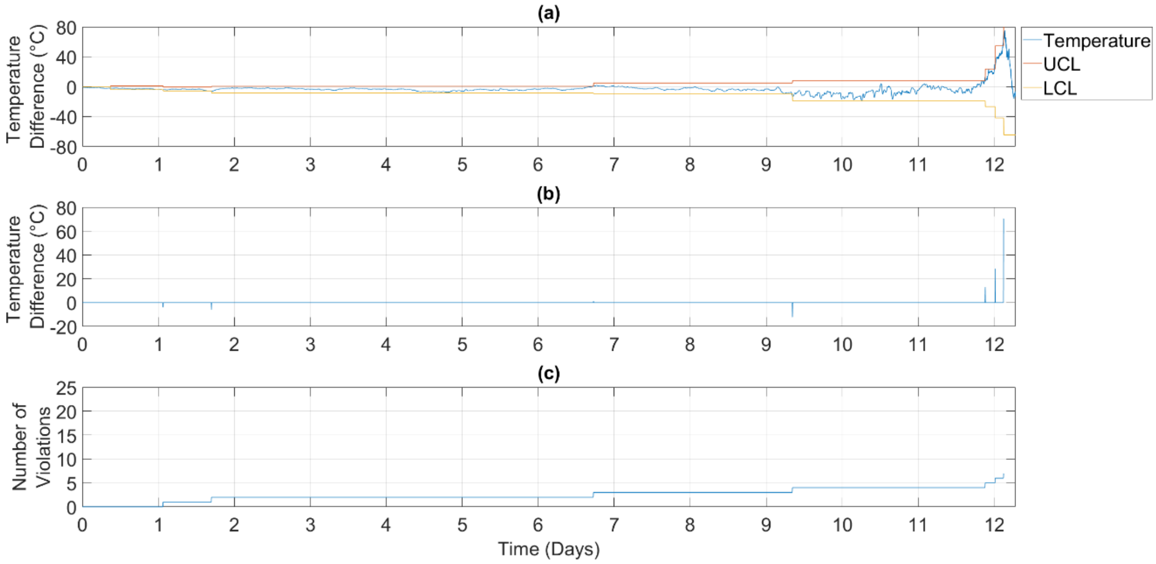

Figure 132 - Violation number for 'smoothing factor' 0.2, window size of 160 data points and non-stationary calculated limits: (a) Residual Temperature, UCL and LCL representation, (b) Temperature at the point of violation, (c) Cumulative sum of violations detected.

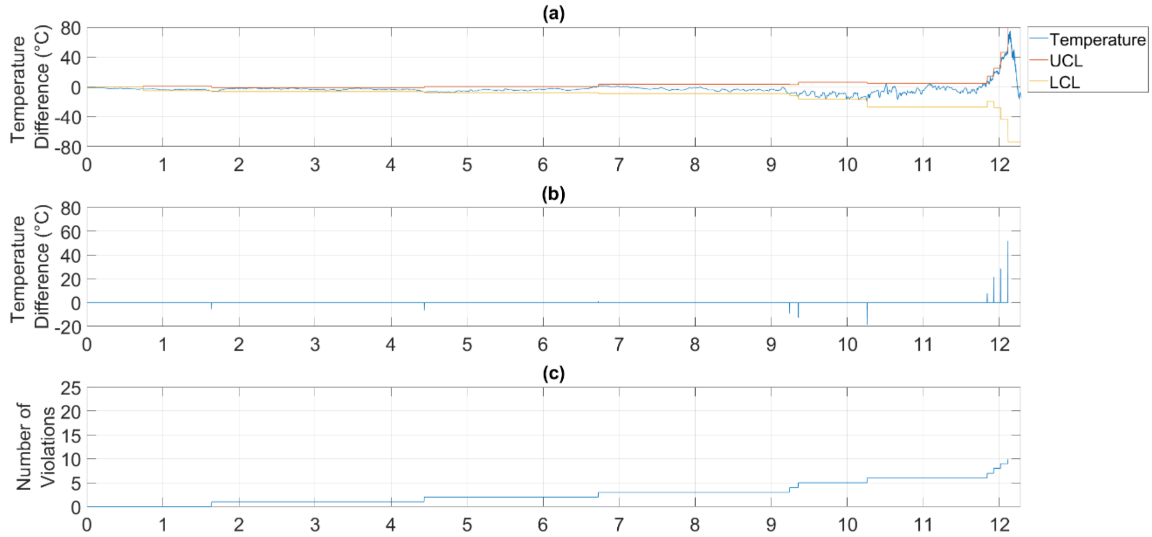

Figure 133 - Violation number for 'smoothing factor' 0.2, window size of 320 data points and non-stationary calculated limits: (a) Residual Temperature, UCL and LCL representation, (b) Temperature at the point of violation, (c) Cumulative sum of violations detected.

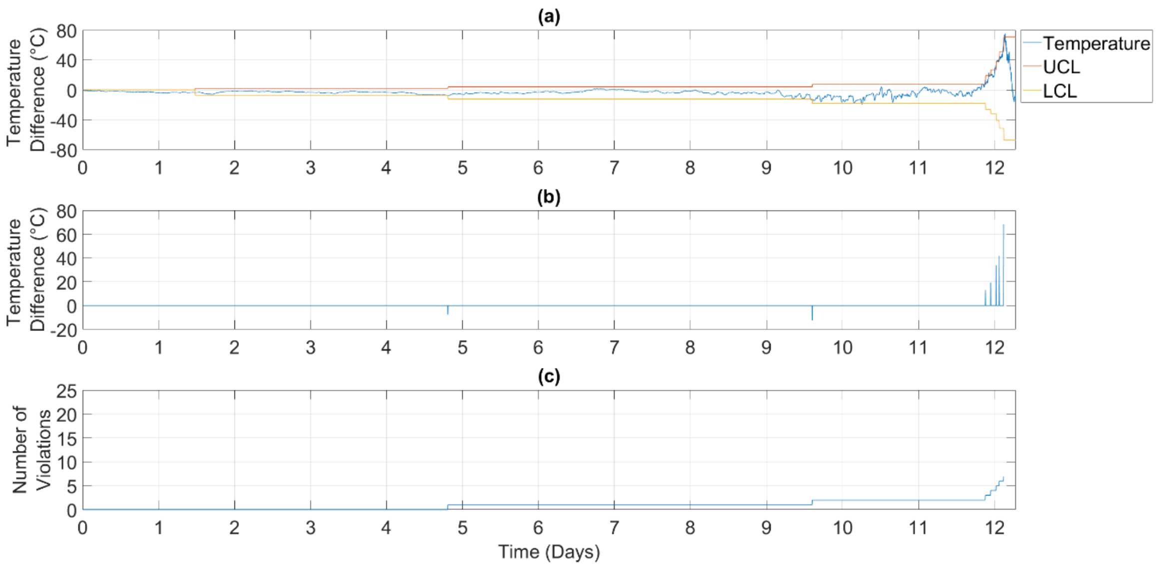

Figure 134 - Violation number for 'smoothing factor' 0.2, window size of 640 data points and non-stationary calculated limits: (a) Residual Temperature, UCL and LCL representation, (b) Temperature at the point of violation, (c) Cumulative sum of violations detected.

Inspecting Figures 133- 138, the window size which was deemed to provide the most useful information in terms of damage detection was the large 640 data point window. Due to its sensitivity towards the latter stages of wear, this rolling window size was preferred. As discussed previously, the indication of a fault within the system with these types of control limit-recalculating charts, was said to be the rate of which violations occur after each recalculation. An example of this can be seen within Figure 134, where towards the failure region of the bearing liner's life, a number of violations occur rapidly. Due to the scarcity of data which currently exists from the test bench, a precise value of the violation occurrence gradient which could be deemed as indicating damage was not able to be determined but this must be considered prior to implementing this type of method. Although a value for the damage gradient was not able to be determined, in order to observe how the code reacts to a premature failure of the liner material, samples 1 and 3 were once again considered. Window lengths of 320 and 640 were chosen to be investigated as they yielded the best visual results in terms of time of damage detection (Figure 135 & Figure 136).

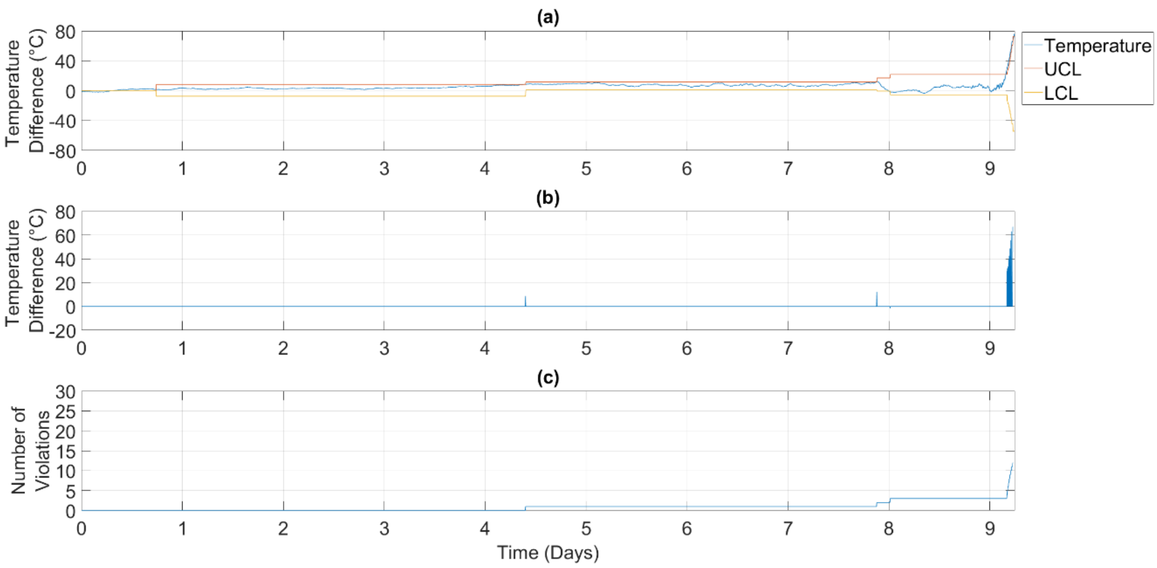

Figure 135 - Violation number for 'smoothing factor' 0.2, window size of 320 data points and non-stationary calculated limits: (a) Residual Temperature, UCL and LCL representation, (b) Temperature at the point of violation, (c) Cumulative sum of violations detected.

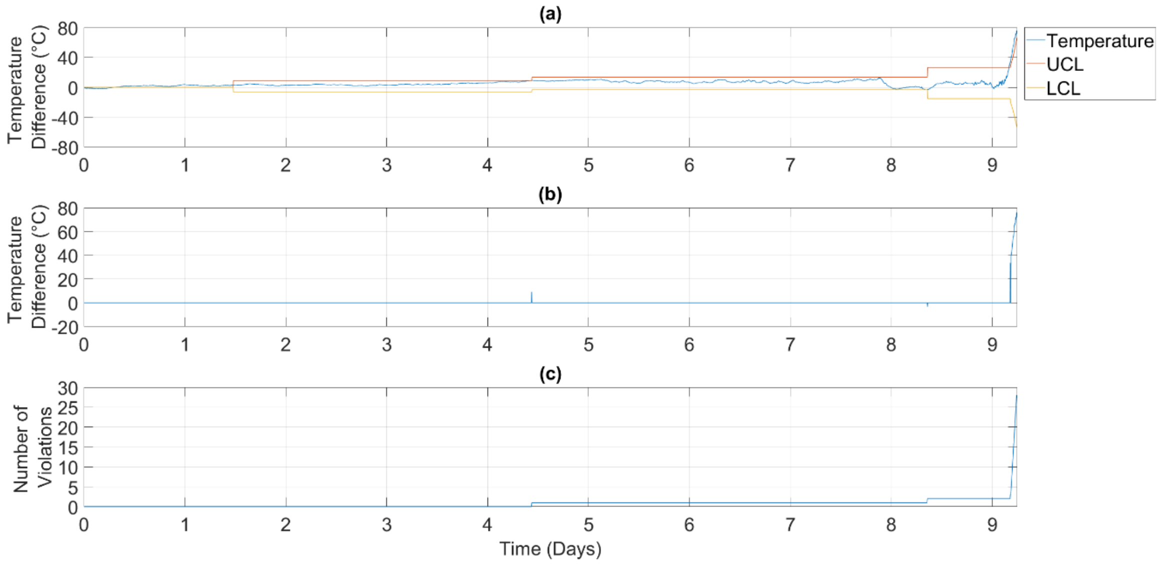

Figure 136 - Violation number for 'smoothing factor' 0.2, window size of 640 data points and non-stationary calculated limits: (a) Residual Temperature, UCL and LCL representation, (b) Temperature at the point of violation, (c) Cumulative sum of violations detected.

Similar to the previous technique used, where the control limits were kept the same throughout the analysis, this type of analytical method is able to detect what can be assumed to be damage occurring at a similar point in time. Between days 4 and 5, where the temperature deviation between the two sample data sets increases, the algorithm is able to start recording violations which occur when the control limits have been surpassed. In general, it was observed that the larger rolling window was most effective when trying to dampen the wear-in phase violations. The challenge posed with this type of technique is, once again, the determination of the length of training data required to produce a sensitive and robust algorithm. Unfortunately, the detection of the majority of violations with this method occurs towards the failure stage of the bearing liner, where the temperature difference between the two samples starts to increase rapidly. In a real-life scenario the detection of the bearing fault would be required to be detected much earlier on in the wear process, in order to allow sufficient time for the aircraft to be grounded and undergo a maintenance interval on the flagged, potentially damage, bearing.

Due to the scale of this potential research study, with regards to the selection of appropriate training data length for the Upper and Lower Control Limits, it was decided at this stage to try and develop a method which would require no rolling window but only a small initial training set period. Through the use of the first 40 data points, an initial value for the UCL and LCL was calculated. The residual data of the two temperature sets will in turn start to be included in the algorithm and a recalculation of the control limits will occur when a violation is detected. With this method, during the recalculation of the control limits, all the data prior to the point of violation was considered. Once again, a smoothing constant of 0.2 was used (Figure 137).

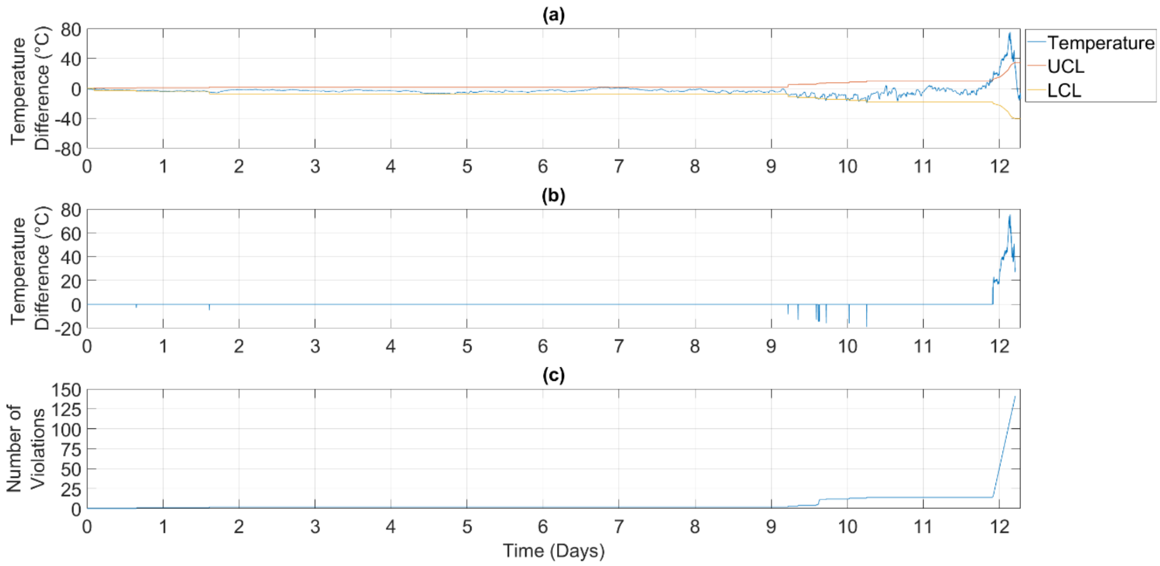

Figure 137 – Sample 1- Sample 4: Violation number for 'smoothing factor' 0.2, window size of 40 data points and rolling calculated limits: (a) Residual Temperature, UCL and LCL representation, (b) Temperature at the point of violation, (c) Cumulative sum of violations detected.

The nature of this UCL and LCL recalculation method allows the wear-in period violations to be dampened and more emphasis can be given to the violations occurring at the later stages of wear. A key feature which can be seen within Figure 137, is the rate of change of the cumulative sum of violations between the area of large deviations, between days 9 and 11. Sample 1 and Sample 3 were next considered in order to observe how this type of control chart can react to a premature failure of the bearing liner, as shown in Figure 138.

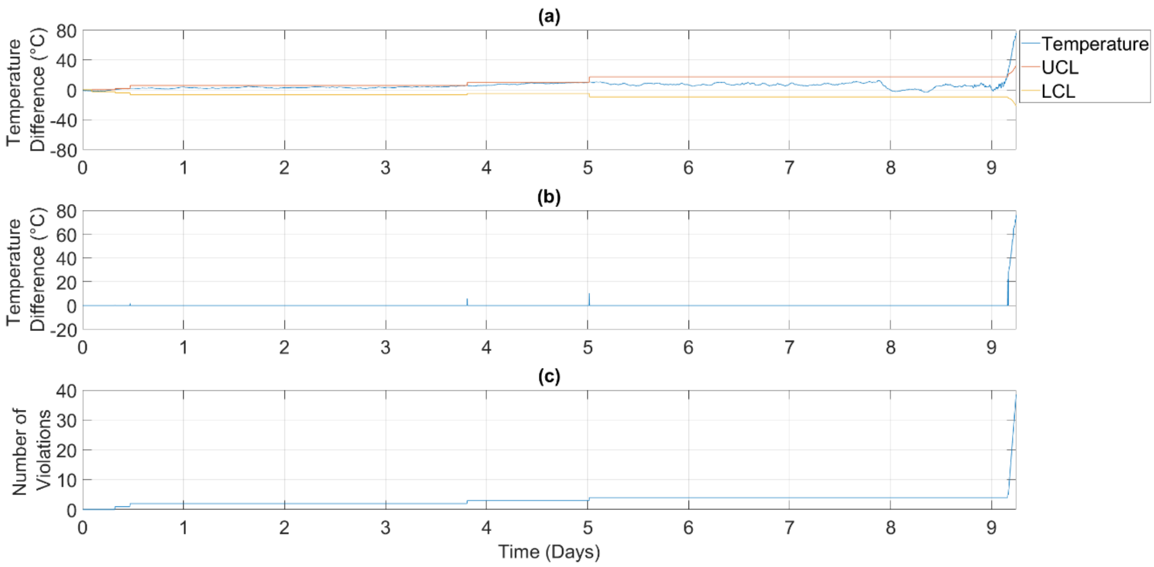

Figure 138 - Sample 1- Sample 3: Violation number for 'smoothing factor' 0.2, window size of 40 data points and rolling calculated limits: (a) Residual Temperature, UCL and LCL representation, (b) Temperature at the point of violation, (c) Cumulative sum of violations detected.

Although this method was successfully applied upon samples 1-4, its output for Samples 1-3 was not accurate. Although some detection was made at days 3.8 and 5, no clear increase in violation was detected past day 5 until the failure region was once again reached. Due to this technique's ability to 'dampen' early life violations, it was decided to proceed with a further study regarding the effect the smoothing factor 'a' has upon the time of detection.

5.4.3 The effect of altering the smoothing constant 'a'

The smoothing constant 'a' was investigated in order to view how its alteration can affect the results as a whole. This study was conducted on the preferred control chart damage detection method of no-rolling window and recalculation of the UCL and LCL. Four control charts were created with the smoothing constant 'a' taking values of 0.2, 0.4, 0.6 and 0.8 and an initial window width of 40 data points (Figures 143 – 146).

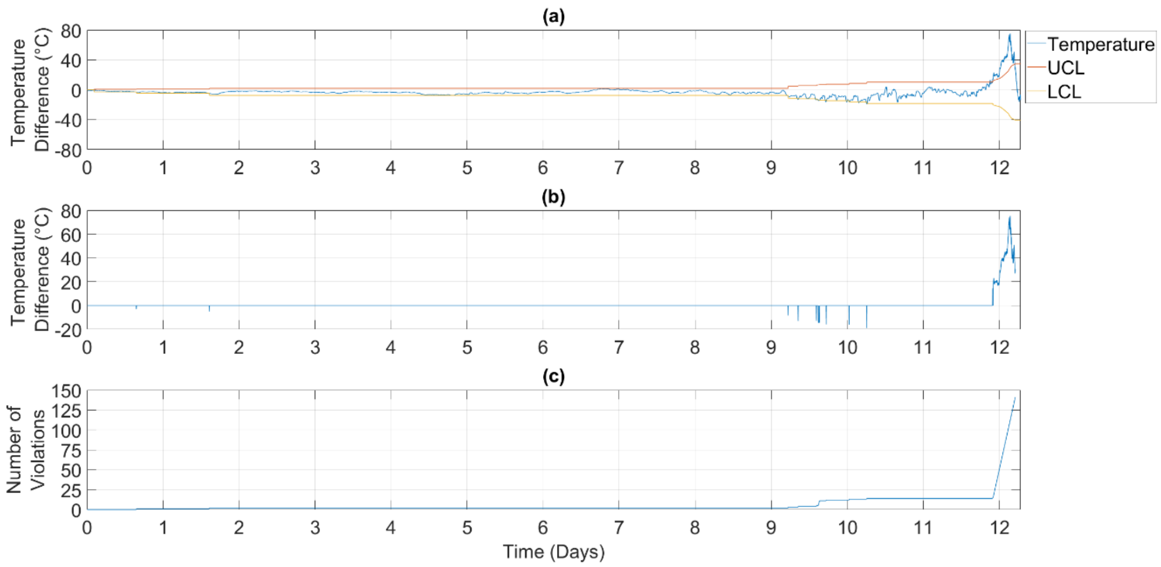

Figure 139 - Sample 1- Sample 4: Violation number for 'smoothing factor' 0.2, window size of 40 data points and rolling calculated limits: (a) Residual Temperature, UCL and LCL representation, (b) Temperature at the point of violation, (c) Cumulative sum of violations detected.

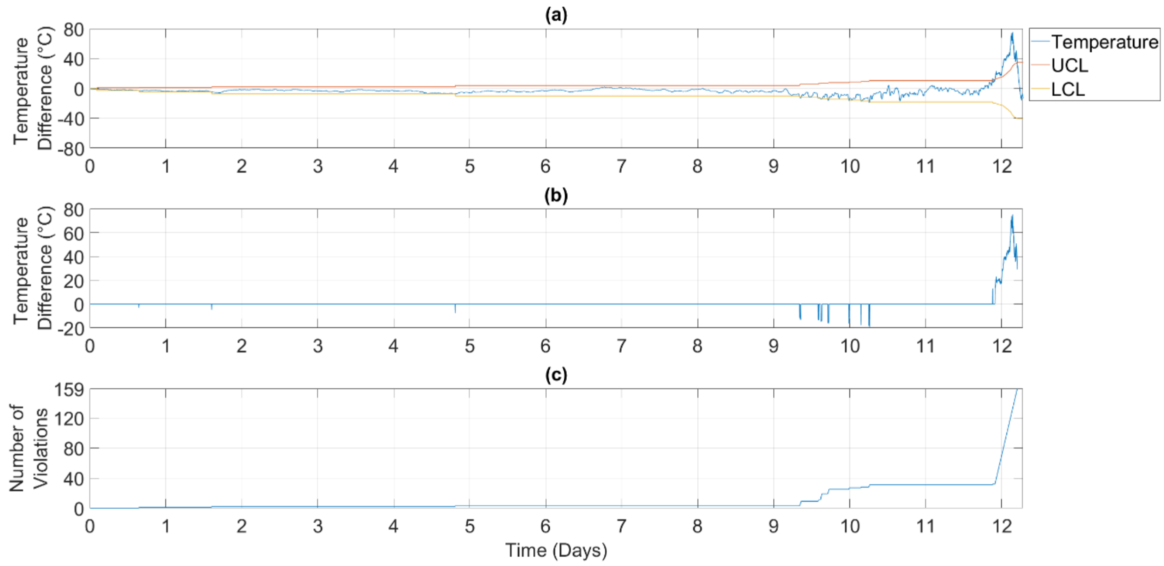

Figure 140 - Sample 1- Sample 4: Violation number for 'smoothing factor' 0.4, window size of 40 data points and rolling calculated limits: (a) Residual Temperature, UCL and LCL representation, (b) Temperature at the point of violation, (c) Cumulative sum of violations detected.

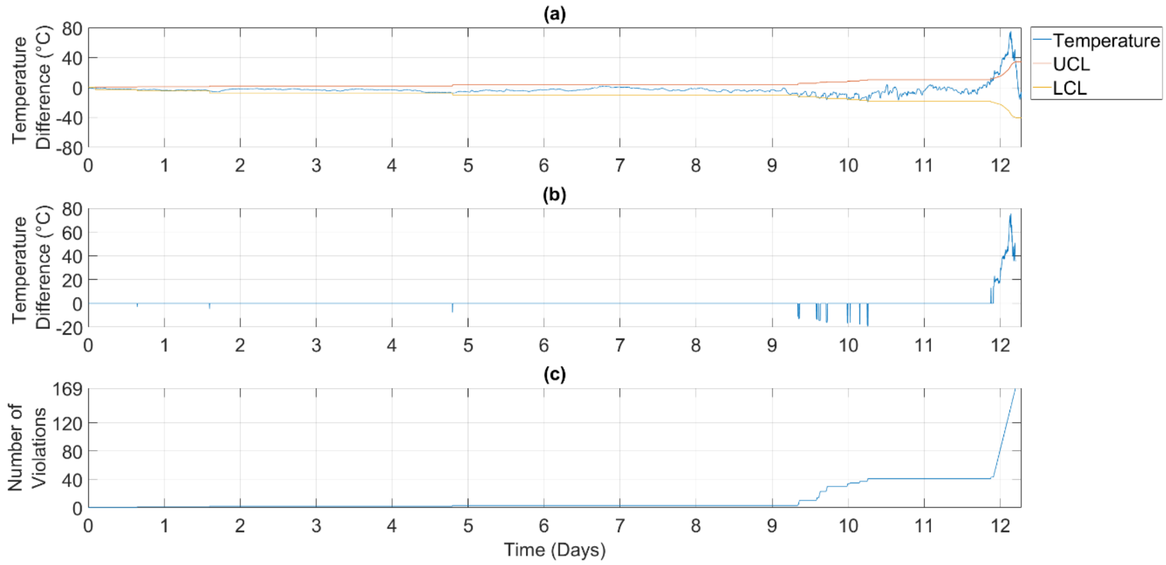

Figure 141 - Sample 1- Sample 4: Violation number for 'smoothing factor' 0.6, window size of 40 data points and rolling calculated limits: (a) Residual Temperature, UCL and LCL representation, (b) Temperature at the point of violation, (c) Cumulative sum of violations detected.

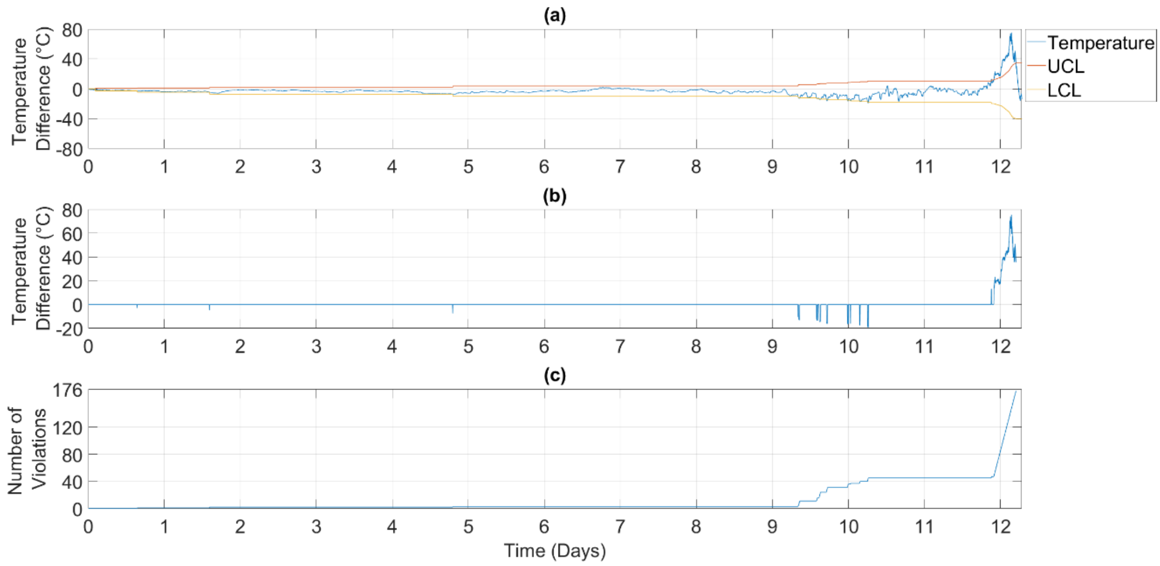

Figure 142 - Sample 1- Sample 4: Violation number for 'smoothing factor' 0.8, window size of 40 data points and rolling calculated limits: (a) Residual Temperature, UCL and LCL representation, (b) Temperature at the point of violation, (c) Cumulative sum of violations detected.

As expected, when the value of the smoothing constant 'a' increases, and therefore the weight of the new considered value in relation to the historic data increases, the number of cumulative violations increases.

Although the absolute values increase, the trend of number of violations with respect to time remains very similar throughout the range of 'a' values used. As seen in Figure 143 the detection of the point of separation between samples 1 and 4 was improved when using a higher 'a' value.

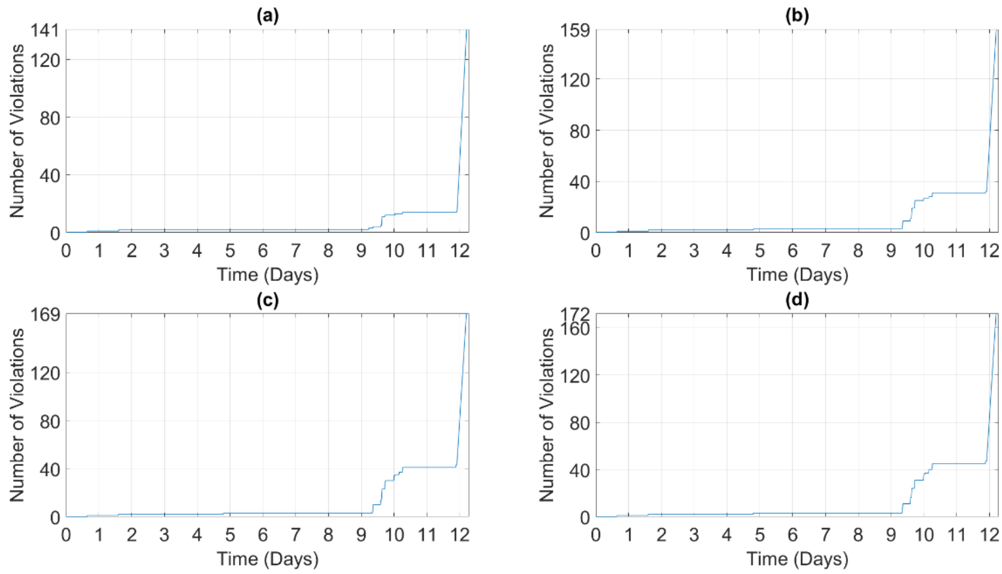

Figure 143 - Cumulative Sum of violations for the comparison of samples 1 - 4 with a smoothing factor 'a' of: (a) 0.2, (b) 0.4, (c) 0.6 and (d) 0.8.

Therefore a higher value of the smoothing factor provides sensitivity to the detection of a temperature violation in the latter stages of wear, while also providing a low sensitivity towards temperature violation in the early stages of wear.

In order to confirm the findings, a range of smoothing factors consisting of 0.2, 0.4, 0.6 and 0.8 were applied to the sample 1-4 tailored EWMA charts with stationary and changing limits with a training data set of 640 points. The cumulative sum of violations of each method are presented in Figure 144 and Figure 145.

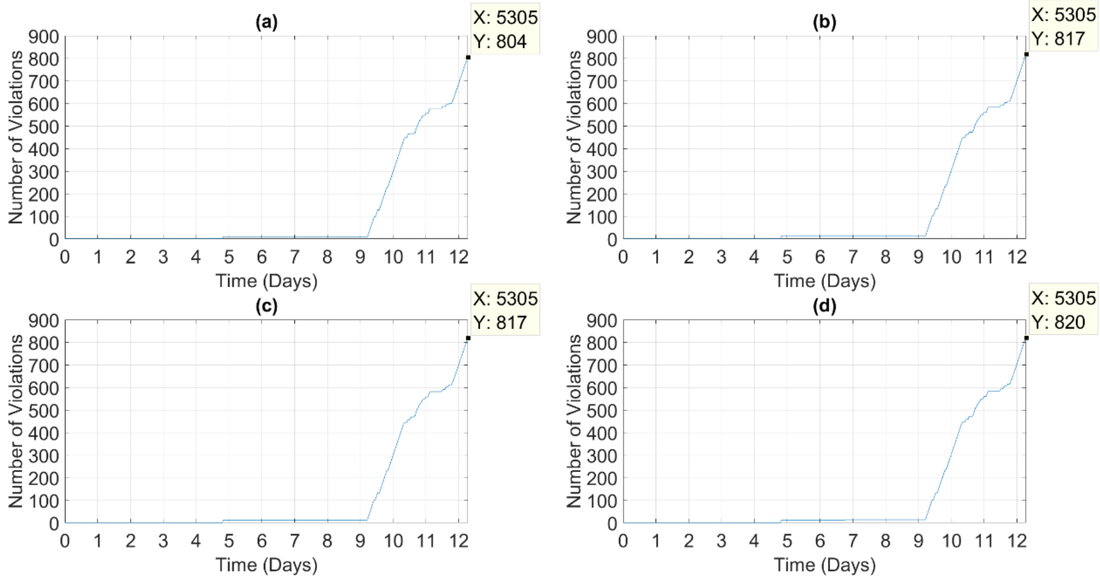

Figure 144 - Effect of changing smoothing factor 'a' on the sensitivity of the tailed EWMA charts with stationary limits : (a) Smoothing factor 'a' 0.2, (b) Smoothing factor 'a' 0.4, (c) Smoothing factos 'a' 0.6 and (d) Smoothing factor 'a' 0.8.

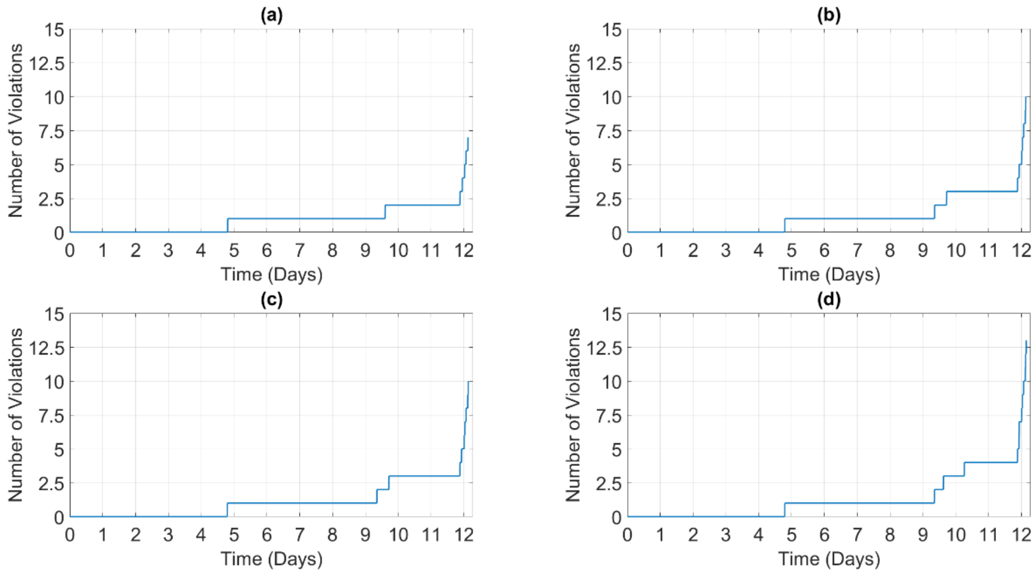

Figure 145 - Effect of changing smoothing factor 'a' on the sensitivity of the tailed EWMA charts with changing limits : (a) Smoothing factor 'a' 0.2, (b) Smoothing factor 'a' 0.4, (c) Smoothing factos 'a' 0.6 and (d) Smoothing factor 'a' 0.8.

As seen in Figure 144 where the limits are stationary, the effect of changing the smoothing factor is negligible when considered as a percentage of the total violation detected. Figure 145 however displays a significant increase in the temperature violations detected as a percentage between the 0.2 ‘a’ and 0.8 ‘a’ cumulative violation sums. It was therefore agreed that in each case, a larger value of ‘a’ was more appropriate for violation detection.

5.5 Application of developed techniques to a series of data gathered

In order to determine the accuracy of the developed techniques, the two data sets which have accurate corresponding wear data (Figure 78, Page 103 and Figure 107, Page 130) were used. To note, the un-sampled data sets were chosen to be used in the following study in order to replicate the real-world scenario with regards to data volume. The four sets of parameters which were used consisted of:

a) Tailored EWMA charts with stationary calculated control limits, smooth factor ‘a’ of 0.8 and a training period of 64000 data points.
b) Tailored EWMA charts with changing calculated control limits, smooth factor ‘a’ of 0.8 and a training period of 64000 data points.
c) Tailored EWMA charts with rolling control limits, smooth factor ‘a’ of 0.8 and a training period of 4000 data points.

The data from each of the sample combinations for both tests are presented in terms of the cumulative sum of violations against the wear depth of the sample under consideration (Figures 150 – 159). In turn, the decision logic of the algorithm is discussed in order to give the reader an understanding of how the final version of the algorithm is envisaged to operate.

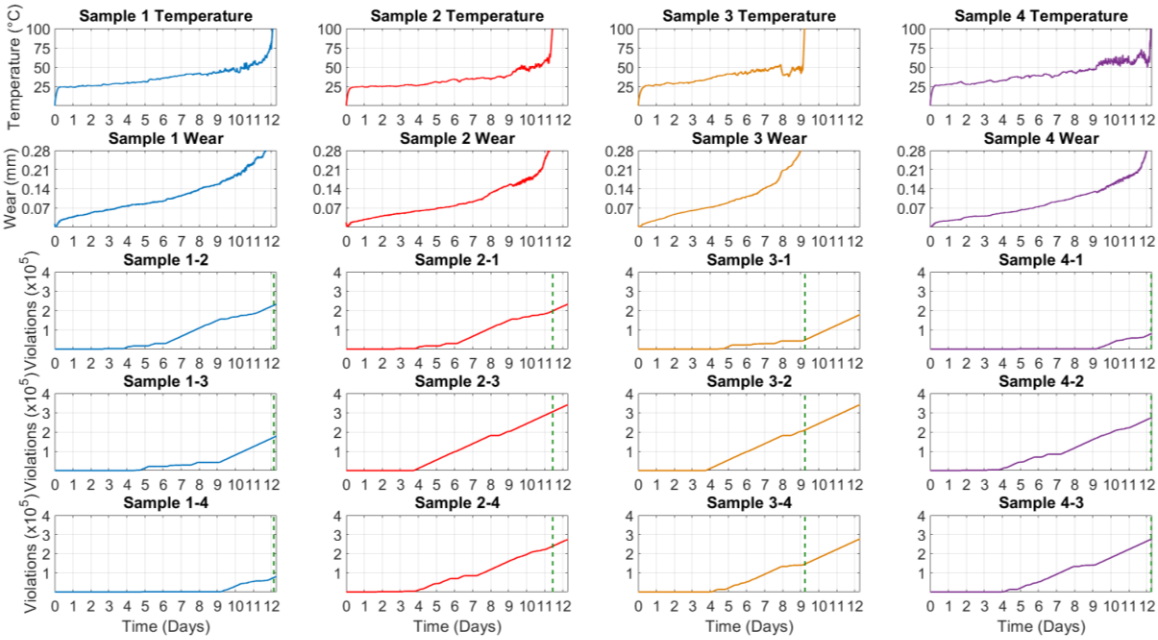

*Figure 146 – Test 3: a) Tailored EWMA chart results **with stationary limits** in terms of violations compared to temperature and wear of each sample. The dashed green line represents the end of the test of the specific sample under consideration.*

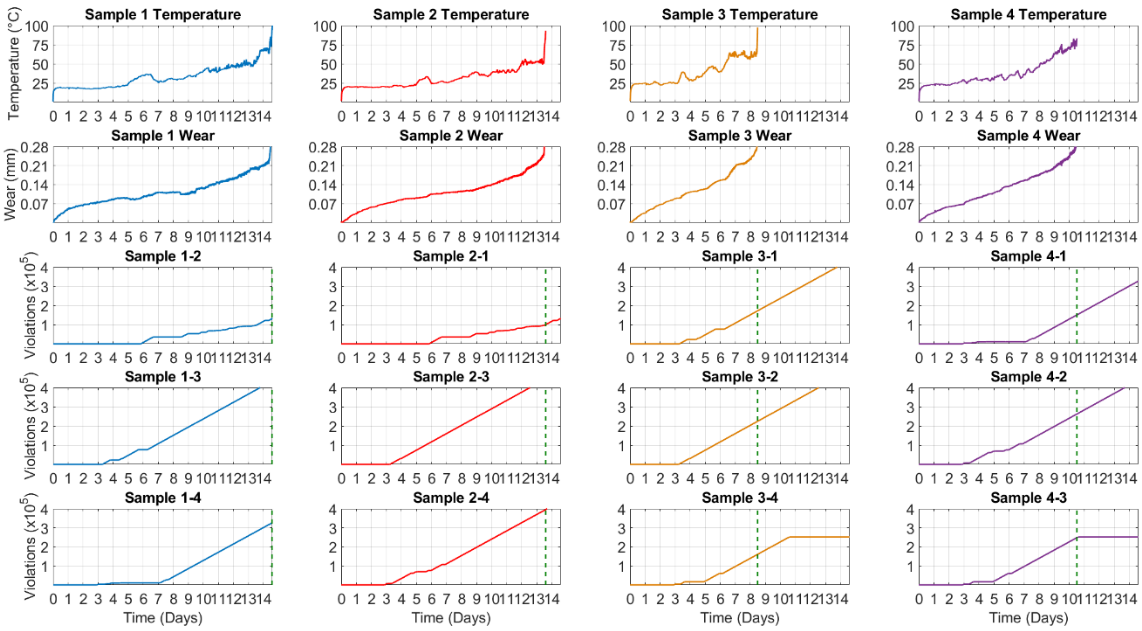

*Figure 147 - Test 4: a) Tailored EWMA chart results **with stationary limits** in terms of violations compared to temperature and wear of each sample. The dashed green line represents the end of the test of the specific sample under consideration.*

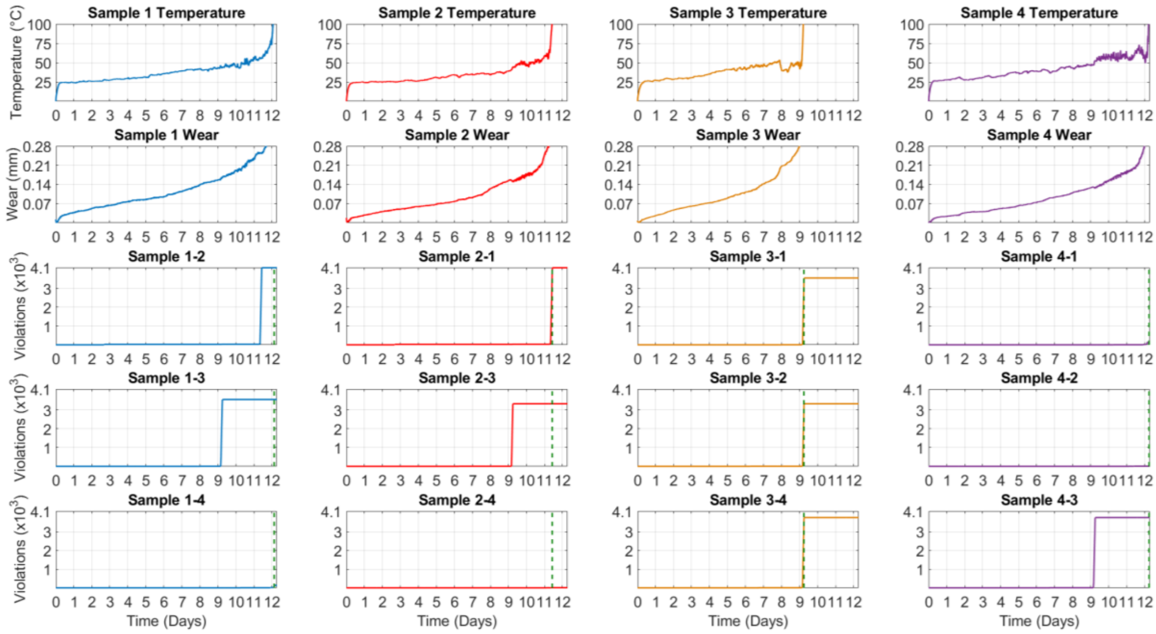

Figure 148 - Test 3: b) Tailored EWMA chart results ***with changing limits*** *in terms of violations compared to temperature and wear of each sample. The dashed green line represents the end of the test of the specific sample under consideration. Large Scale.*

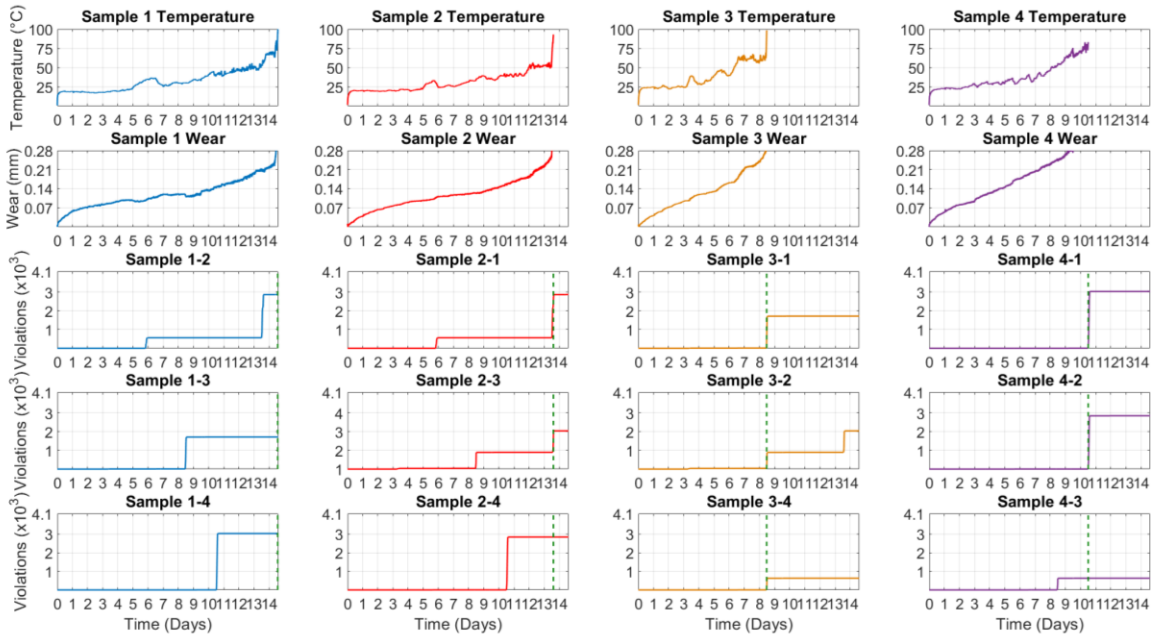

Figure 149 - Test 4: b) Tailored EWMA chart results ***with changing limits*** *in terms of violations compared to temperature and wear of each sample. The dashed green line represents the end of the test of the specific sample under consideration. Large Scale.*

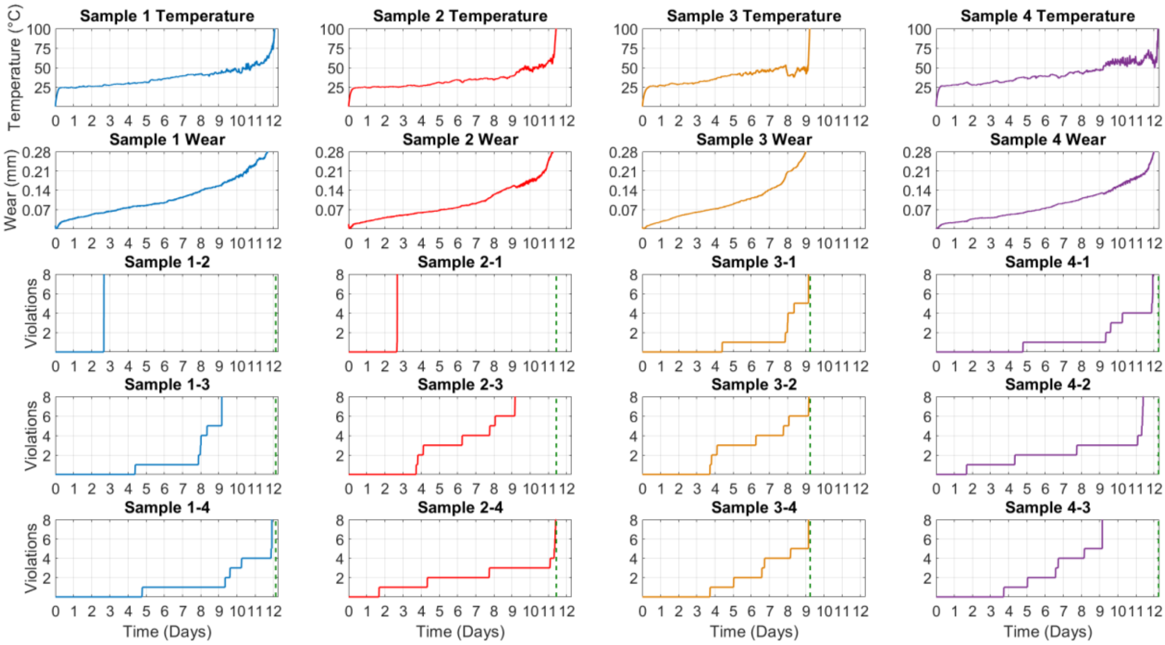

*Figure 150 - Test 3: b) Tailored EWMA chart results **with changing limits** in terms of violations compared to temperature and wear of each sample. The dashed green line represents the end of the test of the specific sample under consideration. Small Scale.*

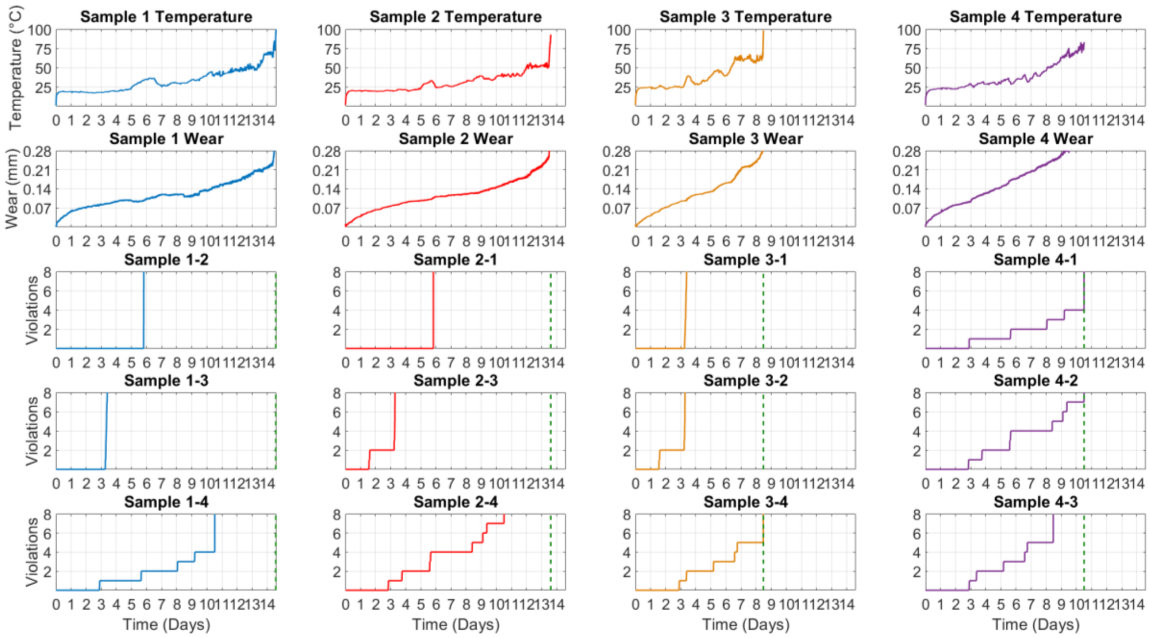

*Figure 151 - Test 4: b) Tailored EWMA chart results **with changing limits** in terms of violations compared to temperature and wear of each sample. The dashed green line represents the end of the test of the specific sample under consideration. Small Scale.*

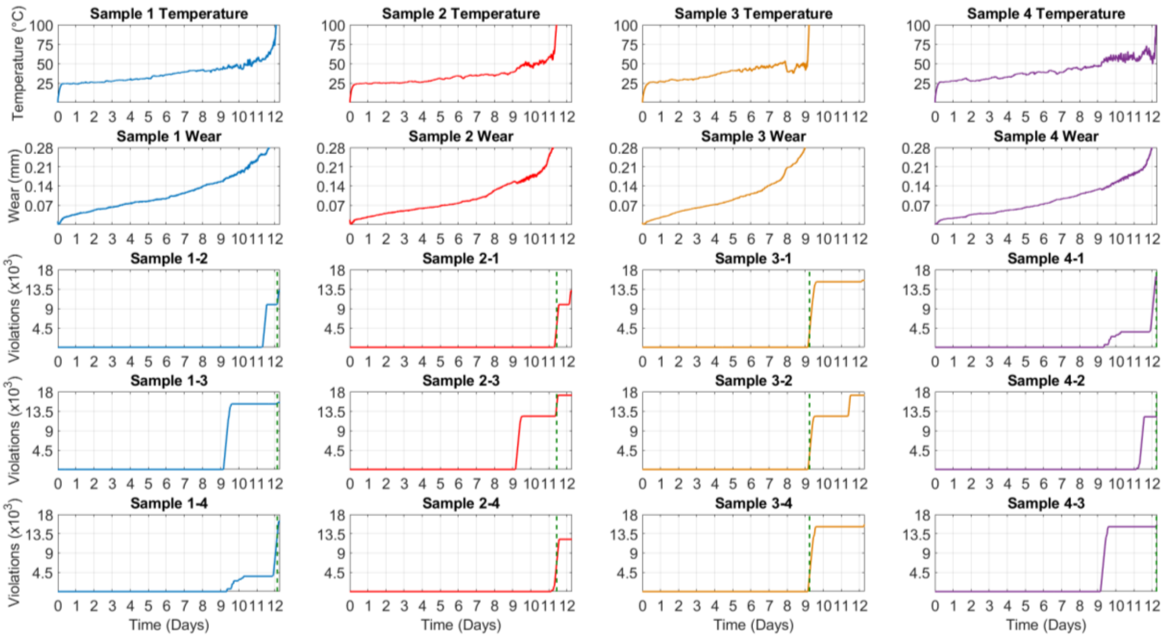

Figure 152 - Test 3: c) Tailored EWMA chart results ***with rolling changing limits*** *in terms of violations compared to temperature and wear of each sample. The dashed green line represents the end of the test of the specific sample under consideration. Large Scale.*

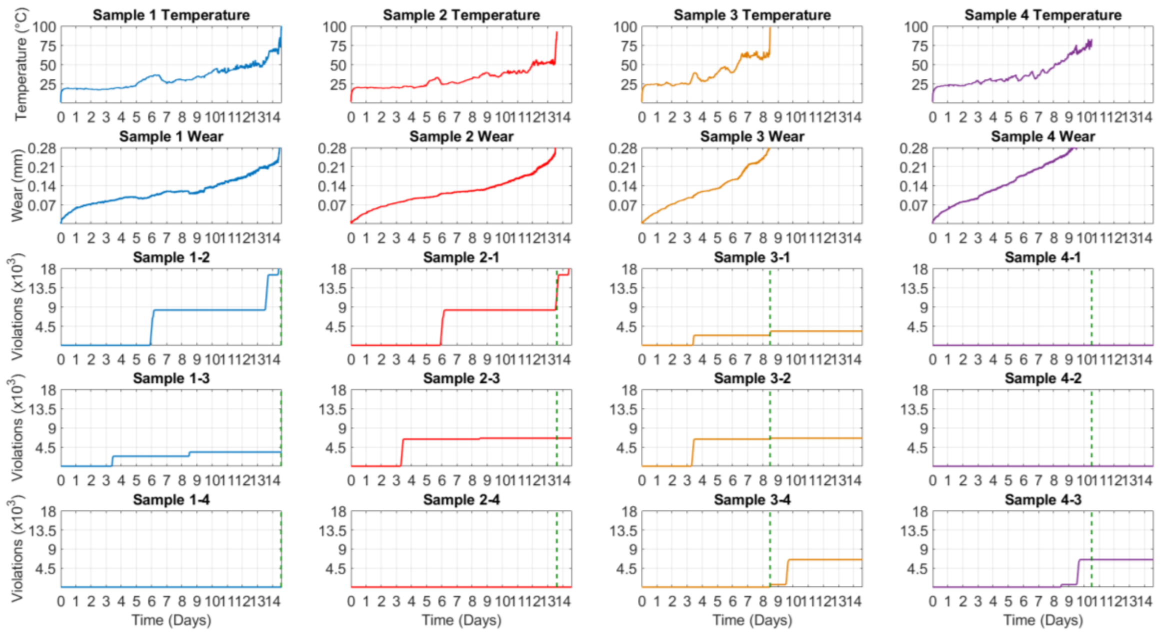

Figure 153 - Test 4: c) Tailored EWMA chart results ***with rolling changing limits*** *in terms of violations compared to temperature and wear of each sample. The dashed green line represents the end of the test of the specific sample under consideration. Large Scale.*

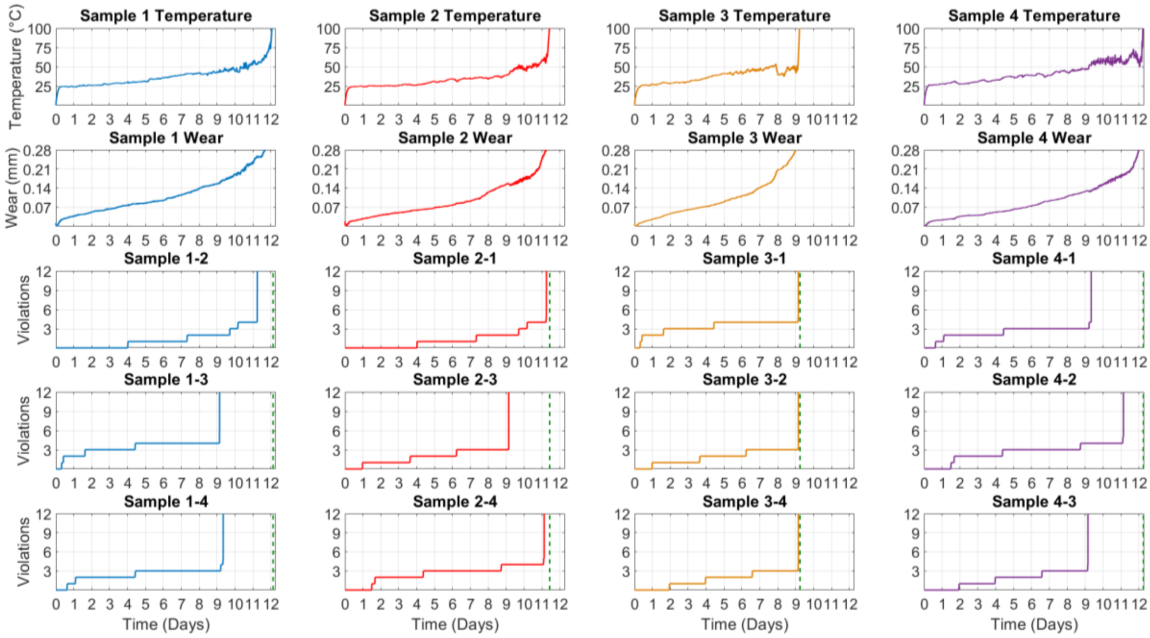

Figure 154 - Test 3: c) Tailored EWMA chart results ***with rolling changing limits*** *in terms of violations compared to temperature and wear of each sample. The dashed green line represents the end of the test of the specific sample under consideration. Small Scale.*

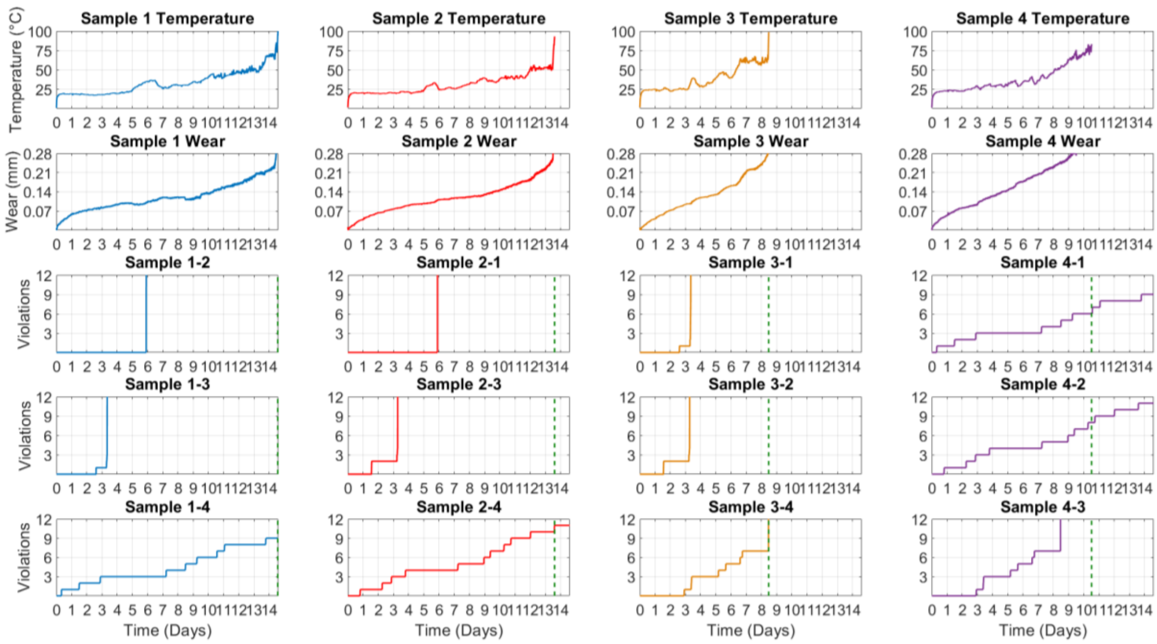

Figure 155 - Test 4: c) Tailored EWMA chart results ***with rolling changing limits*** *in terms of violations compared to temperature and wear of each sample. The dashed green line represents the end of the test of the specific sample under consideration. Small Scale.*

5.5.1 Tailored EWMA charts with stationary calculated control limits – Results discussion

Figures 150 - 159 show the results for each method that the algorithm can utilise, in order to produce an output in terms of violations. In order to understand how the above graphs can be used to detect damage, the real-life application must be considered. In flight, the code is envisaged to create a warning signal to the pilot when a pitch control bearing has shown a deviation from all of its mating pairs. After the warning signal, the bearing should be inspected and if the wear appears to be approaching its replacement criteria a new bearing would be fitted in place of the damaged one. Unfortunately this was not able to be done and during each test, all the samples ran until failure. Although this may seem appropriate, in terms of the algorithm development and damage detection of each sample in laboratory conditions, as soon as one bearing liner sample fails, the remaining pairs are left with one less possible comparison.

In order to explain the logic behind the algorithm's envisaged operations, the data sets of the stationary window EWMA control charts were considered (Figure 146 &
Figure 147). For this type of chart, a significant deviation was said to occur once 1000 residual temperature data points consecutively breached the control limits set.

Within the first set of data which represented Test 3 (Figure 146), it can be seen that sample 2 was first to deviate away from all three of its mating pairs. Collective deviations occur at day 3.97. At the time of deviation the wear depth of the bearing liner was 0.059mm. Further, samples 1-3-4 were only able to be compared with each other and shortly after the deviation of sample 2, sample 3 had failed at a time of 5.02 days and a corresponding wear depth of 0.091mm. In a real application, samples 1 and 4 would still have a complete set of temperature comparison as the bearings would have been replaced and operating at the same environmental conditions but during the experiment only one comparison between the two remaining samples was possible. This results in a deviation being detected by the two samples but the sample responsible for such deviation cannot be identified. It can be seen that the final alarm for the mating pair was given at day 9.52 with a corresponding wear depth of 0.138mm for sample 4 and 0.175mm for sample 1. It is therefore seen that within this dataset, the algorithm was able to identify the two prematurely failed bearings prior to large temperature deviations occurring.

In order to see if these results translated to a secondary dataset, test 4 was analysed using the algorithm and the results can be seen in

Figure 147. The first sample to be flagged in this instance was sample 3 at day 3.53 with a corresponding wear depth of 0.1069mm, followed by sample 2 at day 6.17 with a corresponding wear depth of 0.1120mm. The final comparing pair deviated at day 7.36 with sample 1 wear of 0.1164mm and sample 4 wear of 0.1634mm. Table 6 allows the reader to view these results with respect to the current replacement criteria used by helicopter operators (0.12mm) and to also view the algorithm's efficiency in detecting premature failures.

Table 6 - Detection results from tailored EWMA control charts with stationary limits.

Sample Number	Time of Failure (Data Point)	Time of Failure (Days)	Wear Depth (mm)	Detection Order	Failure Order	Wear Past Replacement Criteria (mm)
Test 3						
1	4.113	9.52	0.175	3	3	0.055
2	1.713	3.97	0.059	1	2	-0.061
3	2.167	5.02	0.091	2	1	-0.029
4	4.113	9.52	0.138	3	4	0.018
Test 4						
1	3.178	7.36	0.1164	3	4	-0.0036
2	2.667	6.17	0.1120	2	3	-0.008
3	1.523	3.53	0.1069	1	1	-0.0131
4	3.178	7.36	0.1634	3	2	0.0434

Table 6 shows that, with the data available, this type of control chart was able to predict both premature failing bearing liner in each test successfully. In test 3, the order in which these were detected was reversed but detection occurred at very similar times. Although a few of the wear depths at the time of alarm were above the replacement criteria, the magnitude by which the criteria were exceeded was deemed by the industrial supervisors not to be of concern. The main anomaly detected from these results, was the wear depths of sample 2 – test 3 and sample 2 – test 4. As both of these were detected very early on in the wear life of the bearing, in a real application the aircraft would have had to undergo an inspection interval which would not find significant signs of damage. In order to avoid such an early detection, further work is required into tailoring the control limit parameters to provide the correct sensitivity for the algorithm. Further datasets, when available, are also required to be used with this method in order to increase the confidence of the presented results.

5.5.2 Tailored EWMA charts with changing calculated control limits - Results discussion

The second technique which was utilised consisted of the recalculation of control limits once a violation had occurred (Figures 152 – 155). The effect of such a corrective technique, can be seen in the scale of the cumulative violations. Due to its recalculating nature the number of violations which can occur prior to failure can only be allowed to reach a maximum threshold value with single figures. Unfortunately using this type of technique a distinct threshold value could not be determined. For the purpose of the analysis a threshold value of 2 allowed recalculations, therefore 3 violations, was chosen. The results are presented in Table 7.

Table 7 - Detection results from tailored EWMA control charts with changing calculated limits.

Sample Number	Data Point of Failure ($x10^5$)	Time of Failure (Days)	Wear Depth (mm)	Detection Order	Failure Order	Wear Past Replacement Criteria (mm)
Test 3						
1	3.453	7.99	0.1388	2	4	0.0188
2	3.447	7.98	0.1233	1	2	0.0033
3	3.453	7.99	0.2061	2	1	0.0861
4	4.154	9.62	0.1386	3	3	0.0186
Test 4						
1	3.478	8.05	0.1185	3	4	-0.0015
2	2.412	5.58	0.1010	2	3	-0.019
3	2.235	5.27	0.1335	1	1	0.0135
4	3.478	8.05	0.1756	3	2	0.0556

Through the use of this method, the bearing liner failure order was able to be predicted correctly for test 4 but unfortunately the effect was not the same for test 3. The incorrect premature detection of the failure of sample 1 altered the order at which these samples were predicted to fail. A positive result from this technique was the wear depth at the time of detection. Excluding sample 3 from test 3 and sample 4 from test 4, all of the detected samples had a wear depth which was very close to the replacement criteria of the pitch control bearings. The wear depth of sample 4 – test 4 is not an issue due to its remaining life of 0.0844mm but sample 3 – test 3 at the time of detection is close to metal to metal failure with only 0.0539mm of wear left in the bearing liner. To note, past the region of 0.15-0.18mm wear, the glass fibre rich region comes into sliding contact which causes a rapid stage of wear.

Although correct detection was exhibited in most cases, this technique is not preferred due to the low violation threshold of 2, which is required to brand the comparing sample as 'deviating'. A concern is raised due to the possibility of one of the bearings being subjected to environmental noise during or prior to operation (direct sunlight on one of the bearings for example) which might cause the threshold of 2 violations to be overcome. To further develop this technique, once again, a larger number of complete data sets are required to allow the algorithm's behaviour to be completely understood.

5.5.3 Tailored EWMA charts with rolling limits – Results discussion

The final technique utilised a recalculation of its control limits by including all prior data points to the occurring violation (Figures 156 – 159). Due to the similarity of the techniques, the same threshold value of 2 violations was applied in order to flag a deviation. The results are presented in Table 8.

Table 8 - Detection results from tailored EWMA control charts with rolling changing calculated limits.

Sample Number	Data Point of Failure ($x10^5$)	Time of Failure (Days)	Wear Depth (mm)	Detection Order	Failure Order	Wear Past Replacement Criteria (mm)
Test 3						
1	4.195	9.71	0.1767	3	4	0.0567
2	4.195	9.71	0.1643	3	2	0.0443
3	2.693	6.23	0.1140	1	1	-0.006
4	2.864	6.86	0.0880	2	3	-0.032
Test 4						
1	2.555	5.92	0.0944	2	4	-0.0256
2	2.555	5.92	0.1011	2	3	-0.0189
3	1.47	3.40	0.0948	1	1	-0.0252
4	1.47	3.40	0.1054	1	2	-0.0146

Through the use of this technique, the premature failing bearing liner (Sample 3 in both cases) was able to be detected first. Once again the algorithm produced a false prediction as seen by the outputs of sample 2 of test 3 where its flag time was the same as sample 1 and above sample 4. The wear depths at the time of detection are very similar to each other and also to the replacement criteria with only exception being sample 1 of test 3. Even at the wear of 0.1767mm exhibited by sample 1 at the point of detection, a remaining useable life of 0.0833mm is available for the bearing liner before failure.

5.6 Conclusion

In order to detect damage within a bearing liner in a system of bearings, a method whereby statistical process control charts can be utilised was investigated. These charts utilise upper and lower control limits with set parameters and are able to detect deviations past these set thresholds. The data points at which these thresholds were exceeded were recorded and accumulated to allow the inspection of the time and wear depth of each sample at the point of significant violation occurrence. The control limits set by the operator, were applied using theory already existent within industry. Although the results produced were deemed satisfactory for a feasibility study, further work is required in order to increase the confidence in their results. Further, the point at which a flag is set also requires future work. Currently a value of 1000 consecutive points was used for the stationary limit charts and a recalculation/violation allowance of 2 was given to the changing control limit charts. These values were coarsely picked in order to view the feasibility of the control chart system and should be further investigated.

Although there are many ways of which the control chart algorithm can be improved, the results produced from the two data sets provided, were said to be successful. Through the use of all three techniques, all of the wear depths at the point of flagging averaged a value of 0.1265mm with a standard deviation value of ±0.035mm which is very close to the 0.12mm replacement criterion imposed by the helicopter maintenance teams. It was therefore deemed a successful feasibility study, notwithstanding the recommended further work.

Chapter 6: Temperature cross-sample correlation, volatility & recovery investigation.

6.1 Temperature cross-sample correlation theory

Having extensively studied the patterns displayed by the temperature coupon data sets, it was clear that all of the data followed a specific trend consistent with existing knowledge of the wear behaviour of similar self-lubricating materials. This typical behaviour may be seen in Figure 156. It consists of a wear-in period which is relatively aggressive until the third-body transfer layer, along with conformity of the bearing sliding surfaces is achieved, followed by a region of steady wear rate (the plateau) and finally the failure period which consists of a generally aggressive and unpredictable wear behaviour (Evans, 1981).

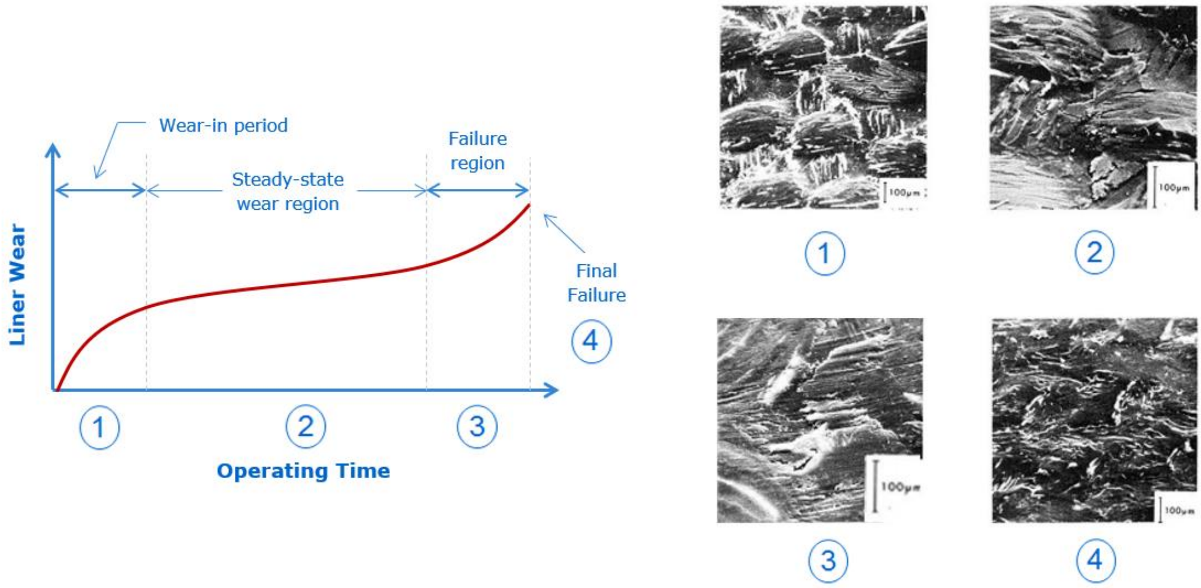

Figure 156 - Schematic of the self-lubricating material wear process (left) and SEM images from literature, representing wear periods (right (Lancaster, et al., 1980)).

It was noticed that the temperature exhibits interesting patterns when the bearing is coming to the end of its life and is transitioning to the glass fibre backing region of the composite liner, before reaching metal to metal contact and therefore failing. Due to the linear nature of the plateau region, a simple comparison between the temperature data sets would allow the output of a numerical value which will compare the two data sets, until the point of deviation.

Having the concept in mind, the next step was to produce an algorithm which will signal damage via a single numerical measure of similarity. To achieve this, the data generated from the laboratory coupon test was plotted and in turn investigated further. Figure 157 shows the temperature trends of two Samples, 1 and 4.

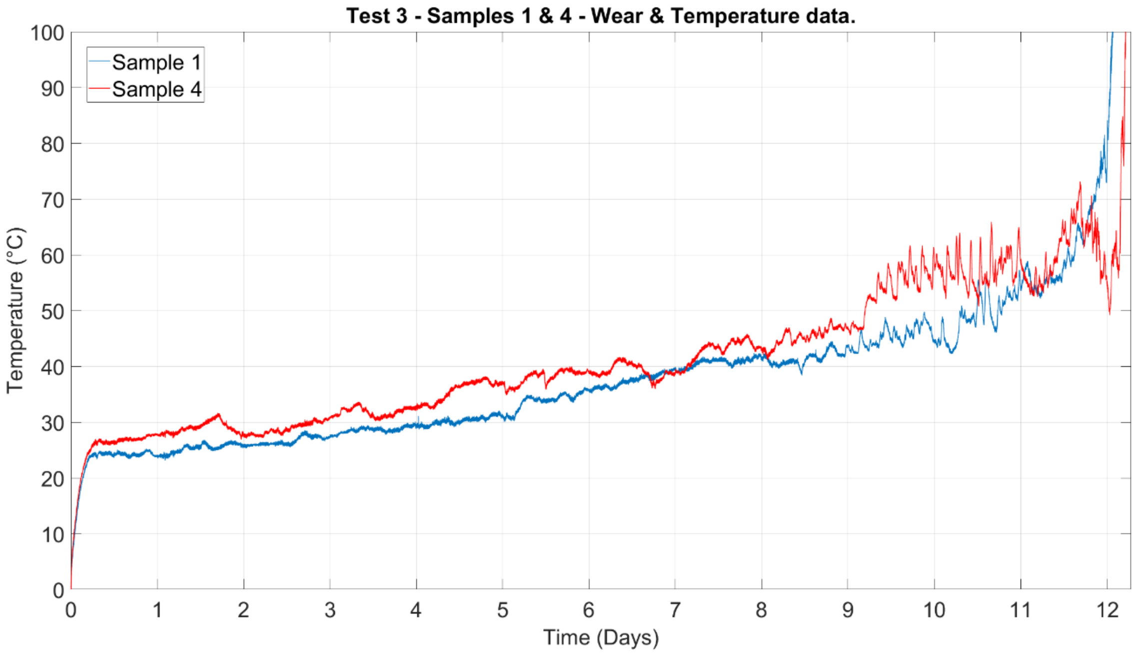

Figure 157 - Temperatures of Sample 1 and Sample 4 plotted vs Time.

By studying Figure 157, it can be seen that both temperatures, under identical testing conditions, exhibit very similar trends until day 10 of the experiment was reached. At this point, the temperatures appear to follow different patterns. Evaluating the data further, it was proposed that the relationship between the two temperatures shown in Figure 157 can be expressed via a single output consisting of the correlation coefficient between the two data sets. This coefficient will in turn be compared to the other bearing liner sample pairs and if it undergoes a significant drop, a flag will be given for that specific bearing pair. Once all three pairs with containing a common sample have been flagged, the bearing liner sample is assumed to be damaged.

By definition, correlation is described as a statistical technique which is used to measure and describe the strength and direction of the relationship between two variables (Shevlyakov & Oja, 2016). The correlation between two variables is measured by the correlation coefficient which is a single value used to quantify the relationship. For the purpose of this study the Pearson product-moment correlation coefficient (ρ) was used, which varies in value from $-1 < \rho < 1$, 1 describing a strong positive correlation, 0 being no correlation and -1 a strong negative correlation.

Before proceeding with the creation of a MatLab code to perform this type of analysis, a simple plot between the two variables was created in order to see if any type of visual relationship exists between temperature signals from two bearings. The plot between the two variables shown in Figure 158 was divided into three ranges relating to the wear depth values corresponding to depths where the liner material undergoes a composition change. These ranges consisted of 0.00mm to 0.15mm, marked in blue, which related to the PTFE rich sliding surface of the liner (the actual region is between 0.15-0.18mm but for the purpose of this test the lower value was chosen). The wear depth between 0.15mm - 0.25mm is represented as the green values and this region is the glass fibre rich structural backing of the liner and finally, marked in red, is the breakdown of the transfer film and the end-of-life metal to metal contact achieved between 0.25mm - 0.30mm.

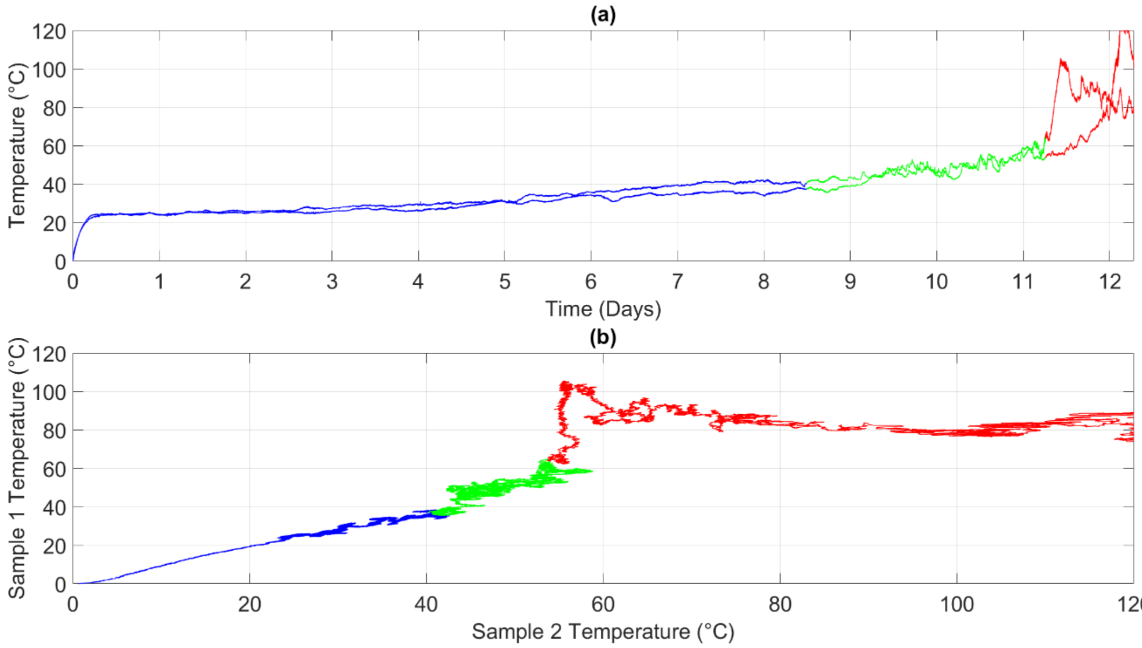

Figure 158 - (a) Representation of temperature data split, (b) Relationship between Sample 1 and Sample 4 temperature data.

It can be seen within Figure 158 that when no damage has occurred in either of the components under test, a very strong positive correlation exists between the two parameters and as the damage becomes greater the correlation between the components starts to reduce in amplitude. It is assumed that an ideal result which represents a pair of undamaged bearings would consist of a straight line, i.e. a slope of unity. Intuitively, this method was of great interest and gave confidence to proceed to develop the Matlab script. The script was designed to take two sets of data and output the Pearson product-moment correlation coefficient (ρ). The coefficient itself can be calculated between two data sets by the following equation (Brookes, 2014):

$$Corr(X, Y) = \frac{Cov(X,Y)}{Std(X) \cdot Std(Y)} \tag{12}$$

Equation (12) states that the Pearson product-moment correlation coefficient is equal to the covariance of X and Y, where X and Y represent the two data sets under test, divided by the product of the standard deviations of X and Y. Further, the covariance between X and Y can be described as:

$$Cov(X,Y) = \sum_{i=1}^{N} \frac{(x_i - \overline{x}) \cdot (y_i - \overline{y})}{N} \tag{13}$$

Where $\overline{x}$ and $\overline{y}$ represent the mean value of X and Y respectively. To simplify further, the standard deviation of X can be written as:

$$Std(X) = \sqrt{\frac{\sum(x_i - \overline{x})^2}{n-1}} \tag{14}$$

Where x_i is the current value under test and $\overline{x}$ is the mean value of X within a data set of n values. The standard deviation of Y can be calculated by replacing x_i and $\overline{x}$ with y_i and $\overline{y}$ respectively. Therefore by combining equations (12), (13) and (14) the correlation coefficient can be represented in its simplest format, as shown in equation (15):

$$corr(X,Y) = \frac{[(x_i - \overline{x}) \cdot (y_i - \overline{y})]}{\sqrt{\frac{\Sigma(x_i - \overline{x})^2}{n-1}} \cdot \sqrt{\frac{\Sigma(y_i - \overline{y})^2}{n-1}}} \tag{15}$$

6.1.1 Preliminary investigation

This investigation was conducted in order to develop a damage detection method, achieving a single output of the Pearson correlation coefficient, for a complete data set would not allow for the onset of damage to be shown. Therefore a technique where coefficients are calculated for sub-sets of data within the originals was created. The method starting by calculating the correlation of data sets containing just points 0 and 1, and then proceeding to the next data sub-set of points 0 to 2, and so on, each time increasing the size of the sub-set by 1 and calculating a new coefficient. The coefficients were in turn plotted against time and a curve was created which would potentially indicate when damage occurred by a decreased Pearson correlation coefficient value since the two data sets would be deviating at that point. Some preliminary results are shown in Figure 159.

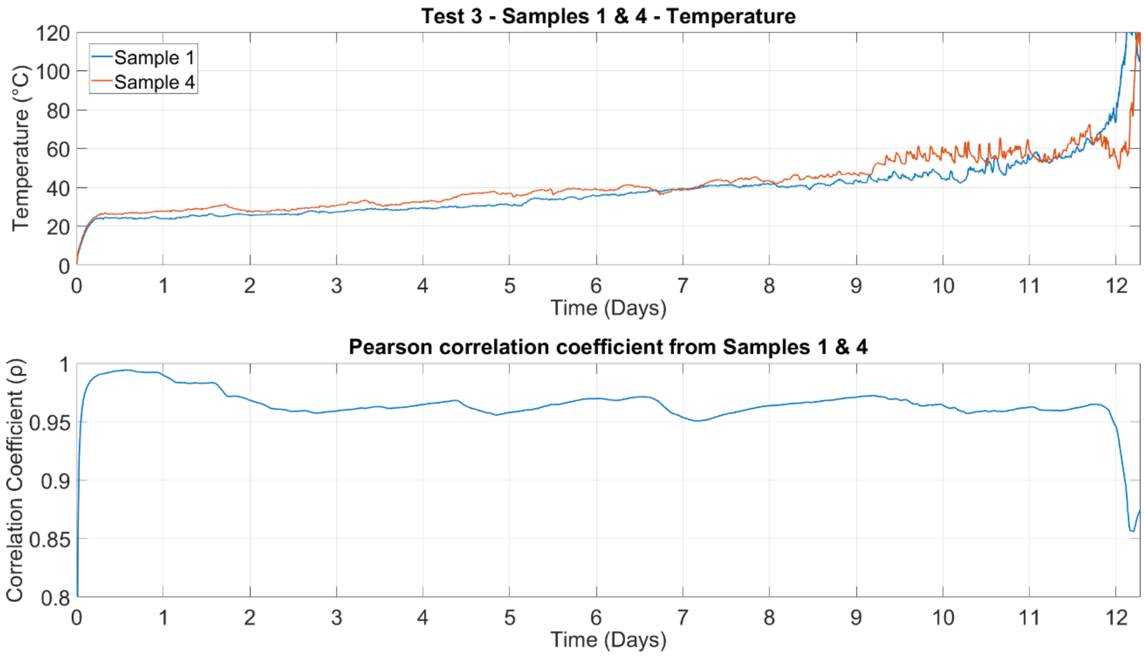

Figure 159 - Sample 1 vs Sample 4 temperatures vs Time & Correlation Coefficient vs Time.

It can be seen in Figure 159 that the temperature deviation of Sample 4 from Sample 1 is detected by the correlation coefficient, but there is a problem with the time of detection. Ideally the coefficient curve needs to be sensitive enough to allow for detection at the point of initial separation on day 9.2, but this is not the case. A small reduction of some 0.02 in the correlation coefficient can be seen but the significant decrease does not occur until the point of critical damage, which in the case of condition monitoring is of no use. The reason behind this late signs of damage, is the amount of data being considered when the initial damage point is reached. The correlation coefficient at the point of damage is predominantly determined by the previous data and therefore the value at the initial point of separation had very little influence towards the determination of the Pearson coefficient. To investigate how this technique behaves with a premature bearing failure, sample 1 and sample 3 were investigated (Figure 160).

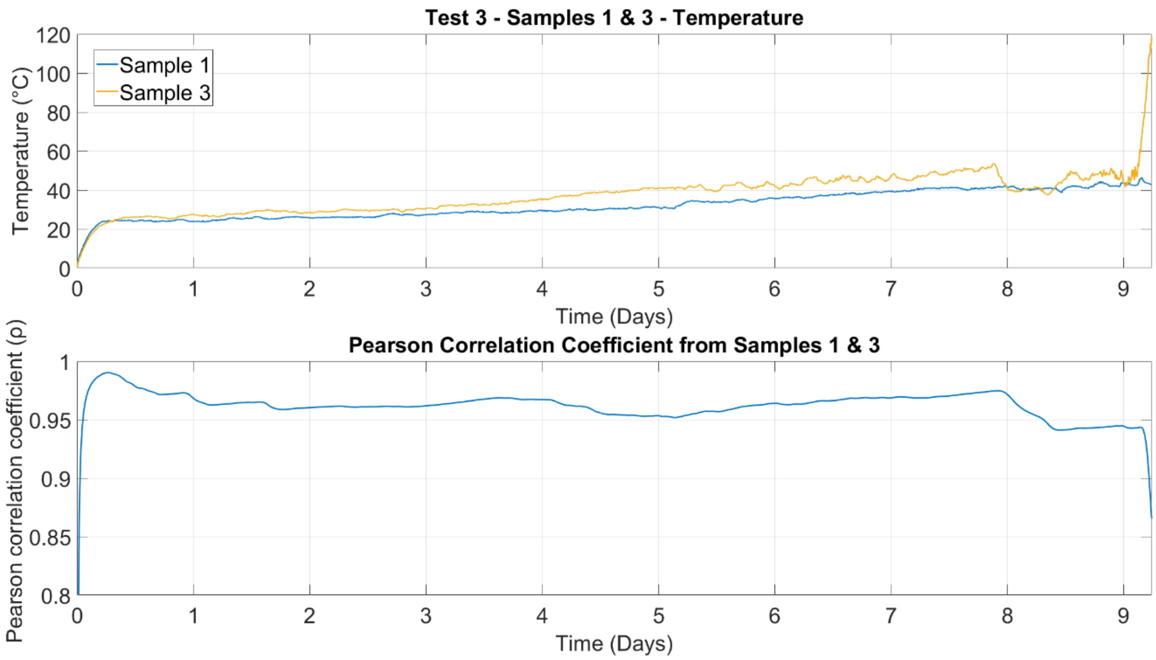

Figure 160 - Sample 1 vs Sample 3 temperatures vs Time & Correlation Coefficient vs Time.

With comparison to the previously discussed control chart techniques, this type of method is able to detect temperature deviations between the two data sets at approximately the same time interval. It is of great importance to capture the start of the temperature deviation at the earliest stage possible and this is achieved by the decreasing correlation coefficient. Furthermore, a second sharp drop in the correlation coefficient indicated the point of critical damage, which is represented in the temperature data set as a drop in the Sample 3 temperature towards the end of day 7.

6.1.2 Effect of window width on results

To allow for a more sensitive approach when determining the time of initial damage, rolling windows of data were used instead of the whole data set up to the current point. Therefore a rolling window of 172800 data points (2 days), was used in order to calculate the coefficient. Referring back to Equation (15), we can see that the number of samples used is now always a steady number of n=172800 and the data used to calculate the correlation coefficient initially consisted of points 1: 172801. After the coefficient is calculated, the MatLab script will pass onto the second window, consisting of the data points 2: 172802 and so on. In this way when the sign of damage is reached, the coefficient will be more sensitive to a change between the two temperatures, indicating the onset of damage. Both samples 1 and 4 and Samples 1 and 3 from the third test were considered (Figure 165 & Figure 166).

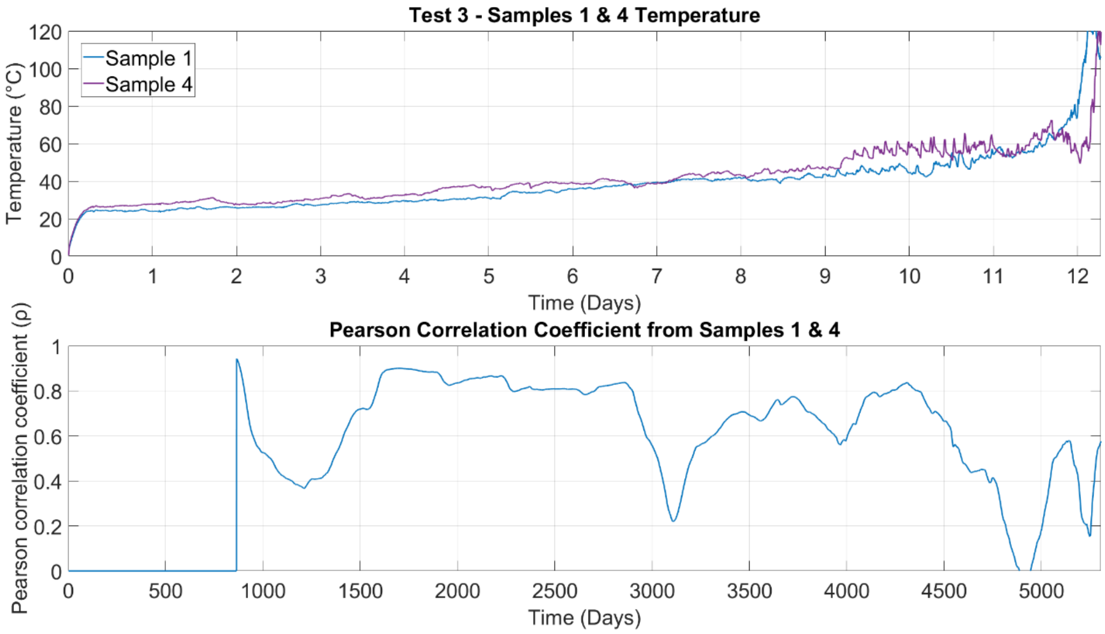

Figure 161 - Sample 1 vs Sample 4 temperatures vs Time & Correlation Coefficient vs Time with a 172800 data point lag (training set)

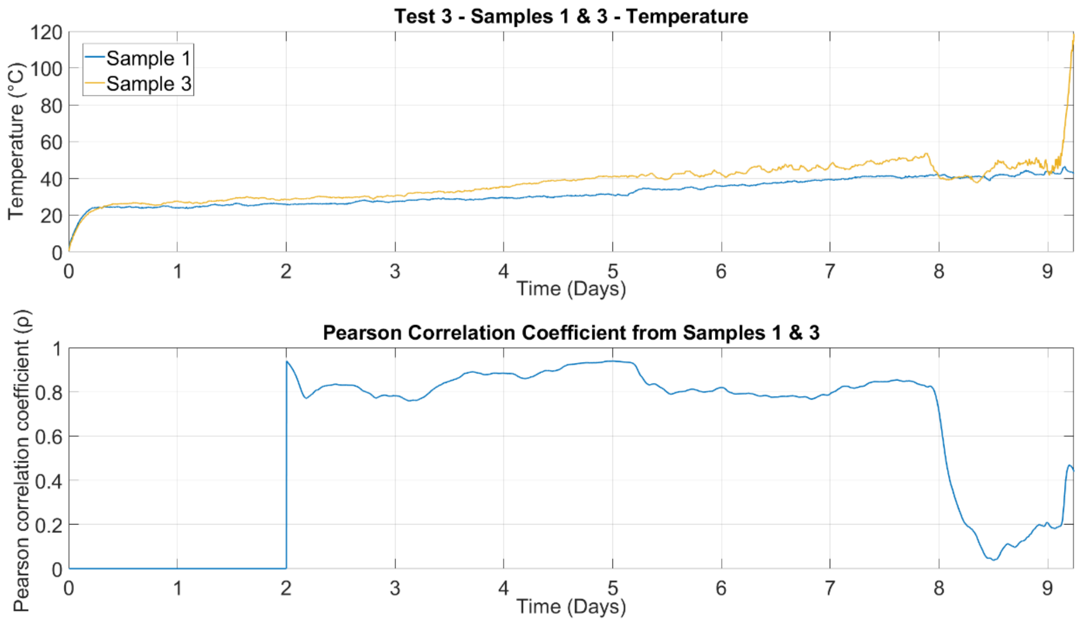

Figure 162 -Sample 1 vs Sample 3 temperatures vs Time & Correlation Coefficient vs Time with a 172800 data point lag (training set)

As seen in Figure 161 and Figure 162, the sensitivity of the code is much more desirable due to its more rapid recognition of signs of damage in relation to time. Further, a study upon the data from samples 1 & 3 of test 3 was conducted, which consisted of three window lengths under investigation of half a day (43200 data points), 1 day (86400) and the already calculated 2 day (172800 data point) training window (Figure 163).

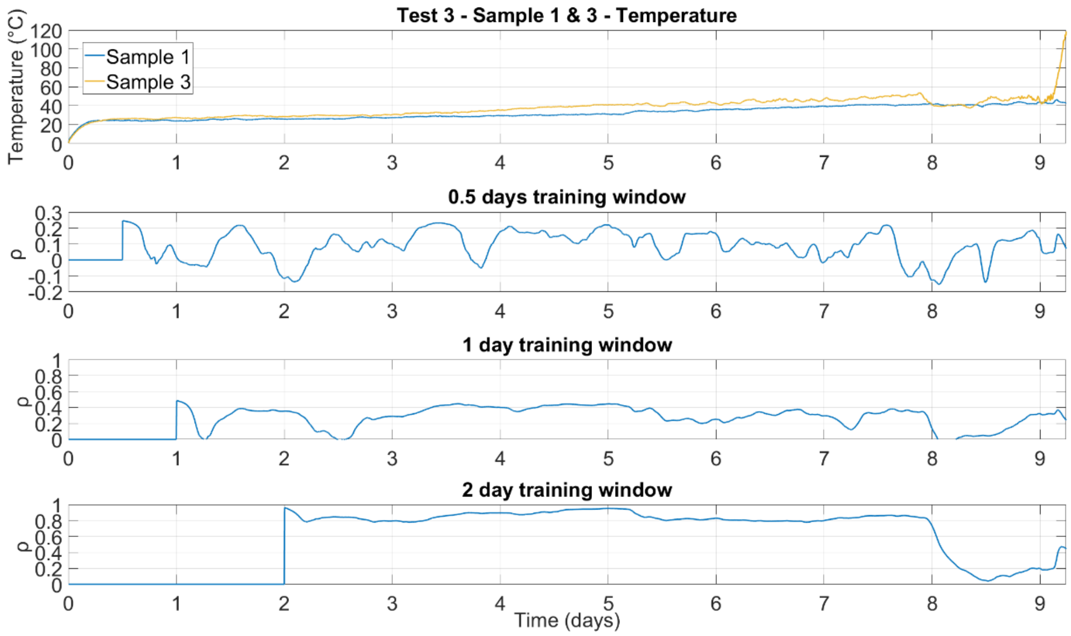

Figure 163 - Effects of training data set length with regards to correlation coefficient sensitivity.

6.1.3 Effect of instrumentation noise on results

Having observed the effect of the window widths with regards to the sensitivity of the code, a set of simulated data was created, in order to eliminate variables such as noise produced by the instrumentation during the data acquisition process. The use of simulated data was to allow a detailed investigation of the response of the Pearson cross-product correlation coefficient to a diverging set of temperature data. An artificial data set with similar data point length to the temperature data of sample 3 – test 3 was generated via a MatLab script to allow for the simulation of a damaged bearing and more specifically the rapid temperature increase as damage occurs, as shown in Figure 164.

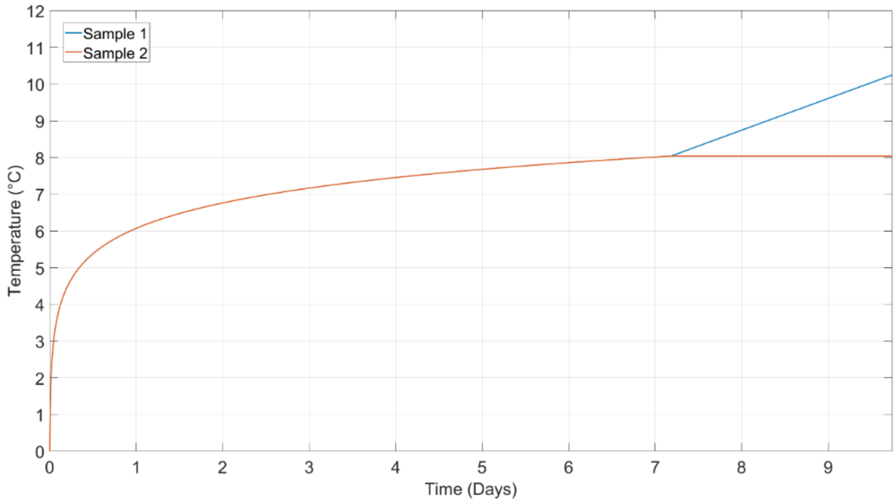

Figure 164 - Simulated results for bearing failure.

This set of data was created to replicate the idealised damage scenario. Initially the temperatures of the two bearings follow an identical curve up to the point of damage at 7.2 days data points for both samples, followed by a distinct increase in temperature for Sample 2, representing a damaged bearing. Three plots were created from these data in order to represent the impact of increasing the training set size with regards to the sensitivity of the code as a whole. They were compared to the non-windowed code as shown within Figure 165.

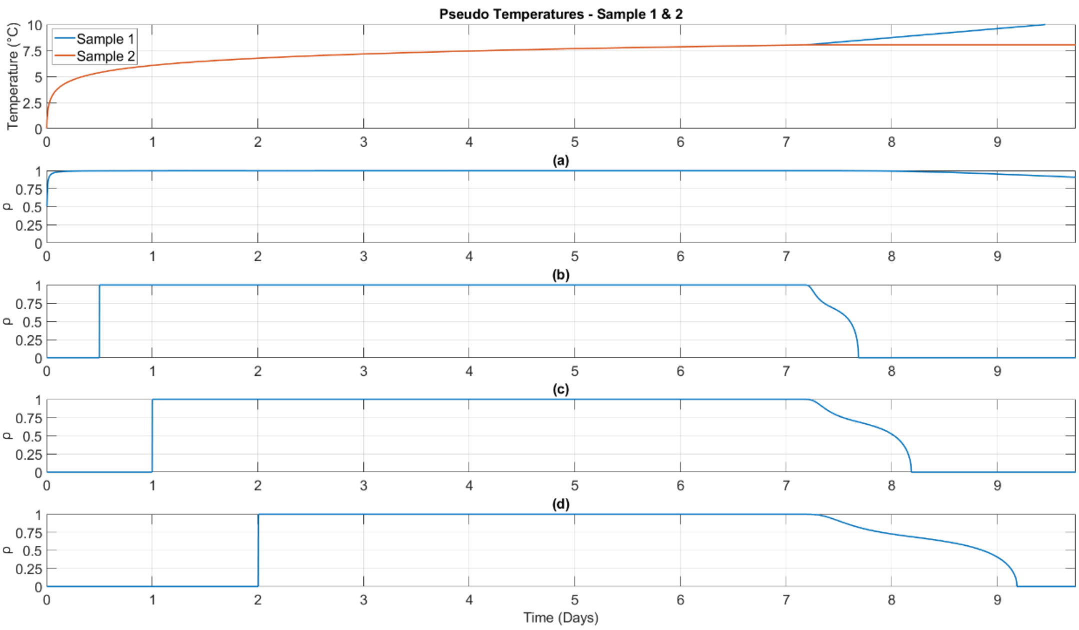

Figure 165 - (a) Expanding window, (b) 43200 (0.5 Days) window, (c) 86400 (1 Day) window, (d) 172800 (2 Days) window.

As it can be seen within Figure 165, the larger the window size, the less sensitive the code will be in terms of damage detection. This is intuitive since with a smaller window of consideration, the sudden increase in temperature will have a greater impact. This can also be seen within the equations discussed in the earlier section, specifically within equation (14) which calculated the standard deviations of the two variables.

The final investigation conducted, was the situation where a bearing is running at a hotter temperature than its pair but it still operating as normal and is in turn subjected to a failure (Figure 166).

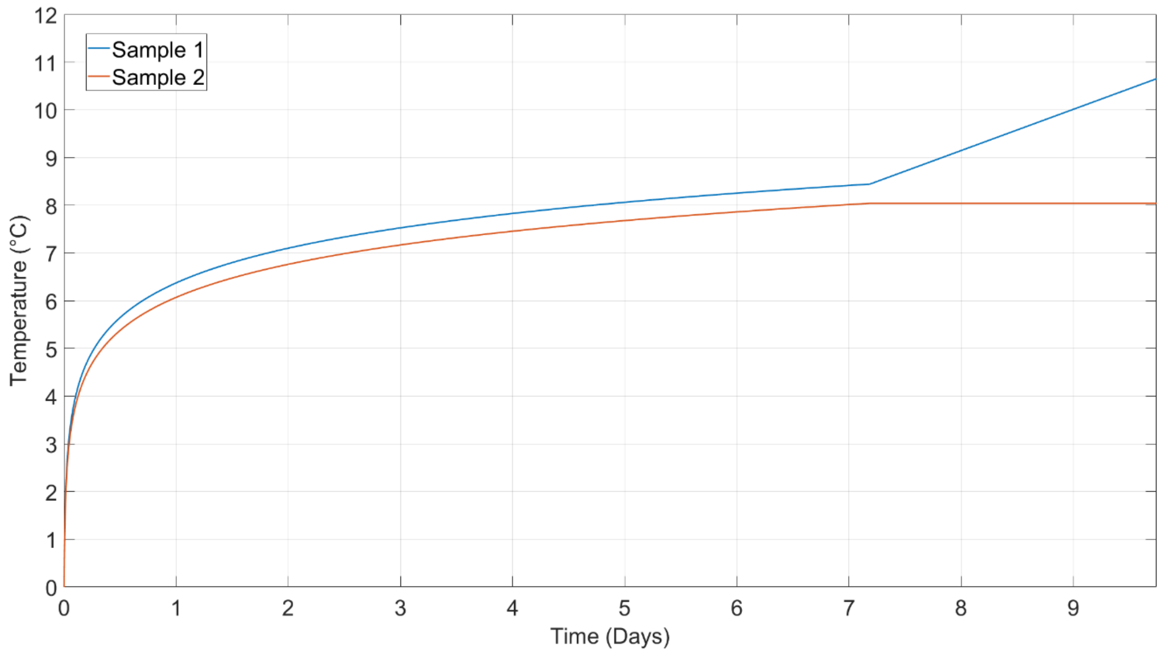

Figure 166 - Simulated results for bearing failure with a temperature offset.

The same window width ranges were in turn applied to the data and the corresponding Pearson correlation coefficients are presented in Figure 167.

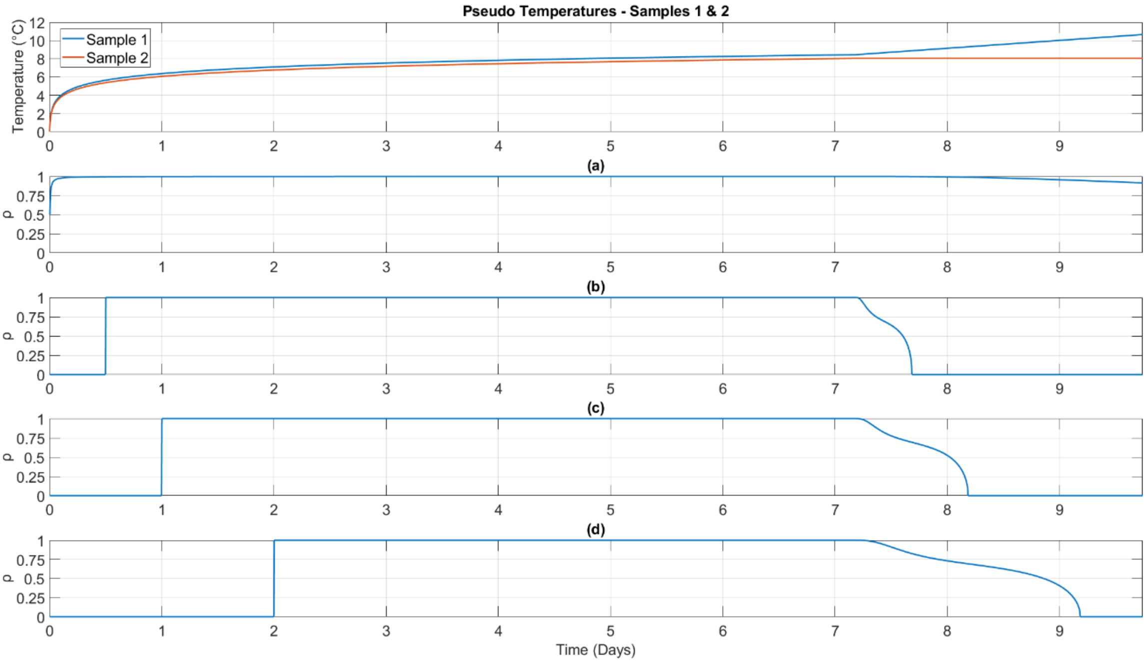

Figure 167 - (a) Expanding window, (b) 43200 (0.5 Days) window, (c) 86400 (1 Day) window, (d) 172800 (2 Days) window.

As it can be seen by comparing Figure 165 and Figure 167, the temperature offset introduced had little to no effect upon the detection of the temperature deviation by the algorithm.

Having established that a small training set is ideal within an ideal data set, in terms of damage detection sensitivity, a pair of simulated temperature datasets were created which included random noise, to aim towards a more realistic scenario. Figure 168 below, shows the idealised temperature data set, and also shows the level of noise applied to the original signal.

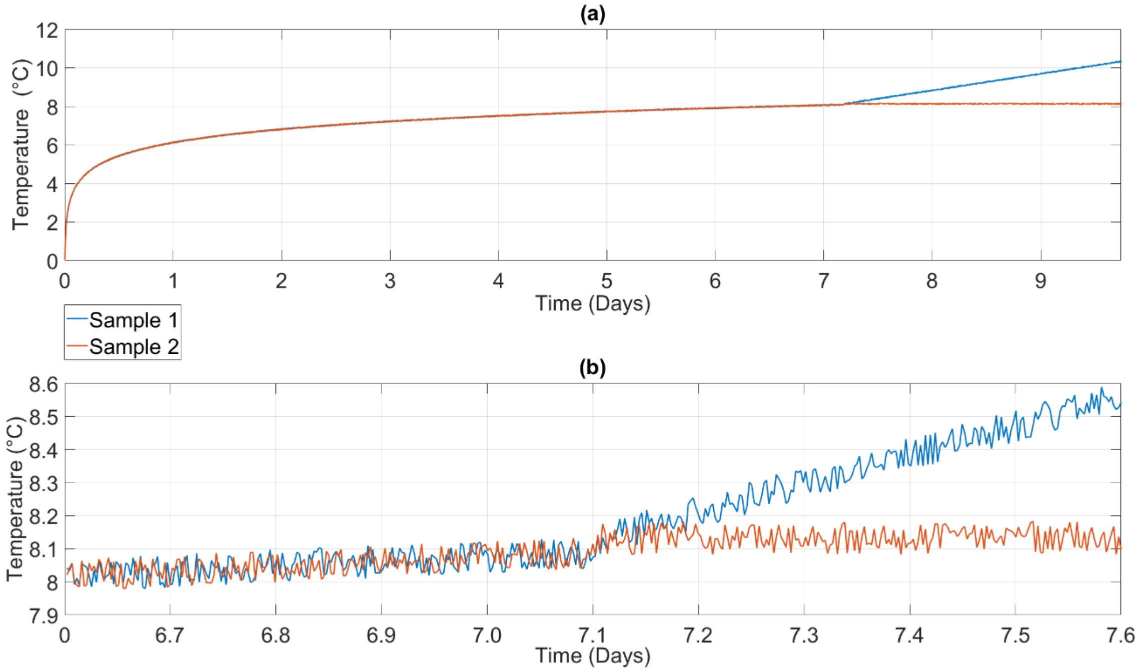

Figure 168 - (a) Ideal curves with noise inclusion, (b) Zoom-in of ±1 day (86000) data points around the separation point to illustrate the incorporated random noise levels.

After the noise was introduced to the original data sets, the same Matlab script was applied to the new signals with the same method as previously shown in Figure 167. The results are shown in Figure 169.

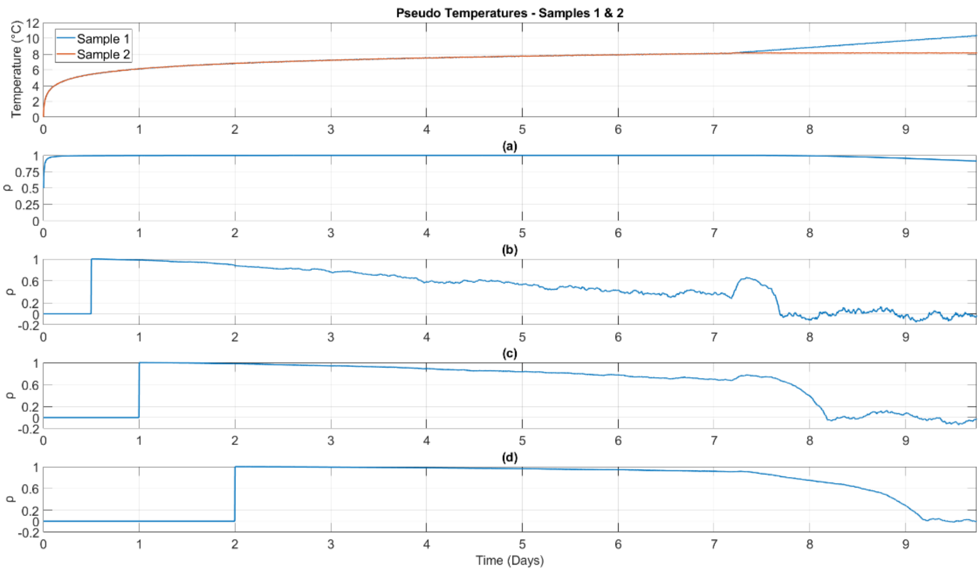

Figure 169 - (a) Expanding window, (b) 43200 (0.5 Days) window, (c) 86400 (1 Day) window, (d) 172800 (2 Days) window.

As observed, the patterns of the correlation coefficients now exhibit a completely different behaviour in terms of sensitivity. Figure 169 shows that the deviation in temperatures from the noise induced dataset was still detected in each base. This can be seen in the sharp rise and in-turn drop of the Pearson correlation coefficient. Also, the correlation coefficient can be seen to slowly approach 0 when a small window width is introduced but the wider windows (a) and (d) provide a certain robustness to this phenomenon. This phenomenon can be explained by considering the effects of the window width in relation to noise. As the noise is a completely random variable applied to an existing signal, as the window width becomes shorter, the randomness of the noise overpowers the pattern of the previously existent signal, circumstances which could be described as a worst case scenario for the type of condition monitoring method proposed. To illustrate this random noise effect, the two sample temperature data 0.5 days prior to the point of separation were plotted against each other (Figure 170).

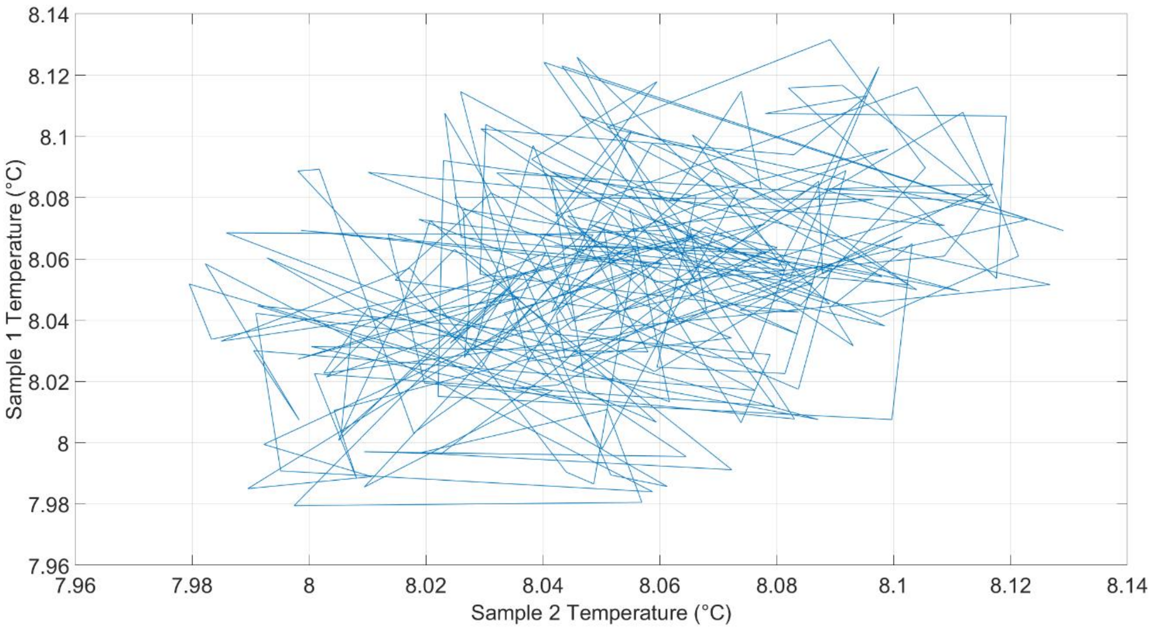

Figure 170 – XY plot of Samples' 1 & 2 Temperatures.

It is believed that the sudden increase in the Pearson correlation coefficient after the point of separation was due to the introduction of some form of pattern after a period of heavy noise.

6.1.4 Application of techniques upon a set of experimental results

Once the affecting parameters had been investigated, the two sets of data, as seen in section 5.2.3, were processed by the algorithm in a similar fashion as previously. The four window widths as seen in Figure 169 were investigated and their outputs graphically represented with corresponding temperature and wear results of the samples under investigation (Figures 175 – 184).

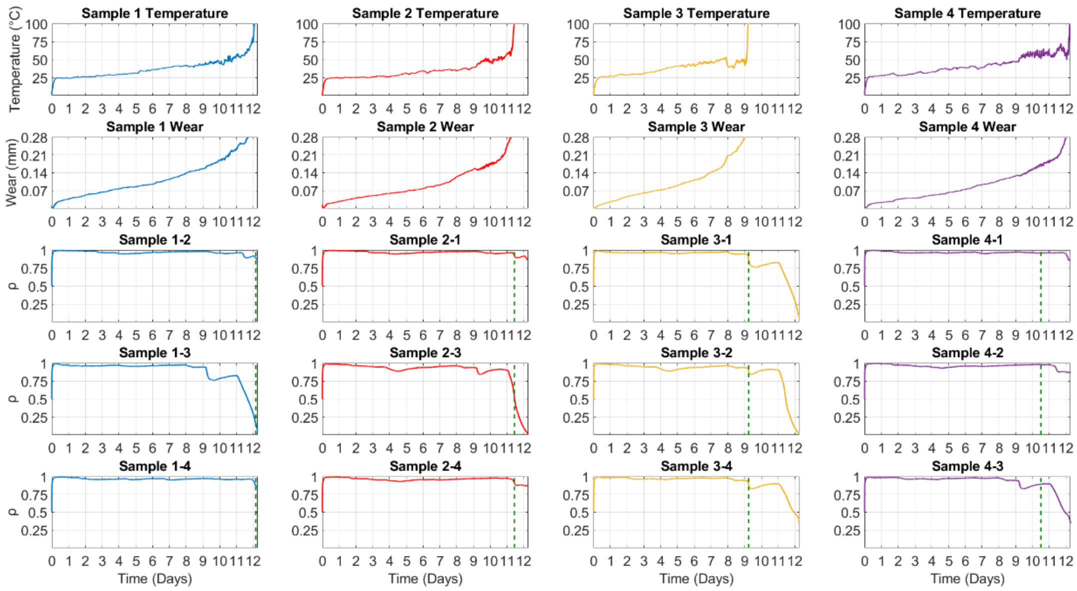

Figure 171 – Test 3 – Samples 1-4: Pearson correlation coefficient results with an expanding window (Large Scale).

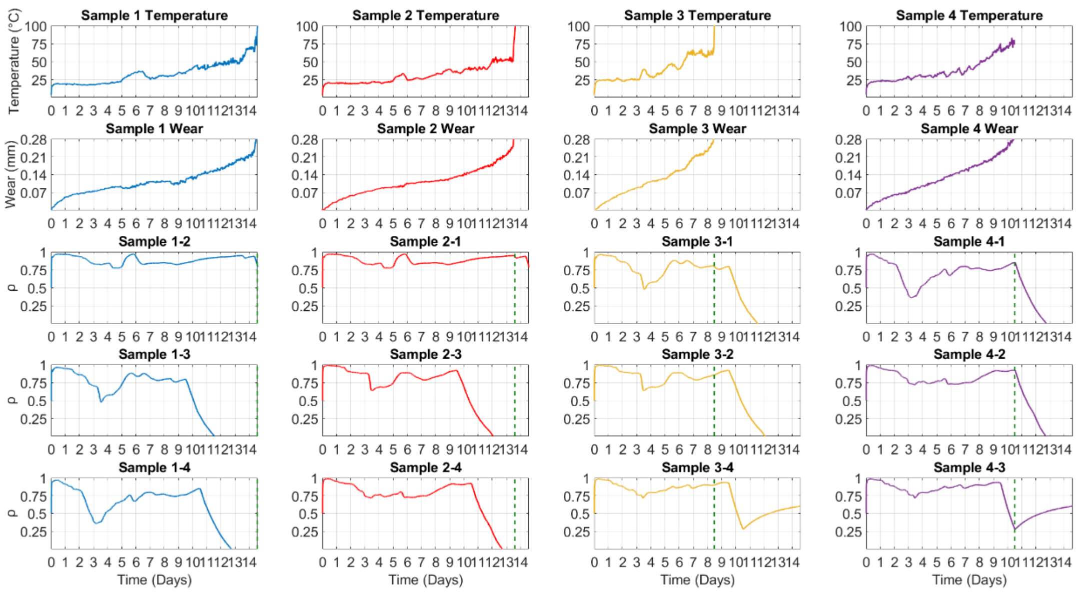

Figure 172 - Test 4 – Samples 1-4: Pearson correlation coefficient results with an expanding window (Large Scale).

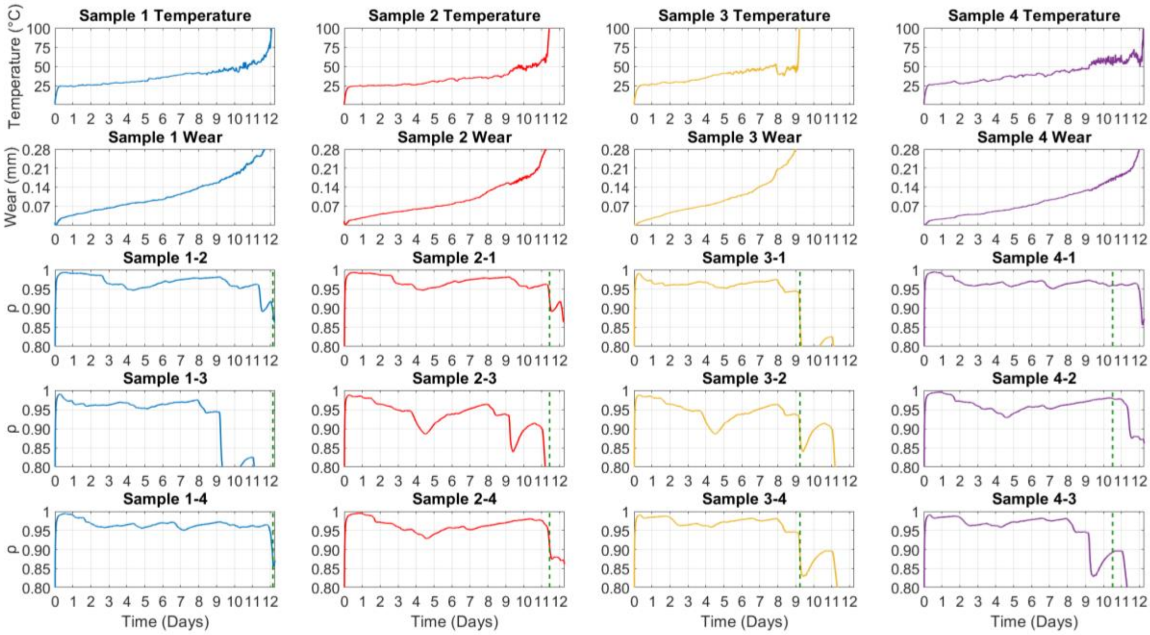

Figure 173 - Test 3 – Samples 1-4: Pearson correlation coefficient results with an expanding window (Small Scale).

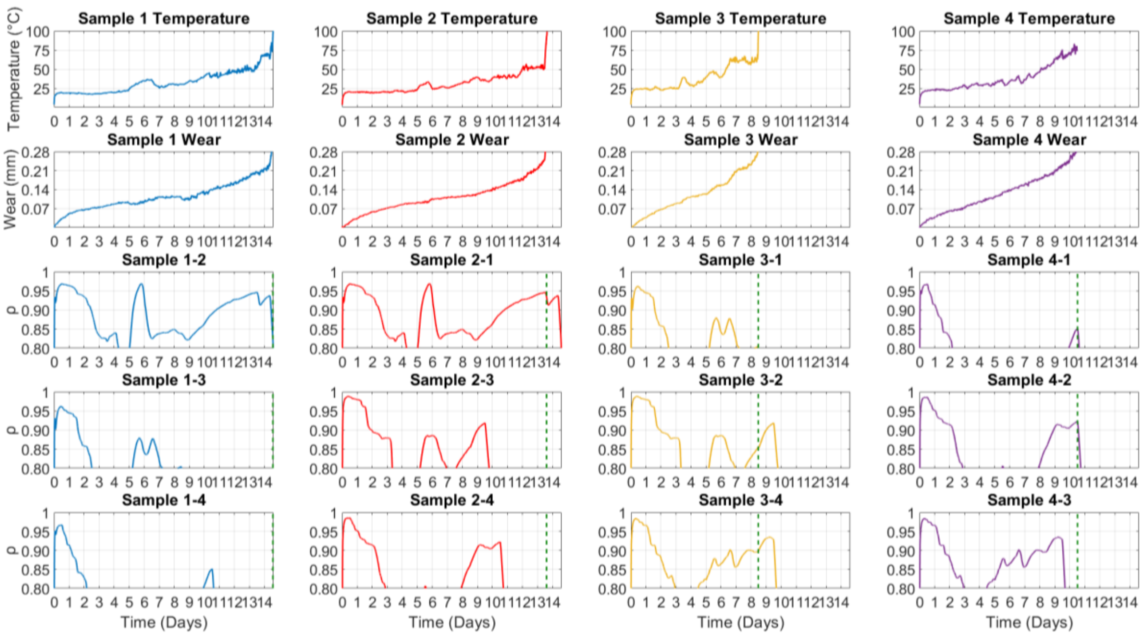

Figure 174 - Test 4 – Samples 1-4: Pearson correlation coefficient results with an expanding window (Small Scale).

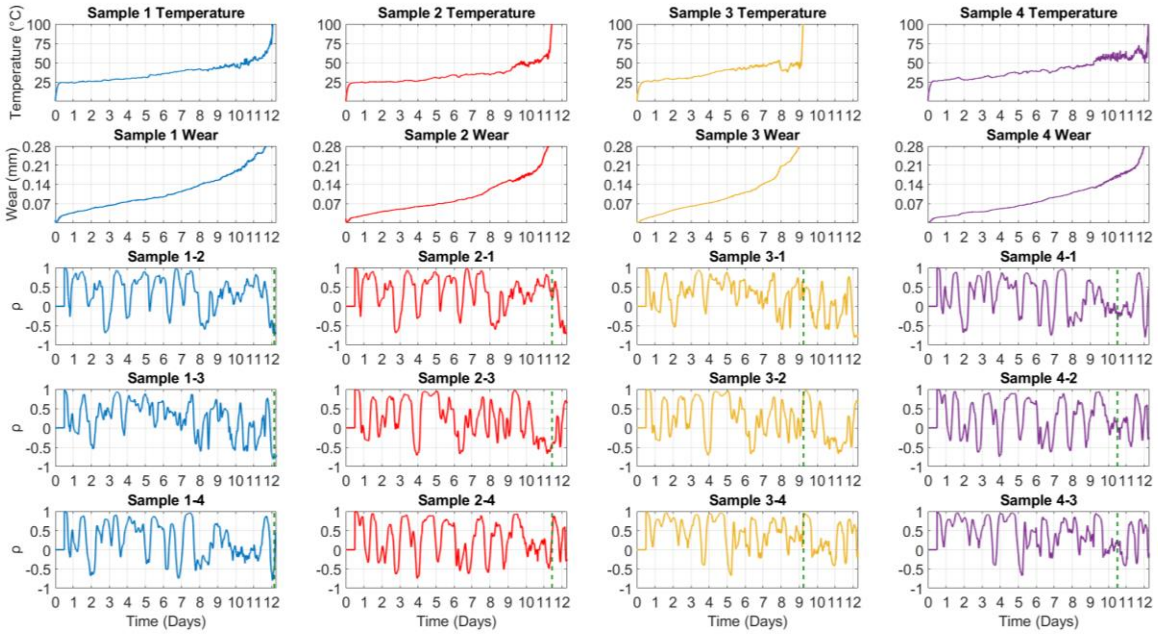

Figure 175 - Test 3 – Samples 1-4: Pearson correlation coefficient results with a rolling training set of 0.5 days (43200 data points).

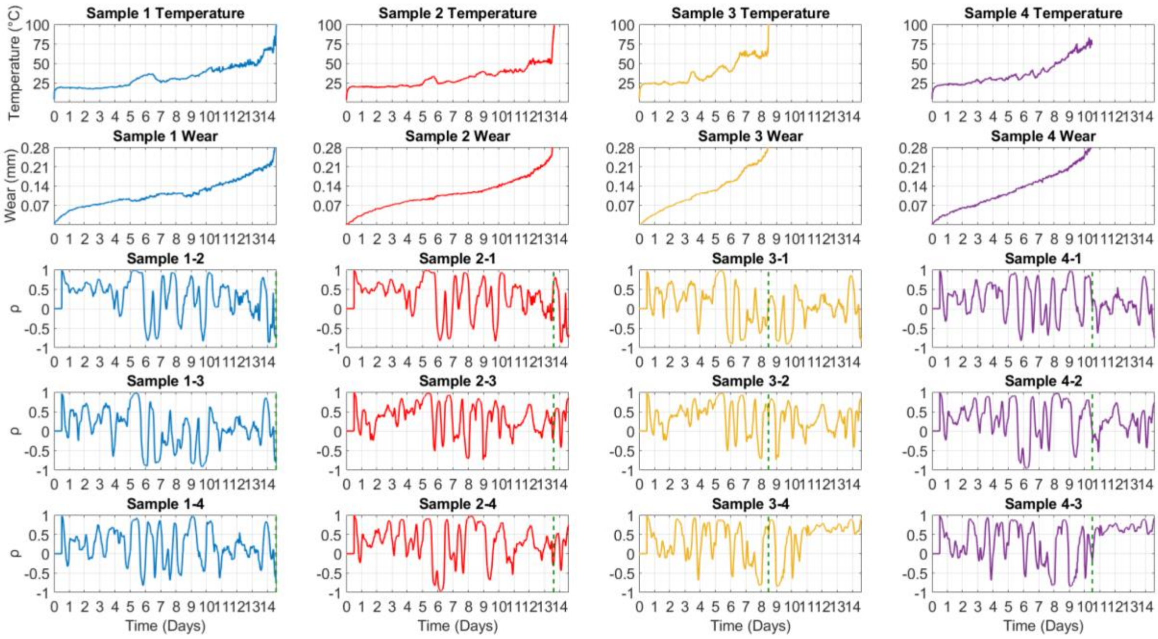

Figure 176 - Test 4 – Samples 1-4: Pearson correlation coefficient results with a rolling training set of 0.5 days (43200 data points).

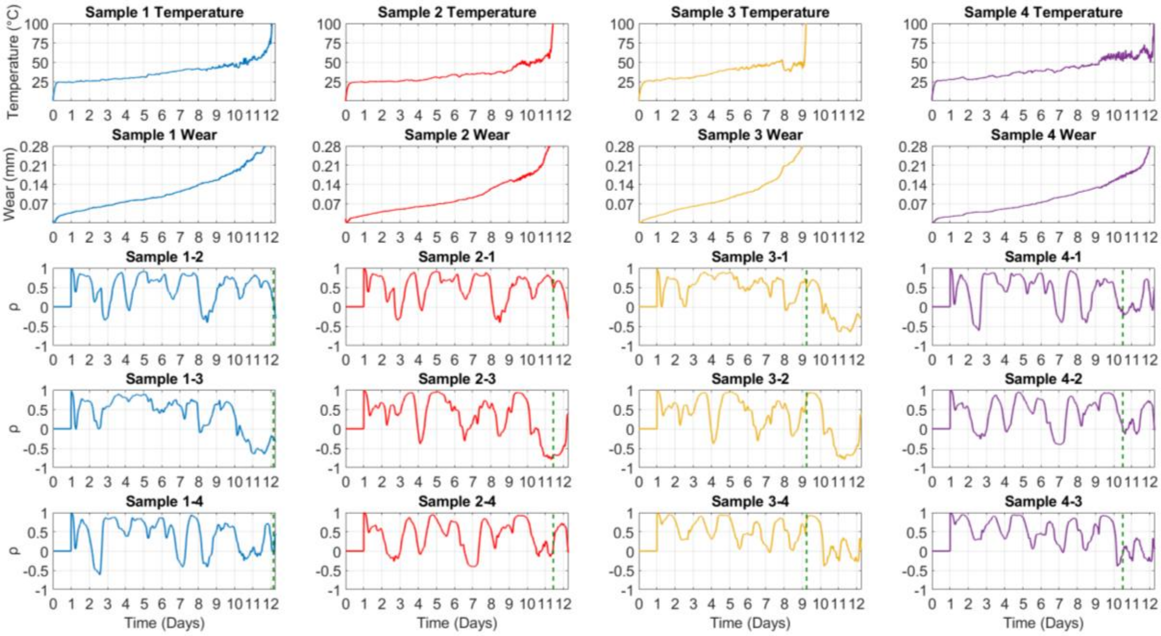

Figure 177 - Test 3 – Samples 1-4: Pearson correlation coefficient results with a rolling training set of 1 day (86400 data points).

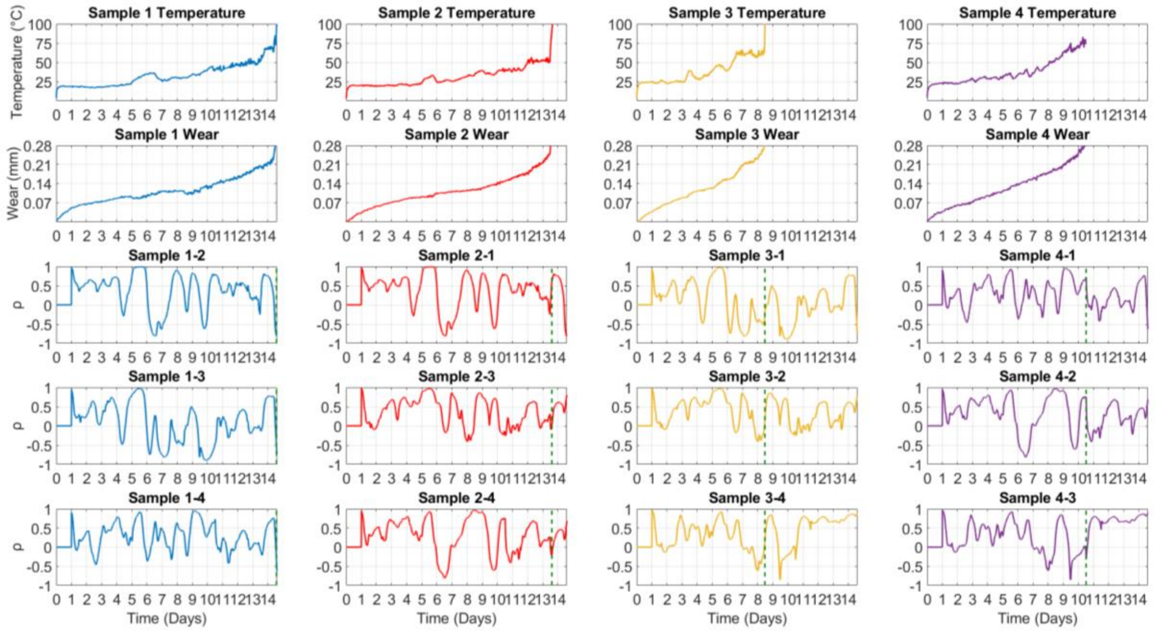

Figure 178 - Test 4 – Samples 1-4: Pearson correlation coefficient results with a rolling training set of 1 day (86400 data points).

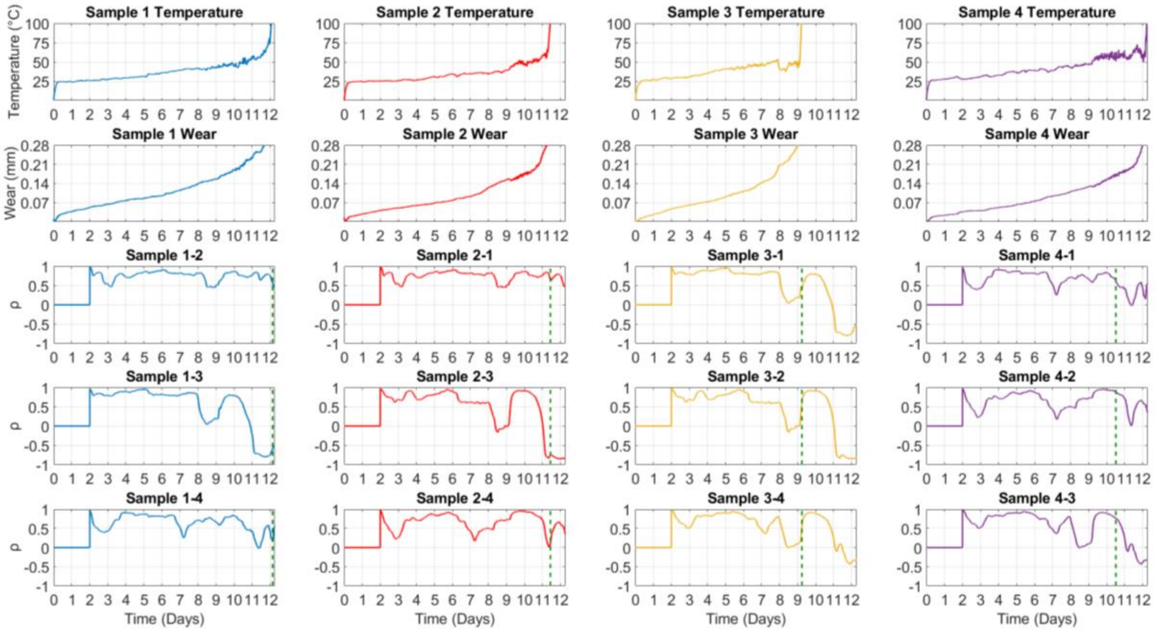

Figure 179 - Test 3 – Samples 1-4: Pearson correlation coefficient results with a rolling training set of 2 days (172800 data points).

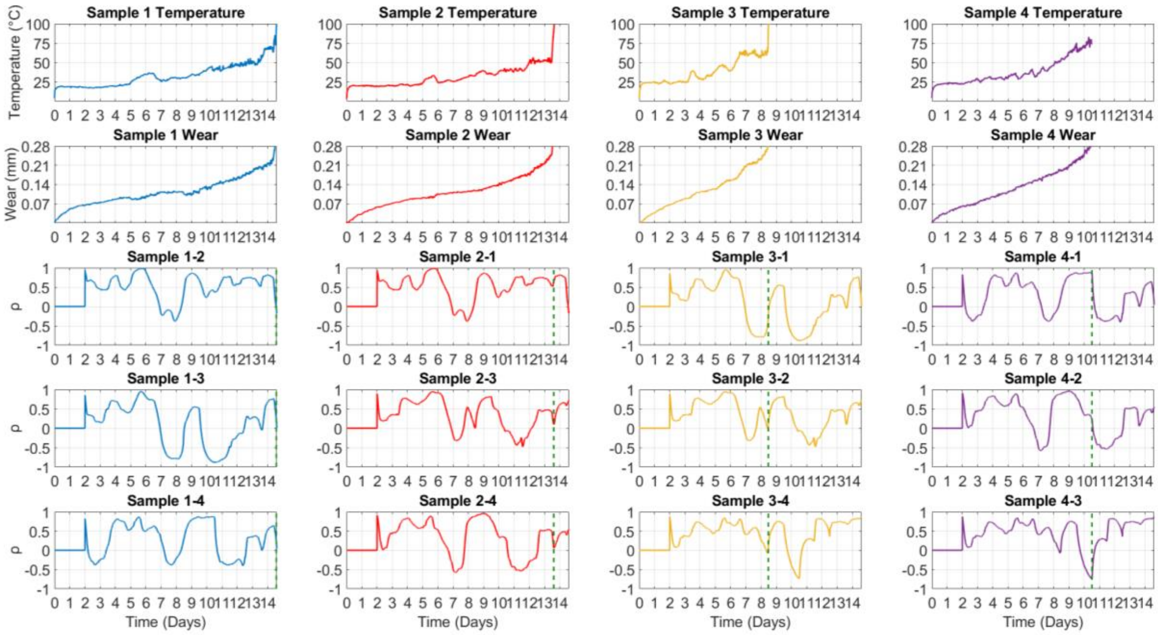

Figure 180 - Test 4 – Samples 1-4: Pearson correlation coefficient results with a rolling training set of 2 days (172800 data points).

Within Figures 179 - 184 it can be seen that a short rolling window is too sensitive to the current events considered within the rolling window and therefore the correlation coefficient produced overly sensitive to local events compared to overall longer-term trends. As the window width is increased, it can be seen from Figure 183 & Figure 184 that the correlation coefficients have become less volatile but have also been able to effectively detect points of temperature deviation between the datasets. It is important to note that the Pearson correlation coefficient becomes negative when a temperature dataset which has been running at a lower temperature moves to a value higher than its mating pair.

As discussed in section 5.2.3, the final algorithm is envisaged to have threshold inputs at which it will flag a pair of bearing liners as temperature deviations are recorded. These thresholds have not yet been accurately calculated and are part of the future work required, but for the purpose of analysis a manual threshold of 0.5ρ was assigned.

Table 9 - Test 3 & 4 Results: Detection times and wear depths of the Pearson correlation coefficient with a window width of 2 days (172800 data points).

Sample Number	Time of Failure (Data Point)	Time of Failure (Days)	Wear Depth (mm)	Detection Order	Failure Order	Wear Past Replacement Criteria (mm)
Test 3						
1	348700	8.07	0.1395	2	3	0.0195
2	350200	8.11	0.1274	3	2	0.0074
3	350200	8.11	0.2090	3	1	0.0890
4	297700	6.89	0.0907	1	4	-0.0293
Test 4						
1	119900	2.78	0.0712	2	4	-0.0488
2	119900	2.78	0.0686	2	3	-0.0514
3	91400	2.11	0.0671	1	1	-0.0529
4	91400	2.11	0.0636	1	2	-0.0564

From Table 9 it can be seen that the algorithm was able to detect a temperature deviation at an average wear depth of 0.143mm with a standard deviation of ±0.048mm which currently stands at 0.023mm above the replacement criteria. Although the wear depth at the time of detection was appropriate for samples 1-2-4, sample 3 was detected at a dangerous level of wear of 0.209mm. Furthermore, the algorithm was not able to accurately detect the order of failure of test 3. On the other hand the order of failure was correctly assumed for test 4 with bearing liner samples 3 & 4 failing first and 1 & 2 later in time. Unfortunately wear depth recorded at the time of detection underperformed the results from test 3 with an average wear depth detection of 0.068mm. In order to compare the techniques, the same evaluation was applied to the results from the expanding window method (Figures 175 - 178). Before proceeding, it can be seen that the difference in scales of these two separate tests would cause an issue in identifying a feasible level of correlation decrease in order to flag the bearing pair. Therefore for the purpose of analysing this set of data, a correlation threshold of 0.90ρ was used.

Table 10 - Test 3 & 4 Results: Detection times and wear depths of the Pearson correlation coefficient with expanding window.

Sample Number	Time of Failure (Data Point)	Time of Failure (Days)	Wear Depth (mm)	Detection Order	Failure Order	Wear Past Replacement Criteria (mm)
Test 3						
1	524600	12.14	0.28	0	3	0.16
2	494100	11.44	0.28	0	2	0.16
3	399200	9.24	0.28	0	1	0.16
4	453900	10.51	0.28	0	4	0.16
Test 4						
1	106700	2.47	0.0703	3	4	-0.0497
2	106700	2.47	0.0648	3	3	-0.0552
3	81500	1.89	0.0633	1	1	-0.0567
4	95700	2.22	0.0599	2	2	-0.0601

As seen from Table 10, the algorithm failed to detect any significant temperature deviation from test 3 and this is shown in the high Pearson correlation values shown in Figure 177. Due to these high correlation coefficients, the values did not drop below the set threshold and therefore no bearing failure was detected. Although the wear data at the time of detection from test 4 were once more premature with respect to the replacement criteria, the order of failure was correctly predicted by the algorithm. This success was unfortunately dwarfed by the inability of the code to detect damage within test 3.

As a technique, this method is very responsive to changes in temperatures if the correct window length of data is considered. Although some results were undesirable, in particular the failure of detection for one data-set, this method was deemed to have potential and future studies should be conducted upon further sets of data generated from the test bench. Future work upon this topic should also include the potential tailoring of the thresholds for the specific data-set under consideration, similar to the approach for the tailored EWMA charts.

6.2 Temperature curve volatility characteristics

Having previously discussed comparative techniques such as using difference signals, or correlation techniques, as damage detection methods, the raw temperature data sets were further investigated in order to evaluate if further temperature-based characteristics could be indicators of damage. Referring back to Figure 77 and Figure 78 (Page 103) one can notice that when the liner wear depth approaches the glass fibre backing region, at the depth of approximately 0.15-0.18mm, the temperature characteristic begins to alter.

At this wear depth milestone, it is believed that the temperature begins to behave in a volatile manner due to the higher friction coefficient of the glass fibre structural fibres. This is also represented by a small level of increased vibrations as demonstrated by fluctuations on the wear curves in Figure 77 and Figure 78 at the point of glass fibre contact. For the purposes of condition monitoring, these temperature fluctuations were thought of as a marker for the liner wear depth. Therefore, if a technique could be employed which could identify the onset of these fluctuations, a prognostic measurement could be produced by a complete algorithm.

At this stage it was evident that some measure of signal deviation from the instantaneous mean had to be employed. The standard deviation of the individual data sets was the most obvious route to take, but the technique had to capture the variation of the standard deviation throughout the testing procedure. To achieve this, a rolling window was once again used to evaluate the standard deviation of the data sets at each point during the wear process of test 3 and 4. Figure 181 and Figure 182 show the effect of the window size on the detection of such deviations in temperature.

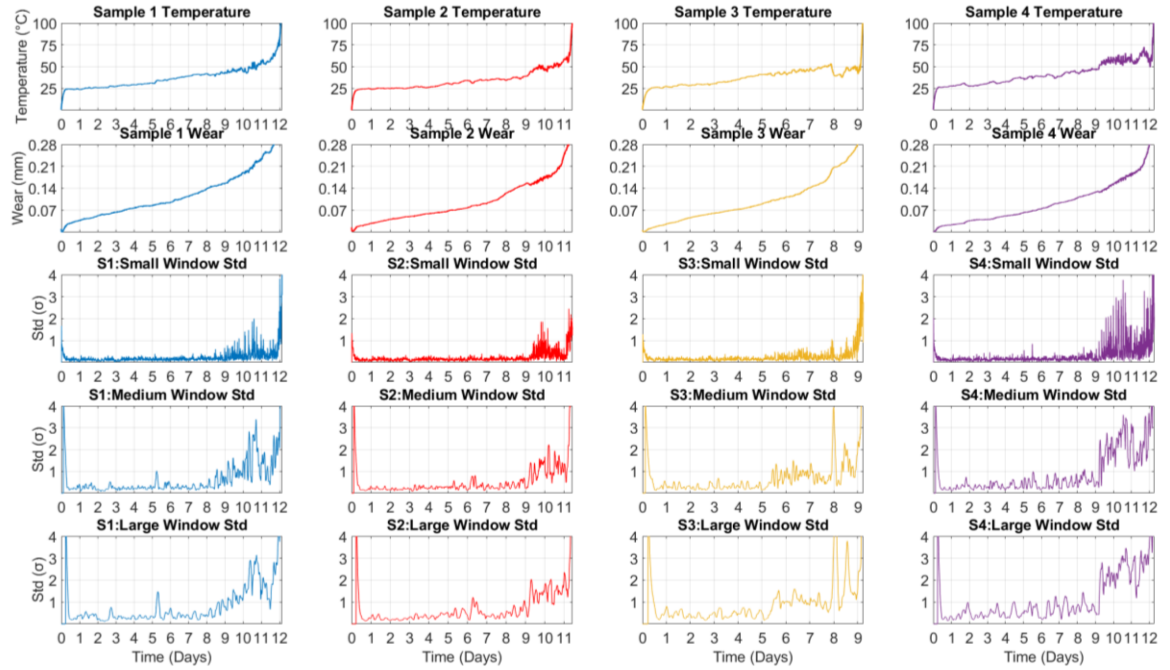

Figure 181 – Test 3 - Effect of rolling window size on the detection and amplitude of temperature deviation. Small window 500 data points, 5000 data points, 10000 data points (568320 total data points available)

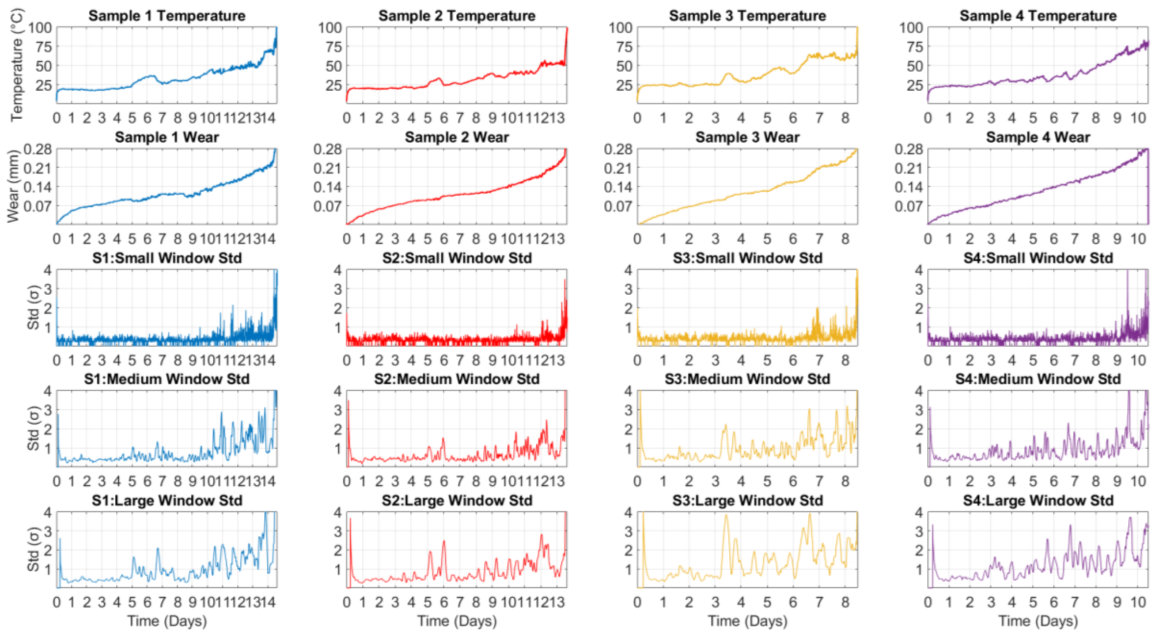

Figure 182 - Test 4 - Effect of rolling window size on the detection and amplitude of temperature deviation. Small window 500 data points, 5000 data points, 10000 data points (568320 total data points available)

It can be seen from Figure 181 and Figure 182 that the smaller rolling window of 500 data points was able to provide a low level of standard deviation up to the point of a wear depth of 0.15-0.18mm where, in both tests and all samples, the standard deviation had a significant increase. Due to the nature of the rolling small data window, when a temperature fluctuation occurs as seen in sample 3 of test 4, the standard deviation remains relatively slow. As more data points during the fluctuation are introduced, the calculated standard deviation of the larger data windows increase and are therefore affected by such a trend. Although this technique appears to detect the material composition change of the bearing liner, the wear depth at which it does so is beyond the acceptable replacement criteria of 0.12mm. This technique might not be able to be used as a diagnostic method of damage due to the time of detection, but it can be applied as a fail-safe method as part of a larger overall monitoring algorithm in order to spot sample pairs which have gone undetected by the previously developed techniques.

6.3 Temperature recovery investigation

Temperature recovery was a feature of the coupon test, which essentially simulated the take-off and landing of the rotorcraft. This was seen as a decrease to ambient temperature and increase back to thermal equilibrium as seen in Figure 77 (Page 103) between the days of 0 and 1. It was observed that the bearing liner which reached the highest plateau value failed first and the one which reached equilibrium last failed last. In order to validate if this was a consistent feature of the wear process, an investigation was carried out into the relationship between the time taken to reach thermal equilibrium and the liner's wear depth.

The test bench which was dedicated to the author's work, did not have the capability to provide such cooling effects consistently and autonomously. Due to the long testing time required by the liner material to fully wear under considerable loads, ranging from 1 to 2 weeks, it would be unfeasible to stop-start the test manually. For this type of investigation, the full bearing test bench (Rig H) had to be utilised which was located at the factory facility of the industrial supervisor, as explained in Chapter 3. This test bench wears fully assembled bearings under specific loading and reciprocating conditions which provide both a cooling period and a rest period for the bearing. The cooling period was in the form of a water injection close to the sliding surface region and this is typically carried out in order to replicate certain flight conditions as defined in the test qualification specification AS81819. The previously mentioned rest period consisted of an autonomous stop of the test bench's motor which brings the bench to a standstill. During this rest period, a quasi-static measurement of bearing wear is taken, which also includes physical parameters such as friction and torque. Such parameters have been found to have a link with the wear depth of the bearing.

For the purpose of this test, the water contamination was turned off and the cooling period which was used, consisted of the previously described rest period. This type of contamination is part of the qualification standard 81819 used on Rig H as part of SKFs standard practice. Figure 183 shows the full temperature curve with respect to curve number.

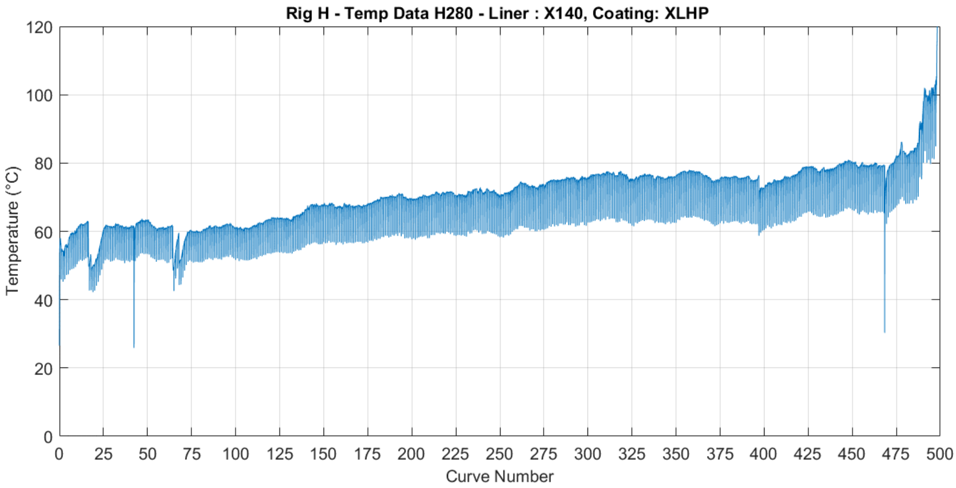

Figure 183 - Temperature vs Curve Number.

The curve number on the abscissa, represents the number of start-stop cycles which had occurred throughout the test. In order to fully understand the nature of this cooling and plateau period, a detailed view showing the cooling period and subsequent temperature plateau is shown in Figure 184.

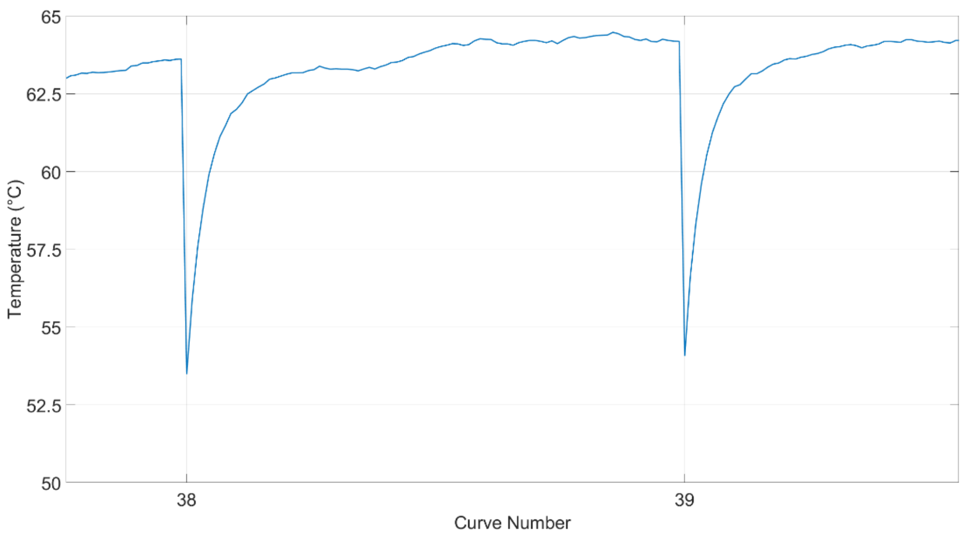

Figure 184 - Rig H testing cycle between quasi-static measurements with respect to temperature.

In order to analyse this type of data, a MatLab script was created, which applied a curve fit using polynomials up to a quartic curve (Equations 16 – 20), to each of the curves from the point of test re-start until the next stop for one particular cycle Figure 185.

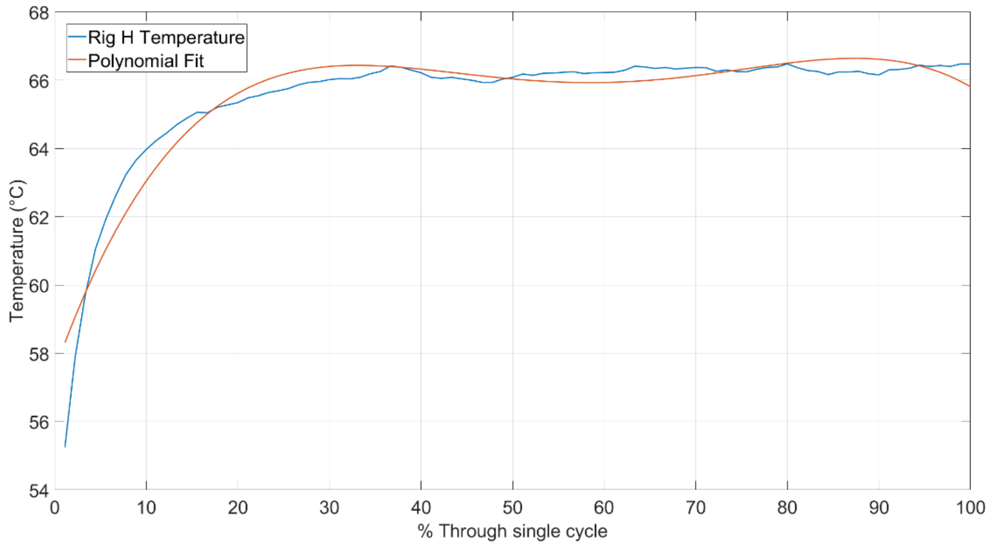

Figure 185 – Fourth order polynomial fit upon a recovery curve.

Each of the four coefficients, along with the constant term were in turn plotted in terms of curve numbers and patterns, which may show signs of wear were then considered.

$$y = \boldsymbol{a_0} + a_1x + a_2x^2 + a_3x^3 + a_4x^4 \qquad (16)$$

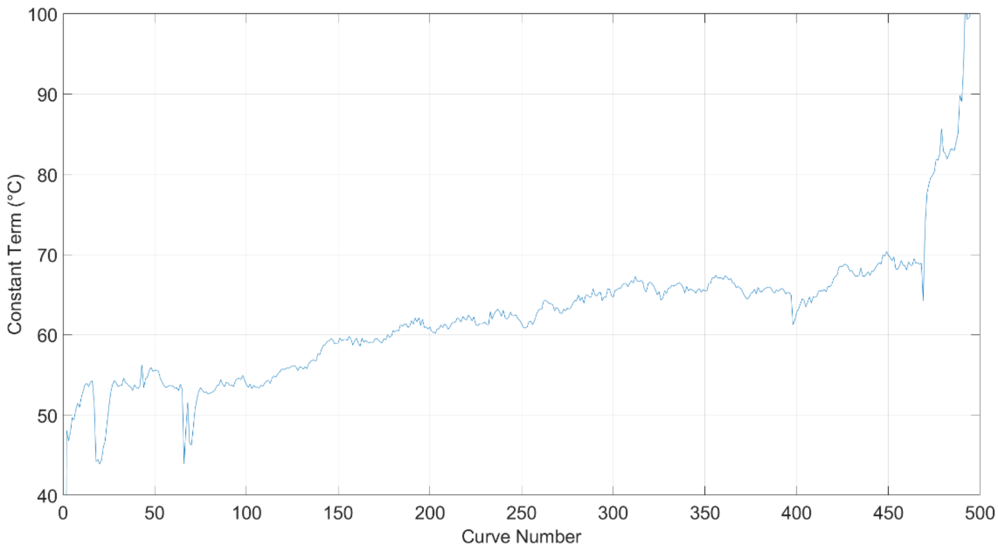

Figure 186 – Constant term progression vs curve number.

$$y = a_0 + \boldsymbol{a_1 x} + a_2x^2 + a_3x^3 + a_4x^4 \tag{17}$$

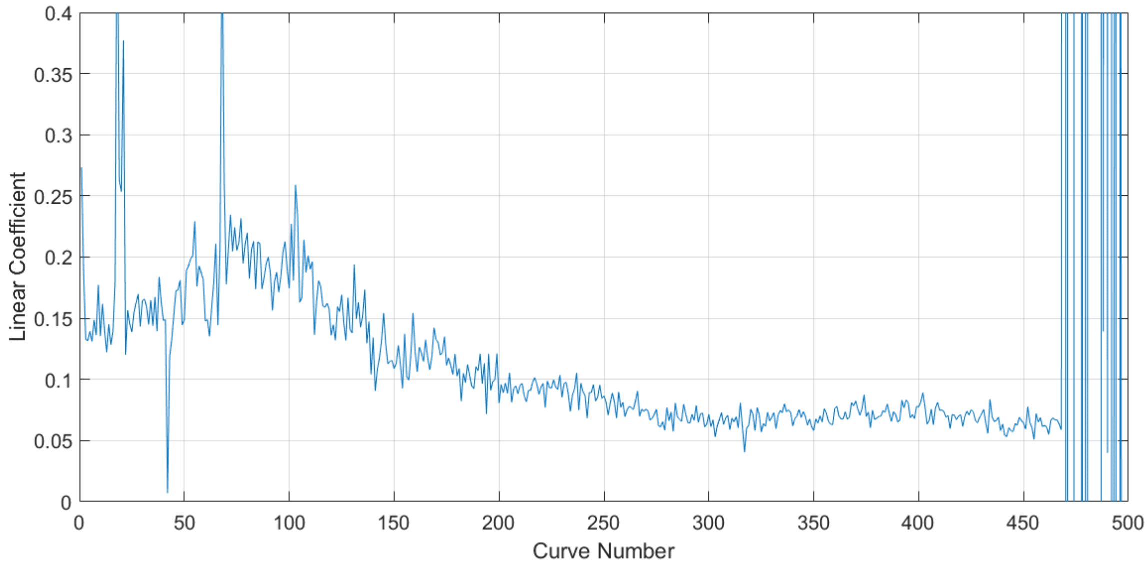

Figure 187 - Linear Coefficient progression vs curve number.

$$y = a_0 + a_1x + \boldsymbol{a_2 x^2} + a_3x^3 + a_4x^4 \tag{18}$$

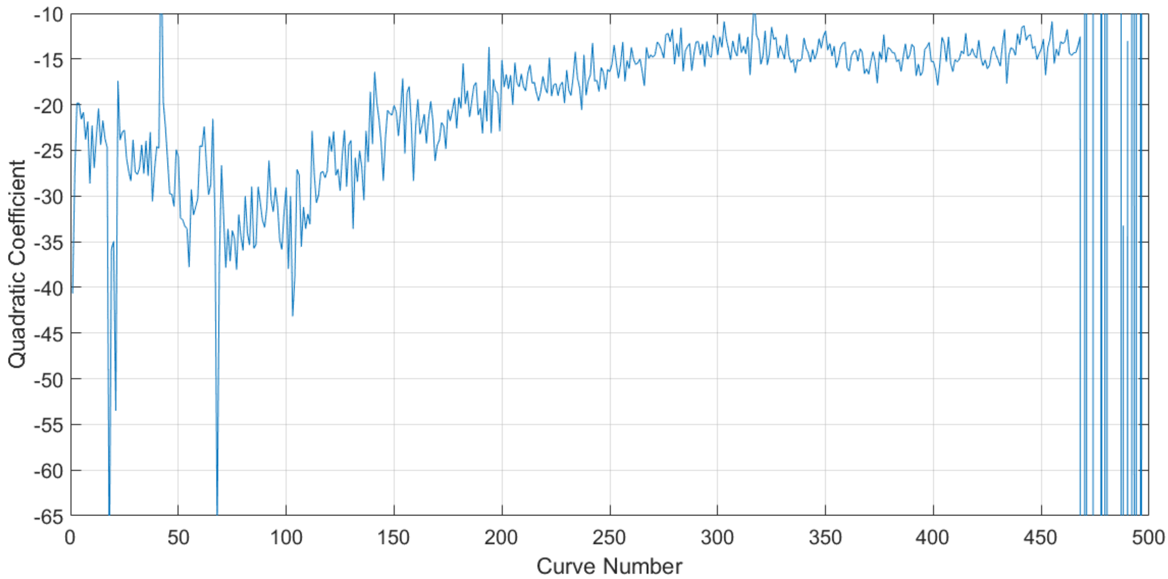

Figure 188 - Quadratic Coefficient progression vs curve number.

$$y = a_0 + a_1 x + a_2 x^2 + \boldsymbol{a_3 x^3} + a_4 x^4 \quad (19)$$

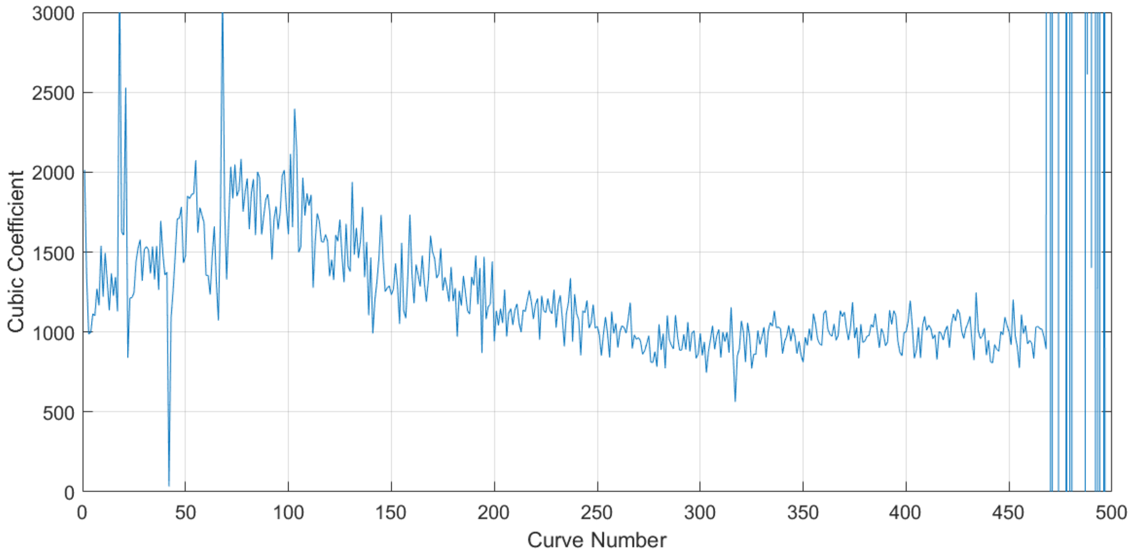

Figure 189 - Cubic Coefficient progression vs curve number.

$$y = a_0 + a_1 x + a_2 x^2 + a_3 x^3 + \boldsymbol{a_4 x^4} \quad (20)$$

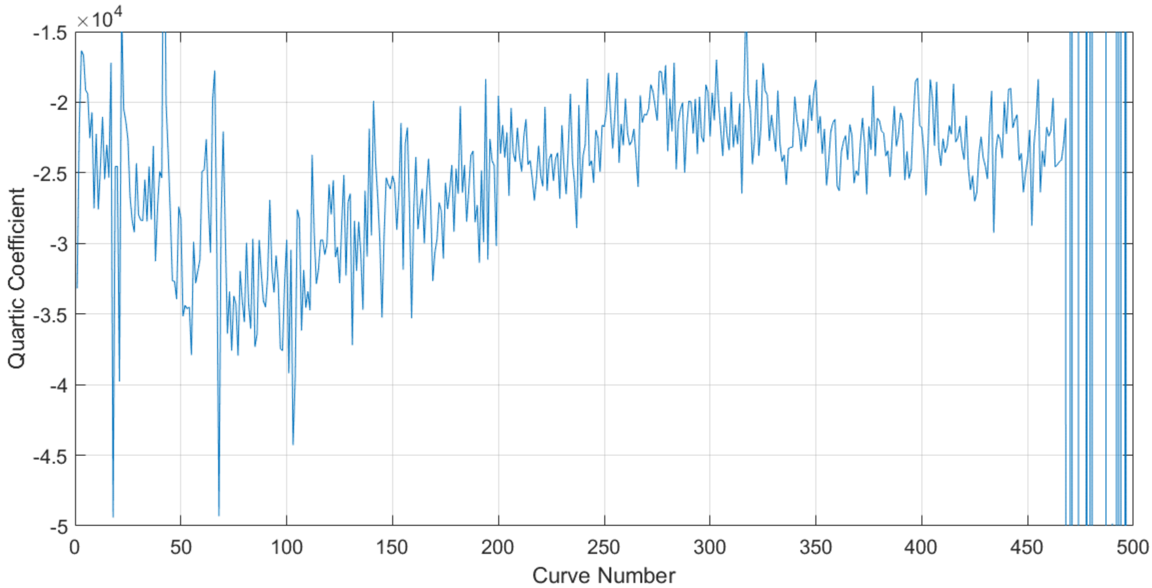

Figure 190 - Quartic Coefficient progression vs curve number.

Unfortunately, the results of this investigation are difficult to interpret and do not seem to yield any useful information. One point which could potentially be said to occur, is the identification of when the bearing has reached its steady wear phase, and this could possibly be represented by regions of the coefficient graphs where the coefficients have become more stable. To further note, the high amplitude of coefficients between the data points of 450 and 500, were said to be corrupted data due to a power cut incident at the factory site where the test bench had to be restarted.

It was concluded at this point that the reasoning and intuition behind this type of analysis was correct but further analysis techniques would be required in order to extract useful information from the data sets provided and the technique was not pursued.

6.4 Temperature analysis discussion

All of the techniques in this chapter have shown potential for damage detection or prediction of life. These techniques have positive and negative aspects, which help them to be unique in their style of operation. Figure 191 shows the four developed condition monitoring methods in their respective order with relation to wear.

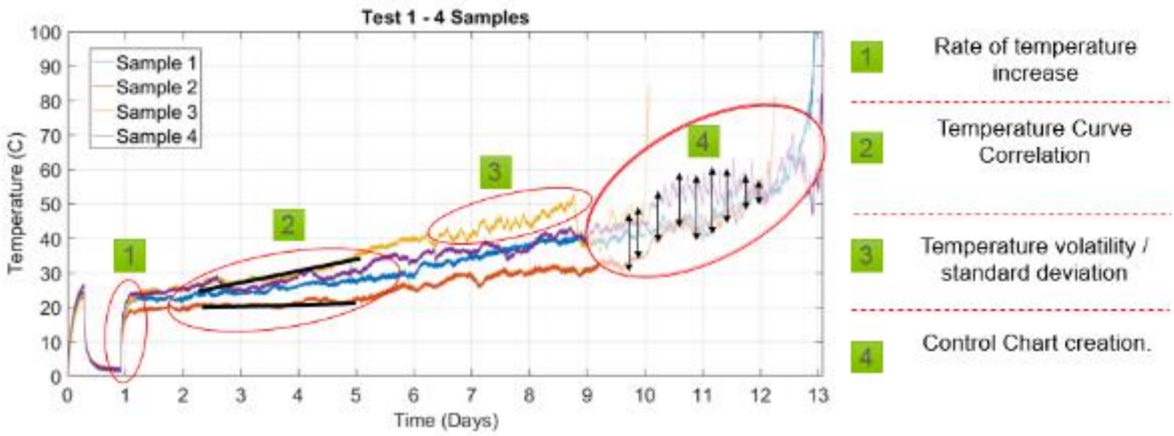

Figure 191 - Condition monitoring technique developed in relation to temperature, as a measured physical parameter.

Unfortunately, full investigation of the rate of temperature rise technique was not possible, due to the lack of data which was available to the author through the course of the research programme. The method was able to show some potential with regards to the curve fitting coefficient, but was not able to be directly related to any wear patterns, nor could they be speculated to be affected by any type of material property. Therefore at this stage, this method requires further investigation and development.

The temperature correlation investigation was one of the most successful approaches developed, due to its simplicity and versatility which depended on only a few factors during the analysis. With an expanding window, no external training set was needed in order to output a viable damage detection signal via the use of the correlation coefficient. Furthermore, by modifying the technique to include a rolling window, the algorithm became more sensitive to deviations of temperature which occurred during the experiment. Both of these correlation-based algorithms were mostly able to detect when a temperature deviation was occurring and therefore provided an indication in the form of the decreasing correlation coefficient. This signal occurs during the phase of liner wear, when the composite self-lubricating liner material undergoes a material composition change from the PTFE rich region to the structural glass fibre backing. By knowing the wear depth at which this transition region occurs, which is a property of the liner design, this condition monitoring method could provide an indication when the liner has reached this exact wear depth. Having carried out an investigation into the effect of noise with respect to signal disruption, it was concluded that by potentially tailoring these methods together, an overall robust system architecture could be created. This requires further work in the future with multiple data sets.

As previously mentioned, when the material composition transition period occurred, it displayed some useful temperature trends. During the data analysis phase of the research programme it was noted that as this transition period occurs, the temperature started to become more volatile than previously exhibited. This phenomenon was used to provide another indication that the wear had reached the transition to the glass fibre backing. By calculating the standard deviation via a rolling window throughout the length of the test, it was possible to, reasonably accurately, identify this material composition transition. This was presented graphically and matched the previously explored techniques discussed above.

Finally, the use of statistical process control charts was investigated in order to identify small deviations between temperature measurements, and to track the growth of these deviations over time. By using standard and bespoke control charts, the advantages and disadvantages of each technique could be understood and further improved in order to provide a sensitive method of damage detection. The trouble with such control charts, occurs when trying to create a general approach to suit all testing in real life applications. As the self-lubricating bearings will change in geometry and application, a wide range of data must be collected in order to confidently produce the upper and lower action limits as described within the chapter. If these control limits are too tight in order to provide extra safety, then the code would produce alarm points very early on into the wear process when small deviations are occurring. On the other hand, if the control limits were too lenient then the alarm points may be delayed or potentially not be triggered at all. This could in turn be a safety concern for the operator.

The most likely implementation of the temperature techniques would involve a combination of all techniques. This would allow increased confidence in temperature-based techniques with respect to robustness and outputs. Ideally, a second physical parameter would need to be monitored within the system in order to account for potential unwanted noise coming from one physical parameter. Strain was thought to be included as a measurement, but time did not allow for the alterations required to be made upon the test bench. This was also a feature which was discussed and will be implemented in future results.

6.5 Conclusion

Temperature, as a physical parameter, was utilised in order to create a variety of condition monitoring techniques which were able to effectively detect the beginning of the failure of a self-lubricating liner material. Currently in industry the replacement criteria for such self-lubricating bearings occurs at a wear depth of 0.12mm and a maintenance interval occurs every 50 flight hours of the rotorcraft. The reason for this short flight hour time between checks is the factor of safety as these plain bearings are classified as critical components, due to their requirement to control the pitch of the rotor blades. When this replacement criterion is compared to the wear curves, as shown in Figure 192, it can be seen that the developed techniques come very close to this criterion.

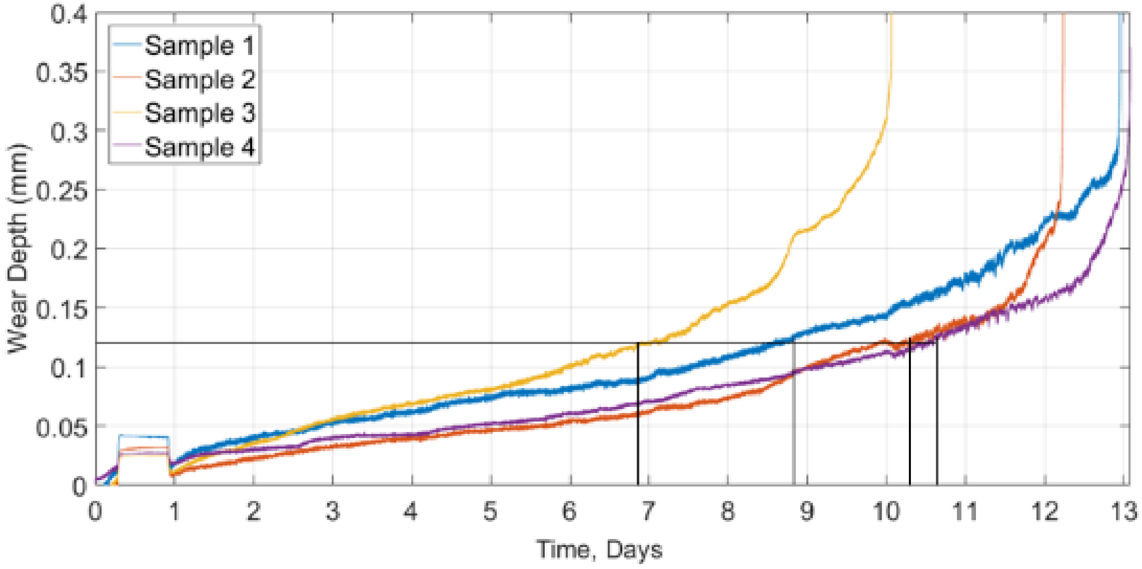

Figure 192 - Wear data with relation to the industrial replacement criterion of self-lubricating bearing.

This could potentially be utilised since the aircraft would not have to make such regular maintenance and inspection pauses and a single alarm point, could provide vital information to the maintenance team in order to plan the following interval. To finally note, this type of technique was developed in laboratory conditions and therefore could be very dissimilar to real flight temperature data. Therefore the next logical step towards achieving this type of condition monitoring technique is the gathering of real test aircraft temperature data.

Chapter 7: Test-bench results – Acoustic Emission

7.1 Introduction

7.1.1 Review of existing techniques

Acoustic Emission (AE) is widely used as a Non Destructive Testing (NDT) technique in the field of condition monitoring. This type of monitoring technique originates from a range of tensile tests conducted by French scientist Henry Louis Le Chatelier. During the testing procedure, he recorded stress waves which originated from the Aluminium samples under test and related this phenomenon to stress jumps within the material. Over the years, the monitoring of such phenomena, which can include crack initiation / growth, material dislocations, composite laminate delamination *etc.*, has been applied to a wide range of static applications such as the structural health monitoring of pressure vessels (Rogers & Stambaugh, 2014). A further step was taken when this NDT technique migrated to larger static structures such as bridges, for applications ranging from the structure construction phase, quality control monitoring, to structural integrity assessment and monitoring of existing structures (Nair & Cai, 2010). Proven useful in static structures, AE has also been applied to the monitoring of machinery including tool wear, pumps, gearboxes, engines, rotating structures and most importantly bearings. A wide range of research has been conducted into health monitoring of rolling element bearings using AE, but currently no such analysis techniques have been applied to self-lubricating bearings.

7.1.2 Potential techniques for main rotor pitch control condition

Initially, a literature study was conducted in order to investigate data analysis techniques which had been previously applied to self-lubricating materials and specifically in reciprocating conditions. Unfortunately, no published work was found on AE monitoring of self-lubricating materials at all. More widely, some limited work on AE monitoring of machinery characterised by reciprocating motion was found in the literature. Two examples of published papers were found to correlate strongly with this type of reciprocating motion. The first study was conducted on the Acoustic Emission generated by the reciprocating contact between piston ring and cylinder liner in diesel engines, which focused on the reciprocating motion of the piston. In turn the Acoustic Emission amplitude was related to the pressures of each of the four engine stroke sequences and in turn correlated to the angle of the crank (Douglas, *et al.*, 2006). The common technique of Route Mean Square (RMS) was used in order to find a positive correlation between the pressure of the four strokes and the RMS amplitude. Therefore the RMS was deemed a useful technique to utilise when analysing Acoustic Emission data gathered from a reciprocating environment. Furthermore, as discussed within Chapter 2, due to the repeatable nature of AE data in reciprocating environments, a study was conducted whereby damage was able to be assessed within a reciprocating environment via the use of pattern recognition (El-Ghamry, *et al.*, 2003).

7.1.3 Justification of Acoustic Emission monitoring

In the previous chapter, a justification of the choice behind the measurement and gathering of temperature data was given. This justification was application specific when considering the main rotor pitch control conditions. The purpose of gathering Acoustic Emission data for these types of conditions, was to further understand the tribological conditions which occur during the wear phases of the liner material. Due to the complexity of the main rotor composition it was decided that implementation upon the aircraft would require further work into wireless and miniaturised sensing technologies.

7.2 Testing Procedure

7.2.1 Instrumentation selection

In order to be able to record the AE generated by the composite material during testing, piezoelectric sensors were required to be fitted as close to the test samples as possible. The sensors selected for this purpose comprised of R15S narrow band sensors which provided a very high sensitivity between 50 – 400 kHz, with a high temperature operating range of -65°C to 177°C. The sensor signals passed through a 40db preamplifier, which was in turn connected to Acoustic Emission data acquisition system, provided by Physical Acoustics, which consisted of a 4 channel PCI-2 wavestreaming system. In order to monitor all samples under test, four R15S sensors and four 40db preamplifiers were connected to the data acquisition unit.

7.2.2 Sensor location

Sensor location is very important when monitoring Acoustic Emission. This occurs due to the attenuation of the stress waves, as the distance between sensor and source is increased. The attenuation problem also increases when the stress waves have to pass through a series of mating surfaces or interfaces. This phenomenon occurs due to the scattering of the stress waves when coming into contact with air pockets created between such material interfaces. In order to minimise this type of unwanted attenuation, the material interfaces would have to include an external medium between the two connections. Such materials can include silicone adhesive or, if an adhesive effect is not required, grease can be applied. These materials essentially fill in the microscopic gaps between the mating surfaces and therefore provide a more appropriate transmission path for the stress waves. A second way of minimising this attenuation effect, is by decreasing the distance of the sensor from the stress wave source (Miller, *et al.*, 2005).

In order to determine the most appropriate sensor locations, an attenuation test was conducted on the test rig arms. This test consisted of the bonding of AE sensors in multiple places upon the arm and in turn a Hsu-Nielsen source was generated at the point where the liner composite / counterface contact would exist. This Hsu-Nielsen source is created by the fracture of a brittle graphite lead which can be found in mechanical pencils. The diameter of the graphite cylinder is required to be 0.5mm and in order to release the correct elastic stress wave, the angle of the cylinder when breaking must be roughly between 45° and 30°. Along with the mounting of the R15S sensors, two Nano30 sensors were bonded onto the metallic arm in order to test their viability. Even though the operating frequency range of both sensors lay within a similar frequency band, the Nano30 sensors consist of a much smaller geometry which would make them preferred to the larger R15S sensors. The experiment set-up is shown within Figure 193.

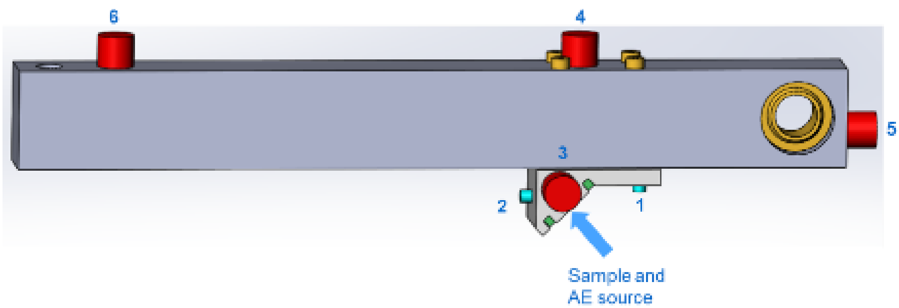

Figure 193 - Location of R15S sensors (red) and Nano30 sensors (blue)

Before conducting the testing procedure, the effectiveness of the acoustic coupling between the sensors and the arm had to be evaluated via the use of a Hsu-Nielsen source in order to confirm a good transmission path between the ceramic face of the sensors and the steel arm. Presented below (Figure 194) are the results from this investigation.

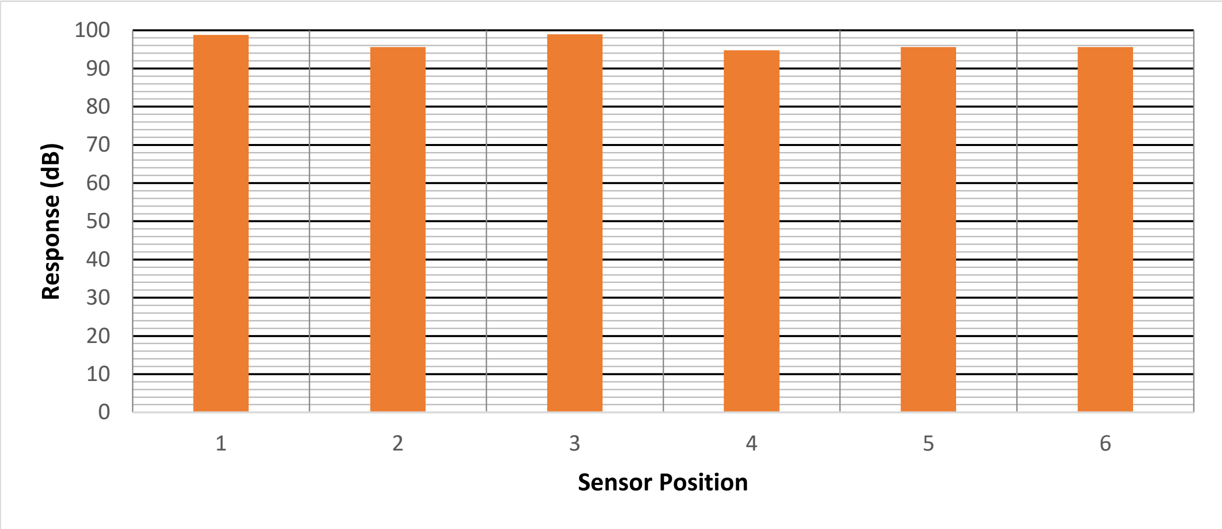

Figure 194 – Bonding strength investigation prior to the attenuation test of all 6 sensor locations.

It is important to note that the response rate of 100 dB is considered as a perfect bond and anything above the amplitude level of 90 dB is considered as an acceptable bond. Therefore all of the above attenuation paths to each of the 6 sensors, was deemed acceptable before proceeding with the test. The results shown within Figure 194 consist of the average value of 10 pencil break tests for each sensor. This was done in order to minimise the effects of variation in the Hsu-Nielsen source. After the test was conducted it was clear to see that the R15S sensor in position 3 was the sensor which provided the greater response to the generated source and therefore this sensor type, along with sensor location 3 was chosen for the AE testing reported in this thesis (Jenkins, 2014).

7.3 Analysis and results

7.3.1 General pattern recognition

During the wear testing of the self-lubricating material, Acoustic Emission data was gathered periodically in the form of wavestreams (recording of the raw, amplified but unfiltered/thresholded output of the AE sensors). Due to the duration and dynamic nature of such a test, it was decided that gathering a single, 1s wavestream every 30 minutes at 2 MHz from each sensor would provide enough information with regards to the structural health progression of the composite liner. It would not be feasible to record the raw AE signals continuously for the entire duration of a 10 to 14 day long test, given that each 1s wavestream file is some 20 Mb in size. Figure 195 shows a wavestream, which was gathered during the initial wear-in phase of the test from Sample 1.

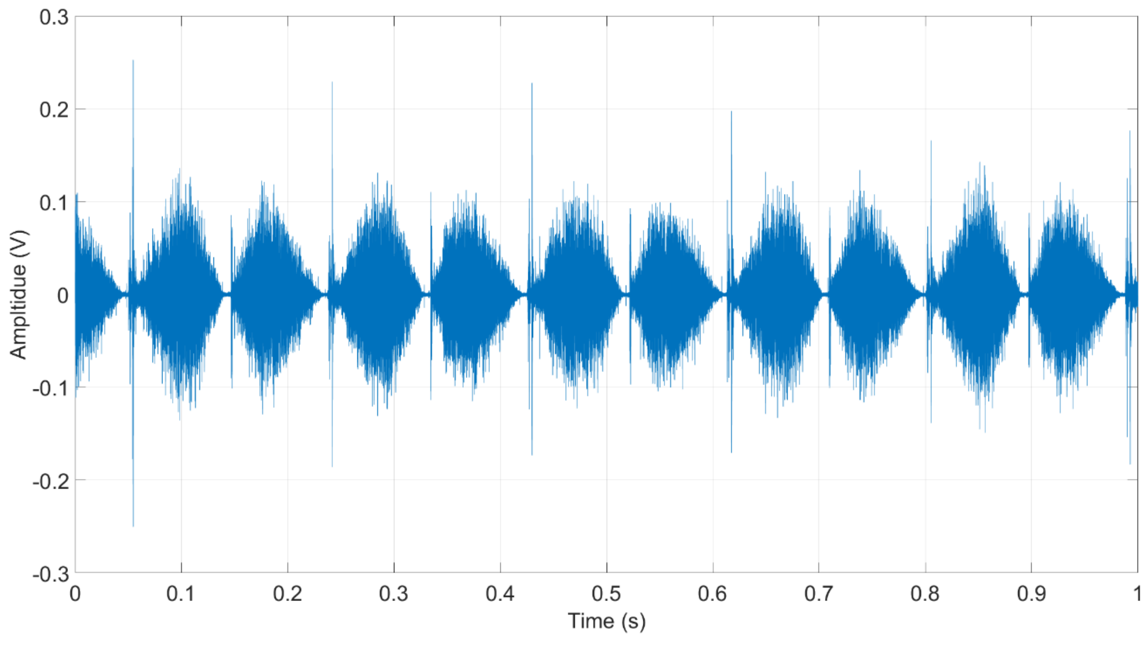

Figure 195 - Wavestream gathered in the wear-in phase of the bearing liner under test.

Some key features can be seen from this raw wavestream. There is an inherent diamond shape to much of the AE signal, which appears to be repeatable and on a timescale which suggests that it is related to the reciprocating motion of the counterface with one complete reciprocation cycle of the counterface producing two diamond shaped AE signals. This behaviour was thought to be caused by the changing sliding speed of the counterface during the reciprocating. As the counterface approaches the central 0° position, it is rotating at the highest angular velocity and as it reached the extremes of ±10°, the counterface was instantaneously stationary with zero angular velocity as it changed direction. It was hypothesized that the point of highest amplitude displayed on the diamond-shaped portions of the wavestream data equated to a crank reciprocation angle of 0° at the counterfaces' maximum angular velocity. This velocity profile is also confirmed by Douglas *et al.* (2006). Figure 196 shows the progression of the AE amplitude in terms of the piston's link arm crank angle, with the acronym TDC meaning Top-Dead-Centre where the piston has a velocity of $0ms^{-1}$.

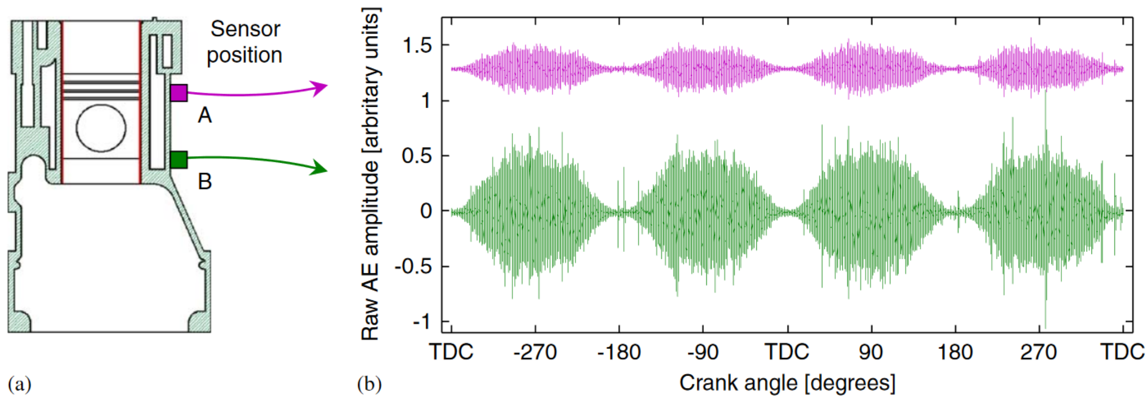

Figure 196 - Motored engine A: (a) cross-section showing AE sensor positions, and (b) measured raw AE against cylinder 3 crank angle (Douglas, et al., 2006).

In order to validate this assumption, an investigation was conducted which focused on precisely gathering a wavestream which would be synchronised to the reciprocation angle of the crank. To achieve this, a hall-effect sensor in conjunction with small cylindrical magnets were used in order to produce a signal nominally at the reciprocating angle of -10°. This signal was used, via the LabVIEW data acquisition system, to trigger the recording of a wavestream by the AE system, with its start nominally aligned with the counterface position of zero angular velocity.

This triggered test was conducted three times in order to increase the confidence of the results. Figure 197 shows the three raw wavestreams overlaid.

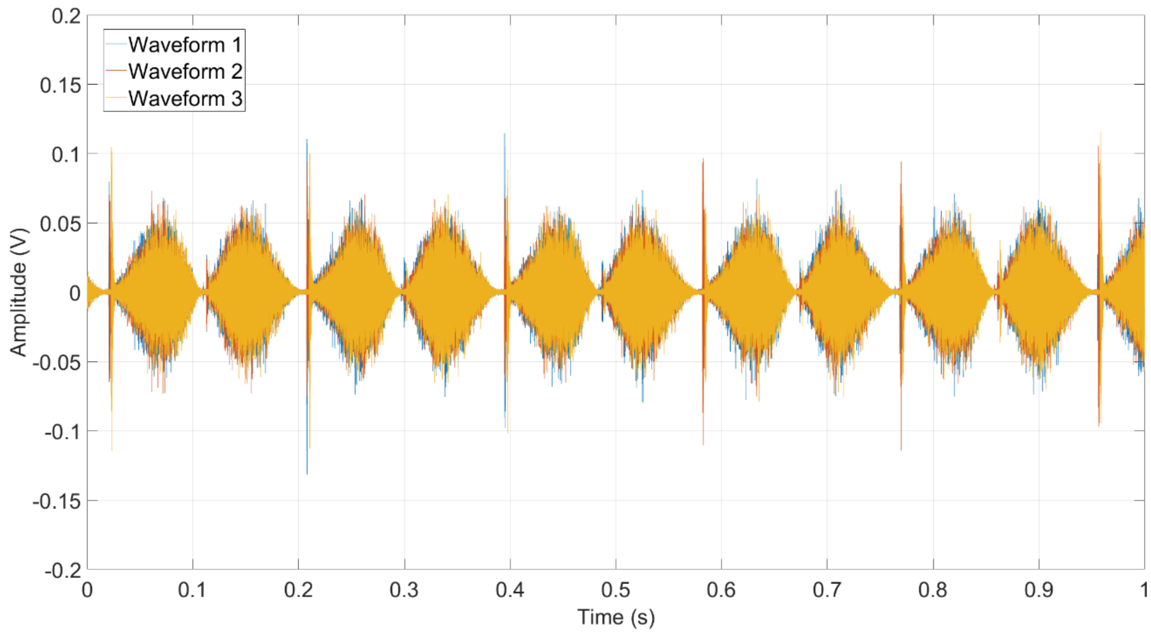

Figure 197 – Trigger test wavestreams, initiated at a crank angle of -10° = 0 ω^2.

By inspecting Figure 197, the conclusion can be made that the lowest amplitude of the raw wavestream was related to the position of the crank, where the counterface had an angular speed of zero. It is believed that the AE wavestream started recording slightly ahead of the zero velocity position, due to the Hall Effect sensor producing an output based on proximity of the metallic crank arm to it – it is likely that the signal was therefore produced slightly ahead of the exact zero velocity position. Figure 198 displays the relationship established between position, velocity and AE signal established by this investigation.

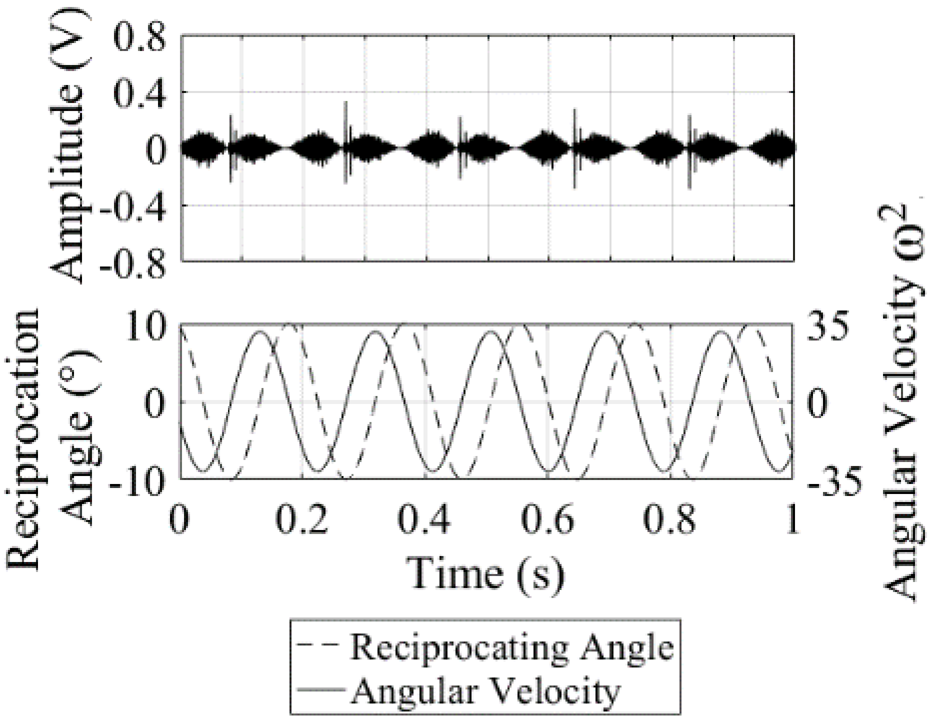

Figure 198 - Wavestream amplitude in relation to the Reciprocating Angle (°) of the crank arm and the Angular Velocity ω^2 of the counterface.

A further characteristic of the raw data was the sharp transient bursts of activity at the start of each oscillation. A few potential sources of these peaks were considered, which included potential stick slip or adhesion of the self-lubricating material or due to reverse shear stresses during the position of angular direction change.

7.3.2 Wavestream progression

Following investigation of a single wavestream, gathered at the early stages of wear, the next step towards understanding the raw data, was to observe how the wavestreams developed over the full test duration. Figure 199 shows four wavestreams which were gathered at different stages of the wear period.

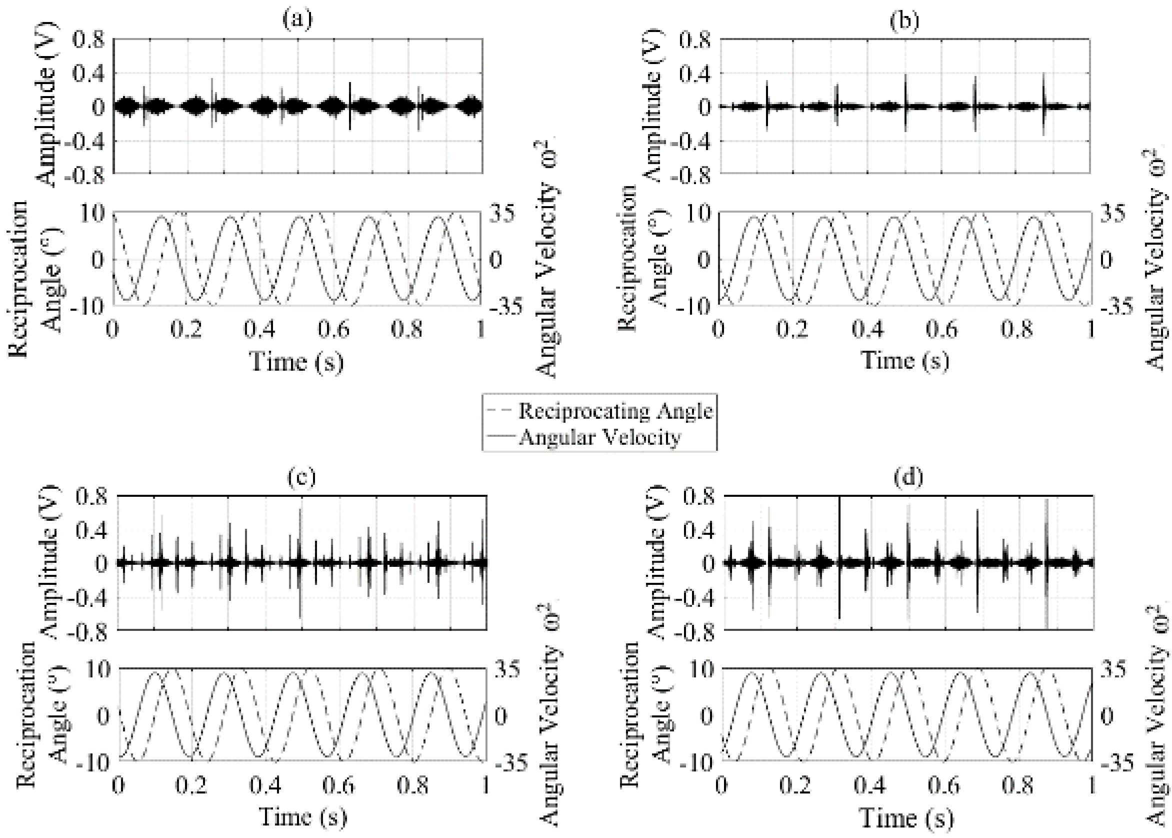

Figure 199 - Four waveforms gathered throughout the testing procedure. (a) Wear-in phase, (b) Plateau phase, (c) Glassfibre backing region, (d) End of life region.

As can be seen, the transition periods between the four phases of wear are accompanied with some key characteristic changes in the wavestreams. Initially, as originally assumed, the period where a transfer layer of PTFE was in the process of being formed upon the counterface, was the most aggressive. This was said to occur due to the sliding surfaces not being conformal and therefore high contact pressures occurring between the asperities of the counterface and the liner composite. At this stage, the transient waves at the start of the reciprocation are present but they do not seem to dominate the wavestream pattern. As the plateau region is reached and therefore a degree of conformity between the two sliding surfaces has been established, the amplitude of the wavestreams appears to decrease, potentially due to the reduction in friction associated with the establishment of a transfer layer. Also it was noticed that, during this phase, the transient bursts of energy at the start of reciprocations had increased their energy as displayed by the increase in amplitude. This phenomenon could be related to a higher degree of adhesion at the momentary position of zero velocity between the mating surfaces, as the counterface had achieved a PTFE transfer layer and therefore more polymer to polymer contact was present within the sliding region. Further research is required in order to confirm this theory. Within the glass fibre region of wear, further time domain changes started to occur. When contact is initiated between the structural backing of the liner and the counterface, at approximately 0.15-0.18mm of wear, multiple transient bursts of Acoustic Emission data became apparent within the raw wavestreams. This was thought to be related to either glass fibre cracking or even scoring of the liner. Finally, within the end of life region, the transient bursts increased in amplitude once more and the mid-reciprocation bursts started to become more significant. During this stage of wear the amplitude of the overall diamond shaped clusters had increased one more, again pointing towards these being friction related.

To conclude, the wavestreams show clear changes as the wear of the liner progresses. The aggressive nature of the latter stages of wear is portrayed graphically in the time domain and later work within this thesis investigates the extraction of time-domain features to enable characterisation of the wavestreams.

7.3.3 Frequency domain analysis

The first step taken into processing the raw wavestream data gathered throughout the experiment, was to transfer the data in the frequency domain in order to investigate patterns and potential signs of damage which would not be seen purely by visual inspection of signals in the time domain. In order to achieve such an analysis, a MatLab code was created which:

1. Loads the initial wavestream file.
2. Analyses the wavestream data via a Fourier Transform technique.
3. Outputs the data onto a matrix.
4. Loads the next file in sequence and repeat steps 1-3 until all the wavestreaming files have been processed.

At this stage it is important to note that the preferred Fourier Transform technique which was used consisted of a binned Fast Fourier Transform (FFT) (Pullin, *et al.*, 2012). This method was chosen due to its quick analysis speed and its ability to adjust the coarseness of the frequency bins in which the data would be processed. These two features of a binned FFT must be balanced since a reduction in coarseness leads to the analysis time required to process the data increasing.

Figures 204 – 207 present the spectrograms which were created by meshing the analysed data together with respect to time. During the test which lasted some 13 days, 620 wavestreams were processed and stitched together. The meshed processed data from channels 1-4 are displayed below.

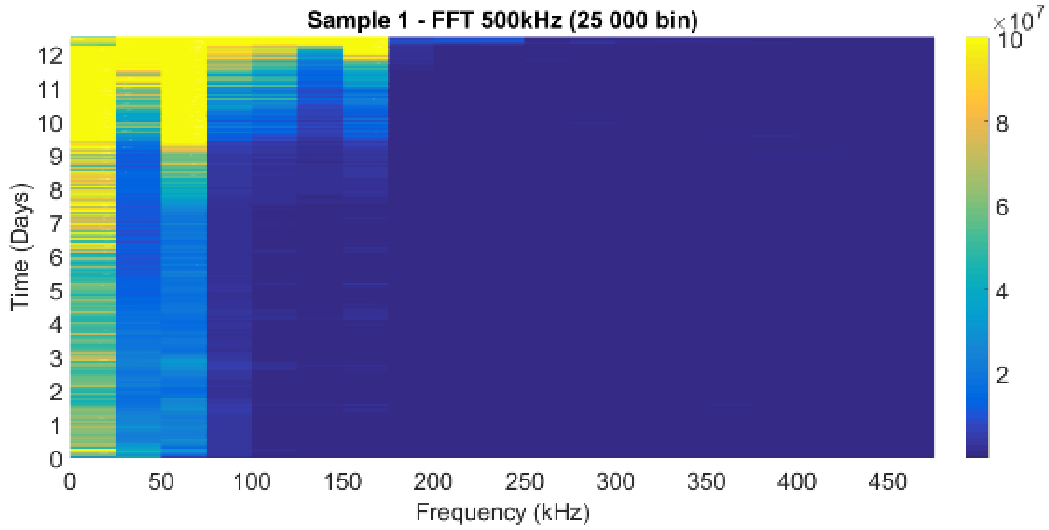

Figure 200 – Coarse Binned FFT of Channel 1 data.

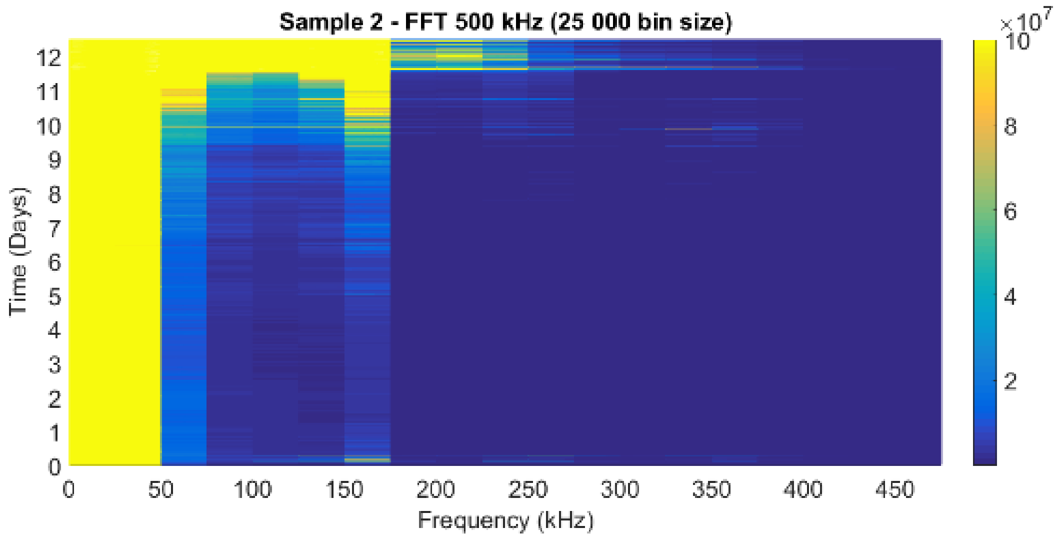

Figure 201 - Coarse Binned FFT of Channel 2 data.

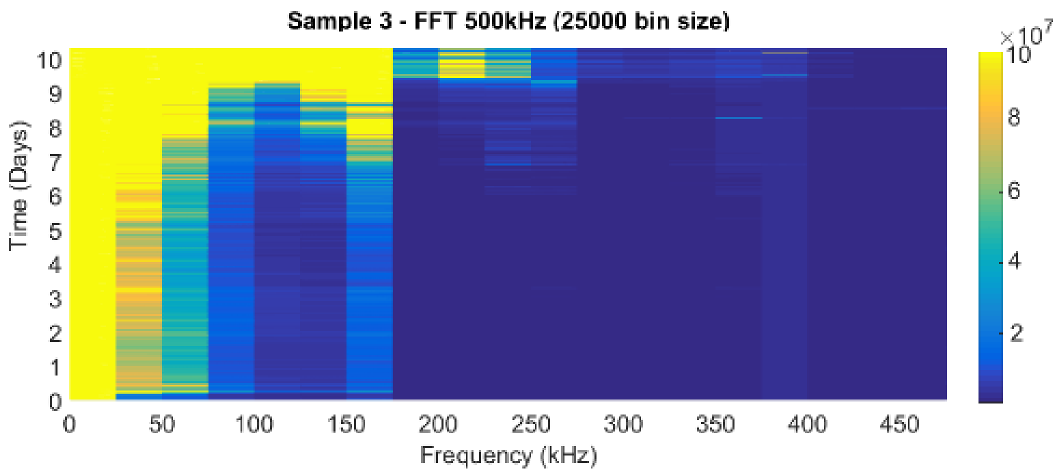

Figure 202 - Coarse Binned FFT of Channel 3 data.

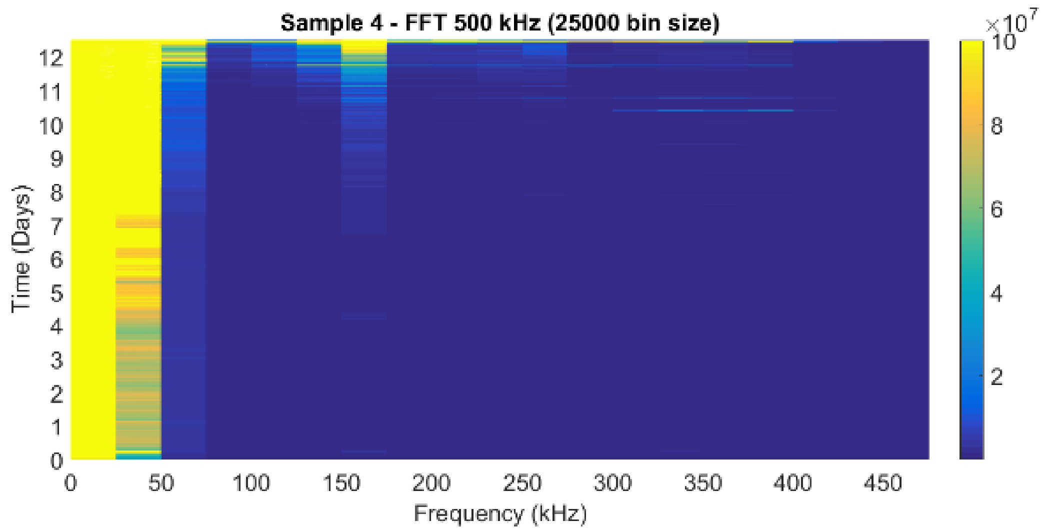

Figure 203 - Coarse Binned FFT of Channel 4 data.

Before analysing these spectrograms, it is important to justify the abscissa scale in terms of its maximum value. This end value of 450 kHz was chosen due to the frequency response of the sensor which has a high sensitivity between the regions of 50 – 400 kHz. In order to save computational time, a coarse version of the binned FFT was created for each of the channels in order to identify the frequency ranges of interest. In Figures 204 - 207 one can see the images selected after many attempts in altering the colour bar scale in order to identify these areas of interest. The bands of main importance which were consistent between the four channels, were in the lower frequency region and existed between 25 kHz and 250 kHz. Some amplitude alterations were also observed in the higher frequency regions between 300 kHz and 400 kHz, but for the purpose of this analysis these were not investigated further due to time constraints. It was nonetheless deemed important for a future study to be conducted into the reason why such wide broadbands of emissions were being produced.

Between the regions of interest, it was believed that the lower bracket of frequencies between 0 kHz and 50 kHz were mainly overpowered by what was likely to be AE due to mechanical noise from the test bench, since it was present throughout the test and seemed uncorrelated with wear. This unfortunately masked any detail that could have potentially been investigated within these lower frequency bands. The main area of interest was identified of being the region of 125 kHz to 175 kHz. As the test progressed these frequencies of interest seemed to increase in amplitude with time and therefore could be directly related to the wear depth of the liner material. This band appeared to behave in a very similar manner when compared between samples. In order to investigate this phenomenon further, a set of finer binned FFTs were conducted for each sample and the results are displayed in Figures 208 - 211.

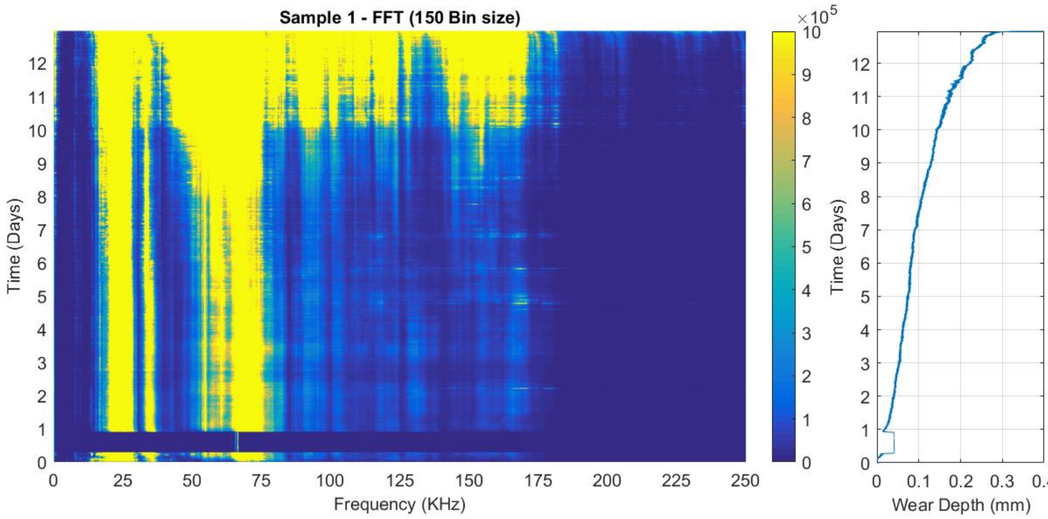

Figure 204 - Fine Binned FFT of Channel 1 data.

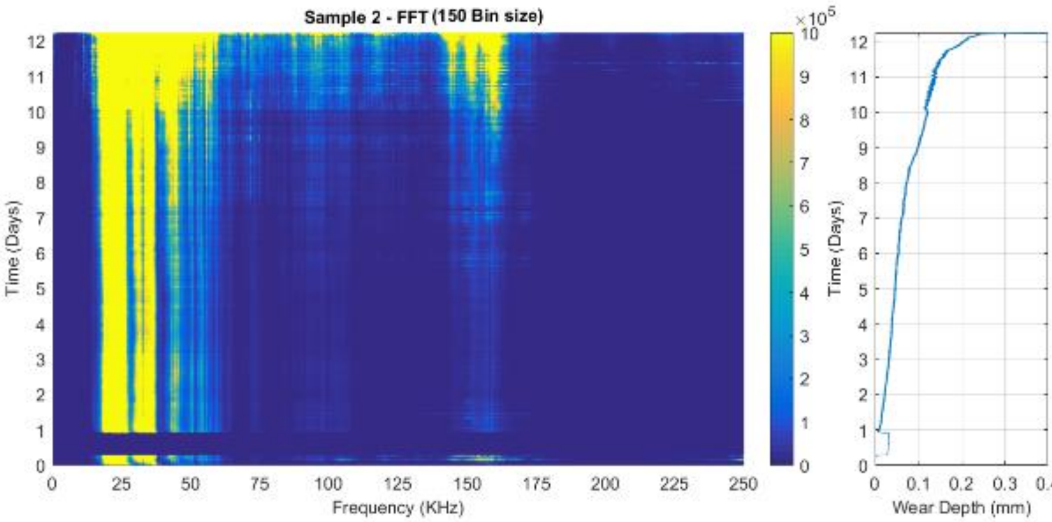

Figure 205 - Fine Binned FFT of Channel 2 data.

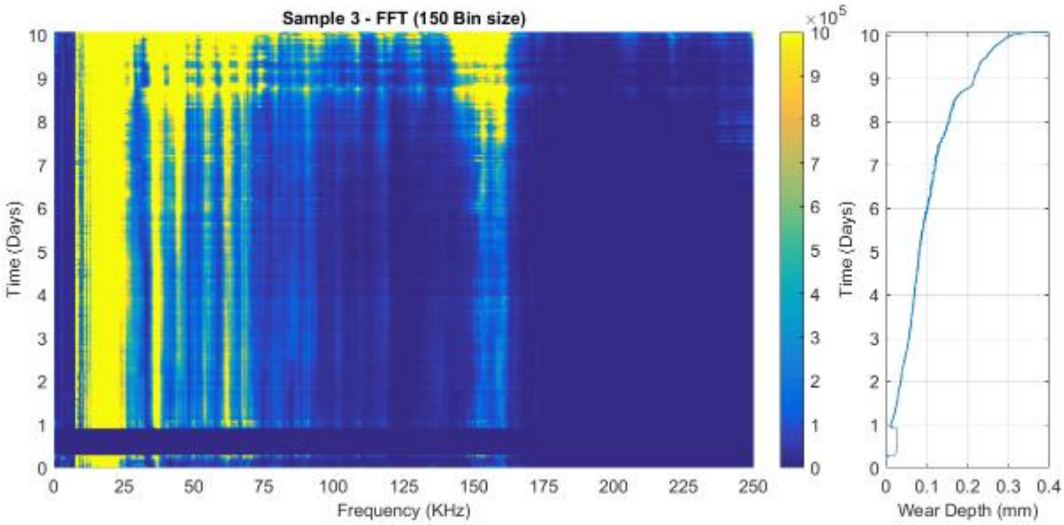

Figure 206 - Fine Binned FFT of Channel 3 data.

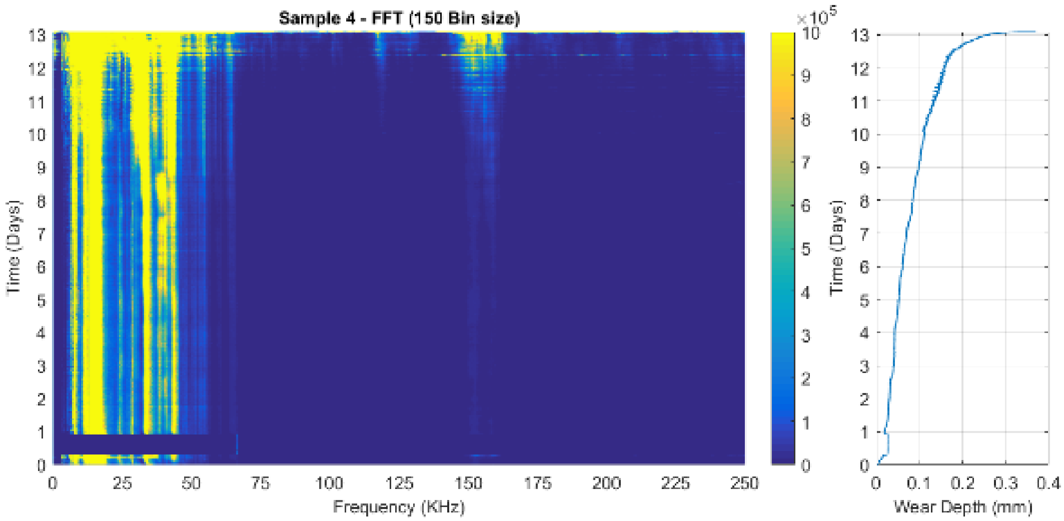

Figure 207 - Fine Binned FFT of Channel 4 data.

Considering these spectrograms in detail, allows direct comparison between the amplitude of the spectrogram FFTs and the wear depth during the time of testing. The goal of the thesis as a whole was to develop a condition monitoring technique to sensitively detect wear and therefore eliminate the chances of critical damage occurring. In order to do so, the frequency content and amplitude of the AE signals had to be able to be compared to specific wear depths. In order to try and establish this type of relationship, the region where the material composition of the liner underwent a transition from the PTFE rich region to the glass fibre structural backing was examined in detail. This region occurs at a wear depth of between 0.15mm and 0.18mm of wear.

As seen by the time domain inspection of the raw wavestreams, the FFT spectrogram clearly shows signs of this transition period. When considering Channel 1 for example, it can clearly be seen that when this glass fibre rich region is reached, a large increase in amplitude across most of the frequencies considered occurs. This phenomenon can also be seen in the previously mentioned 125 kHz – 175 kHz region throughout the channels under consideration. Therefore it can be said that when this transition period occurs, it can be detected and has the potential of being the basis of a usable technique to indicate to the maintenance team of the rotorcraft the exact wear depth, or at the very least the wear phase of the bearing. In order to further investigate the numerical value of such a change in amplitude, the energy of the specific frequency bands were taken into consideration (Figures 2012-215). Due to the range of amplitudes which were present throughout the test, each frequency band was allocated a specific amplitude scale. To further note, the time scales were cropped to the corresponding time of failure of the specific sample under investigation.

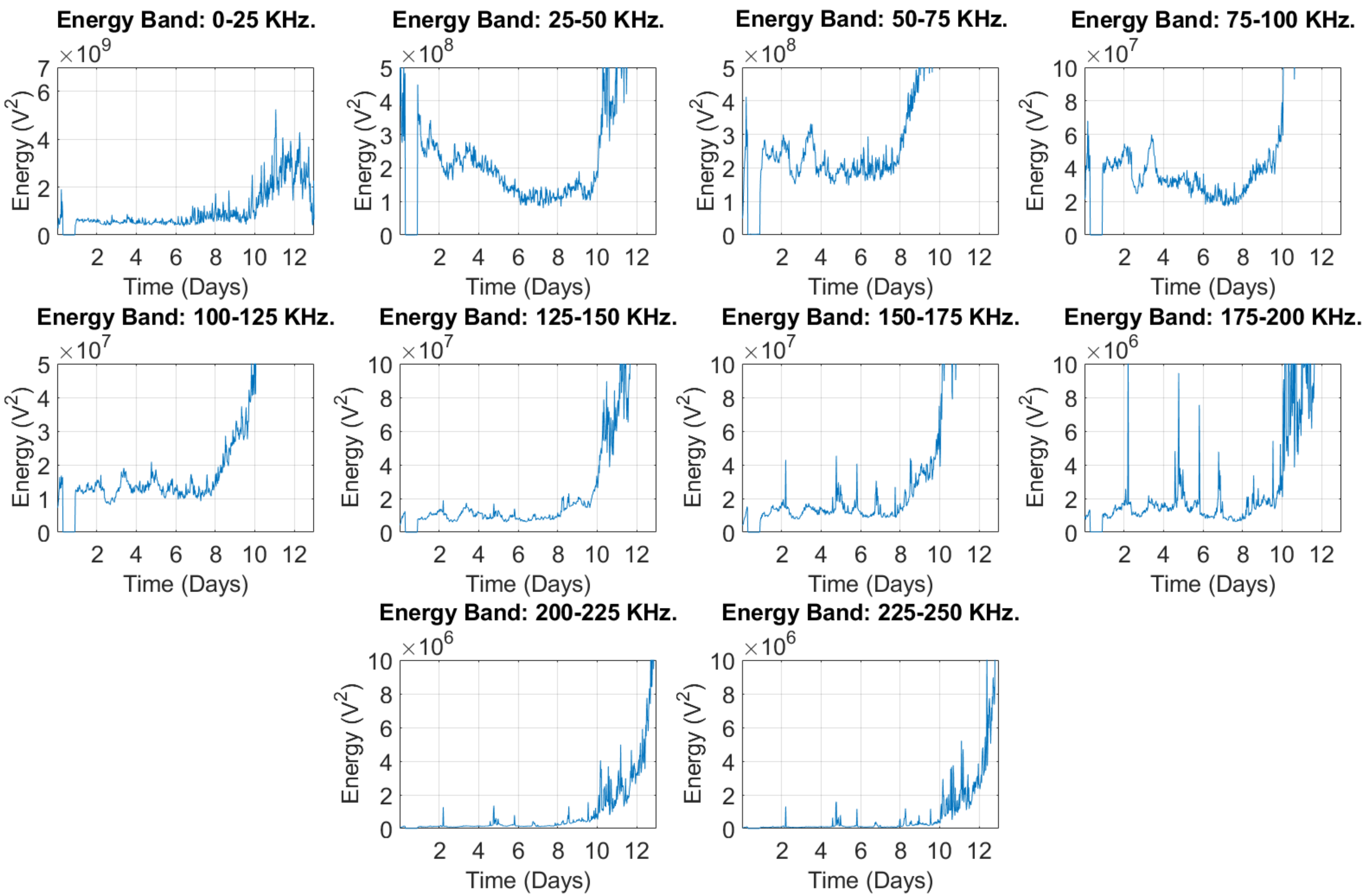

Figure 208 - Energy bands vs time – Channel 1.

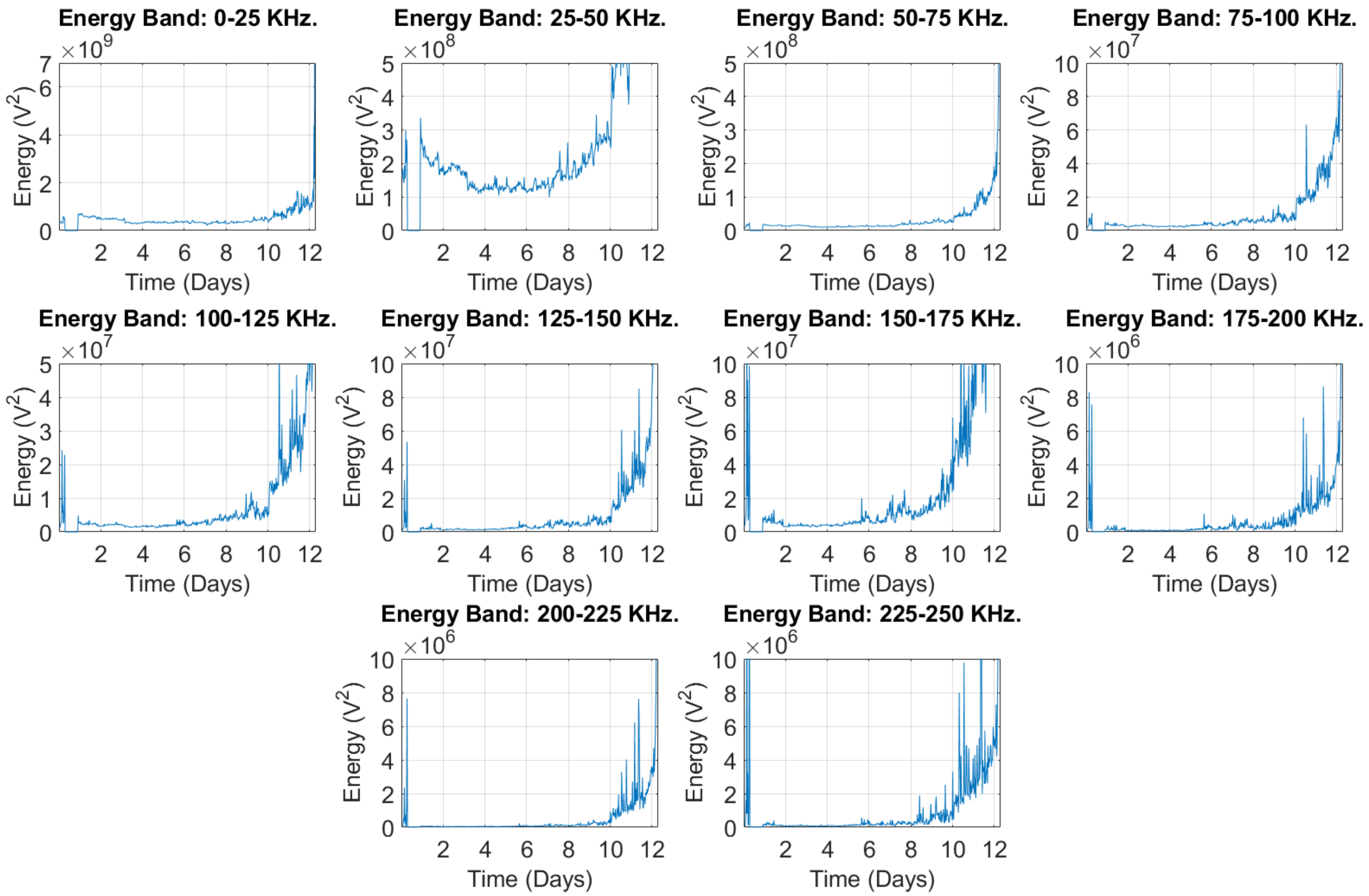

Figure 209 - Energy bands vs time – Channel 2.

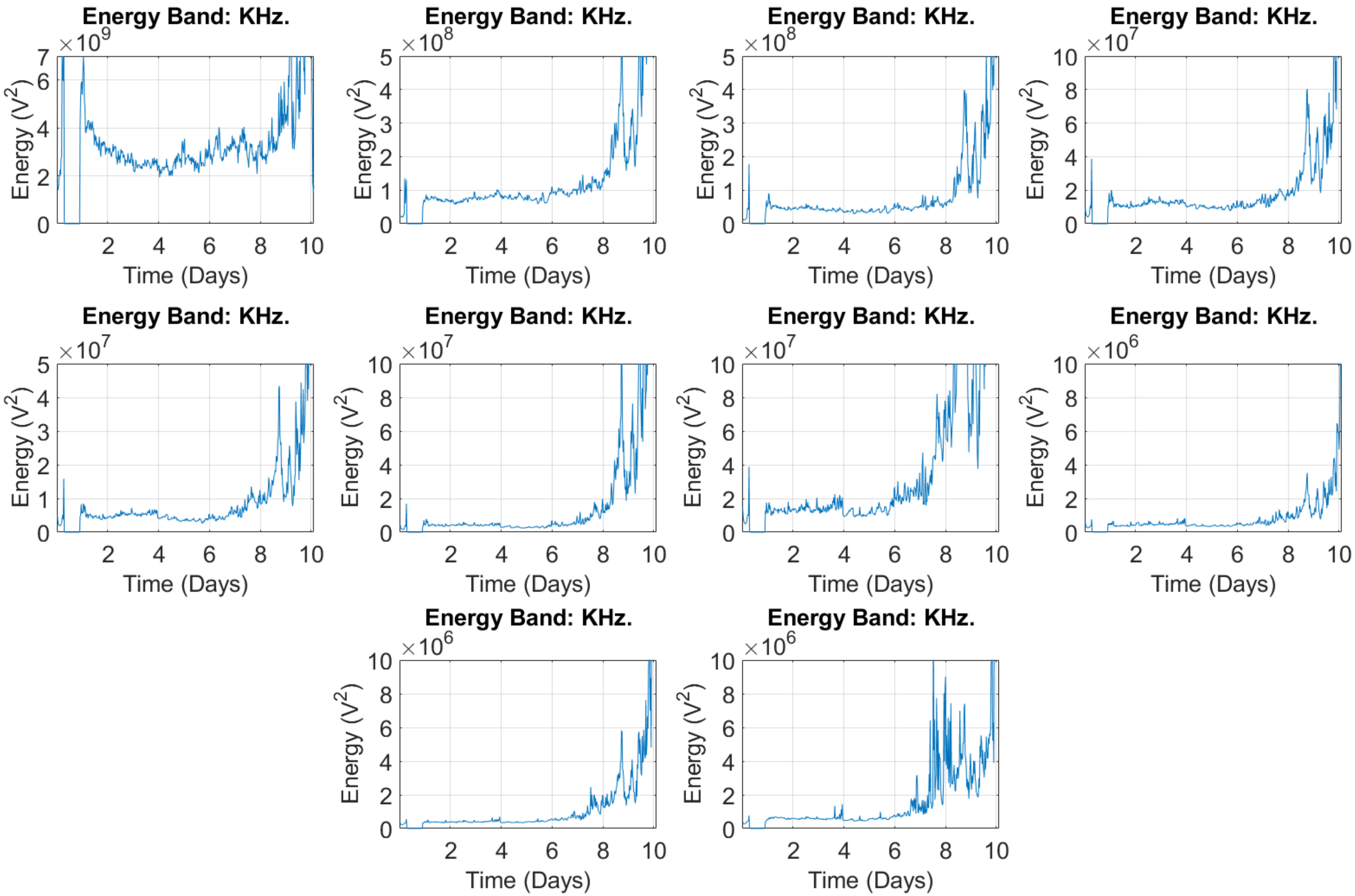

Figure 210 - Energy bands vs time – Channel 3.

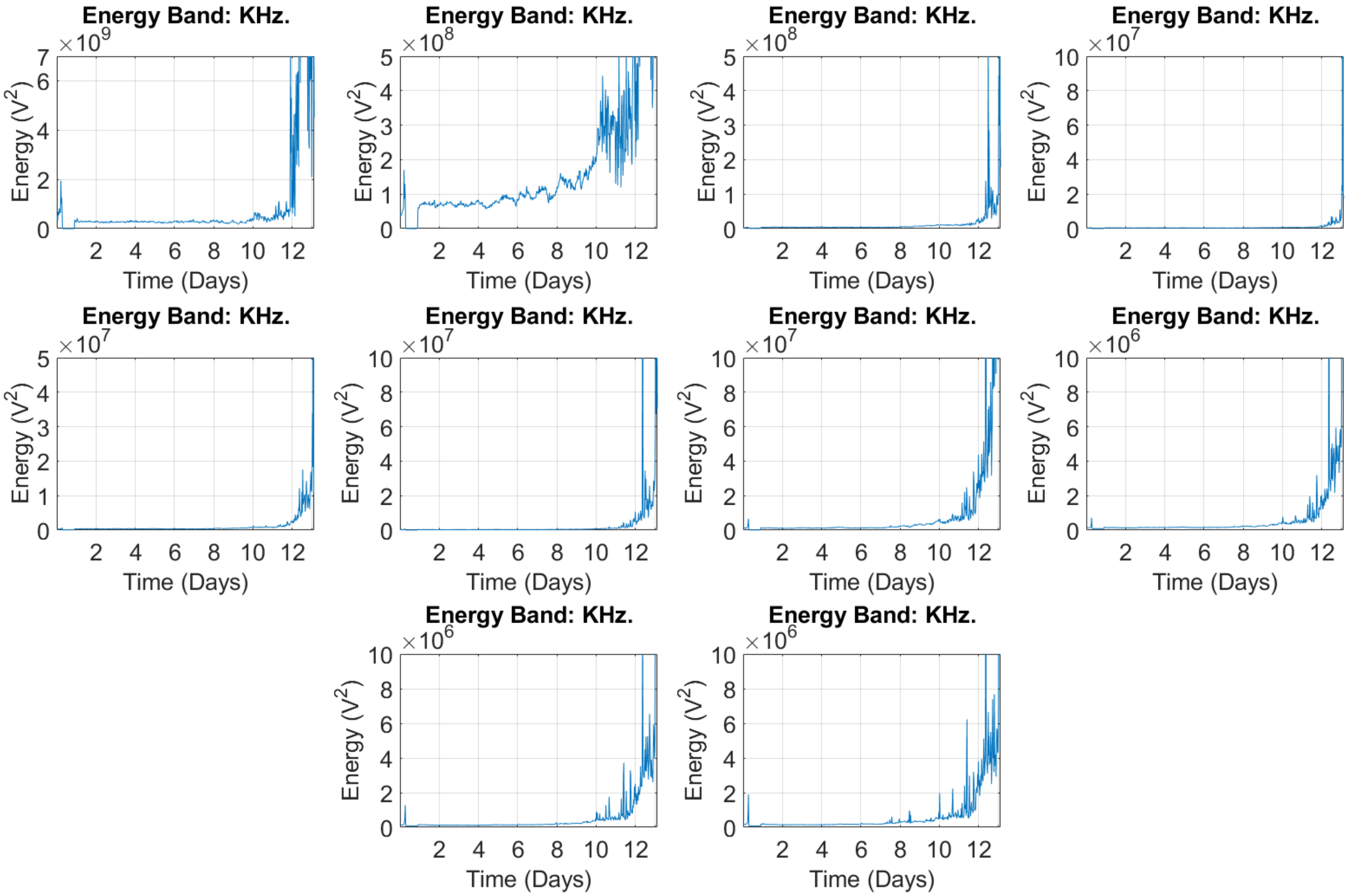

Figure 211 - Energy bands vs time – Channel 4.

In order to minimise repetition of broadly similar results, the analysed results from sample 1 will be discussed in detail. By considering the absolute values of the energy bands within Figure 208, some interesting trends can be observed. The amplitudes of the first three energy bands, 0-25 kHz, 25-50 kHz and 50-75 kHz, develop throughout the life of the test. As noted by literature, the initial wear-in phase of the bearing liner comprises of an aggressive wear nature, until a third body transfer layer has been developed upon the counterface. This pattern can be spotted within these energy bands, as the amplitude was initially at a higher level when compared to the energy values during the plateau region of the bearing liner's wear. This phenomenon could also be attributed to the non-conformal sliding interface between the cylindrical counterfaces and the flat samples, which would produce very high contact pressures at the start of the test due to the nature of the growing line contact. With regards to the plateau phase, which occurred between days 2 and 10, the amplitude of the energies within the majority of the energy bands remains at an approximately steady level, particularly in the 100-175 kHz energy bands. This plateau period is described as the least aggressive, in terms of the rate of liner wear rate, and once again the relatively non-volatile nature of the energy amplitudes confirms this speculation. Although these observations aid the understanding of the tribological conditions of the composite liner material during its wear phases, they do not provide a clear indication of the initiation of damage. This was due to the relatively calm nature of the wavestreams collected.

As previously discussed in the coarse FFTs produced in Figures 204 - 207, an interesting phenomenon starts to occur during the material composition transition period, at approximately 0.15 to 0.18mm of liner wear. Considering the example of sample 1, this occurs at approximately 10 days. By investigating the energy bands within Figure 208, one can observe that the energies of all frequency bands during the time of transition increase drastically. As previously mentioned, this could be attributed to the glass fibre-rich structural backing of the liner material coming into contact with the steel counterface, significantly increasing the generation of AE at the contact. At this point a series of wear mechanisms could potentially cause this increased amplitude, such as glass fibre cracking. This phase of liner wear could in fact be a catalyst to the rapid wearing of the liner material past this point. Although the structural backing is crucial to providing structural support to the material as a whole, wearing of this region could introduce glass fibre contaminants to the sliding surface. These hard particle contaminants could further aid the destruction of the liner via scoring. When hard particles enter the sliding contact region, they induce an uneven sliding surface geometry and therefore act as agressive asperities which leads to increased local contact pressures. This would in turn increase the friction coefficient of the bearing as a system and initialise an unwanted temperature increase. This temperature increase, although a negative attribute in tribological performance terms, proved very interesting and potentially useful in indicating damage, as described in the previous chapter, which considered damage detection via the use of temperature data alone. In order to validate the findings, the same analysis was applied to a further data set, where the wear of the bearing liner samples was recorded accurately in order to aid the comparison. Figures 216 - 219 show the binned FFT analysis from test 4 – Samples 1 – 4.

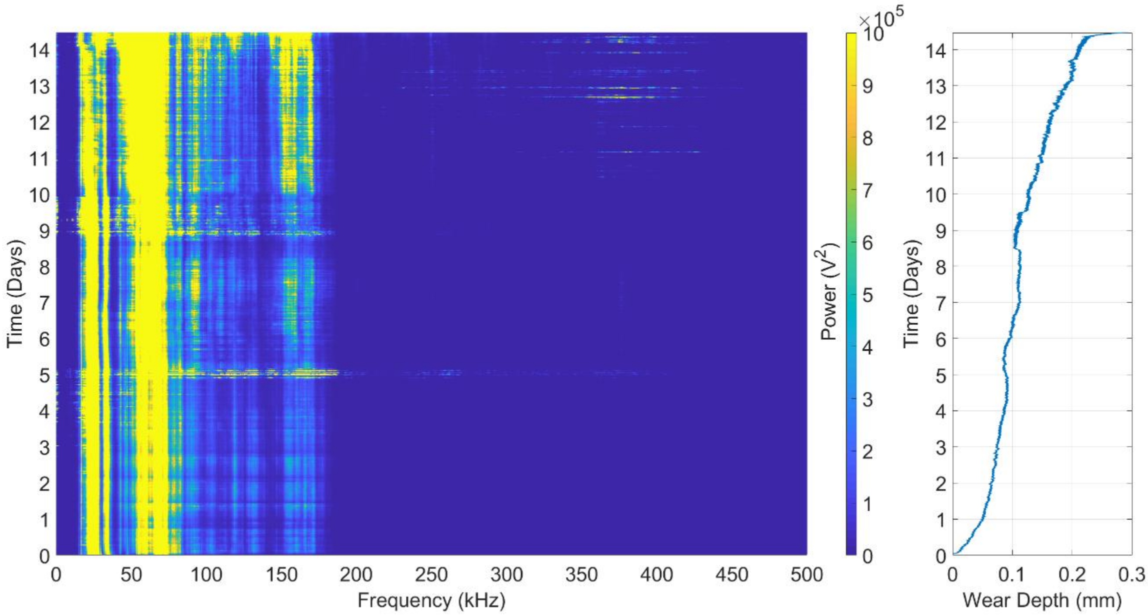

Figure 212 - Fine Binned FFT of Channel 1 data.

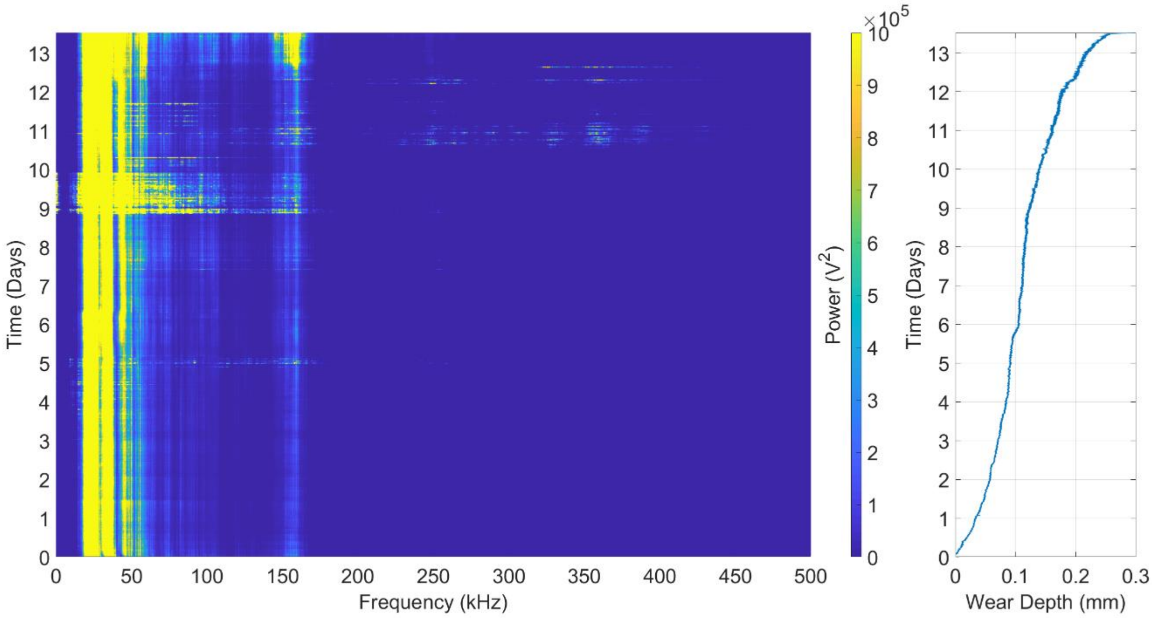

Figure 213 - Fine Binned FFT of Channel 2 data.

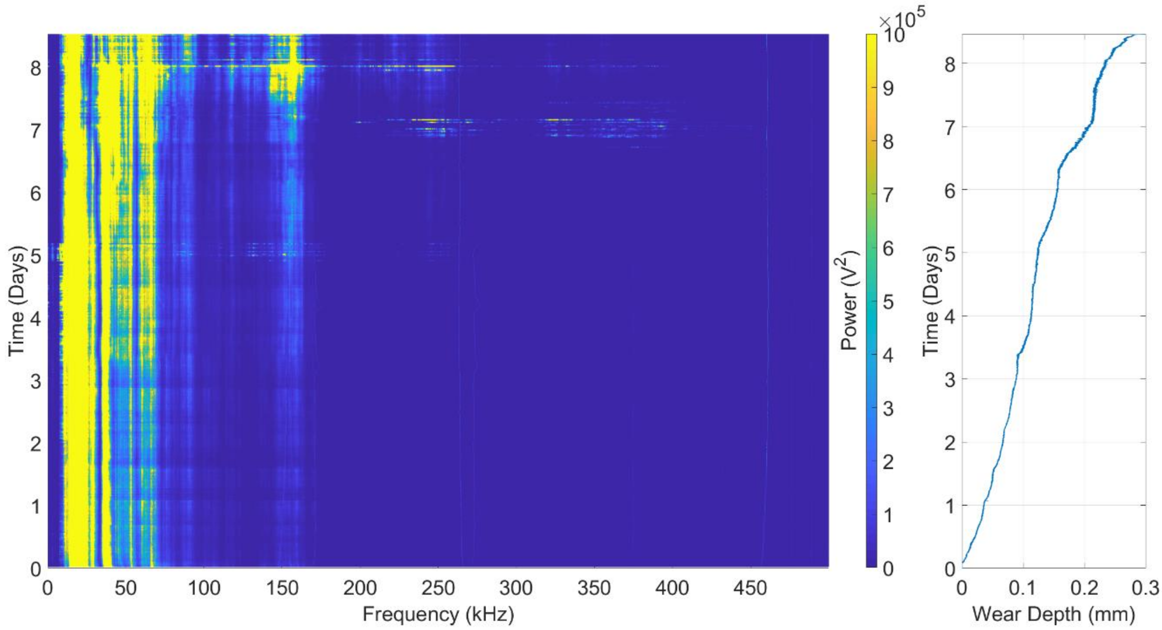

Figure 214 - Fine Binned FFT of Channel 3 data.

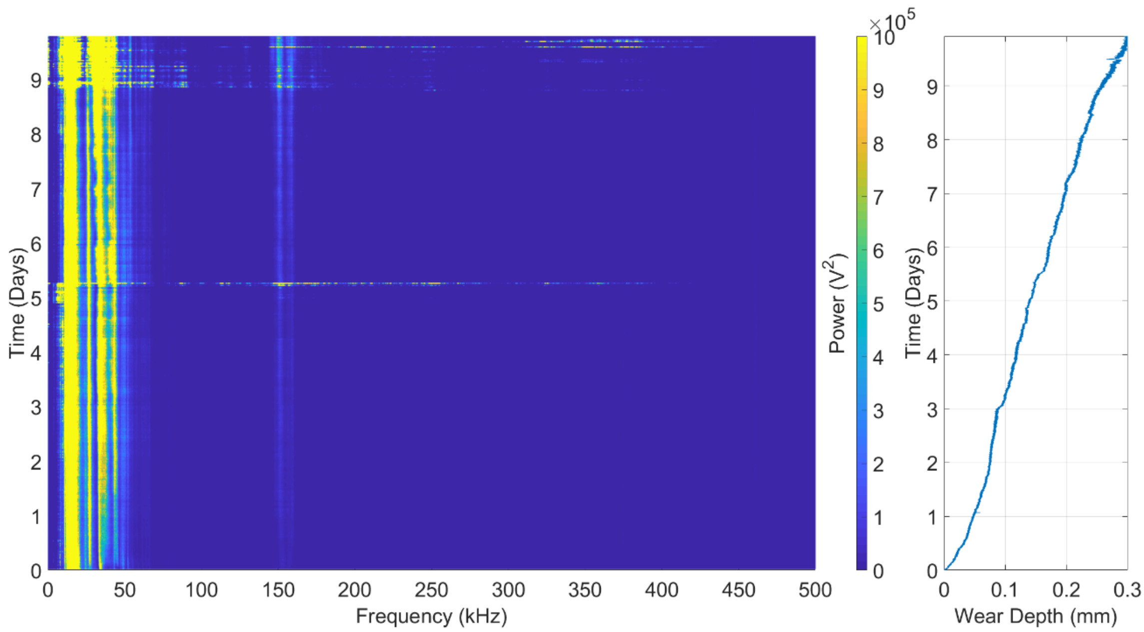

Figure 215 - Fine Binned FFT of Channel 3 data.

Figures 216 – 219 show very similar characteristics to the detailed analysis of the third test conducted. In all of the samples, it can be seen that the amplitude of the frequency band of 125-175 kHz can be seen increasing, as the glass fibre rich region (0.15-0.18 mm) is reached with the exception of sample 4. It was speculated that a minor misalignment could have occurred upon sample 4 during the testing procedure which lead to the inaccurate wear depth measurements. Furthermore, an anomaly within the test can be seen between days 5-6 and 9-10. The reason for the high amplitude recorded AE signals are currently unknown but it is speculated to have been a temporary fault with the test bench, as all samples were subjected to the noise at identical times.

This type of damage detection technique, could be extremely useful within the context of a condition monitoring system. When monitoring the health of such a critical part during flight, the use of more than one parameter as an indicator of bearing health would be beneficial in terms of increasing the robustness of a monitoring system. Using Acoustic Emission as either a secondary or in fact primary parameter could provide a much deeper insight into the tribological behaviour of the bearing as a system, during the hours of flight. Potential problems with regards to the physical application of the sensors required include the mounting points upon the rodend, along with the transmission of the gathered wavestreams to the data processing unit within a rotating environment such as the rotorcrafts main rotor, and the volume of data recorded by an AE system. In order to overcome the geometric issue regarding the position of the AE sensor, a 3D printed AE sensor could be incorporated within the design upon the face of the rodend. Although ideal, these types of sensors are still within the development phase and would be a future consideration as a solution. In order to overcome the issue with the AE system's energy intensiveness, a study is proposed to be conducted, where a flat response AE sensor would be mounted upon one of the samples and in turn the results would be analysed via an FFT. In turn, the frequency bands which appear to yield the most positive results could in turn be extracted and compared across different types of tests i.e. coupon testing with a static load, full bearing test with a static load and a full bearing test with a dynamic load. After the desired frequency bands have been determined, a narrowband AE sensor can be selected with an operating frequency range, which matches the one of the investigation. An additional future study is proposed, where the sampling frequency of the already collected data would be reduced and the effects on the final resulting analysis methods would be noted. If this investigation was to be successful, the real-time sampling frequency of the system, could in turn be reduced therefore allowing the system to operate in a less energy intensive state.

7.4 Glass fibre cracking investigation

7.4.1 Experimental setup

Previously discussed was the phenomenon which was speculated to contribute towards the increased amplitude at a certain wear depth during the liner material's wear process. This phenomenon was hypothesised to be linked to contact between the glass fibre structural backing region of the bearing liner and the steel counterface. In order to test this hypothesis, it was proposed to carry out an experiment where the noise of the test bench could be isolated and this material transition investigated in more detail. Initially, it was proposed to fit guard sensors around the area where Acoustic Emission was recorded, to allow the AE system to disregard background noise and extraneous signals. An initial study was conducted but was found to require an unfeasible number of extra AE sensors in order to provide the required guarding effect, leading to a lack of capacity on the PCI-2 PAC 4-Channel system used for data gathering.

Therefore, it was decided to use a ball on flat reciprocating wear test bench, described in Chapter 2. Due to its simplicity and single sample measurement, this test bench theoretically provided lower background AE signal levels and, due to the point contact nature of the test, a more gradual approach to the glass fibre region during a test. This test bench provides a reciprocating motion of the bearing liner material in contact with a counterface, in the form of a steel sphere. Small flat samples were prepared in order to fit the mounting clamp of the test bench. The load was applied via a vertical weight mounting guide and locked in place with a lock-nut. Taking into consideration the nature of this elliptical contact, the weight application was conducted by calculating the average contact pressure present during an experiment conducted on the 'Rig Q' test bench. The weight which was deemed appropriate for this test was 75N and the contact pressure evolution with respect to the bearing liner's is presented within Figure 216.

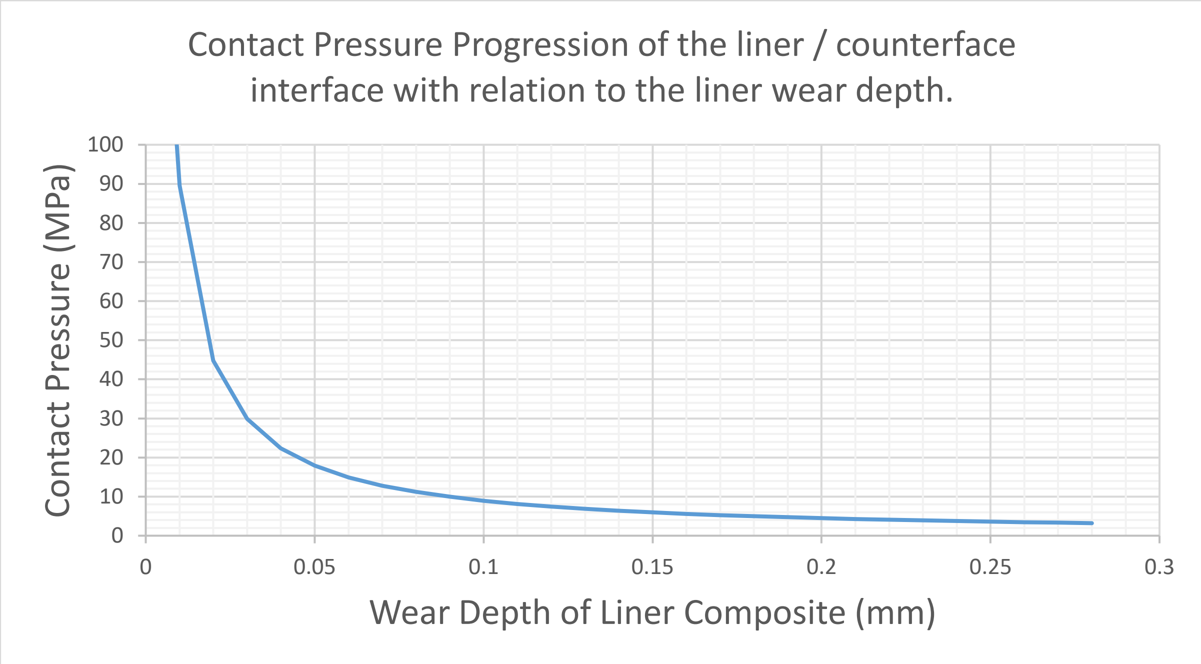

Figure 216 – Contact pressure evolution of the sliding contact between the counterface ball and the bearing liner.

An image of the test bench, along with the loading region is provided in Figure 217.

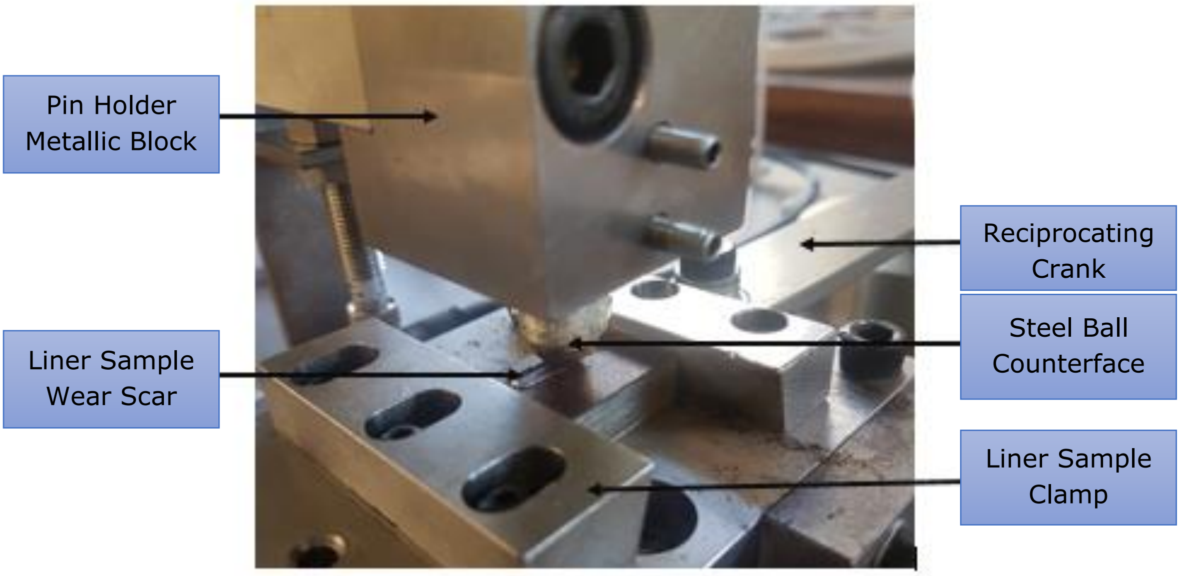

Figure 217 – Labelled contact region between the bearing liner sample and steel ball (counterface).

As previously discussed within the sensor location section of this chapter, the attenuation path to the Acoustic Emission sensor from the source of stress wave generation, is critical with regards to stress wave detection. Initially an R15S sensor was adhesively bonded on the metallic block with silicon Loctite. During an attenuation test, where a Hsu-Nielsen source was produced upon the steel ball, no stress wave was able to be detected by the AE sensor at that location. It was therefore decided to modify the pin design in order to provide a sensor location with an appropriate distance from the stress wave source and minimise the number of material interfaces which would attenuate the stress wave. Due to the geometry of the pin, a sensor with a smaller diameter had to be selected. A general study was conducted with regards to the size and frequency response of the sensor and it was found that a Mistras Nano30 Sensor provided the best balance between size and frequency response. This sensor had the advantage of a smaller overall geometry (7.93 mm diameter), along with a good frequency response over the range of 125-750 kHz. In order to mount the sensor, a flat section, 8mm in size, was machined onto the pin in order to facilitate the attachment of the new Nano30 sensor. Figure 218 shows the machined flat, along with the adhesively bonded sensor.

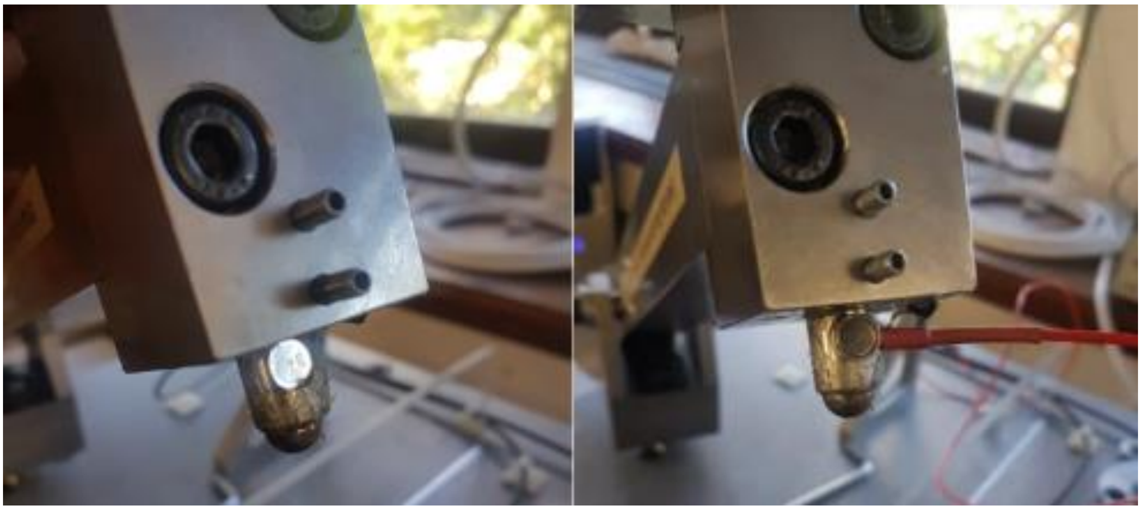

Figure 218 –Machined flat on the ball-holder pin (left), Nano30 sensor adhesively bonded onto the machined flat (right)

Once the sensor was fully bonded, the experiment was run until metal to metal contact was achieved to ensure the bearing liner had fully worn. In order to monitor the wear, an inductive sensor located underneath the loading arm was used to measure the vertical displacement of this component, as shown in Figure 222. Once the geometrical advantage of the loading arm was taken into account, this displacement measurement could be converted into a wear measurement at the contact point.

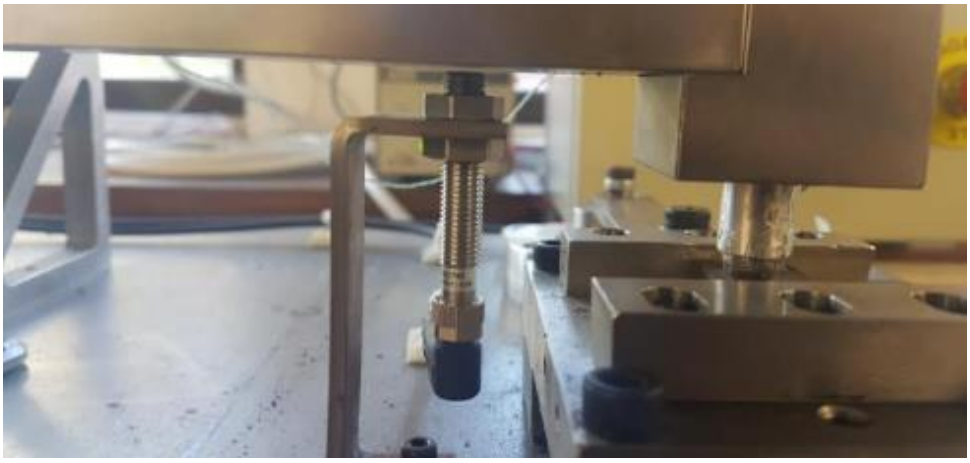

Figure 219 – Image of inductive sensor used to measure the wear of the bearing liner.

7.4.2 Results

Throughout the test, wear and temperature were collected as seen within Figure 220, where the temperature is displayed as a temperature rise above ambient.

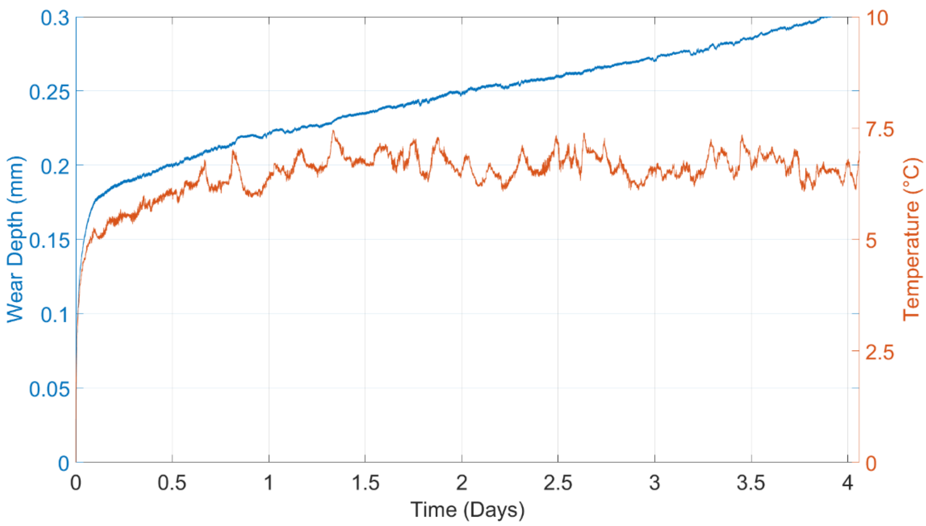

Figure 220 – Wear and Temperature results from the reciprocating test bench test.

Unfortunately the temperature results did not yield any positive results. This was speculated to be due to the location of the thermocouple, which was mounted a substantial way away from the sliding contact area in order to avoid damage to the sensor. Although the temperature results were not ideal, the main focus of this study was to conduct an investigation on the AE activity of the wearing bearing liner sample with respects to the liner wear depth.

Acoustic Emission data was collected in the form of raw wavestreams with the same time interval of 30 minutes and sampling rate of 2 Mbps as the tests conducted on the Rig Q test-bench. Initially, the raw waveforms were plotted against their respective reciprocation time in order to analyse the pattern of the AE activity (Figure 221).

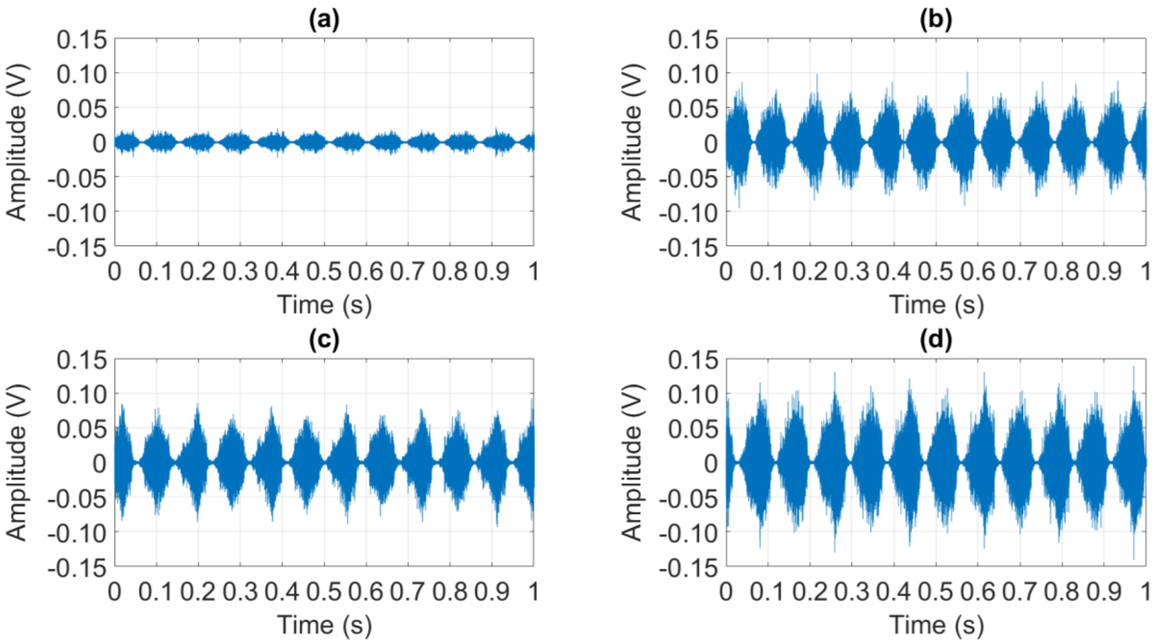

Figure 221 –Waveform progression throughout the test: (a) Wear-in period (2 hours into the test), (b) Start of the steady wear phase (12 hours into the test), (c) Approaching the failure stage (3 days into the test), (d) Approaching failure point (3.7 days into the test).

Figure 221 displays very similar characteristics to the wavestreams which were gathered from the tests conducted upon Rig Q. As seen by all four waveforms, the AE activity follows a very similar speed-related pattern as that seen within Figure 195 (Page 210). Also, the AE activity at the wear-in phase of the bearing liner, was of a lower amplitude than the waveforms collected during the plateau and failure phase. This was speculated to be attributed to the PTFE rich environment at which the sliding contact was operating during this phase. As seen by Figure 220, waveforms (b), (c) and (d) of Figure 221 were all gathered at a wear depth where the glass fibre rich composition of the liner was in contact with the counterface ball.

In turn, the data were analysed using the binned FFT approach as discussed previously and the analysed wavestreams were meshed together, to provide a spectrogram as shown in Figure 222.

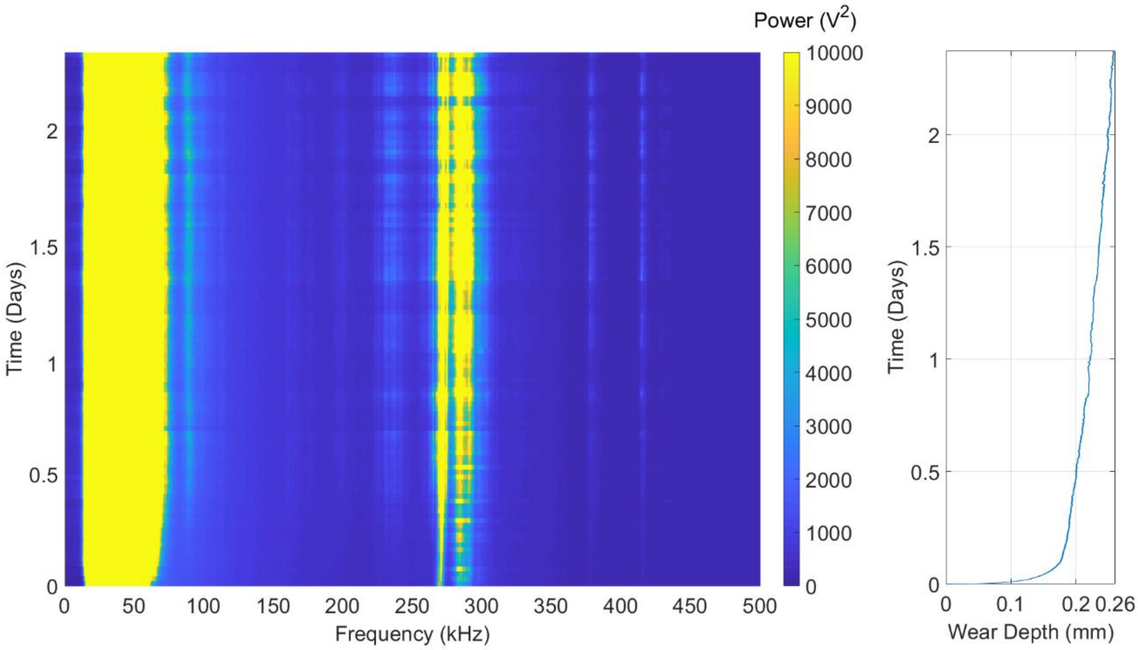

Figure 222 - Binned FFT analysis of reciprocating wear test bench wavestreams.

Initially, it was evident that the type of test which was conducted upon the bearing liner was very aggressive in nature. This is displayed within the wear data, as seen by the rapid wear of the composite liner up to the point of the structural backing, at the wear depth region of 0.15-

0.18mm, which is reached after 2 hours. After that wear milestone, the wear rate throughout the test was relatively smooth until the point of failure. When the wear depth of 0.15-0.18mm is reached, only a small region at the tip of the spherical counterface will be in contact with the glass fibre backing region. Therefore, in order to establish a relationship between the area of contact of the glass fibre backing and the Acoustic Emission activity produced, a simple MatLab code was created which related the wear of the bearing liner to the surface area of the ball counterface which is in contact with the glass fibre structural backing. The MatLab script works on the basis of calculating the surface area of a segment under consideration and is as follows (Equation 21):

$$Area\ of\ glass\ fibre\ contact = 2 * \pi * PinRadius * (Wear - 0.15) \tag{21}$$

By knowing the pin radius (9 mm), along with the wear depth at which this glass fibre rich region is reached (0.15 mm), it was possible to calculate the surface area of the ball in contact with glass fibre. Once again for this type of calculation, a definitive glass fibre transition wear depth had to be chosen, so from the 0.15-0.18mm range, the lower value of 0.15mm was chosen. Figure 223 shows the replotted binned FFT alongside glass fibre contact with respect to time.

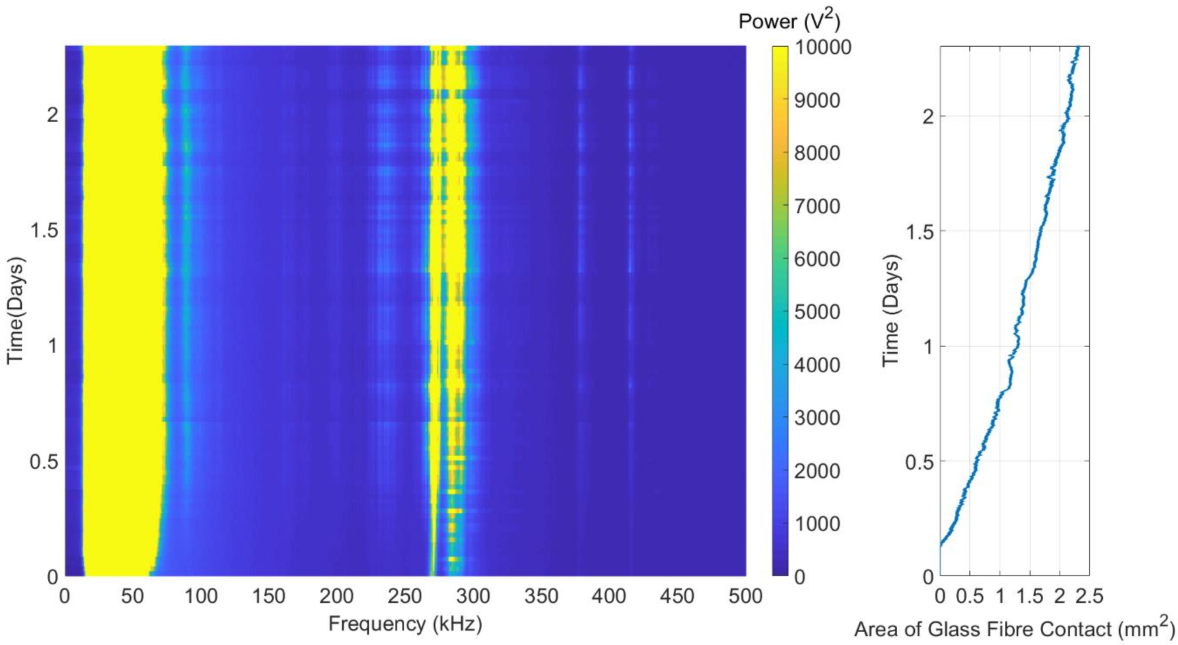

Figure 223 – Binned FFT (left), Surface area of glass fibre contact (right)

In order to analyse the data displayed within Figure 223 further, an energy study was conducted in order to view the progression of energy levels in each frequency band over the length of the testing period (Figure 224). To note, once more the scale of the energy amplitudes varied largely between each frequency band, therefore an individual energy magnitude scale was given for each subplot.

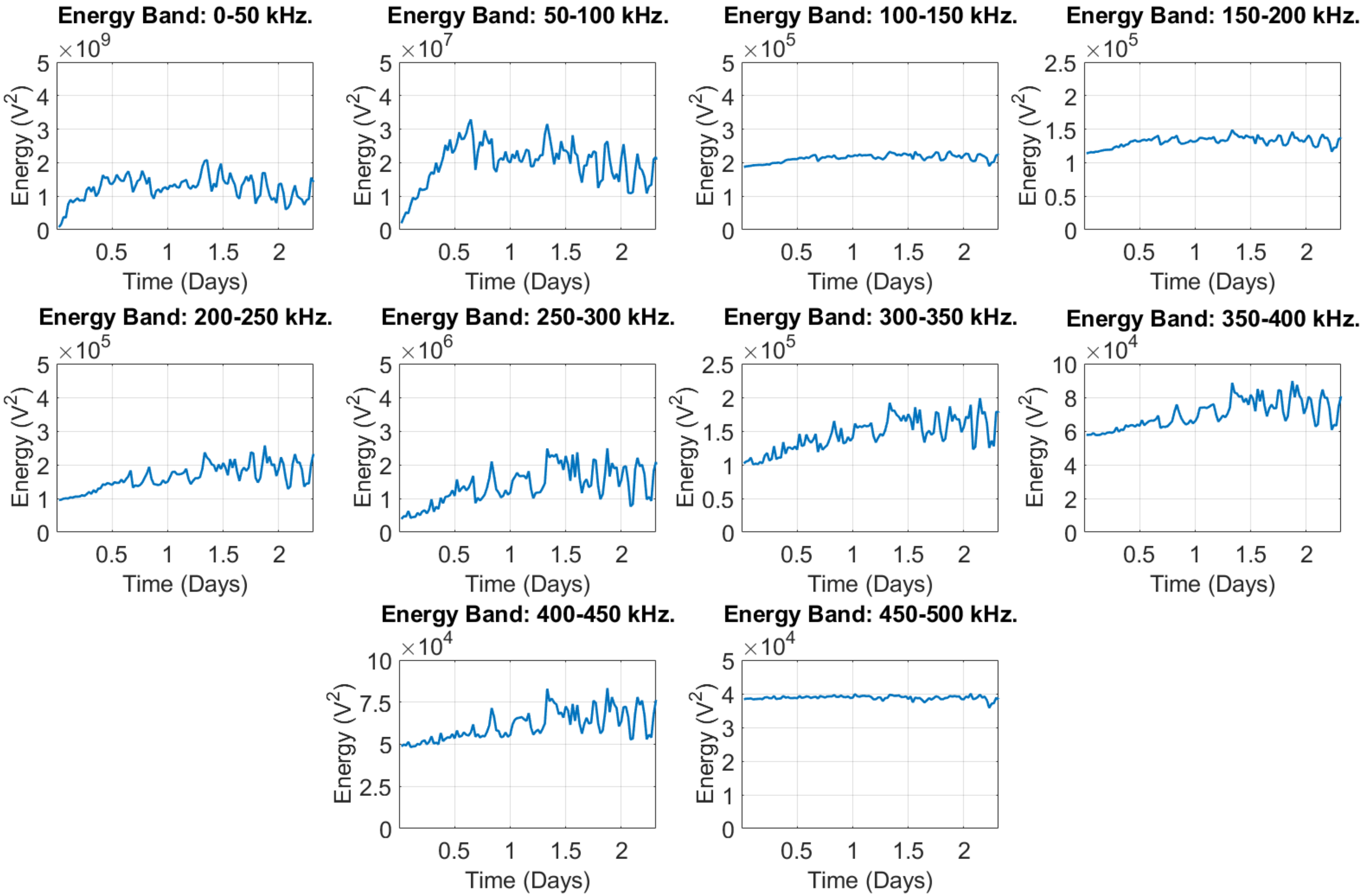

Figure 224 - Energy bands vs time.

As seen by the relationship, as the glass fibre comes into increasing levels of contact with the steel ball, there is a large increase in the amplitude of the energies throughout all frequency bands. The frequency bands which are of highest interest include the 75-125 kHz band, which is faint and increasing in amplitude and the 250-325 kHz band which lays in a higher frequency range. In both cases, an instant increase in amplitude was observed when the structural backing came into sliding contact with the ball.

Therefore it was confirmed that the hypothesised theory which relates glass fibre contact with the increased amplitude of the wavestreams gathered was in fact valid. Future work on this topic could include a study on the mechanics of the glass fibre damage with relation to the amplitude and frequency of the emitted AE signals. As can be seen by comparing the FFTs from the Rig Q test bench data and the reciprocating wear test bench data, a shift in the frequency ranges of importance occurred. This frequency shift could be attributed to the sensor type which was used or potentially the wear mechanics of the reciprocating wear rig. All these factors would need to be included in the continuation of this work.

7.5 Full bearing testing

Although the concept of applying Acoustic Emission monitoring upon the bearing system during flight seems very appealing, the practicality of such an energy intensive system presents some difficulties. In order to retrieve the Acoustic Emission data, a processing unit would have to be located on board the rotorcraft. Although recent advances in miniaturised systems do not rule this out, there are further complications including the sensor wires, which would need to pass through the swashplate of the rotorcraft and into the rotating pitch-link components. Again, this could be overcome by using wireless nodes, but, as one can imagine, this procedure would be of great difficulty due to the complexity of the potentially proposed design, which would require vast amounts of wireless communication qualifications. It is important to mention that all results within this chapter have been non-dimensionalised with respects to the time-axis as a response to a request made from the industrial sponsor.

7.5.1 Preliminary AE study

To allow the evaluation of the potential of an AE condition monitoring technique upon full scale self-lubricating bearings, the SKF test bench (Rig H) was equipped with AE monitoring hardware. In order to gather the required data and allow for direct comparisons between the Rig Q and Rig H results, an R15S sensor was adhesively bonded onto the end of the rodend. To achieve this, a specially instrumented rodend design had to be developed to incorporate a flat mounting point for the AE sensor. Figure 225 shows the sensor position upon the rodend structure.

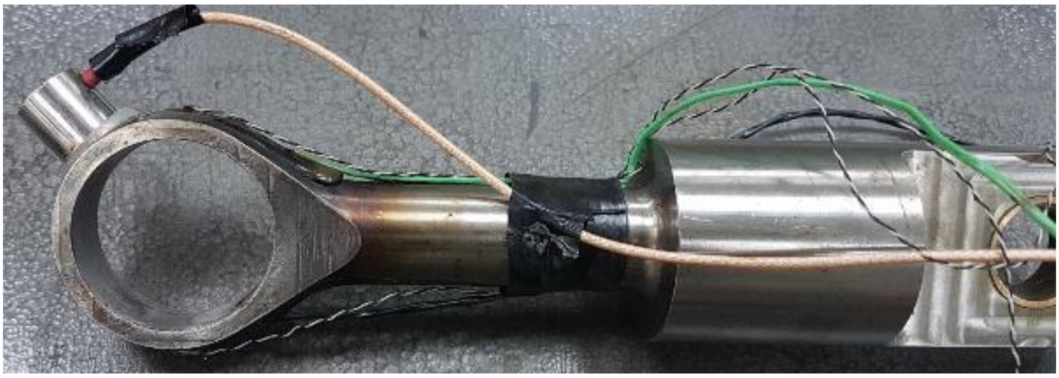

Figure 225 – Rig H rodend with bonded AE sensor and four thermocouples.

Identical monitoring parameters to those used for Rig Q were employed, which consisted of a wavestream being gathered every 30 minutes for a duration of 1s with a sampling frequency of 2 MHz. Initially, the physical parameters of the test were evaluated and these are shown within Figure 226.

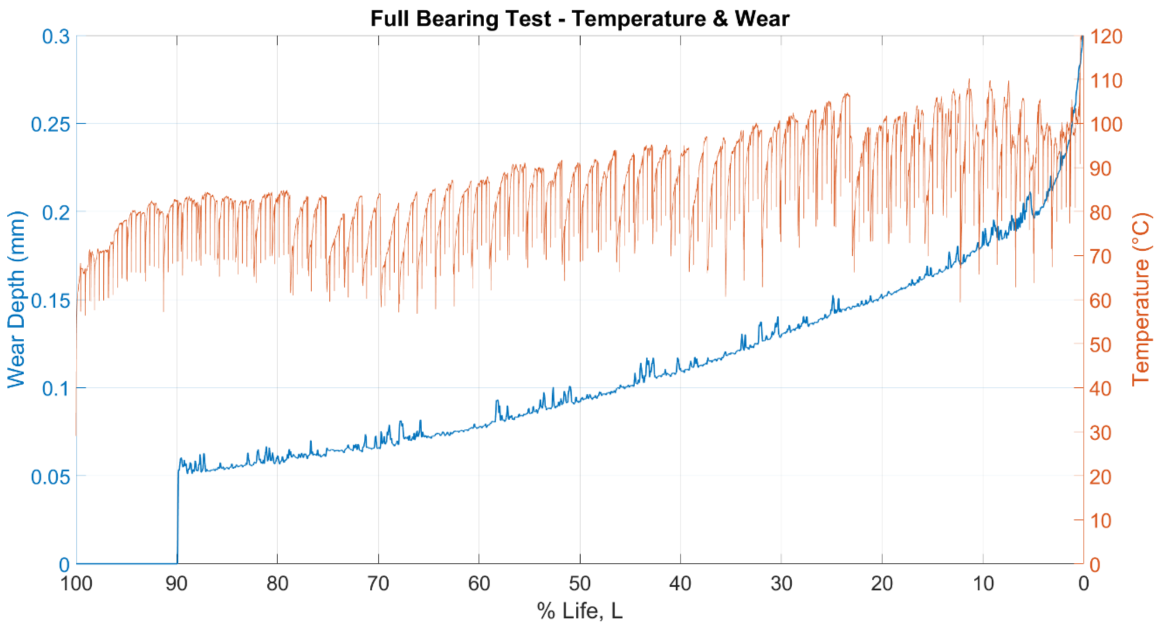

Figure 226 - Physical parameters of a full scale bearing test with respect to the bearing's % Life remaining.

To note, there was an issue with the LVDT of the test bench for the first 10% of the bearing's life and unfortunately no data was able to be gathered during this time period. One may also notice that the temperature graph has multiple peaks and troughs throughout the wear process of the bearing. This was due to the hourly pause of the test procedure in order for the test bench to make the pre-set quasi-static measurements. As previously discussed these measurements included the wear depth of the bearing liner in the form of clearance and also the friction of the bearing during a controlled reciprocation of the inner ball. The trend seen by the temperature results indicated the previously discussed wear-in, plateau and wear out phase of a typical bearing liner. The temperature has an initially high average value during the first day of running in, at which point the sliding temperature falls into a steady state. The plateau period lasted until around 35% of the bearings life, where the temperature started to show signs of increase. During the wear-out or failure phase of the bearing liner, the temperature reached a steady average value of around 100°C during the final day of operation, before finally failing due to metal to metal contact, at which the temperature exceeded an operating condition of 120°C.

In order to evaluate the reason why such temperature changes occur, an investigation into the torque values throughout the wear process was conducted. In order to measure torque during the quasi-static measurement of the test bench, a compressive load is initially applied and a measurement is made during the slow reciprocation of the inner ball (Figure 227).

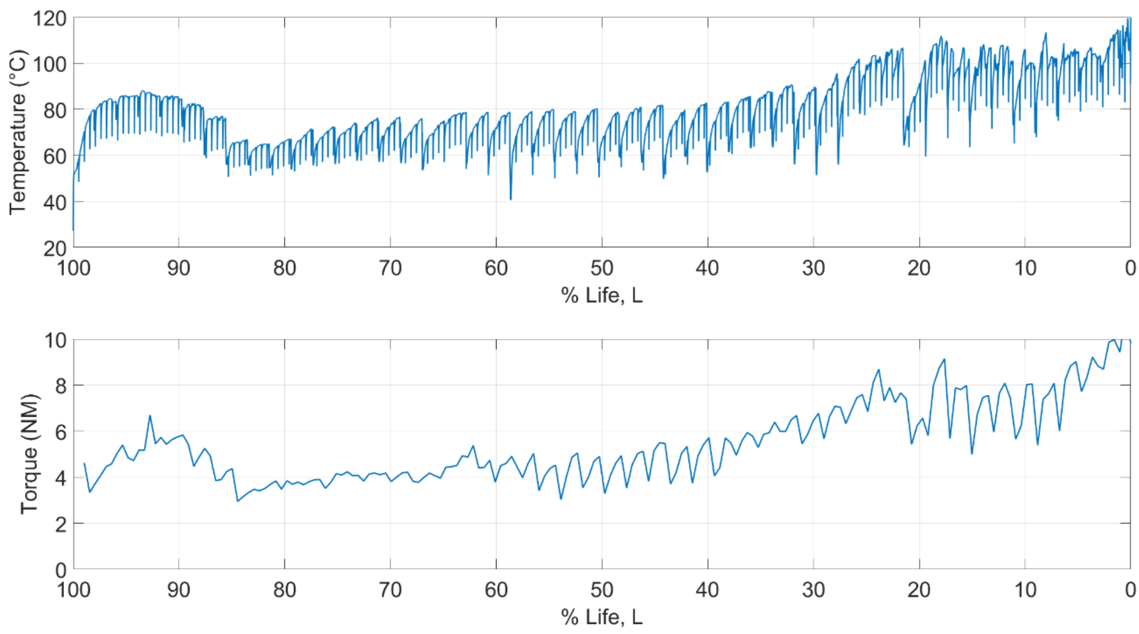

Figure 227 - Temperature and Torque comparison with respect to the bearing's % Life remaining.

As can be clearly seen, the general trend of the temperature curve during the lifetime of the bearing, closely follows that of the compressive torque measurements made during the quasi-static measurements of the test bench. It can further be noticed, that as the glass fibre region comes into contact with the counterface at around 35% Life, the values recorded by the torque measurement become more volatile than their steady state equivalents during the plateau phase. This feature could be further exploited by a condition monitoring system in order to provide an alarm when this glass fibre-rich region is reached.

Having looked at the temperature and wear of the test, to evaluate the behaviour of the acoustic emission results, sets of raw wavestreams were chosen at different wear stages throughout the test and plotted with respect to time (Figure 228).

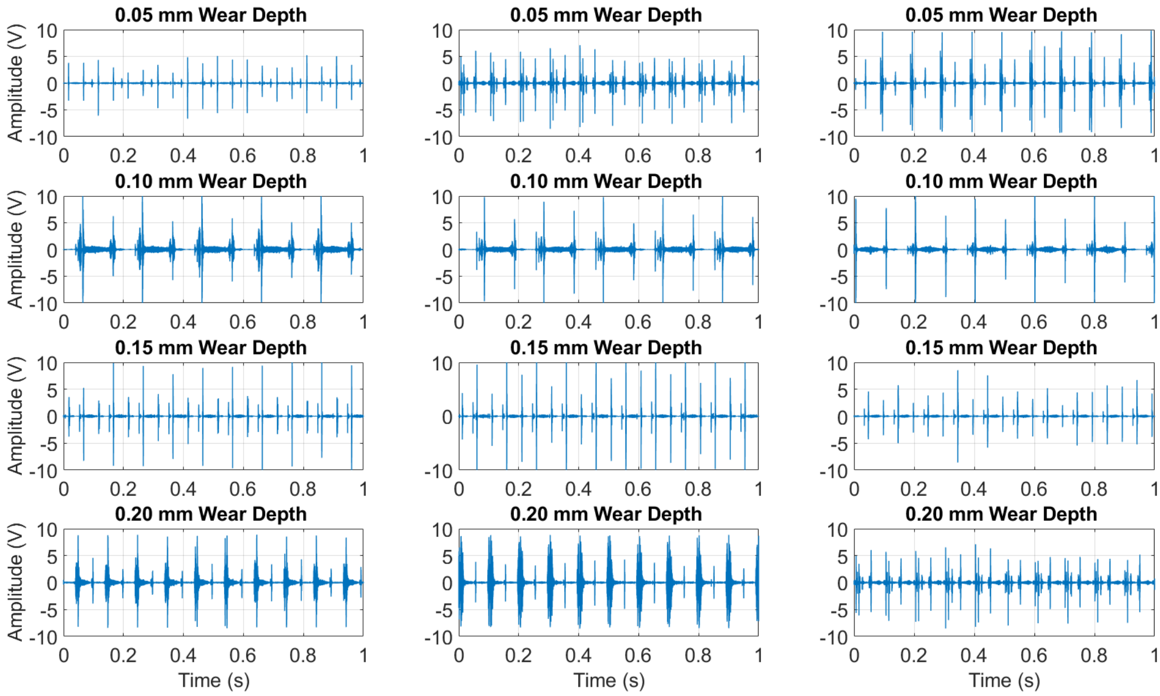

Figure 228 - Raw wavestreams of Rig H through different bearing wear depths.

The initial comparison between the waveforms presented in Figure 228 and those from the Rig Q testing in Figure 199 (Page 212) comes in the form of the amplitude of the recorded stress waves. As it can be observed the peak amplitude of the waveforms gathered from the full bearing test bench largely outscaled those from the coupon test bench. This was speculated to occur due to the larger sliding contact area within the fully conformal bearing as opposed to the accelerated line contact conditions of the coupon test bench. Furthermore, similar amplitude spikes as those observed within Figure 199 can be seen to occur. As previously stated, these spikes occur at the start of an oscillation where the sliding speed is at a zero value. It is hypothesised that these spikes occur due to the stick-slip nature of reciprocating contacts.

A further interesting detail of the waveforms within Figure 228 was the observation of the evolution of the recorded stress waves. Although the shape of the waveforms does not closely match those gathered by the coupon test bench, a similar evolution with regards to wear can be seen. At the start of the testing, the waveforms appear to have low amplitude diamond shapes with multiple spikes being present during each recorded reciprocation. These large busts of energy are speculated to be attributed to the relatively aggressive wear-in period of the bearing liner, as a third body transfer layer is in the process of being formed. During the steady wear phase at a wear depth of 0.10mm, the waveforms appear to increase their mid-reciprocation amplitudes, while also displaying a prolonged and increased amplitude at the point of a reciprocation direction change. Although the reason for this increase was not discovered, it was thought to be potentially attributed to a higher stick-slip magnitude, due to the PTFE rich sliding contact nature during this wear phase. During the phase where the glass-fibre rich bearing liner region becomes present within the sliding contact, the magnitude of the mid-reciprocating amplitude values decreases once more and the mid-reciprocation amplitude spikes become present. These mid-reciprocation amplitude spikes were thought to be linked to cracking of the glass fibres in contact with the reciprocating counterface. Finally, during the latter stages of the bearings life where the majority of the contact is between the structural backing of the bearing liner and the counterface, large stress wave amplitudes were observed throughout the reciprocation motion with a particular increase of amplitude and duration occurring at the points of the reciprocation direction change.

To provide similar analysis as of that applied to the AE data from the coupon testing, a binned FFT was created from the data gathered throughout the bearing's life (Figure 229).

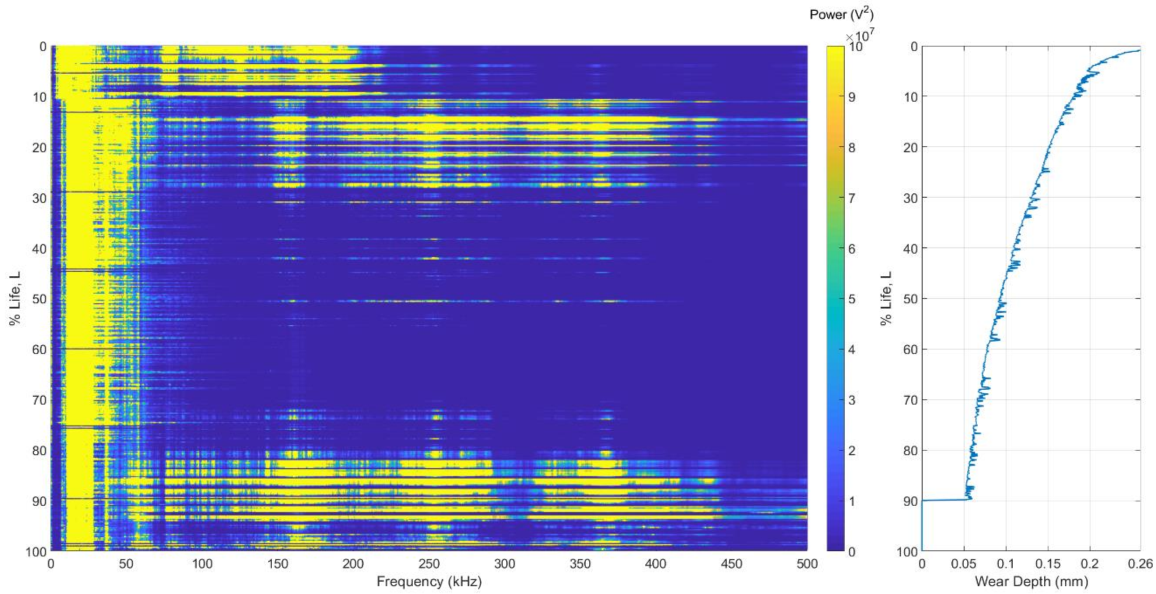

Figure 229 - FFT from a full bearing test with respect to the bearing's % Life remaining.

One can clearly see the amplitude level separation with regards to the wear depth of the bearing. During the wear-in phase, high levels of amplitude are seen with a very wide broadband. Once again, this was speculated to be attributed to the energy required by the bearing as a system in order to establish a third body transfer layer upon the reciprocating counterface. During the steady-state wear region of the test, lower amplitudes were seen in the higher frequency regions when compared to the wear-in phase. As the wear depth approaches the glass fibre transition period, the energies from these higher frequency bands become present once more, indicating higher levels of wear due to the composition change of the sliding contact region. An unexpected event occurred during the failure stage of the bearing, where a clear frequency shift was observed at the lower frequency ranges. The amplitudes at the higher frequencies once more decrease and a roughly 2-3 kHz frequency shift is seen by the consistent energy band between 10-30 kHz. The reason for this shift is currently unknown, but is speculated to have been due to the operating temperature of the sensor at the time which was approaching 100°C. To further investigate the energy of the frequency bands during the wear period, such bands were once more separated and their energies plotted against % Life of the bearing during operation (Figure 230, Page 247). This investigation allows the reader to numerically view the energy amplitudes described previously with regards to the binned FFT analysis. The subplots are once again assigned different scales in order to allow the trend of the energy data to be seen clearly. As previously described, the regions of highest amplitude within the data can be seen during the wear-in phase of the bearing, where the third body layer is being established upon the counterface. During the steady wear phase of the bearing's operation between 80-50% of its remaining life, the amplitude of the waveforms remained at a low value and in turn increasing significantly when the glass fibre region comes into contact with the counterface. It is interesting to note that the energies of the majority of the frequency bands decreases during the end of life stage but as previously discussed this was credited to the malfunction of the AE sensor at the time of recording.

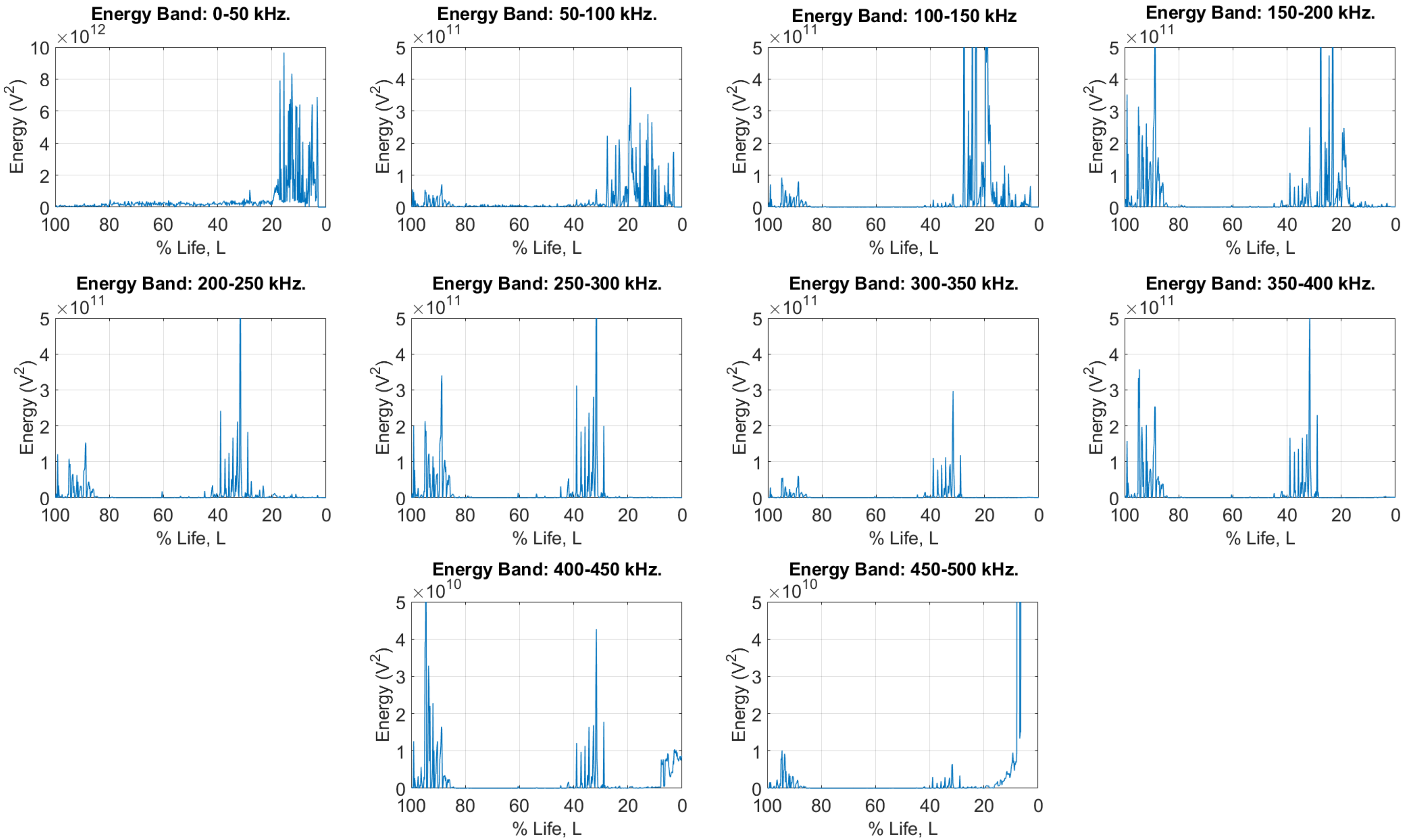

Figure 230 – Energy breakup of frequencies with respect to the bearing's % Life remaining.

7.5.2 Real life application of the AE methodology

Having observed the potential of the acoustic emission results, a solution was to be found regarding the energy intensiveness and sensor integration of the system. In order to tailor the AE application onto a system which would be simple to use via an operator and would not require any sort of requalification for flight, a method which could potentially be used on-ground was proposed. The method consisted of a controlled measurement, via the use of the pilot's controls, in order to achieve a full reciprocation of the blades through a required angle of ±10°. During this reciprocation interval an Acoustic Emission wavestream would be gathered and compared to a healthy signature, which could have been gathered during the healthy period of the bearing i.e. after a small number of flight hours. To achieve such an investigation, the full bearing test within SKF was used and the components under test consisted of a 440C heat treated steel counterface, with the normal bearing liner used in the coupon tests. The only difference in this case was the fully conformal bearing geometry rather than a cylinder on flat coupon test. In order to measure the AE activity during a controlled reciprocation of the bearing, Rig H's quasi-static measurement interval was utilised. After every hour of running time, the test bench would stop to monitor specific parameters such as wear and friction quasi-statically. The friction measurement of the test bench includes a slow reciprocation of the crank arm from 0° to -10°, then to +10° and finally back to 0°. This occurs over a time interval of five seconds, where the wavestreaming data was gathered.

In order to allow for a comparison between the stress waves gathered during operation and of those gathered during the quasi-static test bench measurement procedure, the raw waveforms during identical wear depths were plotted with respect to time (Figure 235).

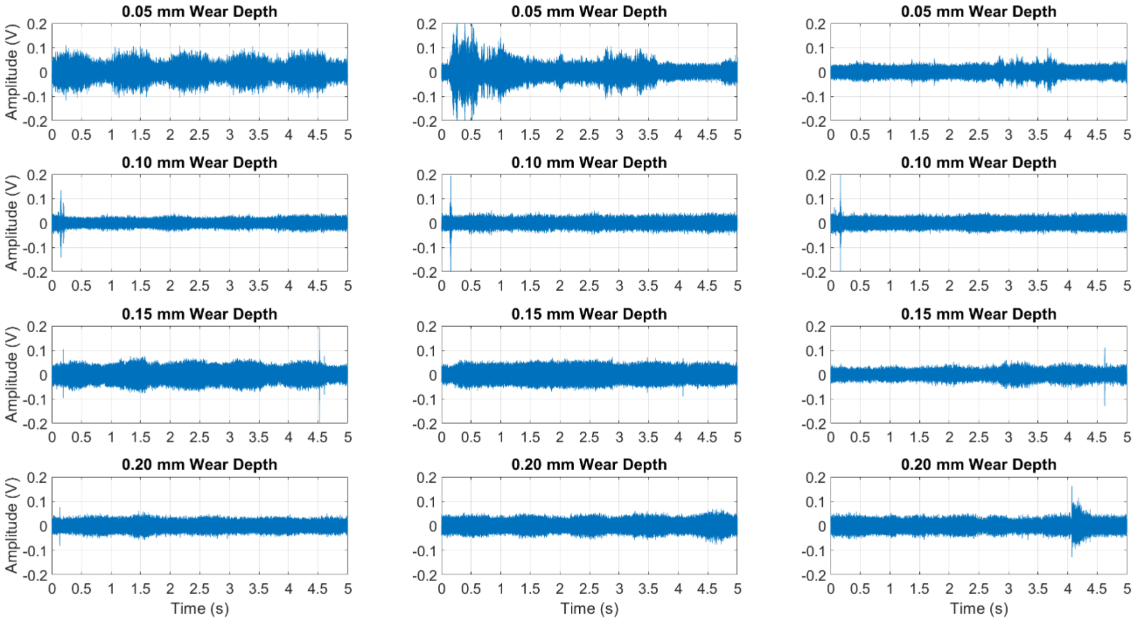

Figure 231 - Raw wavestreams of Rig H gathered during quasi-static measurements, through different bearing wear depths.

It is clear to see that the waveforms gathered during the quasi-static measurements, do not resemble those gathered during the testing procedure. Due to the slow reciprocating speed of the counterface during the quasi-static measurements, the influence of the direction change of the counterface during the required movement was dwarfed.

It was interesting to note that the amplitude of the waveforms gathered followed a similar pattern to those of Figure 228. During the wear-in phase between 0-0.05mm of wear, the amplitudes are comparatively high and in turn largely decrease during the steady-wear phase of the bearing. Furthermore, during the wear-in phase, the waveforms displayed large amplitude spike regions, which were once more attributed to the formation of the third body transfer layer. As the glass fibre region began to come into contact with the counterface at a wear depth of 0.15-0.18mm, the amplitudes of the waveforms increased once more. Finally, during the final wear-out phase of the bearing, the average amplitudes decrease once more with a few regions of increased amplitude spikes. Following these observations a binned FFT was once again produced from the quasi-static measured stress wave data (Figure 236) and the complementary wear and temperature data were also plotted with respect to the % Life of the bearing (Figure 237).

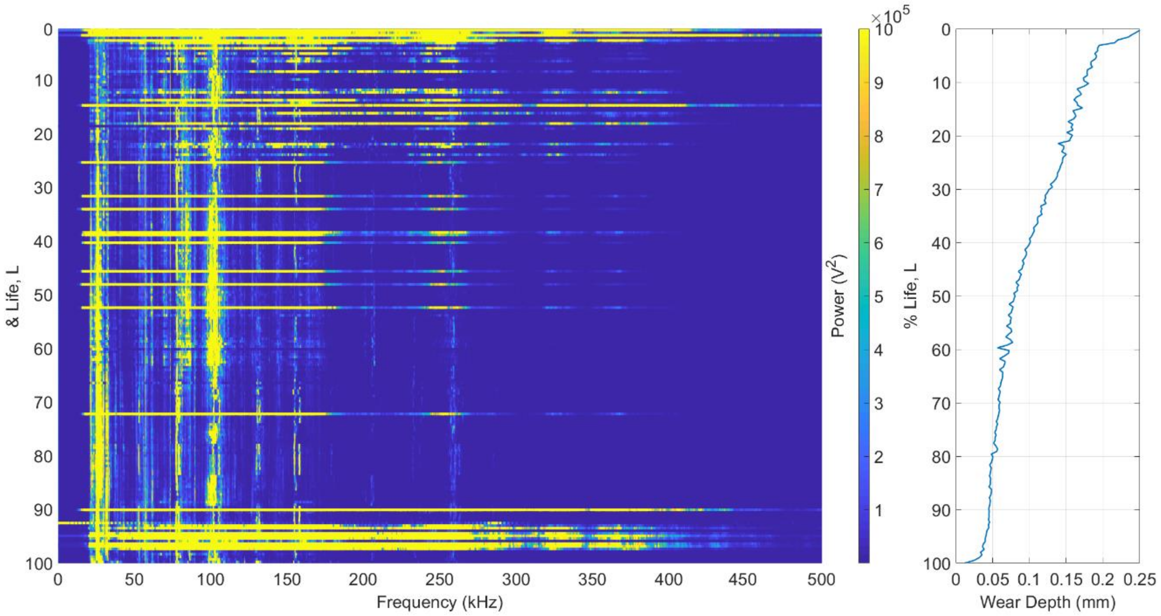

Figure 232 – Binned FFT analysis of the wavestreams gathered during quasi-static measurements of Rig H with respect to the bearing's % Life remaining.

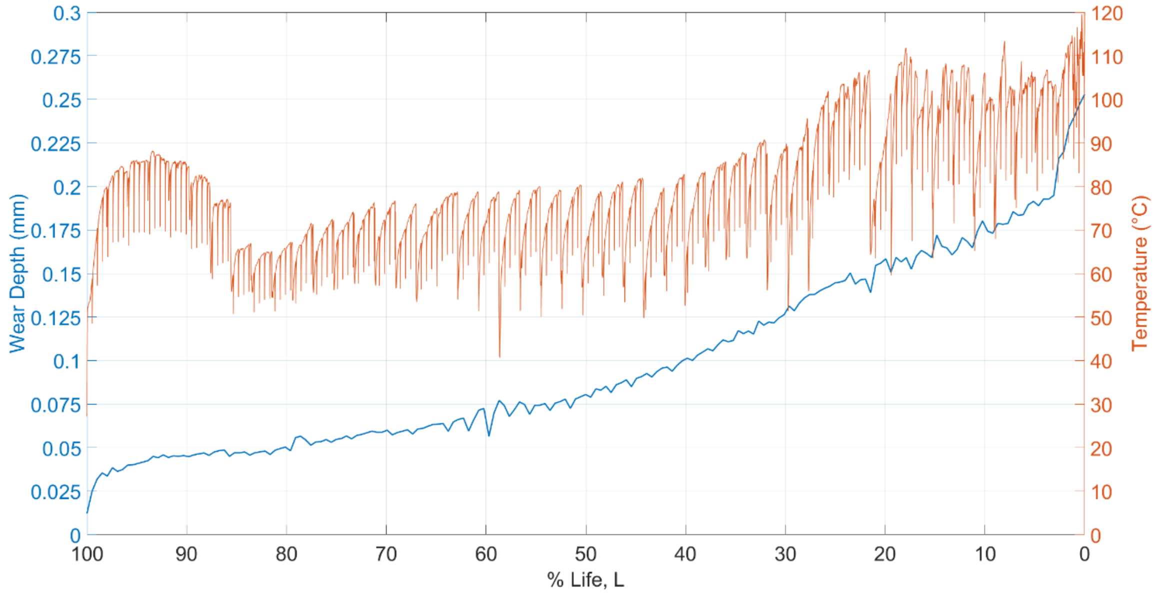

Figure 233 - Physical parameters of a full scale bearing test with respect to the bearing's % Life remaining.

When comparing the FFTs from Figure 229 and Figure 232, large similarities can be seen. The initial wear-in phase once again produced increased amplitude values with a wide frequency range of occurrence. This phenomenon appears to last approximately from 100% to 90% of the bearing's life, but it is interesting to note that this type of aggressive behaviour does not start from the initialisation of the test but after a few hours of running time. The majority of the steady wear phase of the bearing's operation had comparatively low amplitudes across the higher frequencies but as before, maintained the increased amplitude values around the 20-30 kHz frequency range. A few anomalous waveforms were recorded where high energies were observed across the higher frequency ranges and the reason for these emission bands during the steady wear phase of the bearing are currently unknown. As the glass fibre region came into contact with the counterface, the higher frequency bands began once more to display higher amplitude values and these largely increased as the bearing was entering its end of life stage. To further analyse these energy fluctuations, the frequencies were split into bands and their energies were summed and plotted over the % Life (Figure 234). These plotsFigure 234 display the previously discussed energy levels with respects to the different stages of the bearing's wear. A direct comparison can be made with the previous energy band breakup within Figure 230. The energy levels at the described wear phases of the bearing are extremely similar in both analysis of the waveforms gathered during quasi-static and during operating measurements. In order to investigate the AE parameters gathered during the quasi-static measurements further, the parametric AE data shown in Figure 235 can be taken into consideration which was recorded throughout the length of the test, in order to provide a comparison between the quasi-static measurement details and the continual parametric data gathering.

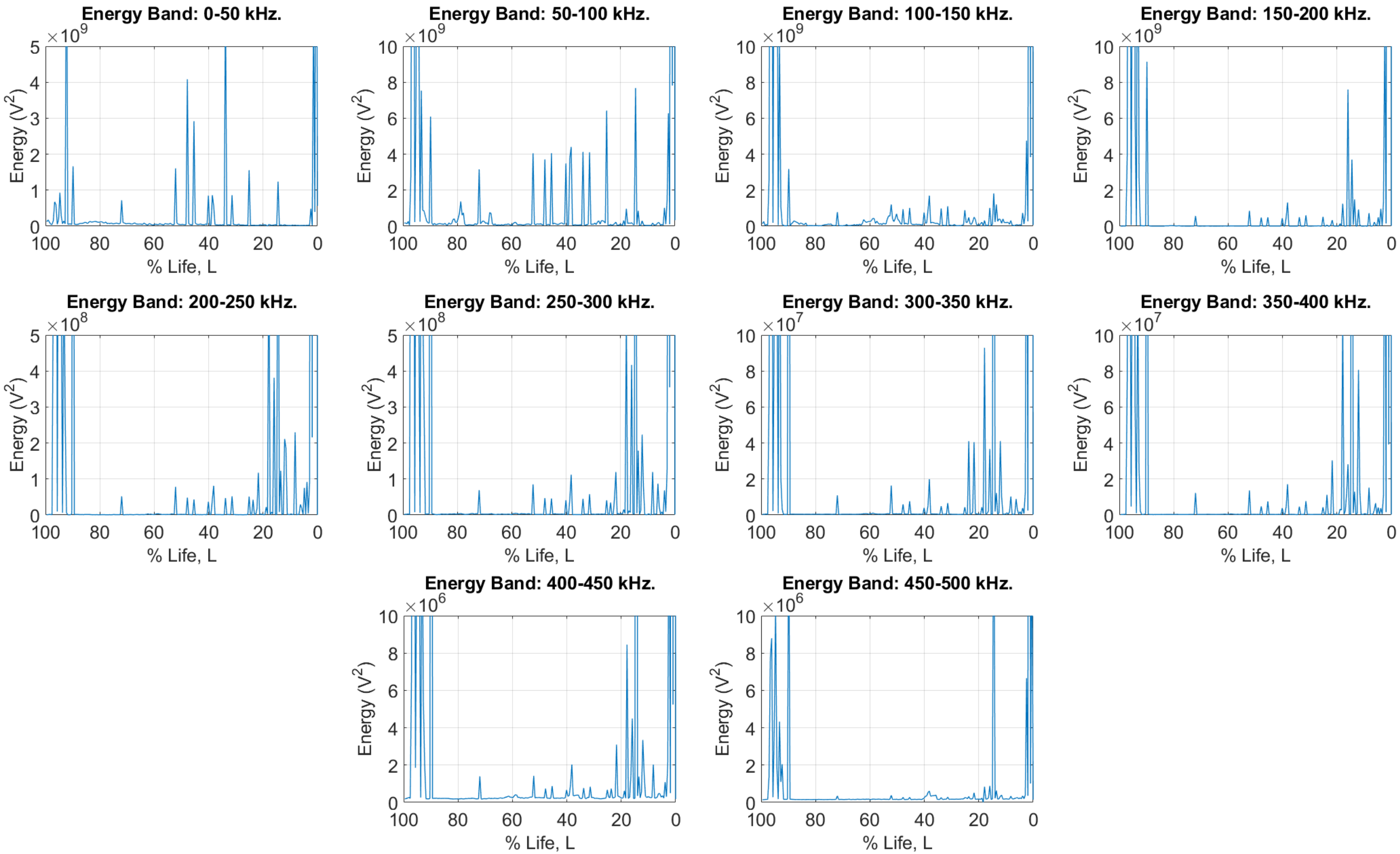

Figure 234 - Energy breakup of frequencies vs % Life with respect to the bearing's % Life remaining.

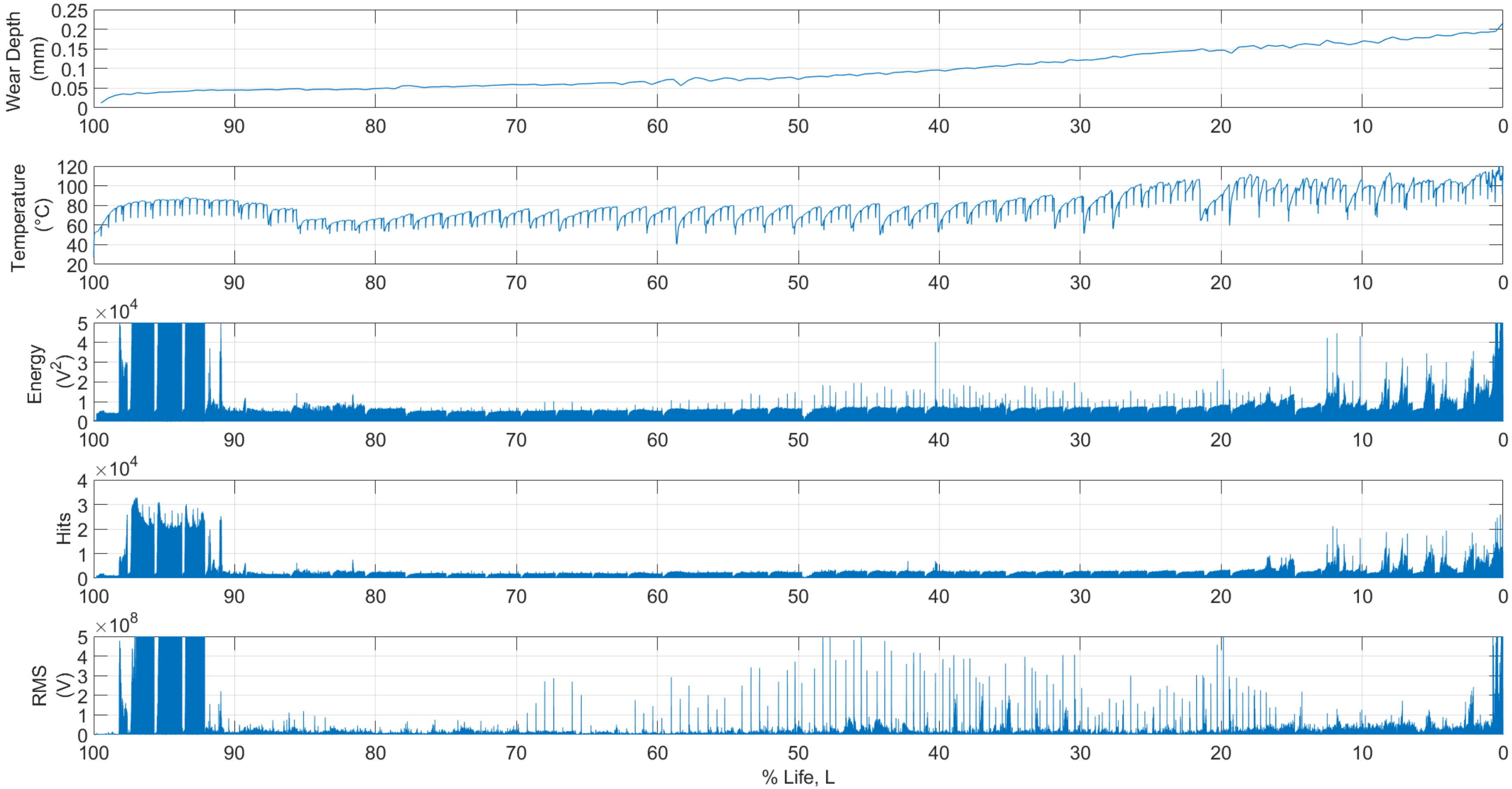

Figure 235 – AE parametric recorded throughout the bearing's % Life remaining.

In the process of gathering the AE hit data, it is important to note that a threshold of 40dB had to be applied, in order to minimise the data size. Due to the dynamic nature of this particular Acoustic Emission monitoring application, a large number of hits are seen even at small amplitudes. Usually within traditional static applications of Acoustic Emission monitoring, each hit is a sign of damage occurring in the static structure. In the case of dynamic applications, the hit data trend is considered. Relating the hit data to both the temperature and wear curves, a very similar trend was seen. Initially, as the bearing was increasing its temperature, due to the running in-phase, a low number of hits were recorded. As the wear-in phase became increasingly aggressive, as indicated by the increased temperature, these number of hits increased drastically and continued until the plateau phase of the wear period was reached. During the plateau region, a lower number of hits were recorded. This was in-turn once more increased when the glass-fibre rich region came into contact with the counterface. Therefore as a trend, it is interesting to note that the hit data follows the curves of the temperature data in a relatively complementary manner.

In order to avoid repetition, the energy and root mean square (RMS) values displayed in Figure 235 are discussed together, since they display similar patterns during the wear process. Considering the example of the energy content of the hit data, very useful patterns may be seen with regards to understanding the wear process of the bearing liner. Figure 235 shows that, during the initial wear-in phase of the bearing liner, the energy value of the waveforms collected, reached their highest point across the whole life of the bearing liner. Using this information, it can be concluded that the bearing liner goes through its most aggressive period of wear during the wear-in phase and not the final wear-out of failure region period as initially expected. Although this high energy region is said to be aggressive, it is hypothesised that the energy present during this period is cause by the establishment of the third body transfer film and is therefore necessary for the long term operation of the bearing. This crucial information can be fed back into the manufacturing processes of the X1 liner material and in turn, a different material composition could be proposed in order to minimise this aggressive wear-in effect which could be limiting the performance of the material.

Furthermore, once a transfer film has been achieved upon the inner ball, the plateau stage is reached and the amplitude of the three monitored parameters was reduced to a lower, steady value. This value remained relatively stationary, disregarding the stopping periods, until the glass fibre material composition transition period was reached at around 7 days. After glass fibre contact had been established, the energies of the waveforms once again increased and became more volatile than the plateau stage. As the wear process edged towards the end of the bearing life, the energies of the waveforms further increased before the test was stopped. This phenomenon can be more easily seen within the energy *vs.* time section of Figure 235.

Although the consistent monitoring of the energy and RMS parameters proved useful in determining the wear depth of the liner material, this full-bearing investigation was set out in order to find a solution to the problem of in-flight measurements. It was stated that Acoustic Emission would be relatively difficult to measure whilst the aircraft was mid-flight and therefore the focus of this test was an on-ground measurement, represented by the data gathered when the test-bench was conducting a quasi-static wear and torque measurement which could be replicated by the pilot's controls while on-ground. Although the FFT spectrogram of the wavestreams provided some trend identification, the benefits of this quasi-static measuring technique comes when compared to the continuous monitoring of the parametric data. Figure 236 compares the values of the energies recording during the whole process of the test with the FFT spectrogram of the periodic wavestream measurements.

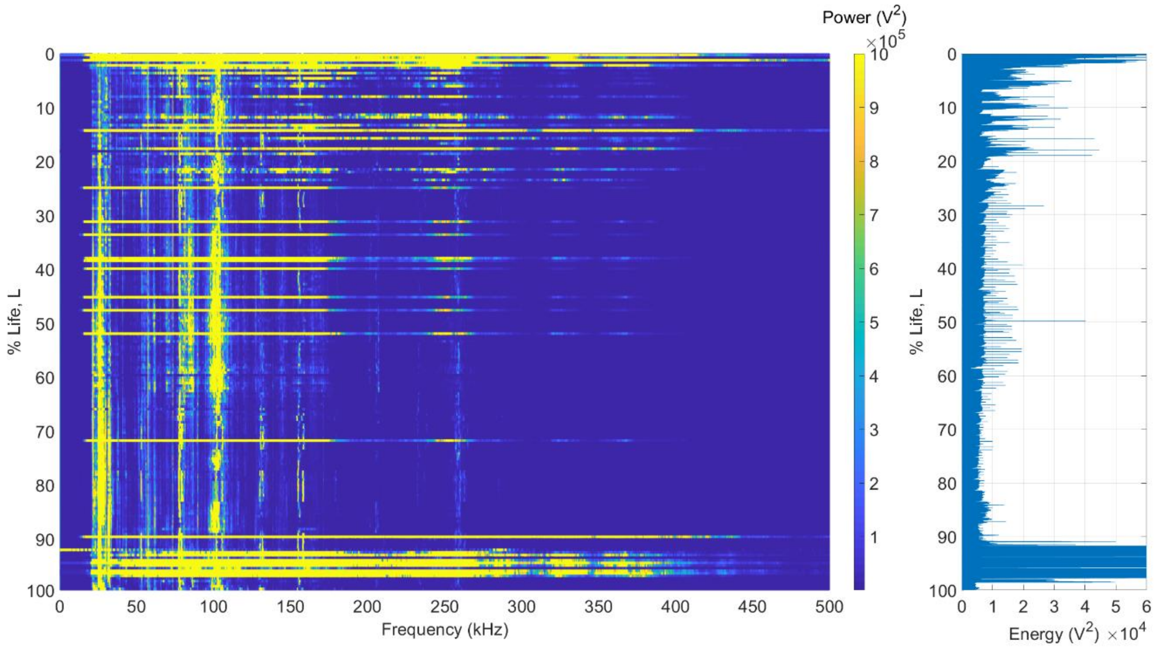

Figure 236 - Comparison between the FFT spectrogram (left) and Energy content of waveforms (right) with respect to the bearing's % Life remaining.

As seen in Figure 236, there is a positive correlation between the data gathered periodically under controlled conditions and the data gathered at high frequency under dynamic bearing testing conditions. By establishing this vital link between periodic and constant AE measurements, the industrial application of bearing health monitoring was deemed to be possible. It is possible to conceive a development of this technique where, during the aircraft's maintenance interval, AE could be monitored whilst a controlled blade reciprocation is conducted by the pilot and the bearings' health could be inferred without having to disassemble the pitch-link components.

7.6 Discussion

Acoustic Emission has proven to be a very useful tool in Non Destructive Testing (NDT) during recent years. Its application to static structures has been established for a very long time and AE is starting to make an impact upon the health monitoring of dynamic applications. In terms of its application to bearing systems, it has been used to monitor fast moving rolling element bearings, albeit under laboratory conditions, as shown by Choudhury & Tandon (2000), in order to detect cracks or defects and therefore prevent unplanned downtime of machinery. With respect to the specific application of self-lubricating bearings, no work had previously been conducted on pitch link control bearings within a reciprocating environment. In fact, no Acoustic Emission work had been conducted upon self-lubricating bearings as a whole and only a few cases were found to include AE in reciprocating environments. An example discussed in literature, was the acoustic emission application upon a piston ring/cylinder liner interaction in diesel engines, investigated by Douglas *et al.* (2006).

In this chapter, the Acoustic Emission wavestreaming data was investigated in the time domain in order to establish initial patterns within the data. The first investigation considered the effect of the cylindrical counterface's angular velocity upon the amplitude of the wavestreams recorded. It was concluded that at the ±10° angular positions of crank reciprocation (i.e. when the crank is stationary and about to change direction), the amplitude of the Acoustic Emission data was at its lowest value, as expected. In turn, it was found that during the period where the counterfaces had their highest velocity i.e. around 0° of the crank's reciprocation angle, the amplitude of the Acoustic Emission data was at its highest. By establishing this comparison, the start and end of the reciprocation could be identified within the raw data.

Within the time domain analysis of the data, it was observed that the wavestreams undergo certain transformations as the wear of the composite liner progresses through its pre-defined stages of wear. During the wear-in period, the amplitude of the wavestreams were of their highest magnitude, during the plateau they reached a steady low amplitude value, and as the glass fibre rich structural backing of the composite liner came into contact with the counterface, large amplitude spikes started to appear on the raw data, mid-reciprocation. These spikes increased in amplitude and frequency until the metal to metal region was reached where the liner had fully worn.

By transforming the raw wavestreams into the frequency domain, these characteristics were investigated further. Via the use of a binned Fast Fourier Transform, the transition period from a PTFE rich material region to the glass fibre structural backing region was detected. This detection was further verified by calculating the energies of the frequency bands, in increments of 25 kHz. All regions at the point of the material transition region reacted aggressively, which was displayed graphically by the large increase in the energy amplitudes during this transition period. Therefore it was proposed that, via the detection of this transition period, a condition monitoring technique could be created where the operator is made aware that this glass fibre structural backing region has started to come into contact with the counterface at a specific wear depth of nominally 0.15-0.18mm.

In order to verify that the cause of this large amplitude increase was due to the glass fibre region, a test was conducted upon a smaller, and therefore less aggressive, test bench. The chosen test bench was a ball on flat reciprocating wear rig which achieved the high contact pressures required, by allowing the contact region to occur between a flat bearing liner sample with a steel sphere acting as the counterface. This investigation confirmed that when the glass fibre rich region came into contact with the steel sphere, the amplitude value of most frequency bands were increased, as visually seen by the binned FFT spectrogram.

Once these phenomena were established, the feasibility of the Acoustic Emission technique was considered. The issue with the application of Acoustic Emission arises when the sensors had to be remote to the processing unit. Due to the large volume of data gathered and data transmission issues which are faced by applying such sensors to the main rotor of a rotorcraft, alternatives to the in-flight data gathering method had to be considered. An on-ground measuring method was proposed, where it was envisaged that if an operator would, non-intrusively, attach an Acoustic Emission sensor to the pitch link bearings and via a pilot-controlled quasi-static reciprocation of the blades, vital information on the bearings' health could be gathered. Initially, the processed data produced a binned FFT where no significant trend could be established. As these data were compared with the continually monitoring of further parametric data, a clear relationship between the periodic and continual data was established. This was in turn related to the glass fibre transition period of the bearing composite liner and once again a clear relationship could be seen. Thus, it was concluded that Acoustic Emission could in fact produce vital information regarding the bearings' current state of health, with periodic measurements only.

7.7 Conclusions

Condition Monitoring as a tool can be extremely useful with regards to maintenance interval planning, when used as a prognostic rather than a diagnostic technique. Through the use of Acoustic Emission monitoring, the author was able to establish a clear relationship between AE and certain wear depths where the self-lubricating material liner's composition changes. A clear trend was seen throughout the analysis techniques used, which varied from the time domain to the frequency domain. This trend related the increase in amplitude of all monitoring factors when the glass fibre structural backing region came into sliding contact with the steel counterface. This could be extended to provide a maintenance interval tool, where non-intrusive sensors could be retrofitted to any aircraft. This versatility is of vital importance, along with the avoidance of bearing health monitoring via the use of intrusive sensors. This allows the techniques developed to be applied without having to requalify the bearing for flight due to not altering the bearings structure. Furthermore, on-ground replicated measurements were shown to give promise to such a bearing health monitoring technique, as clear trends were established between periodic and continual data monitoring during a full bearing test.

Further work should include verification tests where the existing techniques are applied to different loading scenarios. These scenarios can include the alteration of weight application upon one bearing liner within the four arm configuration in order to establish premature failure. Through the live-monitoring of the Acoustic Emission data, the operator should in turn be able to identify when the glass fibre backing region, at a nominal wear depth of 0.15-0.18mm, has come into contact with the cylindrical counterfaces. A further test where both continual and periodic wavestreaming of Acoustic Emission data should be conducted on the full bearing test bench within SKF, in order to establish a further relationship between the two monitoring methods.

Chapter 8: Development of a time domain analysis technique for reciprocating wear conditions

8.1 Introduction

In the previous chapter, the relevant Acoustic Emission monitoring methods which are currently employed within NDT in terms of both static and dynamic applications were discussed. It was found that no significant work had been reported concerning the monitoring of self-lubricating composite liner bearings. Although this field is small, it was surprising to find that there exists a lack of research being carried out in the use of AE to monitor tribosystems operating in reciprocating wear conditions. There are a few studies which have concerned the use of AE in reciprocating machinery environments such as in the study from Gill *et al.* (1998), which focuses on the operating condition of large reciprocating compressors and the study of El-Gharmy *et al.* (2003) who successfully developed an automated pattern recognition system for the diagnosis of reciprocating machinery faults by using such techniques as Acoustic Emission (El-Ghamry *et al.*, 2003). Further, Liao *et al.* (2011) conducted a study on the "stick-slip friction of reciprocating O-ring seals' through the use of Acoustic Emission and finally the study previously mentioned on the Acoustic Emission generated by the reciprocating contact between piston ring and cylinder liner in diesel engines by Douglas *et al.* (2006). It is interesting to note that all of the previous papers have primarily used time domain techniques. Time domain was preferred due to its repeatable nature with regards to the analysis of cyclic patterns within the data. Typical analysis techniques such as calculating the Root Mean Square (RMS) of the raw signals, allowed for the damaged signals to be compared to prior healthy signals numerically. This type of comparative analysis, allows for an analysis technique where no calibration requirements could be possible. This chapter, therefore, is concerned the development of an Acoustic Emission-based comparative method of analysis through the use of pattern recognition, in order to aid the detection of damage within a self-lubricating composite bearing liner.

The following section within this chapter describes the process of developing a new time-domain analysis technique. Prior to doing so, it is important to show how the conventional technique of RMS relates to the wear process of the liner material. The RMS was calculated on the acoustic emission gathered from test 3 (Figures 241 – 244).

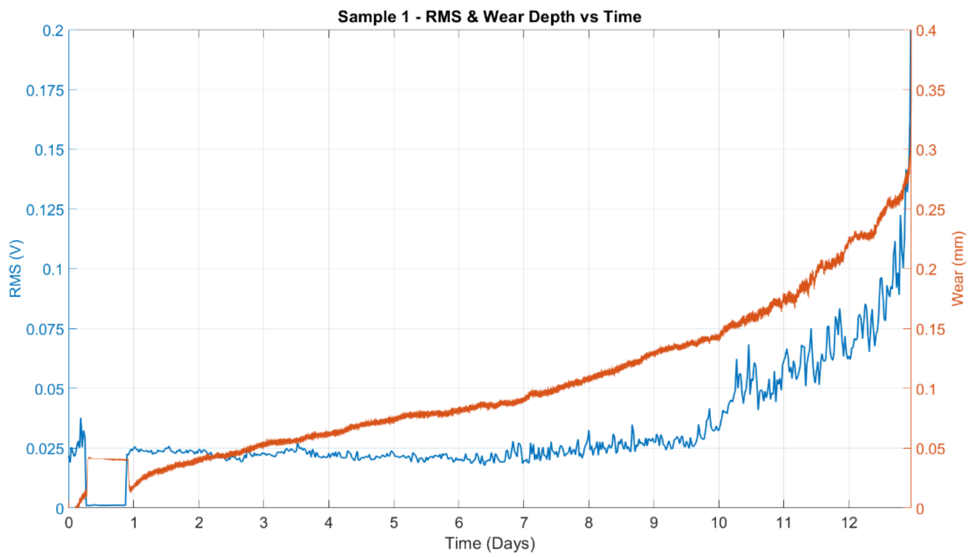

Figure 237 - Sample 1 RMS results.

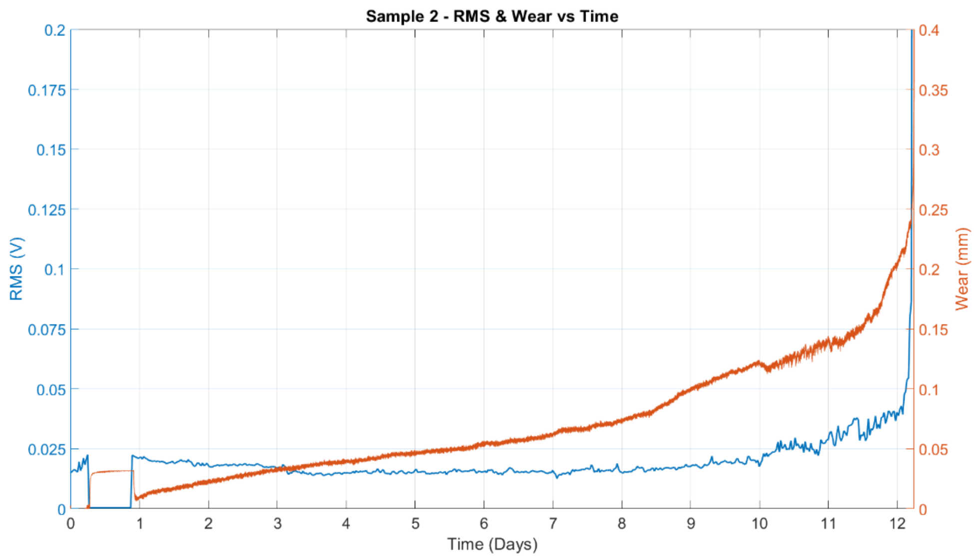

Figure 238 - Sample 2 RMS results.

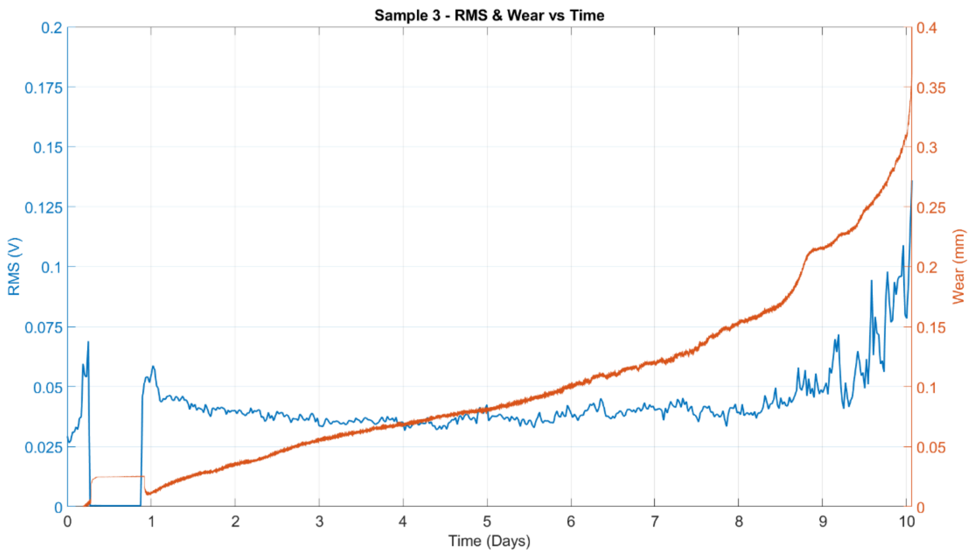

Figure 239 - Sample 3 RMS results.

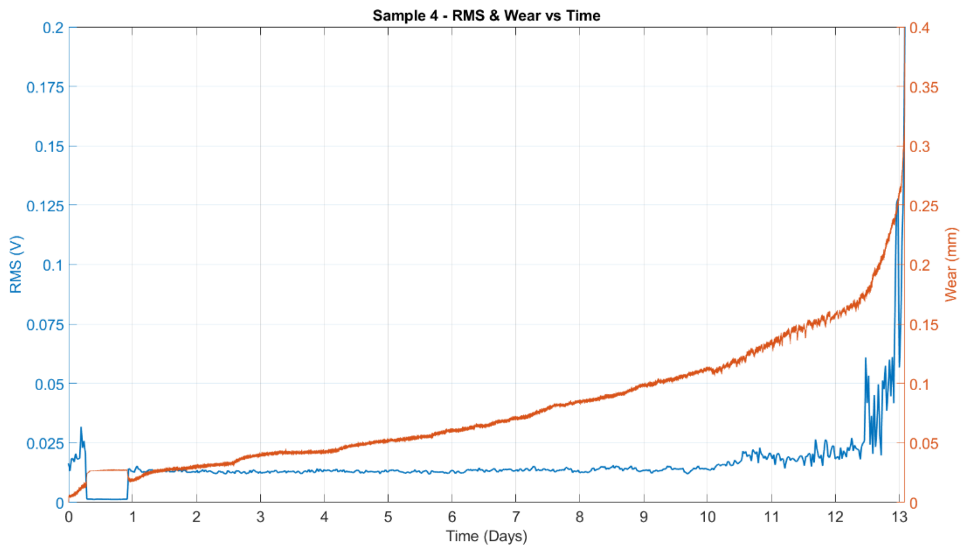

Figure 240 - Sample 4 RMS results.

As seen from Figures 241 - 244, the RMS value of each sample increases when a wear depth of 0.125 – 0.15mm is reached, which relates to the glass fibre rich area of the liner system (0.15-0.18mm). It is also important to note that during the initial stages of wear, where the contact pressures are at their highest, the RMS values were also raised when compared to the plateau phase of the wear curves. Finally, when the metal to metal region was reached, the

RMS values increased exponentially. These features were expected to be observed and ties in with the conclusions made within Chapter 7.

8.2 Development process

8.2.1 Pattern observation

A successful analysis technique has to be sufficiently adaptive, so that it can be tailored to many applications and strict enough to allow the algorithm to detect even the small details. In order to do so, reference back to Figure 195 (Page 208) is required. Certain patterns may be observed within the example wavestreams and are listed as follows:

1. Amplitude of the wavestreams is non-stationary throughout the wear process.
2. Transient bursts of Acoustic Emission are present, particularly during the wear-out phase of the liner material.
3. A distinct two diamond shaped cluster shows the generation of AE by sliding over a complete reciprocation cycle.
4. When the counterface is momentarily stationary, the amplitude of the diamond-shaped AE is at its lowest point.

These key characteristics of the waveforms are also graphically represented upon a wavestream in Figure 241, below.

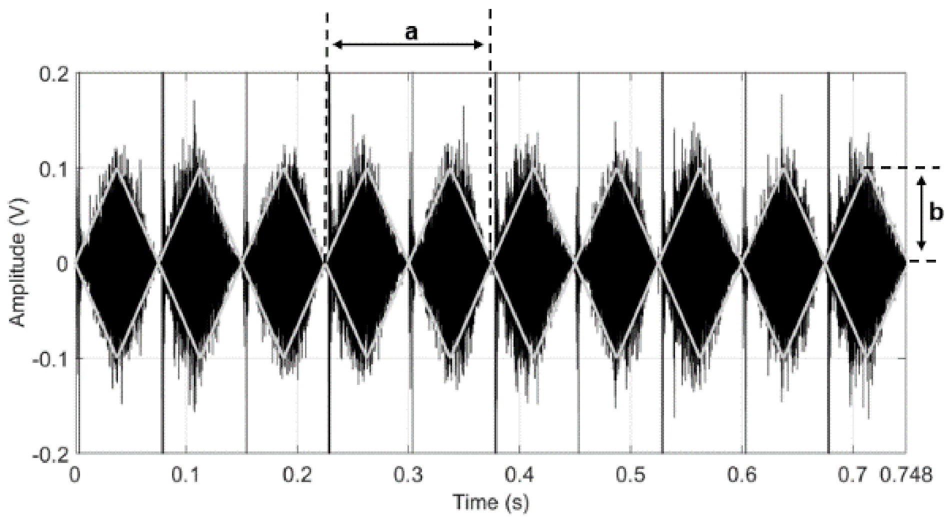

Figure 241 - Parameter: (a) Full reciprocation of the counterface, (b) Amplitude of the wavestream.

8.2.2 Analysis code procedure

In order to extract useful data from the processing of the wavestreams in the time-domain, a MatLab script had to be devised which autonomously characterises the wavestream in terms of the features described in Section 5.2.1, and outputs parameters related to the size or severity of these features. As discussed within Chapter 4, the main characteristics which were investigated and attributed to signs of wear, included the initial transient burst per reciprocation at the points when the counterface was stationary, the amplitude of the wavestreams and finally the mid-reciprocation transient bursts of energy which occur more predominantly towards the end of the bearing liner life. These are shown in Figure 242.

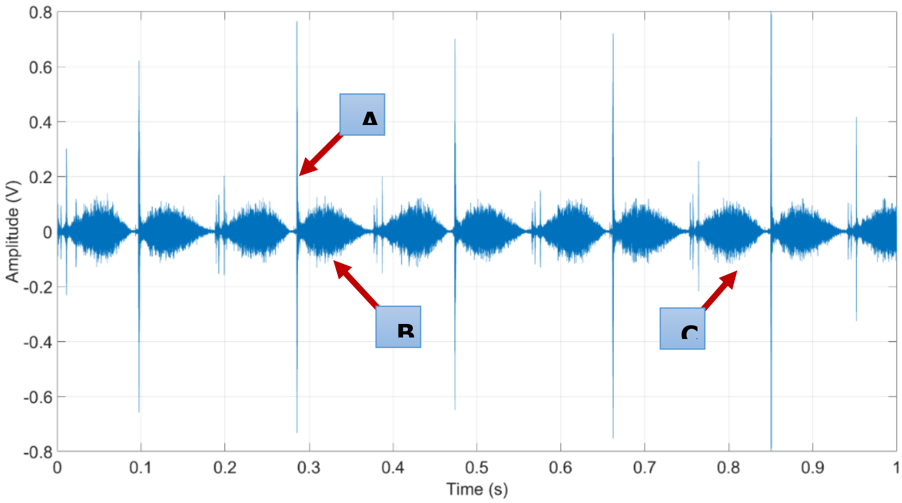

*Figure 242 -Parameters influenced by wear: **(A)** Start of oscillation transient burst amplitude, **(B)** Amplitude of the wavestream, **(C)** Mid-oscillation transient AE bursts.*

The process of the analysis code is shown in a flow chart in Figure 247.

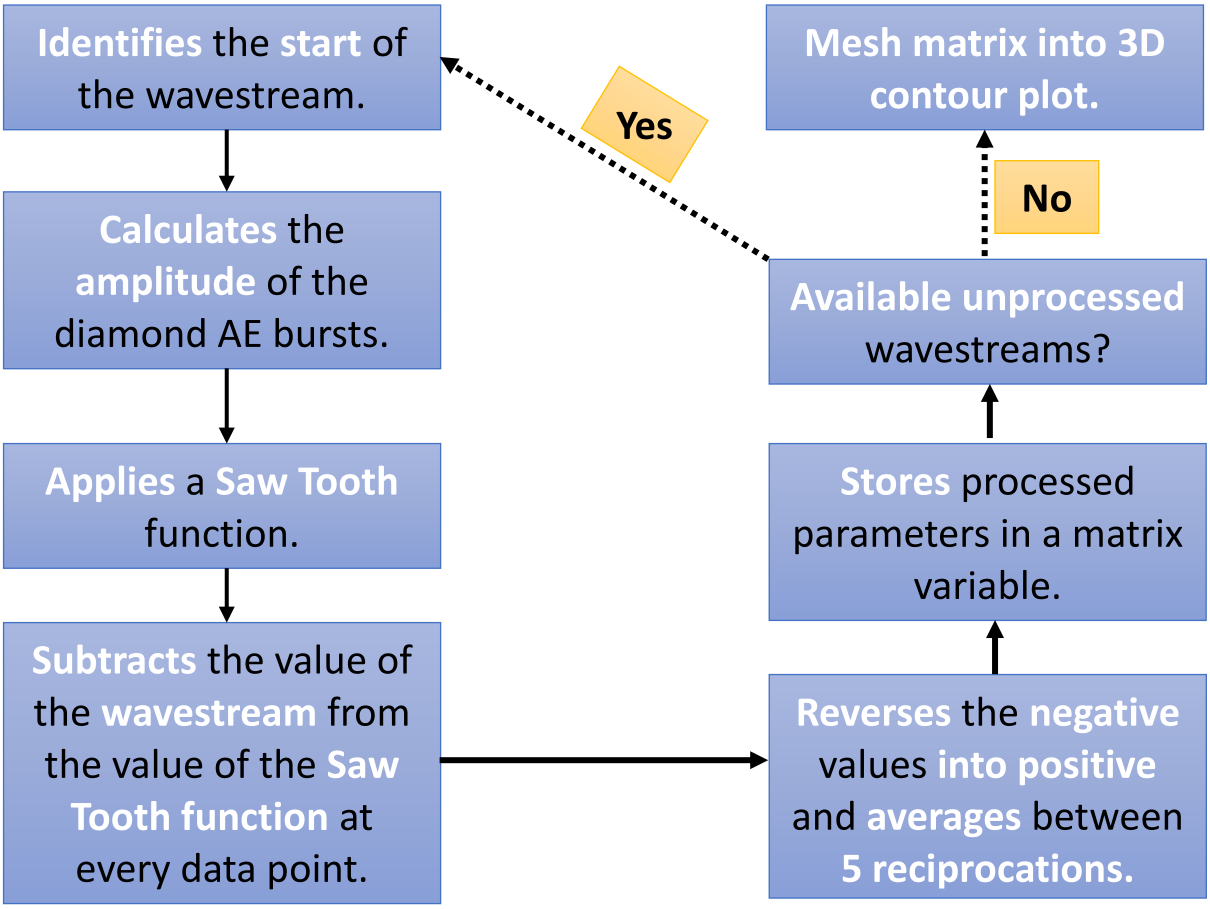

Figure 243 – Flowchart of MatLab script.

Each of the steps defined above is now explained in turn in the following sections.

8.2.2.1 Identification of oscillation start

Initially, it was necessary to identify the start of the reciprocation, which as previously discussed occurs at the lowest wavestream amplitude areas. In order to do so the locations in time of the lowest values of the waveform data are identified. In order to determine if the chosen indices are correctly located, the data length between two indices is compared to the 'expected' data length. The 'expected' data length was defined as the number of data points recorded during the time taken for the counterface to undergo one full reciprocation cycle, as given by Equation 22:

$$\begin{matrix} \mathit{Calculated\ data\ length} \\ \mathit{between\ reciprocations} \end{matrix} = \frac{1}{\mathit{ReciprocationFrequency}} \cdot \mathit{Sampling\ Rate} \qquad (22)$$

Both the reciprocation frequency, along with the sampling rate of the AE data acquisition system were made to be operator input prompt commands, in order to allow the code to be applied to other reciprocating operations. When comparing the data length between reciprocations of the recorded indices against the calculated theoretical data point length, a small degree of error is allowed by the code. If the difference between these two data lengths exceeds this allocated error value, the waveform is classified as 'non-processed' in order for the operator to revise it manually after the code has terminated. An annotated image is provided in Figure 244 which explains these parameters.

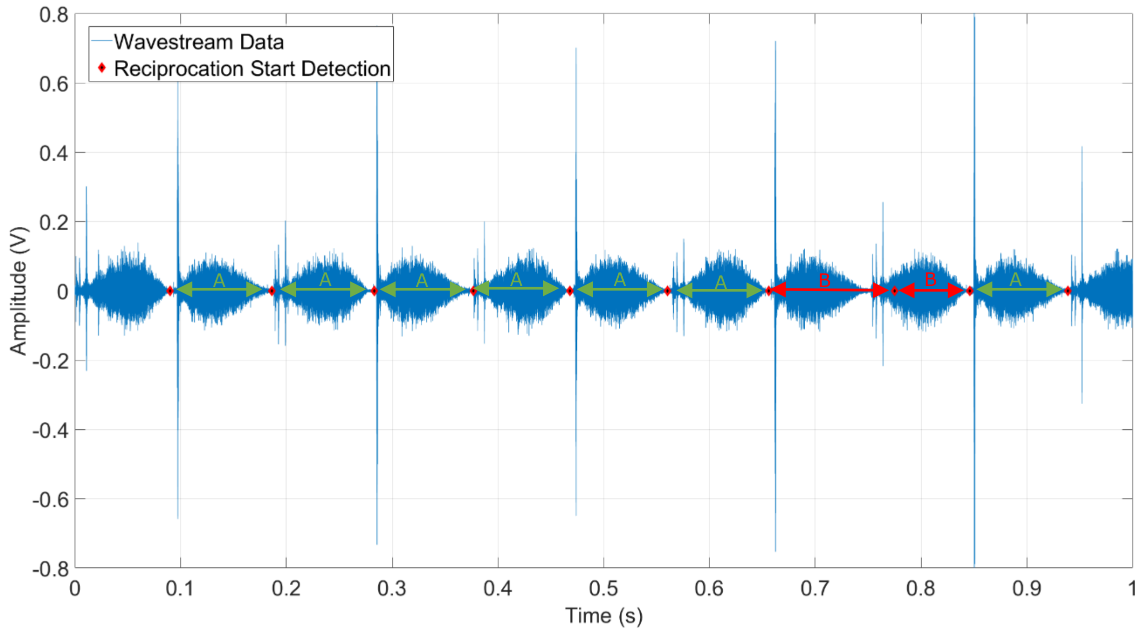

Figure 244 - Annotated figure showing the autonomously calculated indices and their acceptance. Example of: (A) Acceptable location for indices, (B) Not-acceptable location for indices.

For the work presented in this thesis, a 1% error was allowed with regards to the index position, which is calculated from the theoretical data length between reciprocation cycles. After these indices have been acquired, the wavestream is cropped to remove any unwanted data (part reciprocations) prior to the start of the first complete reciprocation. In turn, data relating to partial reciprocations were removed from the end of the wavestream. This is done by dividing the number of indices detected by 2 and rounding down to the nearest number, in order to determine the number of complete reciprocations (2 indices). The final cropped image is presented in Figure 245.

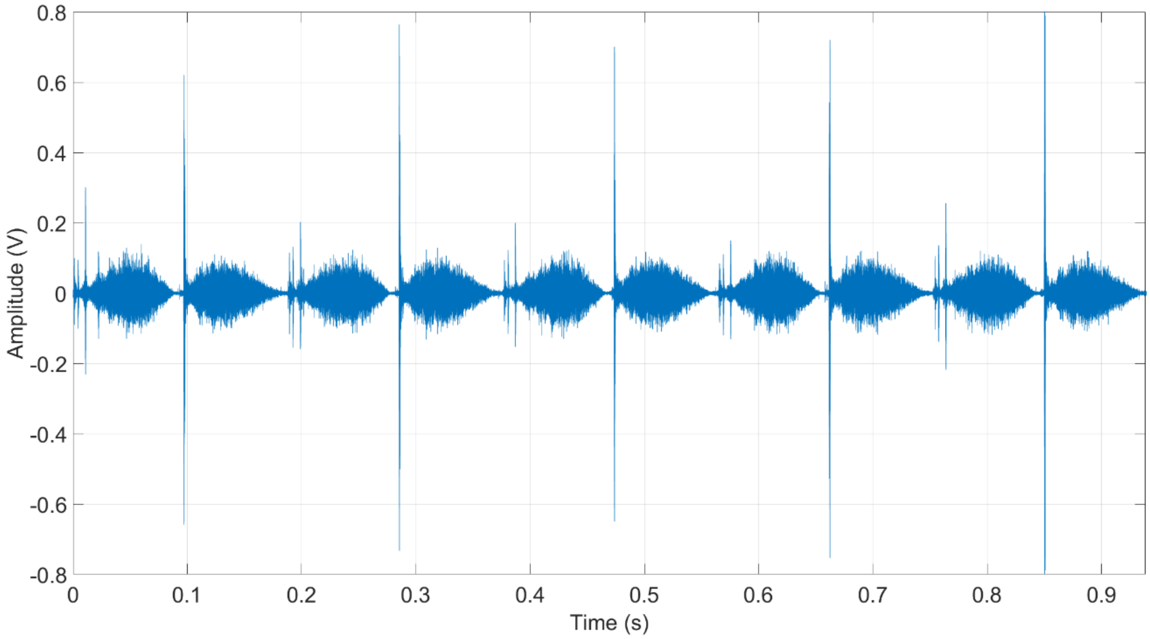

Figure 245 - Autonomously cropped image of required wavestream.

8.2.2.2 Calculation of the maximum wavestream amplitude

Once the indices which correspond to the start and end of a single oscillation had been correctly calculated, it was then possible to identify the maximum amplitude of the AE which occurs mid-reciprocation, i.e. when the crank is at a 0° reciprocation angle. In order to do so, the index of the end of half a full reciprocation and the start of the reciprocation were subtracted and divided by 2 in order to acquire the mid-point. Around this location a band of ±1500 data points was chosen where the amplitude would be calculated. In order to calculate the mean value within this band of 3000 data points, a coarse enveloping MatLab function had to be applied to the wavestream data. The function was responsible for returning the upper and lower peak envelopes of the wavestream data. These envelopes were determined by using a spline interpolation over local maxima, which were separated by at least 150 points (Figure 246).

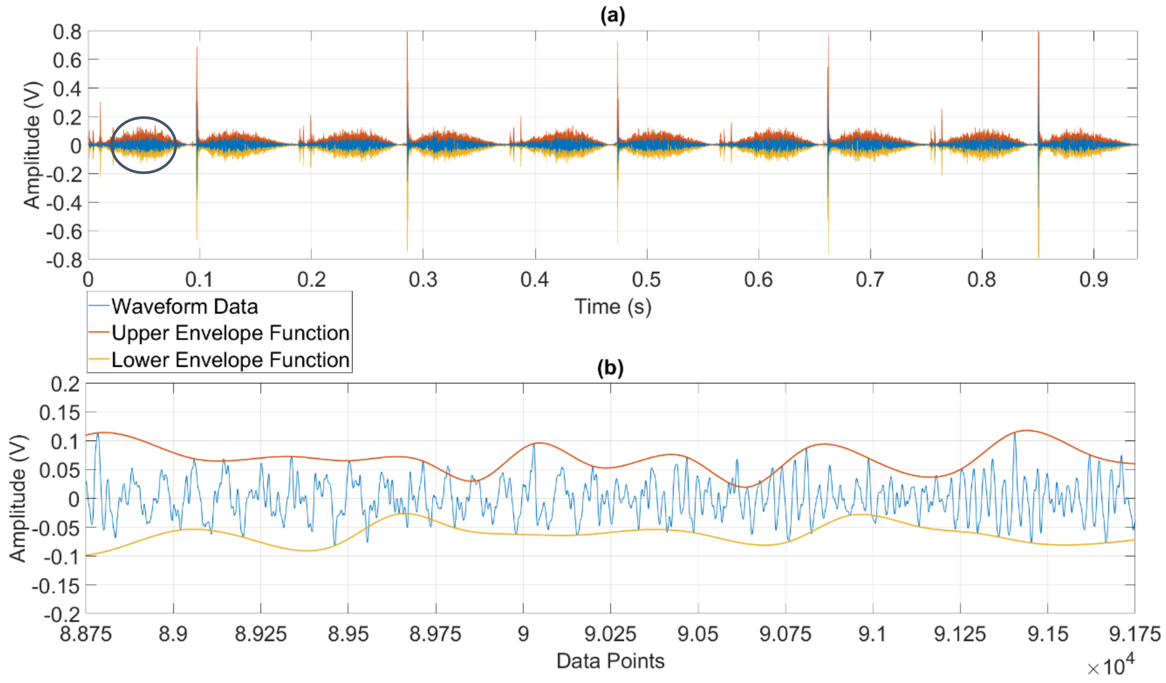

Figure 246 - Example of enveloping technique to determine the maximum amplitude of the waveform (a) full view of the waveform, (b) zoomed in selection of the data point responsible for the amplitude calculation (circled section on (a)).

Although it may seem appropriate to use an 'average' function of the absolute values for this band, the oscillating nature of the AE data would provide an average which would not represent the true required value. Via the use of the average function, a value of 0.0264 V was obtained while the enveloping technique returned a value of 0.0695 V. The mean value of the amplitude is therefore calculated from the values of the enveloping function, which lay in the 3000 data point region. This was conducted for each of the diamond bursts presented in Figure 246 (a) and an average of all the amplitudes was taken as the general value for that specific wavestream (which nominally contained 5 complete oscillations).

8.2.2.3 Saw tooth function application

Once the average wavestream amplitude was calculated, it was stored in a matrix and would in turn be compared to the amplitude values of the wavestreams gathered throughout the wear process of the liner. In order to initiate the second phase of the code which extracts the short transient bursts of Acoustic Emission from the reciprocation-related diamond-shaped bursts of

AE, a sawtooth function was fitted to the wavestream. This function started at data point 0, as it was now an indication of the start of the reciprocation, it was assigned a frequency equal to the reciprocation frequency of the counterfaces and had a peak amplitude of the value calculated by the enveloping technique. This is graphically represented in Figure 247.

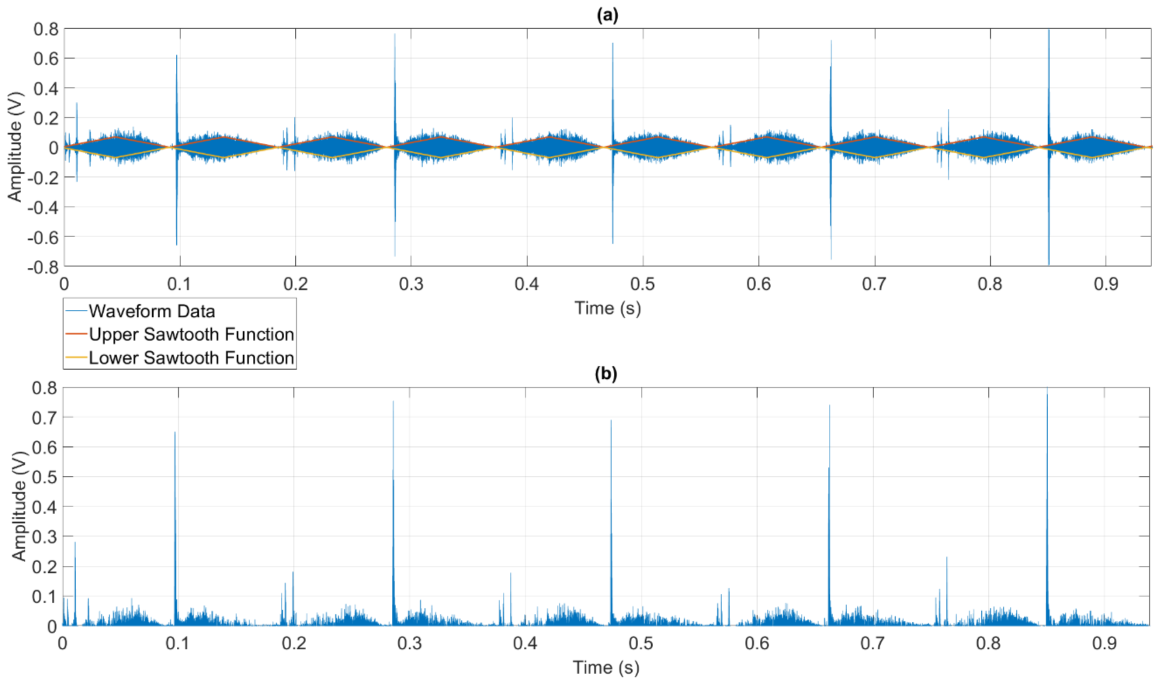

Figure 247 – (a) Annotated method of sawtooth function application. (b) Subtracted sawtooth function from original waveform data.

It can be observed from Figure 247, that the transient bursts and occasional peaks mid-reciprocation, lay outside of this saw tooth envelope function. This was the desired outcome from this stage of the analysis process.

8.2.2.4 Extraction of transient bursts

At this stage, the majority of the analysis framework has already been achieved and a simple subtraction can take place in order to isolate the transient AE bursts. In order to do so, the value of the saw tooth function was subtracted from the value of the cropped wavestream data at each data point and a new data set was created which included only these residual transient bursts.

At this stage, the wavestream data was converted to absolute (positive) values for comparison. Furthermore, the five reciprocations were overlaid and an average value of the transient bursts extracted was taken, therefore creating a single averaged transient burst reciprocation data set. The process is shown graphically in Figure 248.

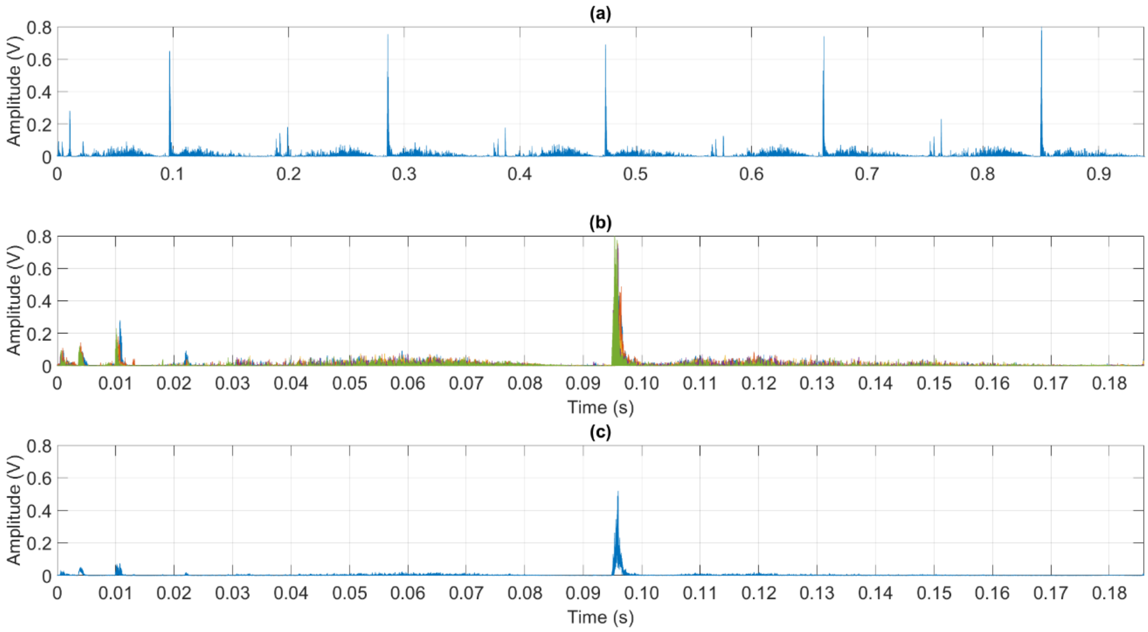

Figure 248 - Graphical representation of: (a) Transient Burst values after subtraction. (b) Five oscillations within the single wavestream overlaid. (c) Averaged transient burst values from the five considered reciprocations.

Figure 248 (c) shows the final form of the required transient burst output from a single wavestream file. During the process of the bearing liner test, wavestreams were collected every 30 minutes and during a 13 day test 624 wavestreams were gathered. The code therefore has produced a transient burst and wavestream amplitude matrix with a length of 624 files, which were in turn meshed in order to enable the results to be visualised in a colour contour plot. In the following section, the code is applied to AE results from the 13 day wear test, and the evolution of both saw tooth function and transient bursts is investigated as the wear test progresses.

8.3 Peak extraction code results

8.3.1 Amplitude results

The first parameter to be investigated was the average amplitude of the raw waveforms when the crank was at a 0° reciprocation angle and therefore the counterface was at its highest angular velocity – in effect, the height of the fitted saw tooth function. If the hypothesis that the AE is related to motion and bulk friction between counterface and sample was correct, then this amplitude parameter should in some way be related to the changes in friction and wear during the various stages of the liner life. In order to avoid repetition, the features which were attributed to signs of wear are discussed for the data analysed from Sample 1 (Figure 253) with the similar results from the other three samples shown for completeness at the end of this section (Figures 254 – 256, Page 273 & 274).

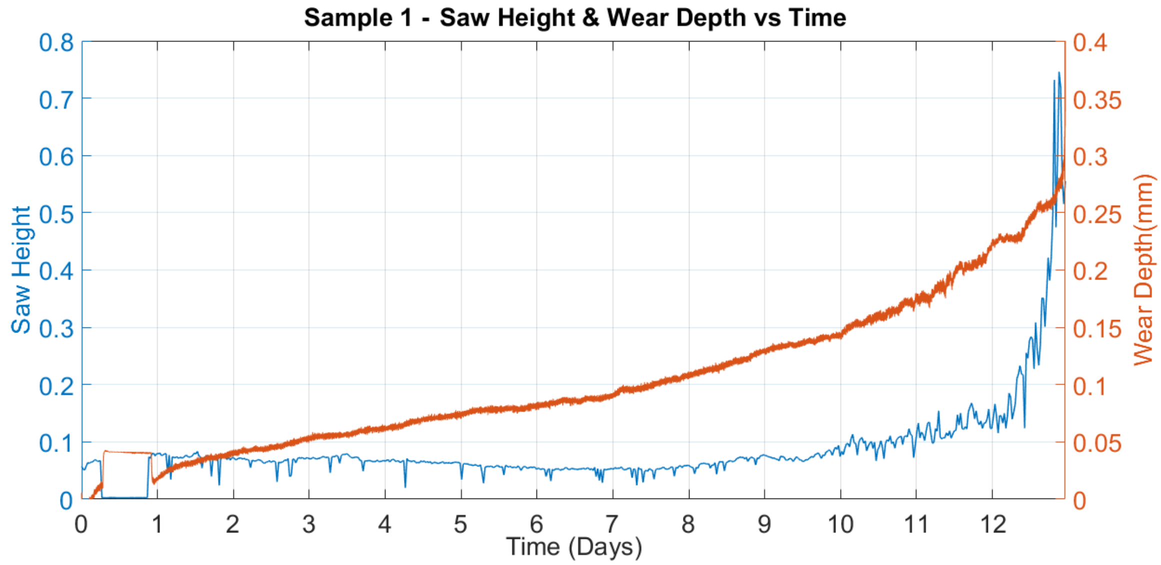

Figure 249 – Wavestream Amplitude Progressions and Wear vs Time of Sample 1.

Figure 249 shows the change in saw-tooth function amplitude as the wear test progresses. A slight reduction in amplitude can be seen from 2 to 3 days onwards, until 8 to 9 days when an increase in saw tooth amplitude can be seen to start to occur. Initially, the amplitude of the wavestreams were higher in magnitude due to the aggressive wear-in period of the liner material against the counterface. This period comes to a less aggressive equilibrium when a third-body PTFE transfer layer is formed upon the counterface and therefore provides a low friction sliding surface for the two components. During the so-called plateau phase of wear, it was observed that the amplitude of these signals remained at roughly a constant level, ranging between 0.045 V and 0.06 V. This plateau period comes to an end, when the glass fibre structural backing region starts to come into contact with the cylindrical counterface at a wear depth of roughly 0.15-0.18mm. From this point onwards, it can be seen that the amplitude of the wavestreams greatly increases before the test was stopped due to metal to metal contact. The significant increase in wavestream amplitude during the latter stages of the test could be a useful parameter forming part of a larger condition monitoring system where once again the wear depth of the bearing liner could be identified due to this amplitude increase phenomenon occurring following the glass fibre structural backing transition point.

Figures 254 - 256 display the results obtained from samples 2, 3 and 4, which all show similar characteristics.

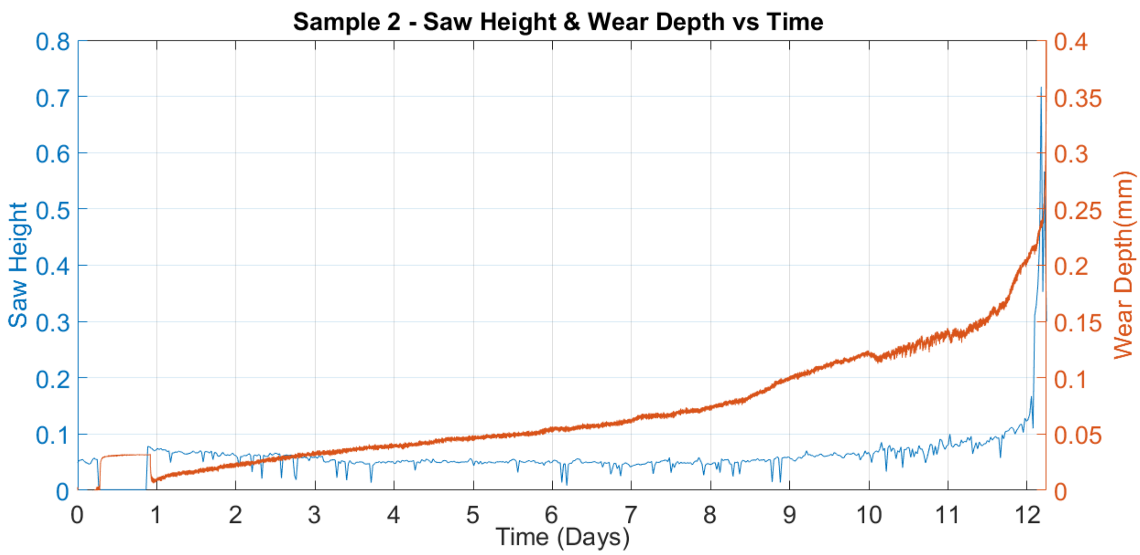

Figure 250 – Wavestream Amplitude Progressions and Wear vs Time of Sample 2.

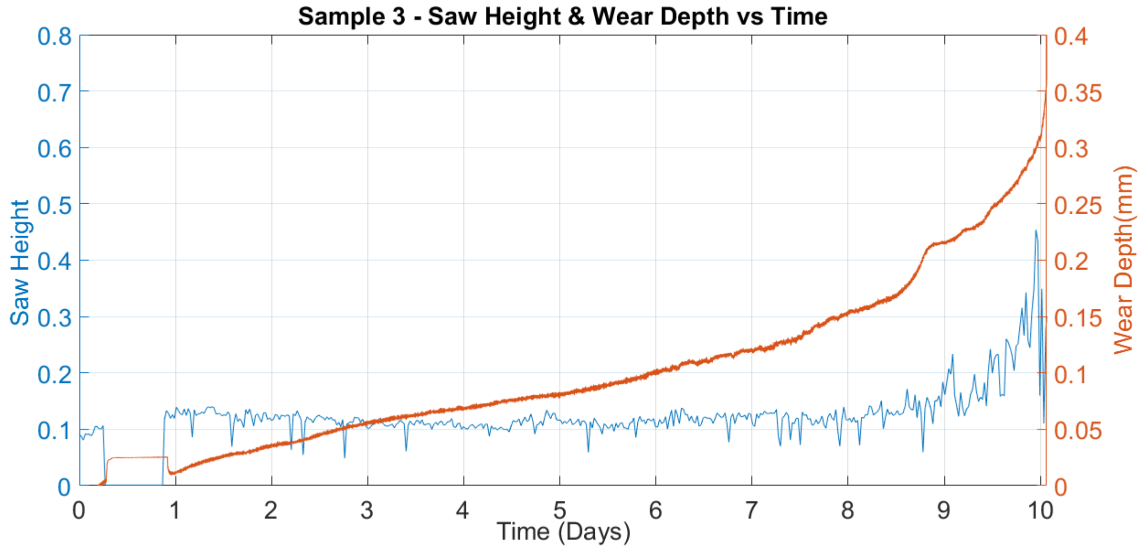

Figure 251 - Wavestream Amplitude Progressions and Wear vs Time of Sample 3.

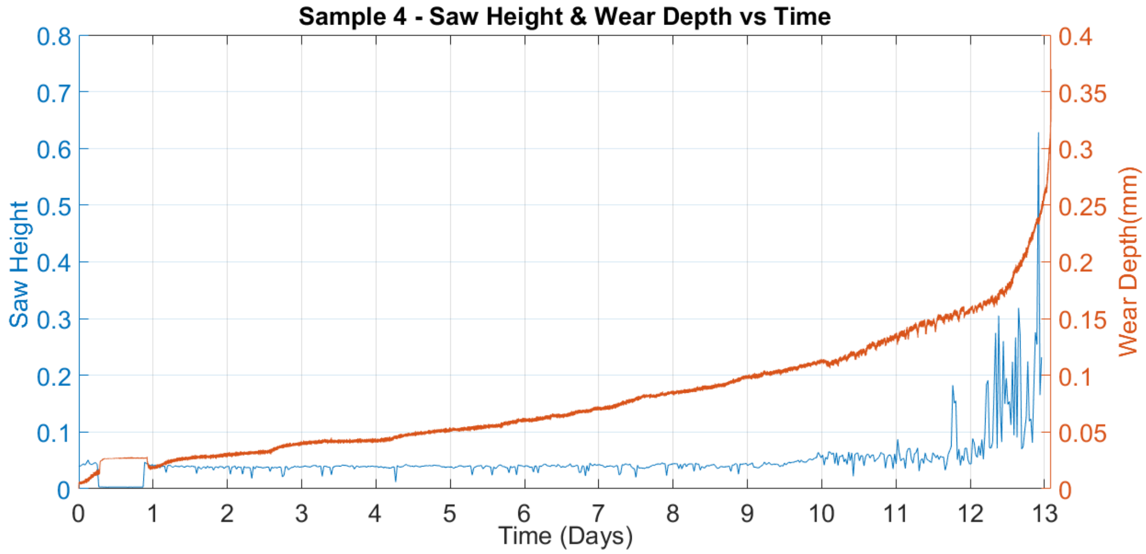

Figure 252 - Wavestream Amplitude Progressions and Wear vs Time of Sample 4.

8.3.2 Transient AE bursts results

The second phenomenon which was observed as a noticeable change when reviewing the wavestream progression in the time domain, as shown in Figure 242, were the transient bursts of Acoustic Emission. These bursts predominately occurred at the start of each reciprocation and in the latter stages of the bearing liner’s life, they started to occur throughout the reciprocation cycle. As described, these transient bursts were extracted per oscillation, averaged and manipulated so that they could be displayed in contour plots, as shown in Figures 257 - 260.

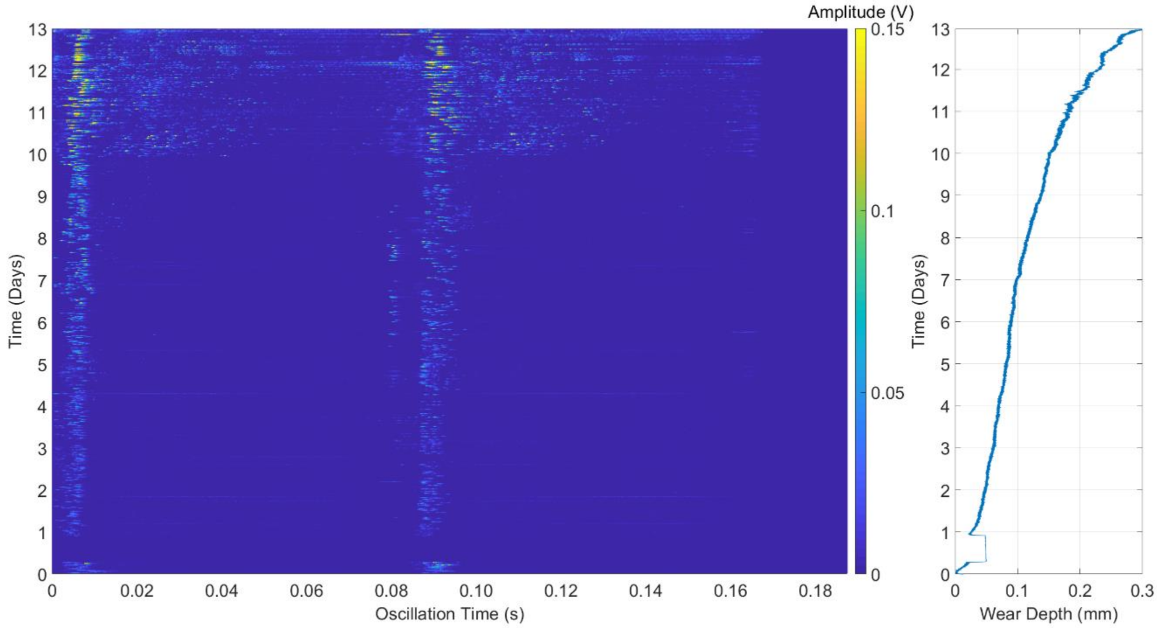

Figure 253 - Sample 1 Peak Extraction Results.

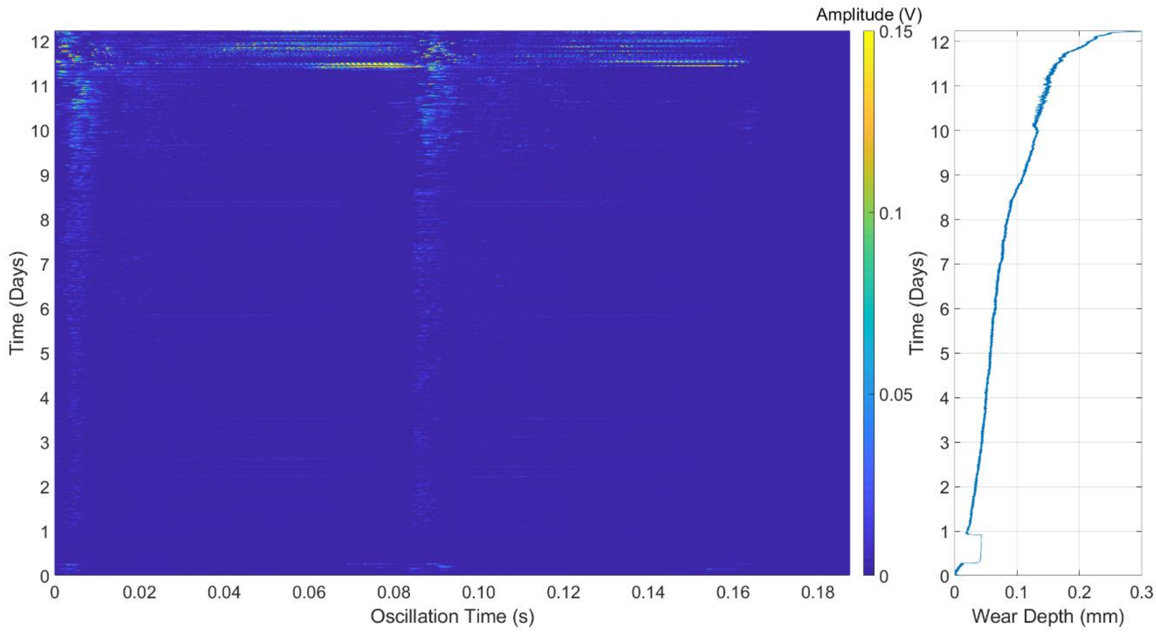

Figure 254 - Sample 2 Peak Extraction Results.

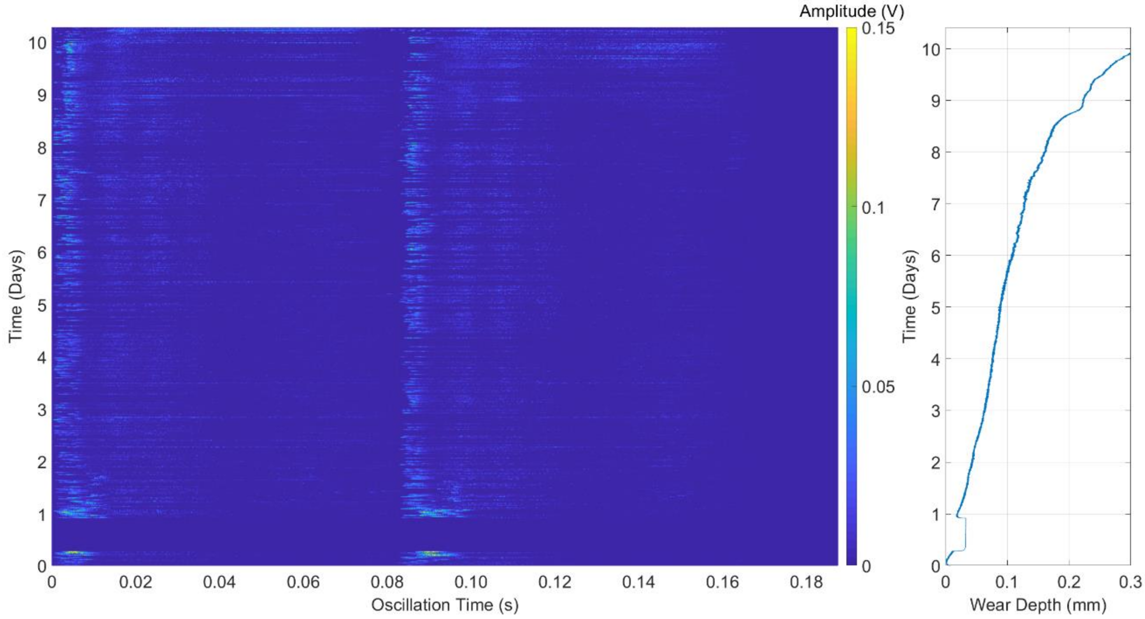

Figure 255 - Sample 3 Peak Extraction Results.

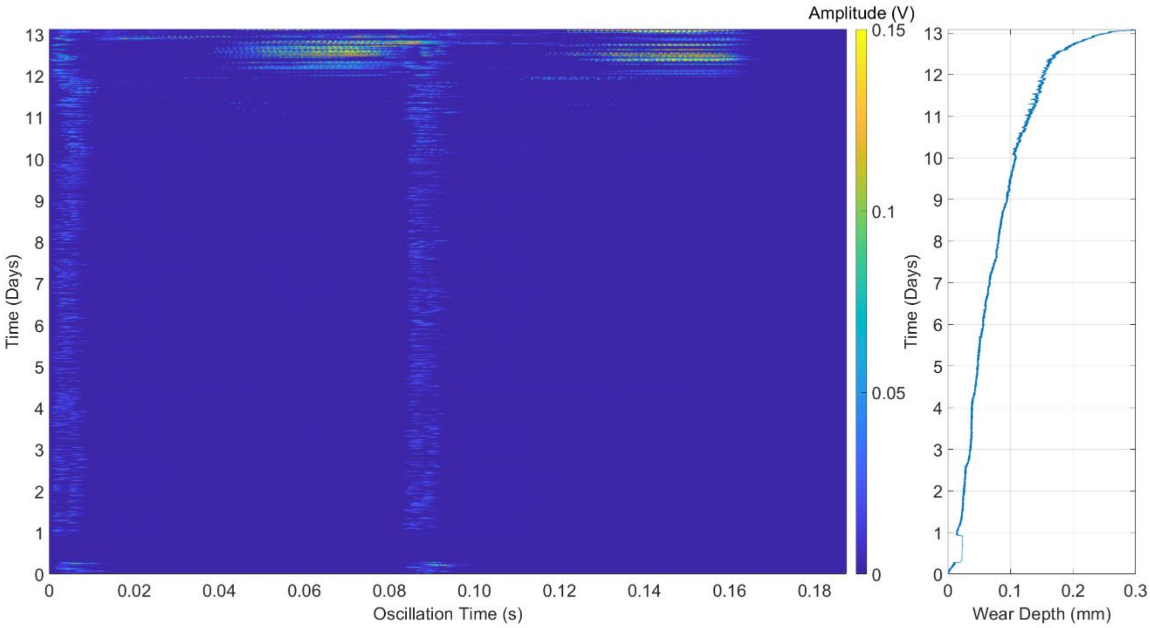

Figure 256 - Sample 4 Peak Extraction Results.

All of the figures are similar in terms of the relationship between wear and the extracted transient bursts. At the start of the test, the bursts of high amplitude are largely concentrated around the points within the cycle when the counterface is stationary. As the test progresses, these bursts occur at all stages within the reciprocating cycle. The amplitude and location of the transient bursts appears to largely increase when approaching the glass fibre structural backing of the liner material, with an exception of sample 3 where a small change was recorded during this transition phase. However, this effect may be masked by the contour levels being chosen to provide a good range of detail in all figures.

As can be seen in Figures 257 - 260, the start of the oscillation at each wavestream appears to alter slightly with respect to time. This was said to occur due to the detection method used by the analysis code to identify the start of the oscillation of the counterface. In future studies, this is an area which could be optimised in order to view these transient bursts in higher resolution. In order to further quantify the peak extraction results, the sum of the transient bursts per wavestream was plotted with respect to time, as seen in Figures 261 – 264.

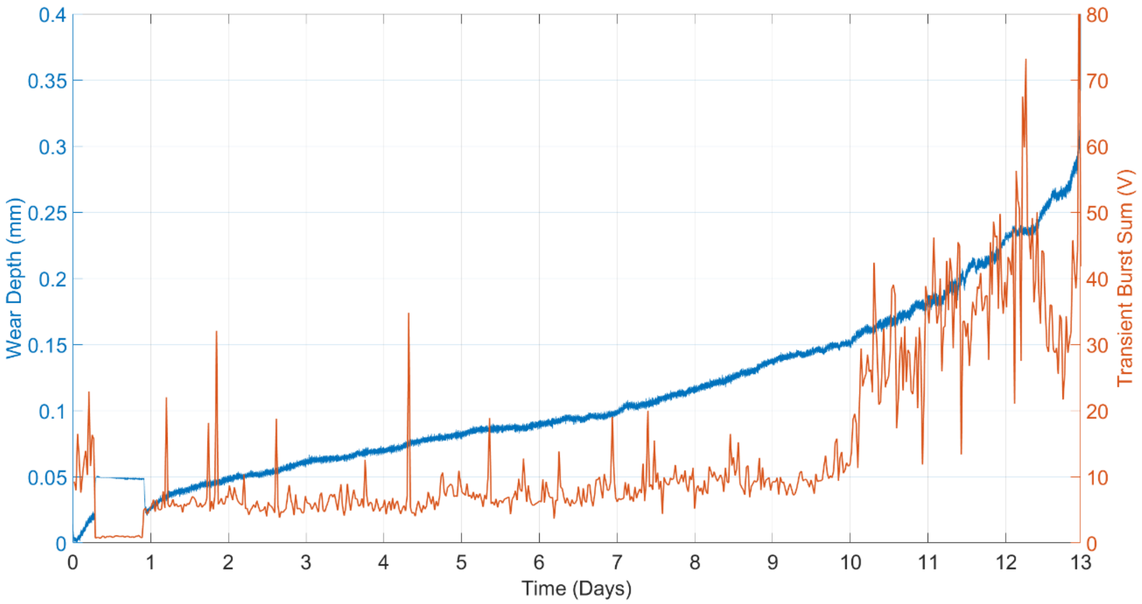

Figure 257 - Peak Power Sum vs Time for Sample 1.

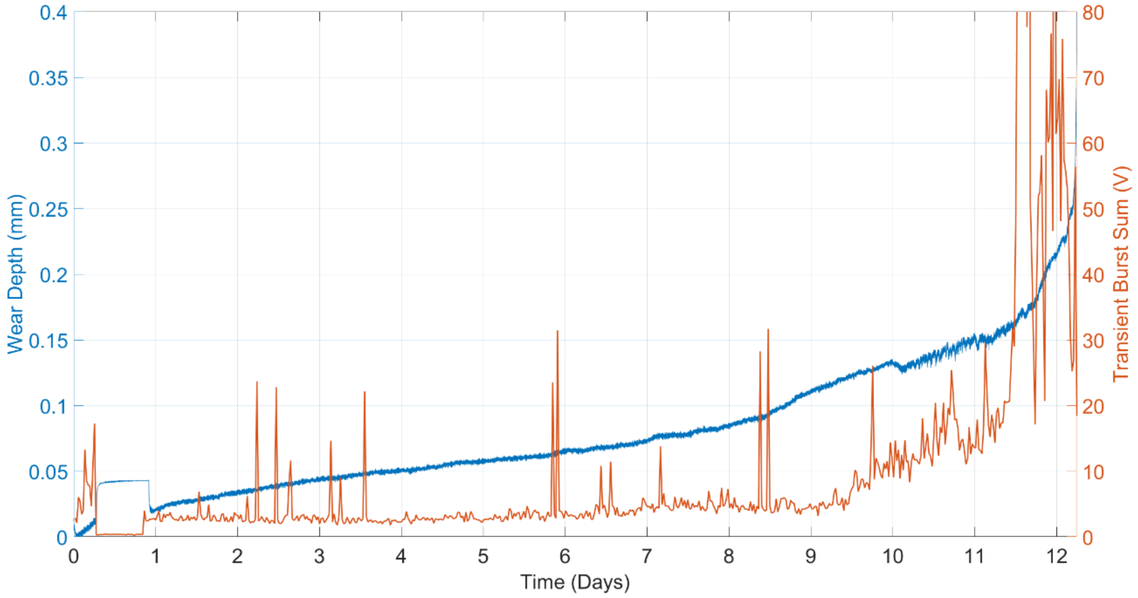

Figure 258 - Peak Power Sum vs Time for Sample 2.

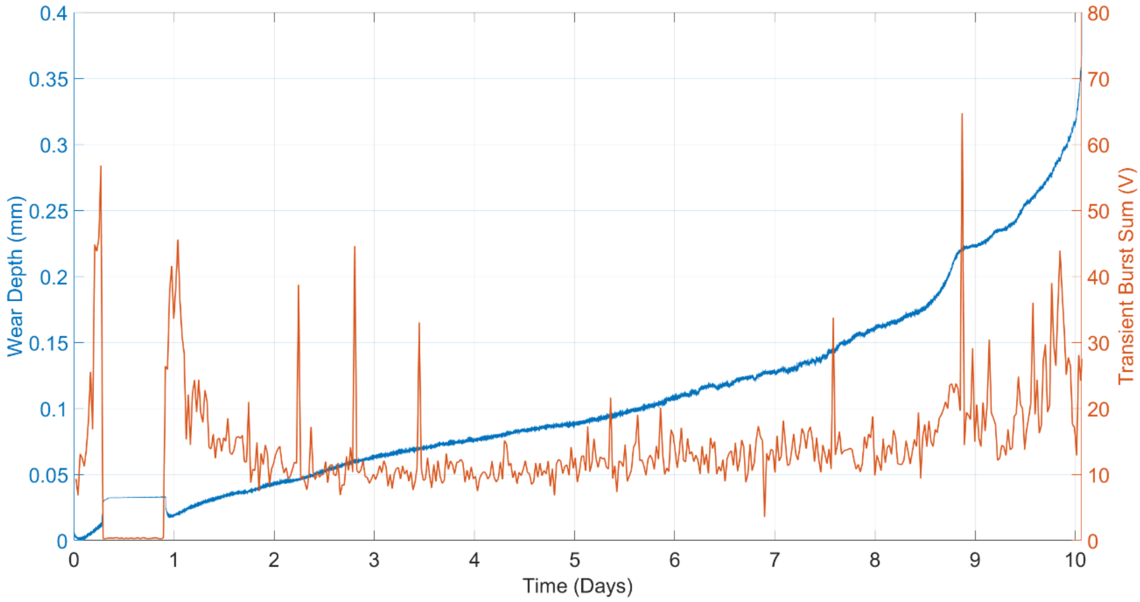

Figure 259- Peak Power Sum vs Time for Sample 3.

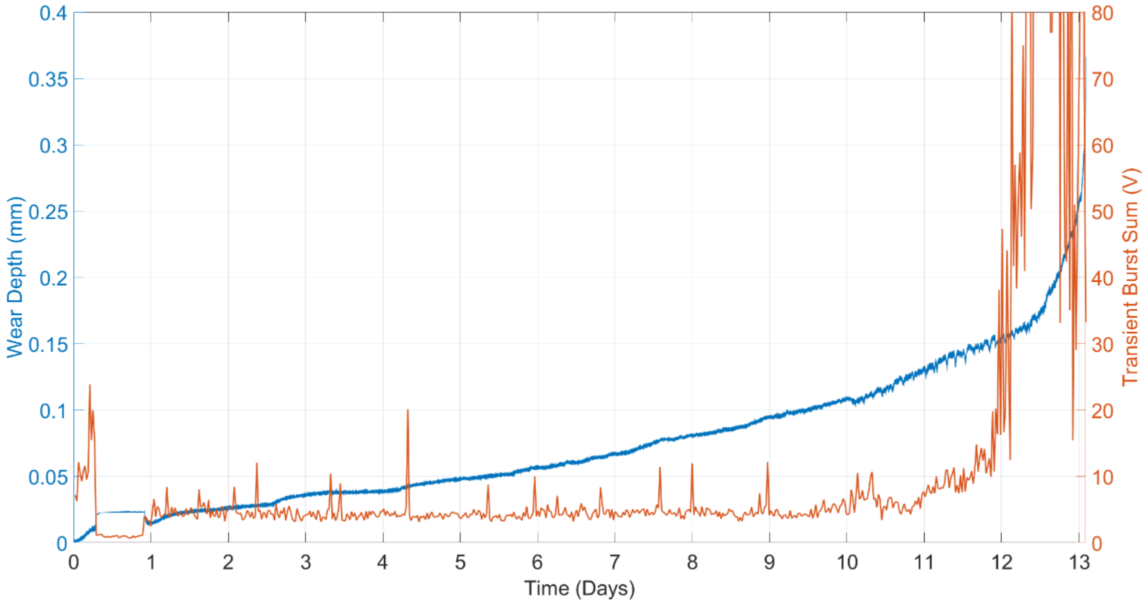

Figure 260 - Peak Power Sum vs Time for Sample 4.

With exception of Sample 2, the sum of the transient bursts per wavestream of the above graphs increase when approaching the critical wear depth of around 0.15-0.18mm. As noticed within Figure 258, the transient burst value appears to increase ahead of the wear depth reaching the glass fibre transition period for Sample 2. This was attributed to a slight misalignment of sample 2, which caused its wear depth readings to be slightly in error. It was also interesting to note that Sample 4 appeared to decrease its peak power numerical value after glass fibre contact had been achieved, but its wavestream amplitude continued rising after this bearing liner material transition period. The reason behind this anomalous decrease in the value of the transient burst sum of sample 4, is currently unknown. By using this sum approach as opposed to the more detailed contour plots, a more easily detectable change for Sample 3 was observed due to this quantification. Alongside, the glass fibre transition period, it was observed that both the amplitudes and the peak power sum values of Samples 1, 3 and 4 displayed higher amplitudes at the wear-in process of the bearing liner, than the values occurring during the plateau phase.

8.4 Discussion

This part of the research program was conducted in order to develop an analysis technique which could be applied to any consistent reciprocating machinery. A review of current literature was conducted which provided only a small number of related papers to the application under consideration. This included both the application of Acoustic Emission monitoring upon self-lubricating composite bearing liner materials, along with the more general application of Acoustic Emission upon reciprocating machinery. The few papers published, used already existing parameters of Acoustic Emission signals such the monitoring of amplitude and RMS.

The development process consisted of an initial visual investigation into wavestream progression during the wear test. This allowed the author to view the changes in characteristics of the collected wavestreams throughout the wear process of the bearing liner. Having observed these changes, certain characteristics were identified, and a method was developed to quantify these characteristics based on the time-domain wavestream data. These parameters included the amplitude of the wavestreams at peak sliding velocity, along with the collection of the transient bursts of Acoustic Emission energy. By comparing these parameters over the period of the testing procedure, the results were graphically represented and clear links to the underlying wear characteristics were able to be seen.

Regarding the wavestream amplitude progression results, it was clear to see that the trend follows the typical wear curve of the bearing liner when in sliding friction with a counterface. In all of the samples, it was observed that the initial wear-in period of the material was more aggressive than the plateau stage of wear. This was expected, as no PTFE third-body transfer layer had been established at the initiation stage of wear and therefore the rough, non-PTFE coated, asperities of the counterface provide an aggressive wear mechanism until this transfer layer is deposited. During this stage, as seen by the full-bearing testing within Chapter 6, Figure 227 (Page 242), the friction coefficient, represented by torque, exists at an increased value until the plateau region is reached. Within literature it was found that the amplitude of the Acoustic Emission energy is related to the frictional energy of the system (Jiaa & Dornfeld, 1990). Within condition monitoring, the ideal characteristic of any system is the ability to apply a prognostic approach with regards to the health of the monitored machinery or component, instead of a diagnostic one. It was therefore very exciting to observe the pattern of the wavestream amplitude values when a certain wear depth was being approached. This wear depth equated to a nominal value of some 0.15-.018mm through the bearing liner, where the structural glass fibre backing is the primary constituent. When this region became the primary sliding surface medium between the bearing liner material and the steel counterface, the energy contained within the wavestream increased as a whole and this provided the ability of the developed code to detect this material transition change accurately.

Furthermore, the transient bursts of energy, displayed by the wavestreams throughout the bearing liner wearing process were collected and displayed. Through the use of MatLab these transient bursts were extracted from their parent wavestreams and displayed graphically. A contour plot was initially created for all four samples which allowed the author to investigate with detail the progression of these Acoustic Emission energy bursts with wear, and their position within the reciprocating cycle. When a clear relationship between the material composition transition wear depth and this parameter under consideration was established, a more straightforward technique for displaying these results graphically was created. This involved the summation of all the transient bursts within an individual wavestream for each sample, plotted against the wear depth of each sample respectively. This type of graphical representation, allowed the clear determination that the glass fibre backing region was able to also be detected through the measurement of these transient bursts of energy.

This method can be directly compared to the results obtained by both the temperature analysis results (presented in Chapter 5) and the results obtained by the more traditional frequency domain analysis, via the use of the Fourier Transform (presented in Chapter 6). In all cases, the structural backing of the bearing liner was able to be detected when it came into contact with the counterface. Although this analysis technique was proven to be functional and provided very similar results to the frequency domain analysis, due to its low maturity level, further work is required in order to increase its accuracy. The type of improvements would require further testing, improved detection of the wavestreams' starting point and finally, a more robust method of measuring the amplitude of the wavestreams.

8.5 Conclusion

A novel time domain method of analysing Acoustic Emission wavestreams within a reciprocating environment was developed. This method was versatile due to its autonomy and ability to be tailored to specific applications via the specification of the test parameters within the MatLab script. The output results were able to consistently detect certain wear characteristics which were investigated in previous chapters. These characteristics included the wear-in transfer layer deposition period, the wear plateau region of the bearing liner and finally the material composition transition region from a PTFE rich environment to the glass fibre structural backing of the bearing liner. The results gathered via the use of this novel technique, were able to be directly compared to both the temperature and the frequency domain analysis method which in turn provide a proposed condition monitoring system with a higher degree of confidence.

Chapter 9: Discussion, conclusions and future work

This PhD research programme was initiated for the purpose of developing a condition monitoring framework for self-lubricating bearings developed by SKF. In order to initiate the project, an extensive tribological understanding of the product was required to be developed by the author in order to apply such understanding to the findings of the testing programme. A literature study was conducted on self-lubricating bearing materials, along with current condition monitoring techniques utilised within rolling element bearings. The methods which were identified as translatable, were then intended to be implemented upon a test-bench. Therefore, a research test bench with multiple sensing capabilities was developed and the identified sensing techniques implemented. The developed test bench consisted of a coupon testing set-up where accelerated conditions were present. In order to validate the findings, full bearing test benches located within SKF were utilised. A database of results was developed consisting of temperature, wear and Acoustic Emission data. These were in turn utilised in order to identify key tribological features of the self-lubricating material under test, which could be used to produce a condition monitoring system.

The initial study focused on temperature which was an appealing measurement parameter from the industrial sponsor's perspective, due to the ability for the measurement parameter to be monitored non-intrusively and was also driven by the sponsor, due to its experience in the potential of temperature as a tribological by-product monitoring parameter through years of extensive full-scale bearing testing. Before allocating a large amount of resource onto developing a condition monitoring technique around such parameter, a feasibility study was conducted. A thermal gradient study was conducted on a fully assembled rod-end to validate that a significant temperature increase was able to be recorded on the outer face of the rod-end as described within section 5.1. After temperature was validated as a useful monitoring parameter, the characteristics of the temperature curves throughout the bearing liner's life under test were investigated. It was observed that as the bearing liner was consumed throughout the wear process the temperature increased significantly during the end-stages of the liner's life. Therefore, a system where a temperature deviation was able to be detected was deemed appropriate. Due to the range of environmental conditions in which a helicopter is intended to operate, an absolute temperature threshold value could not be determined. Therefore a comparative system was developed, where each bearing was compared to others within a system. Therefore the residual temperature difference of each bearing comparison combination was the main focus of the study.

Utilising existing industrial process control techniques, a statistical process control method was developed where deviation of the residual temperature comparisons was able to be detected (Section 5.2). This technique was partly successful in identifying a key feature of the liner material; the point of the material composition transition of the self-lubricating liner. It is known that such a change occurs at a wear depth of around 0.15-0.18mm of the total 0.28mm of available material and therefore, when a deviation was detected between the specific 'failing' bearing and each of the partner bearings within the system, the user assumes that such a wear depth is reached.

Another monitoring technique developed was the comparison between all bearings in a system through the use of the Pearson product-moment correlation coefficient (ρ) (Section 5.3). This coefficient is a numerical output which ranges between $-1 \leq \rho \leq 1$ and effectively describes the trend similarities between two data sets. Once a temperature deviation of one bearing liner within the system had occurred, the Pearson product-moment correlation coefficient was predicted to change in value significantly, therefore acting as an alarm signal. Unfortunately, due to the sensitivity of such method, the results were varied in terms of accurate detection but results showed that a detection between 0.075-0.15mm was possible. It is important to note, that only one late detection was made by the system, while many early detections were present. This would be acceptable as a system due to the prevention of late detection which could be catastrophic, although it may have financial implications of artificially reduced bearing life.

An observation which was made during the life-testing of coupon samples, was the temperature behaviour of the self-lubricating liner during the phase where the material composition change occurs (Section 5.4). During and after such material transitions, the temperature appears to have an increased volatility. This was quantified by applying a rolling window which calculated the standard deviation of the data. It was clearly seen that a high increase of the standard deviation was present during the transition period and it was proposed that such a detection could help aid the reduction of false signals developed within the previously stated techniques.

Finally, the temperature data gathered from SKF's full bearing test bench (Rig H) was utilised. A study was conducted, where the rate of temperature recovery was evaluated but unfortunately the results did not show any positive outcomes that could be related to the phase of wear of the liner material.

Temperature was therefore proven to be a valid parameter to implement into a condition monitoring system due to the specific composition of the SKF liner material. Generally, an alarm signal was able to be produced at the material composition change of the liner at a wear depth of 0.18mm, at which point it is envisaged that the maintenance team of the helicopter in operation would be notified for the specific 'failing' bearing to be inspected and changed.

The second monitored parameter which was identified as a potential condition monitoring signal, was Acoustic Emission. Once again the appeal of this technique lies with its non-destructive nature. The data gathered from such a technique was divided into two analysis types. One consisted of the typical frequency domain analysis and the second of a self-developed time-domain analysis technique.

Initially the waveforms gathered from the experimental set-up were compared to each other within the time-domain, in order to view their progression throughout the wear process of the liner material. Distinctive difference were noticed in the form of amplitude increases, mid-reciprocation spikes and initial spike amplitude (Section 6.3.2). Through the use of a binned Fast Fourier Transform, strong trends were able to be seen in the evolution of the frequency domain with respect to the wear depth of the self-lubricating liner material. By inspecting the energies of specific frequency bands with respect to time, it was noticed that, once-more, when the glass fibre transition period of the liner material was reached a significant activity was recorded.

Having observed the success of such technique on coupon testing, a full-bearing acoustic emission set-up was developed for application upon Rig H (full scale bearing test bench). During this stage, the industrial sponsor proposed a study to be conducted where continuously gathered parametric data was compared with the developed waveform processing technique. This proposition was made in order to validate if such a monitoring technique can be utilised for an on-ground maintenance interval method, the major issue identified with acoustic emission being its energy intensive nature. On the main rotor, power supply is limited and is only possible in small quantities, which would not satisfy the requirements of a high frequency acquisition system. Therefore, if such an NDT technique could take the form of a sensor being bonded upon the rod-end of the helicopter when grounded and in turn the pilot manoeuvring the blades in such a way where a reciprocation is conducted. Such a manoeuvre was conducted by the test-bench during its quasi-static measurements, where the bearing would position itself at a neutral axis and slowly reciprocate through the full range of motion (±10º). Therefore, if the findings of the continual dynamic measurements matched those of the quasi-static, a justification of employing such a technique could be made.

Once again, the findings of such techniques were positive in both the dynamic and quasi-static measurements. In both cases, the energies present within the gathered data were significantly increased when the glass fibre transition period was introduced and therefore this monitoring technique was deemed appropriate for identifying the point of the material composition change of the liner.

In order to evaluate the importance of the features identified in the time domain through visual inspection, a technique to quantify such features was developed. This technique monitored the increase in the amplitude of the gathered waveforms through the use of an enveloping method and further monitored the residual peaks, which occurred outside a fitted saw tooth function (Section7.2).

The findings showed an increase in waveform amplitude and residual peak power sum of the gathered data, which were directly related to the depth of the material composition change. Therefore the time-domain analysis technique was able to identify such a transition period and could be utilised as another form of a maintenance alarm signal.

With regards to future work, the first step towards expanding the current condition monitoring framework developed within the PhD programme, would be to improve the current test-bench by eliminating the possibilities of sample misalignment which could produce skewed results. Furthermore, an increase in the volume of gathered test data is required in order to further validate the current experimental results. A different test procedure is also recommended, whereby the future user of the test bench can alter the loads and speeds of the test in order to view the impact of such parameter changes on the developed techniques.

Regarding the temperature monitoring methods, a significant improvement regarding the control limit calculations is required, in order to tailor such limits to the specific application. Currently, an industrial standard of 3 standard deviations of a training set period is used but this could be made redundant through the development of a more sophisticated process.

A further acoustic emission investigation is also recommended to be conducted whereby the user could utilise a flat response sensor in order to identify further frequency bands of interest. Further, acoustic emission data gathering should be continued, especially in full-scale bearing test benches.

Expansion of the study to consider alternative sensing techniques is essential in order to complement the current sensing methods. Such techniques could include ultrasonic or capacitance measurements. These techniques will require their equivalent instrumentation to be fitted onto the coupon test bench (Rig Q) and consideration should be given, regarding the ability to implement onto full scale bearing test benches present within SKF.

To conclude, all of the developed condition monitoring techniques were either partially or positively successful in the identification of a ‘failing’ self-lubricating liner. Although the progression of wear can be partially tracked with such techniques, the system is predominantly reliant upon the self-lubricating liner’s material composition change to be present in order to detect a large ‘fail-safe’ signal. Although these techniques can be vital towards producing a condition monitoring system for the specific material, they could potentially not be applicable to any new liner material developed by SKF. It can therefore be envisaged that SKF could produce a self-lubricating liner material which retains its tribological performance but is able to produce distinct signals at certain wear depths for the purposes of condition monitoring.

References

Abarou, S. & Play, D., 1986. Wear Transition of Self-Lubricating Composites Used in Dry Oscillating Applications.. ASLE Transactions., 30(3), pp. 269-281.

Abarou, S., Play, D. & Kennedy, F., 1987. Wear Transition of Self-Lubricating Composites Used in Dry Oscillating Applications. ASLE Trans., Volume 30, pp. 269-281.

Aerosurrance, 2017. Aerosurrance. [Online]
Available at: http://aerossurance.com/helicopters/b429-tr-pcl-bearing-failure/
[Accessed 18 01 2018].

AMPEP, 2001. ETI E24.

Anderson, J. C., 1982. Tribology. Wear of Commercially Available Plastic Materials, pp. 255-263.

ASTM, I., 2016. Standard Test Method for Linearly Reciprocating Ball-on-Flat sliding Wear.,: G02.40.

Barron, R., 1996. Engineering Condition Monitoring Practice, Methods and Applications. 1st ed. Essex: Addison Wesley Longman Inc.

Bearing Specialists Association, 2014. Bearing Specialists Association. [Online] Available at: http://www.bsahome.org/tools/pdfs/history_of_bearings_web.pdf

Bell, A., 2009. ARD511: Wear Hypothesis for SKF Airframe Self-lubricating Bearing Technology, Clevedon: SKF.

Bell, A., 2017. Private Communication. Clevedon: SKF.

Bell, A., 2018. Private Communications. Clevedon: SKF.

Belyi, V. A., Kholodilov, O. V. & Siviridyonok, A. I., 1981. Acoustic Spectrometry as Used for the Evaluation of Tribological Systems. Wear, Volume 69, pp. 309-319.

Bernard, P., 2011. Discrete Modelling of Woven Structures.: SKF Ltd..

Bertera, B., Jenkins, D., Martinelli, L. & Price, C., 2015. Wear and Friction Analysis of PTFE., Cardiff: Cardiff University.

Biering, D., 2014. TriStar - Engineered Plastic Solutions.. [Online]
Available at: https://www.tstar.com/blog/rail-industry-safety-and-self-lubricating-bearings
[Accessed 18 01 2018].

Blanchet, T. A. & Kennedy, E. F., 1991. Effects of Oscillatory Speed and Mutual Overlap on the Tribological Behaviour of PTFE and Selected PTFE-based Self-Lubricating Composites. Tribology Transactions, 34(3), pp. 327-334.

BOARD, N. T. S., 2017. Helicopter Specialist's Factual Report , Texas: National Transportation Safety Board.

Bowden, F. P. & Leben, L., 1939. The Nature of Sliding and the Analysis of Friction. pp. 371-391.

Brockley, C. A., Cameron, R. & Potter, A. F., 1967. Friction-Induced Vibration. ASME Journal of Lubrication Technology, pp. 101-108.

Brookes, C., 2014. Introductory Econometrics for Finance: Cambridge University Press.

Carnes, K., 2005. The Ten Greatest Events in Tribology History. June, pp. 38-47.

Choudhury, A. & Tandon, N., 2000. Application of Acoustic Emission Technique for the Detection of Defects in Rolling Element Bearings. Tribology International, Volume 33, pp. 39-45.

Collacott, R. A., 1977. Mechanical Fault Diagnosis and Condition Monitoring - Vibration Analysis. 1 ed: Springer-Verlag.

Cross, E. J., Worden, K. & Qian, C., 2014. Cointegration: A Novel Approach for the Removal of Environmental Trends in Structural Health Monitoring Data. The Royal Society , pp. 1-21.

Davies, A., 1998. Handbook of Condition Monitoring Techniques and Methodology. 1st ed. Cardiff: Chapman & Hall.

Dornfeld, D. A. & Handy, C., 1987. Slip Detection Using Acoustic Emission Signal Analysis. Int. Conf. on Robotics and Automation, March, pp. 1868-1875.

Douglas, R. M., Steel, J. A. & Reuben, R. L., 2006. A Study of the Tribological Behaviour of Pistol Ring/Cylinder Liner Interaction in Diesel Engines Using Acoustic Emission. Tribology International, Volume 39, pp. 1634 - 1642.

Downham, E., 1980. Vibration Monitoring and Wear Prediction. Cambridge, Second International Conference on Vibrations in Rotating Machinery.

El-Ghamry, M. H., Reuben, R. L. & Steel, J. A., 2003. The Development of Automated Pattern Recognition and Statistical Feature Isolation Techniques for the Diagnosis of Reciprocating Machinery Faults Using Acoustic Emission. Mechanical Systems and Signal Processing., 17(4), pp. 805-823.

Evans, D. C., 1981. Self-lubricating Bearings. Industrial Lubrication and Tribology, pp. 132-138.

Evans, D. C. & Senior, G. S., 1982. Self-lubricating Materials for Plain Bearings. Tribology International, pp. 243-248.

Fusaro, R. L., 1990. Self-Lubricating Polymer Composites and Polymer Transfer Film Lubrication For Space Applications. Tribology International, 23(2), pp. 105-122.

Fusaro & Robert, L., 1980. Mechanisms of Lubrication and Wear of a Bonded Solid Lubricant Film, Cleveland, Ohio: National Aeronautics and Space Administration.

Gardos, M. N., 1981. Theory and Practice of Self-Lubricated, Oscillatory Bearings for High-Vacuum Applications. Lubrication Engineering, 37(11), pp. 641-656.

Gawarkiewicz, R. & Wasilczuk, M., 2006. Evaluation of the Sliding Distance in the Oscillatory Motion Movement of Small Amplitude. Esslingen, Automotive and Industrial lubrication., pp. 458-462.

Gill, J. D. et al., 1998. Monitoring of a Large Reciprocating Compressor. s.l., Monash University.

Giltrow, J. P. & Lancaster, J. K., 1967. Carbon-fibre Reinforced Polymers as Self-lubricating Materials. Proc. Instn. Mech. Engrs., 182(3N), pp. 147-157.

Giltrow, J. P. & Lancaster, J. K., 1967. Friction and Wear of Polymers Reinforced with Carbon Fibres. Nature, Volume 214, pp. 1106-1107.

Gnecco, E. & Meyer, E., 2007. Fundamentals of Friction and Wear. :Springer.

Green, T. A., Lockman, S. C. & Steele, K. R., 1964. Acoustic Verification of Structural Integrity of Polaris Chambers. Modern Plastics, Volume 41, pp. 137-139.

Halme, J. K., 2002. Condition Monitoring of Oil Lubricated Ball Bearing Using Wear Debris and Vibration Analysis. Perth, 6th International Tribology Conference.

Huang, M. et al., 1998. Using Acoustic Emission in Fatigue and Fracture Materials Research. JOM, 50(11).

Igba, J., Alemzadeh, K., Durugbo, C. & Eiriksson, E. T., 2015. Analysing RMS and Peak Values of Vibration Signals for Condition Monitoring of Wind Turbine Gearboxes. Renewable Energy, Volume 91, pp. 90-106.

Ingarashi, T., Noda, B. & Matsushima, E., 1980. A study on the prediction of abnormalities in rolling bearing.. JSLE, Volume 1, pp. 71-76.

Jenkins, E., 2014. Evaluation of Wear Behaviour of Existing and New Bearing Liner Materials., Cardiff: Cardiff University.

Jennings, A. D. & Drake, P. R., 1997. Machine Tool Condition Monitoring Using Statistical Quality Control Charts. International Journal of Machine Tools and Manufacture., pp. 1243-1249.

Jiaa, C. L. & Dornfeld, A. D., 1990. Experimental Studies of Sliding Friction and Wear via Acoustic Emission Signal Analysis. Wear, Volume 139, pp. 403-424.

Kim, Y.-H., Tan, A. C. C., Mathew, J. & Yang, B.-S., 2006. Condition Monitoring of Low Speed Bearings: A Comparative Study of the Ultrasound Technique Versus Vibration Measurements. :Springer-Verlag.

King, R. B., 1979. Wear Properties of Dry Bearing Liners at Ambient and Elevated Temperatures. Wear, Volume 56, pp. 37-56.

Kumar, M., Makherjee, P. & Misra, N., 2013. Advancement and Current Status of Wear Debris Analysis for Machine Condition Monitoring.. Industrial Lubrication and Tribology, pp. 3-11.

Kurfess, T. R., Billingston, S. & Liang, S. Y., 2006. Advanced Diagnostic and Prognostic Techniques for Rolling Element Bearings. In: Condition Monitoring and Control for Intelligent Manufacturing.. London: Springer, pp. 153-181.

Lancaster, J., Bramham, R., Play, D. & Waghorne, R., 1982. Effects of Amplitude on the Wear of Dry Bearings Containing PTFE. Journal of Lubricating Technology, Volume 104, pp. 559-567.

Lancaster, J. K., 1978. Accelerated Wear Testing of PTFE Composite Bearing Materials.. Technical Report 78046, pp. 1-16.

Lancaster, J. K., 1981. On the Initial Stages of Wear of Dry-bearing Composites.

Lancaster, J. K., 1982. Accelerated Wear Testing as an Aid to Failure Diagnosis and Material Selection. : Butterworth & Co. pp. 323-330.

Lancaster, J. K., 1990. Material-specific Wear Mechanisms: Relevance to Wear Modelling. Wear, 141(1), pp. 159-183.

Lancaster, J. K., Bramham, R. W., Play, D. & Waghorne, R., 1982. Effects of Amplitude of Oscillation on the Wear of Dry Bearings Containing PTFE. Journal of Lubrication Tribology, Volume 104, pp. 559-567.

Lancaster, J. K. et al., 1980. Third Body Formation and the Wear of PTFE Fibre-Based Dry Bearings. Journal of Lubrication Technology, Volume 102, pp. 236-245.

Li, J. C. & Li, S. Y., 1995. Acoustic Emission Analysis for Bearing Condition Monitoring. Wear, Volume 185, pp. 67-74.

Liao, C. et al., 2011. Study on Stick-Slip Friction of Reciprocating O-Ring Seals Using Acoustic Emission Techniques. Society of Tribologists and Lubrication Engineers., Volume 55, pp. 43-51.

Majumdar, B. C., 2008. Introduction to Tribology of Bearings. :S. Chand.

Mba, D. & Rao, R. B., 2006. Development of Acoustic Emission Technology for Condition Monitoring and Diagnosis of Rotating Machines; Bearings, Pumps, Gearboxes, Engines and Rotating Structures. The Shock and Vibration Digest, 38(1), pp. 3-16.

Miller, R. K., Hill, K. E. & Moore, P. O., 2005. Non-destructive Testing Handbook. Third ed.:Amer Society for Non-destructive.

Morgan , E. J. & Plumbridge, J. W., 1987. The Effect of Humidity on Dry Bearing Torque. Wear, pp. 215-223.

N/A, 1970. Fiberglide and Fiberslip Bearing Liners and Friction Materials. Industrial Lubrication and Tribology, 22(11), pp. 317-318.

Nabhan, A., Ghazaly, N. M., Samy, A. & O, M. M., 2015. Bearing Fault Detection Techniques - A Review.: ResearchGate.

Nair, A. & Cai, C. S., 2010. Acoustic Emission Monitoring of Bridges: Review and Case Studies. Engineering Structures, Volume 32, p. 1704–1714.

Oakland, J. S., 1996. Statistical Process Control - A Really Practical Guide. 3rd ed. Oxford: Butterworth-Heinemann.

Phakatkar, H. G. & Ghorpade, R. R., 2009. Tribology.

PhaseIVEngin, 2018. www.phaseivengr.com. [Online]
Available at: https://www.phaseivengr.com/product/temperature-thin-micro-t-rfid-data-logger-150c-miniature/
[Accessed 16 03 2018].

Pitenis, A. A. & Dowson, D., 2014. Leonardo da Vinci's Friction Experiments: An Old Story Acknowledged and Repeated. Tribol Lett, Volume 56, pp. 509-515.

Pooley, D. M. & Tabor, D., 1972. Friction and Molecular Structure: the Behaviour of some Thermoplastics. London, Proc. Roy. Soc.

Qiu, M., Gao, Z. L., Yao, S. J. & Chen, L., 2011. Effects of Oscillation Frequency on the Tribological Properties of Self-lubrication Spherical Plain Bearings with PTFE Woven Liner. Key Engineering Materials, Volume 455, pp. 406-410.

Raaz, N. A., 2016. Flow Chart of Fabric Manufacturing, Banani: Textile Merchandising.
Research-Center, N., n.d. AE Signal Features. [Online]
Available at: https://www.nde-ed.org/EducationResources/CommunityCollege/Other%20Methods/AE/AE_Signal%20Features.php

Rigney, D. A. & Hirth, J. P., 1979. Plastic Deformation and Sliding Friction of Metals. Wear, Volume 53, pp. 345-370.

Rogers, L. & Stambaugh, K., 2014. Application of Acoustic Emission Technology for Health Monitoring of Ship Structures. Ship Structure Committee.

Rowland, K. T., 1974. Eighteenth Century Inventions. :David & Charles.

SAEAerospace, 2001. AS81819 - (R) Bearings, Plain, Self-Aligning, Self-Lubricating, High Speed Oscillation -65 to +160°F General Specification For, : SAE International Group.

Sano, K. & Fujimoto, K., 1979. Microscopic Aspects of Fracture and Acoustic Emission in Metals. Fundamentals of Acoustic Emission, pp. 131-164.

Sayles, R. S. & Poon, S. Y., 1981. Surface Topography and Rolling Element Vibration. Precis Eng, Volume 3, pp. 137-144.

Shevlyakov, G. L. & Oja, H., 2016. Robust Correlation: Theory and Applications. :Wiley; 1 edition.

SKF, 2013. Internal Communications., Clevedon.

SKF, 2014. Internal Sales Report, Clevedon.

Sliney, H. E., Jacobson, T. P. & Munson, H. E., 1975. Dynamic Load Capabilities of Graphite-fibre-polyamide Composites in Oscillating Plain Bearings to 340°C (650°F). Washingston D.C.: NASA TN D-7880.

Spanner, J. C., 1974. Acoustic Emission Techniques and Applications. 1st ed. Illinois: Intex Publishing Company.
Steijn, R. P., 1968. The Sliding Surface of Polytetrafluorethylene: An Investigation with the Electron Microscope. Wear, Volume 12, p. 193.

Tan, C., 1990. Application of Acoustic Emission to the Detection of Bearing Failures. Proceedings, Tribology Conference, pp. 110-114.

Tan, C. K., Irving, P. & Mba, D., 2007. A Comparative Study on the Diagnostic Capabilities of Acoustic Emission, Vibration and Spectrometric Oil Analysis for Spur Gears. Mechanical Systems and Signal Processing., 21(1), pp. 208-233.

Tetelman, A. S., 1972. Acoustic Emission and Fracture Mechanics Testing of Metals and Composites., Los Angeles: School of Engineering and Applied Science, University of California, Los Angeles..

UE, s., 2018. UE Systems inc. The Ultrasound Approach. [Online]
Available at: www.uesystems.com
[Accessed 17 01 2018].

Watkins, J. C., 1994. An Introduction to the Science of Statistics: From Theory to Implementation. Arizona.

Worden, K., Cross, E. J., Antoniadou, I. & Kyprianou, A., 2014. A Multiresolution Approach to Cointegration for Enhanced SHM of Structures Under Varying Conditions - An exploratory Study. Mechanical Systems and Signal Processing, Volume 47, pp. 243-262.

Zhang, S. et al., 2004. Statistical Condition Monitoring Based on Vibration Signals. QUT.

Zhou, W., Habetler, T. & Harley, R. G., 2007. Bearing Condition Monitoring Methods for Electric Machines: A General Review. Cracow, Institute of Electrical and Electronics Engineers.